A Study of Magnetic Thin Film Corrosion Mechanisms with the Development of a Novel On-Line Coupling Technique and with Microstructural and Magnetic Cross-Sectional Profiling Techniques

Danhua Xu

B.S., Applied Physics, Tongji University, Shanghai, China, 1985

M.S., Materials Engineering, San Jose State University, CA, 1994

A dissertation presented to the faculty of the

OGI School of Science & Engineering

at Oregon Health & Science University

in partial fulfillment of the requirements for the degree

Doctor of Philosophy

in

Electrical Engineering

June 2008

This dissertation "**A Study of Magnetic Thin Film Corrosion Mechanisms with the Development of a Novel On-Line Coupling Technique and with Microstructural and Magnetic Cross-Sectional Profiling Techniques**" by Danhua Xu has been examined and approved from the following Examination Committee:

Dr. Jack M. McCarthy
Assistant Professor of Biomedical Engineering
Dissertation Adviser

Dr. Rajendra Solanki
Professor of Electrical Engineering

Dr. Paul G. Tratnyack
Professor of Environmental and Bimolecular Systems

ACKNOWLEDGEMENT

The work in this dissertation could not have been performed and completed without supports of many people, whom I would like to thank at this time.

First of all, I would like to express my deepest gratitude to my advisor Dr Jack McCarthy for introducing me to the Ph.D program at OGI when the Materials Science and Engineering Department (MSE) was in place. Without his encouragement and inspiration, this research would never get started. His mentorship has been a mainstay of completion of this course with such a long journey. With many changes of the department and the institute, his persistence and enthusiasm have helped make these many years a true learning experience.

Special thanks go to Dr. Margaret Ziomek-Moroz for her initiation of outlining the research content with unconditional guidance at early stage of this research. Extensive discussions and experiments with assistance from her student assistant, Ms. Izumi Reed, at National Energy Technology Laboratory in Albany, OR., resulted valuable information, which led to later development of much more complex experimental setups and theories derived.

I would also like to thank Dr. Milton Scholl for providing professional expertise with extensive discussion and constructive criticism in each step of the experiments. His vision and acute mind helped me to achieve well-organized contents with necessary formulations and ingredients in this research. Without his care and efforts, many critical explanations could be in jeopardy and meaningless. I am obligated to another OGI veteran, Dr. Jody House for sharing her expertise and involvement in many discussions on how to proceed with AFM and MFM measurements and her intuitional support as a member of my qualification committee.

It has been a pleasure to work with many staff members including Dr. X. Gao and Dr. D. Ferrer for all microstructural analysis at TEM laboratory of J. J. Pickle Research Center of University of Texas at Austin. Sharing of expertise and experiences involving TEM imaging techniques and X-ray analysis from this group is highly appreciated. The TEM

works are not achievable without exceptional jobs performed on FIB for sample preparations in Microstructural Analytical Group at Cerium Laboratory of Austin. I thank sincerely to leaders of this group Dr. J. Gazda and Ms. L. Ballast for help.

A huge debt is owed to both technical and business management teams at Fujitsu Computer Products of America, for consistently allocating financial funds to support this research over such a long period of time, even during the quenching budget years. I am also grateful to corporate support for allowing many flexible hours during my research and for providing opportunity of sending me to several training courses associated with instrumentation and processes.

I would like to thank Mr. Takuya Amemiya for handing an opportunity to relocate an ICP-MS from a laboratory of Fujitsu Microelectronic Company to my ownership, which was used as one of the core instruments in this research. Also his liaison role to Fujitsu laboratories and technical staffs providing amicable benefits in obtaining technical assistances is greatly appreciated.

To my colleagues and friends, I thank you for caring, understanding, and cooperation throughout the entire course of my education. Some of my current and former colleagues are specially mentioned for their executive administrative or technical roles involving in helping me to achieve the success of this dissertation, Mr. S. Adachi, Mr. R. Pollocconi, Mr. J. Thompson, Ms. O. Smith, Mr. Y. Sawa, Mr. A. Ito, and Mr. A. Kakehi, etc.

Finally, I would like to thank my family for unwavering support, patience, and dedication to make my world a much happier and delightful.

This dissertation is dedicated to Richard and Ryland Xu and my wife De Qiong – my inspirations!

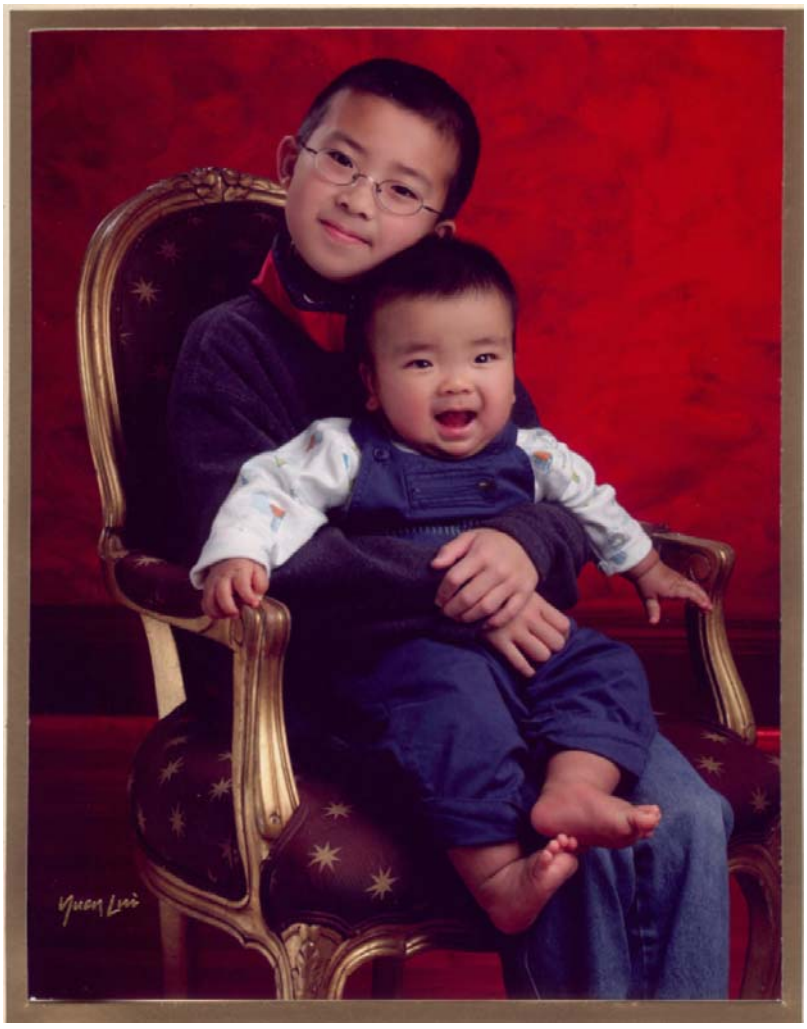

TABLE OF CONTENTS

LIST OF TABLES

LIST OF FIGURES

ACRONYMS:

ICP-MS	Inductively Charged Plasma-Mass Spectrometry
LA-ICP-MS	Laser Ablation-Inductively Charged Plasma-Mass Spectrometry
HPLC-ICP-MS	High Pressure Liquid Chromatography-Inductively Charged Plasma-Mass Spectrometry
IC-ICP-MS	Ion Chromatography-Inductively Charged Plasma-Mass Spectrometry
GC-ICP-MS	Gas Chromatography-Inductively Charged Plasma-Mass Spectrometry
CE-ICP-MS	Capillary Electrophoresis-Inductively Charged Plasma-Mass Spectrometry
CEC-ICP-MS	Capillary Electrokinetic Chromatography-Inductively Charged Plasma-Mass Spectrometry
ICP-AES	Inductively Charged Plasma-Atomic Emission Spectrometry
EC:	Electrochemistry
ESI:	Electrospray Ionization
HCP	Hexagonal Close Packed
FCC	Face Centered Cubic
BCC	Body Centered Cubic
GB	Grain Boundary
SEM	Scanning Electron Microscopy
TEM	Transmission Electron Microscopy
AFM	Atomic Force Microscopy
MFM	Magnetic Force Microscopy

VSM	Vibrating Sample Magnetometer
EDS	X-ray Energy Dispersive Spectrometry
FFT	Fast Fourier Transform

SYMBOLS

ε	Element of interested in ICP-MS measurements
ε_p	Primary element as Li, Y, and Tl
$C(\varepsilon)_t$	Elemental concentration of ε at time *t* from ICP-MS measurement
$C_o(\varepsilon)^n$	Know concentration of solution containing interested element ε used for external calibration before and after ICP-MS measurement
$I_o(\varepsilon)_a^n$	Intensity of mass count of element ε in external calibration solutions with concentration of $C(\varepsilon)^n$ before ICP-MS measurement
$I_o(\varepsilon)_b^n$	Intensity of mass count of element ε in external calibration solutions with concentration of $C(\varepsilon)^n$ after ICP-MS measurement
$I(\varepsilon_p)_t^{10}$	Intensity of mass intensity of internal spikes in electrolyte solutions containing 10 ppb primary element at time *t*
$I_o(\varepsilon_p)_t^{10}$	Extrapolated mass intensity of 10 ppb calibrated primary element at time *t*
$I_b(\varepsilon)_t$	Background intensity of mass count of element ε at time *t*
$\delta(\varepsilon_p)_t^{10}$	Normalized factor of mass intensity for 10 ppb primary element at time *t*

ABSTRACT

A Study of Magnetic Thin Film Corrosion Mechanisms with the Development of a Novel On-Line Coupling Technique and with Microstructural and Magnetic Cross-Sectional Profiling Techniques

A novel combinatory on-line technique coupling Electrochemistry (EC) with Inductively Coupled Plasma – Mass Spectrometry (ICP-MS) for *in-situ* quantitative determination of the corrosion mechanism in magnetic thin film structures has been developed in this research. Detailed construction of a system and a comprehensive methodology was described in this dissertation. Uniformly coated multi-layer magnetic thin film samples with multi-elemental alloys containing CoCrPtB and CrMo/Cr on the Ni/P substrate were used in this research for demonstrations. *In-situ* quantifications conducted in a series of experiments revealed that elemental dissolution was a predominant mechanism during corrosion courses of metallic thin film materials. At the microscopic scale, using results from depletion rate determination as well as cross-sectional analyses of microstructures and magnetic features, elemental passivity was observed to occur, depending on corrosion conditions. Without external influences, surface topographic measurements indicated that passive film could be produced at the macro-scale. The dependence of the dissolution rate of each metallic ion of alloys on electrolyte concentration, potential bias, scanning rate, and corrosion duration suggested that the most critical influential factor in corrosion mechanisms was epitaxial microstructures with strongly-oriented arrangements

of grains and grain boundaries. Through the use of cross-sectional microstructural analysis, including high resolution TEM micrography, electron FFT diffraction, and nano-probe with EDS profiling, variations of elemental spatial distributions at grains and grain boundaries due to the corrosion phenomena were discovered, which provided a comprehensive understanding of occurrences of micro-corrosion in thin film structures. Because of the unique magnetic property of magnetic thin films, extensive studies of field strengths from the surface were also performed in this research. Important magnetization variations were noticed when cross-sectional images were obtained. Finally, models of corrosion kinetics in the multiple layers of magnetic thin film structures were proposed.

CHAPTER ONE

INTRODUCTION

1.1. Magnetic Thin Film – Engineered Materials and Structures

The discovery of advanced magnetic thin film materials and structures over the last several decades has revolutionized the computer and electronic industries, profoundly changed the way humans interact and communicate, and greatly impacted the global economy. A thin film is technologically defined as a layer of materials with a thickness ranging from several angstroms (Å) to several micrometers (μm). Magnetic thin films, which are used as crucial components of non-volatile data storage applications, are synthesized and constructed into multiple layers on both surfaces of a rigid disk by various vacuum deposition methods. In a hard disk drive, a stack of such rigid disks revolves at high speeds while magnetic sensors located on the tip of an actuator sweep across the disk surfaces to magnetize the thin film materials and create a string of magnetic domain transitions. The alternative orientations of the magnetic domains can then be sensed and converted into electric signals of binary code (0 and 1).[1.1] A series of binary codes are then deciphered as recognizable data representing meaningful information. Figure 1.1 shows a glimpse of the device and magnetic thin film structure along with the magnetic pattern.

Today, millions of data storage devices are produced annually, and terabytes of critical information are permanently retained within magnetic thin films, according to industrial consensus.[1.2] It is exciting that a greater than 25% annual compound growth rate (ACGR) for magnetic storage devices has been forecasted if applications for magnetic thin films expand beyond computer electronics to commercial household appliances.[1.3] The increase in applications relies on advancements of thin film science and technologies and magnetic engineering innovations.[1.4]

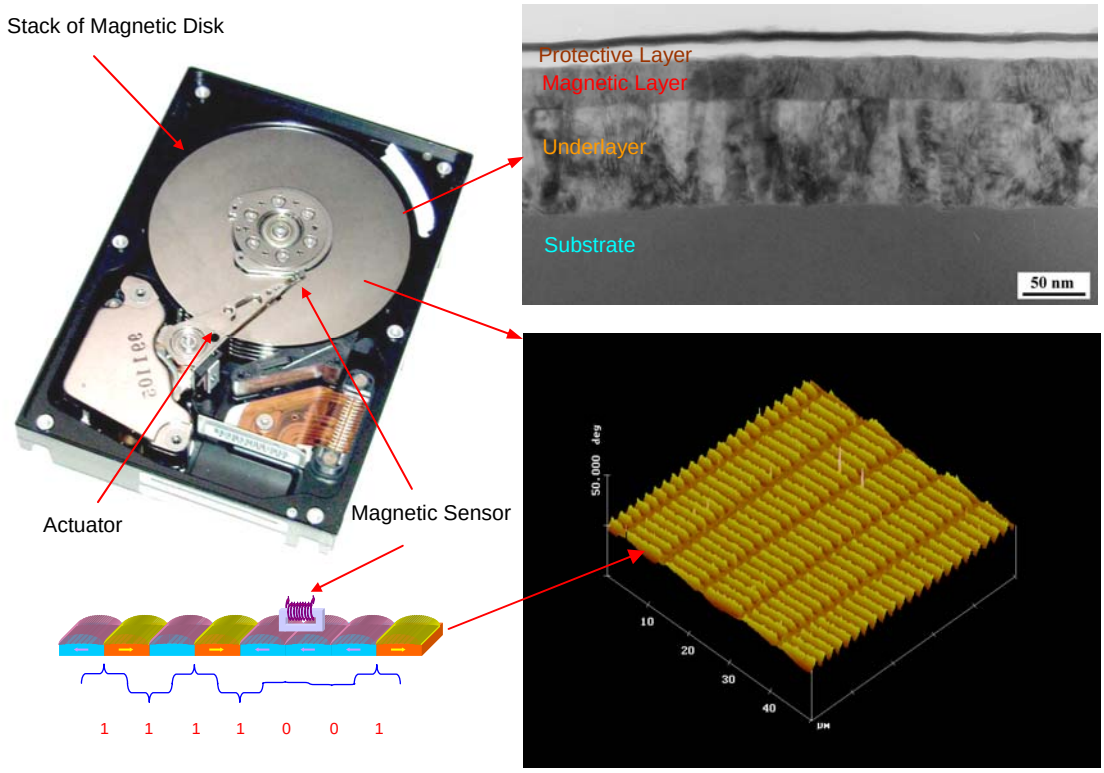

Figure 1.1. A stack of magnetic thin film-coated disks situated in a data storage unit with a cross-sectional image of the multiplayer thin film structure and magnetized pattern

As illustrated in the cross-sectional image, magnetic thin film structures consist of several different thin film layers. The overall magnetic property of the stack of the thin films is predominately created by the magnetic layer, which mostly contains cobalt alloy, such as CoCrPtB, which structural and properties will be detailed in the chapters thereafter. The other non-magnetic layers are equally important in supporting magnetization process. For example, to achieve a desirable magnetic structure, the selection of materials of the underlayer, which is mainly consisted of chromium and chromium alloy, is crucial, while surface protection against corrosion and environmental degradation must also be considered.[1.5]

Over the last half-century, extraordinary efforts have been made to minimize the physical spaces of magnetic transitions so that more information can be stored without increasing disk dimension. Such ever-increasing magnetic recording areal density, which is commonly gauged by the number of magnetic transitions per square inch, has

continuously challenged physical and technological limits of magnetic research and applications.[1.6] Although the thickness of the multilayer structures measured is only several hundred nanometers, the complexity of the multiple magnetic thin film structures and multi-elemental materials will become even more sophisticated as new concepts are developed,[1.7]-[1.9] advanced materials are created,[1.10]-[1.12] and complex structures are designed [1.13]-[1.15] to obtain better magnetic performances for future use. More detailed descriptions and specific, important features of microstructures, magnetic properties, and surface characteristics will be presented in later chapters. Although the construction of magnetic thin film structures and selection of materials have been advanced, the metallic surfaces of thin films are still vulnerable in corrosive environments. This fundamental issue must be addressed.

1.2. A Brief Summary of Corrosion Studies on Magnetic Thin Films

Although the addition of chromium to cobalt-based magnetic thin films could improve corrosion resistance,[1.16] occurrences of localized corrosion, commonly known as pitting corrosion, on film surfaces have still been observed in real applications under certain unfavorable environments.[1.17] The study and observation of localized corrosion of magnetic thin film surfaces was first reported by Smallen *et al.* in 1985.[1.18] Since then, pitting corrosion on a magnetic thin film surface has been commonly recognized as a general characteristic of corrosion on thin films and documented in limited laboratory studies.[1.19][1.20] Most of the corrosion determinations were reported qualitatively due to influences from variable film compositions,[1.21] surface structures,[1.22] and deposition conditions.[1.23][1.24] Over the past two decades, magnetic thin film corrosion studies have largely concentrated on correlating the galvanic properties of the carbon overcoat, shown as a protective layer in Figure 1.1., to deposition conditions and geometric parameters[1.25] because of the overcoat's role in protecting the metallic thin films against corrosion.[1.26] However, corrosion induced from other layers, such as the lubricant layer[1.27] and substrate layer,[1.28] made the corrosion process more unpredictable on the multilayer magnetic thin film structures. Unlike bulky metallic materials, the magnetic thin films are produced with highly-oriented columnar structures in which structural and surface defects and imperfections govern many unique properties, including corrosion resistance.[1.29]

Furthermore, interactions between metallic thin films could yield even more complications with regard to electrochemical reactions. Because of the complexity of the multilayer structural construction, quantitative determination of corrosion has always been a great challenge. Also, significantly, deterioration of magnetic properties due to corrosion on magnetic thin film structures is critical but has not been addressed.

Laboratory demonstrations of the localized corrosion phenomenon on the magnetic thin film surface had been mostly empirical and often theorized with a descriptive understanding of passive film broken mechanisms.[1.30] The initiation of corrosion has been generally recognized as resulting from the breakdown of top coverage due to the presence of chemical contaminants,[1.31] which actively interact with metallic elements through surface defects created by deposition processes[1.32] and structural imperfections.[1.33] In the course of advancements made in magnetic thin film development, electrochemistry methods were carried out in early experiments using various types of solutions, mostly binary Co alloys.[1.34] Later measurements on tri-element magnetic thin film systems obtained very similar results for corrosion current densities and potentials.[1.35] With the electrochemical polarization methods reported in most previous studies, the passivity of magnetic thin films has not been seen as a prominent feature in both low or high pH solutions. In general, having surface protection, compared with having only a bare surface, reduces about 1-order of corrosion current density. It is important to note that the substrate layer possesses about a 4-order higher corrosion current density than what it has without coverage from the upper layers. Thus, different compositions containing either corrosion inhibitors or promoters in different layers of thin films have different electrochemical responses because of competition between oxidation and metallic intrinsic bonding strength.[1.36] These studies provided practical evidence and an empirical understanding of the degradation of magnetic thin film structures and compositions due to corrosion associated with environmental conditions. But the mechanisms involved in the corrosion of multilayer magnetic thin film structures have not been fully understood and addressed since these early experiments.

Most of the studies associated with electrochemical measurements have not concluded their results without input from certain types of analytical methods to explain corrosion

phenomena. Windeln's team summarized the most commonly used surface analytical methods in storage technology for magnetic thin films, which include AFM/MFM, AES, ESCA/XPS, SEM/EDX, and TEM, *etc*.[1.37] AFM analysis is often used to provide surface topographic images and measurements, while MFM is a unique and powerful instrument that reveals magnetic patterns and field strength. Although there have only been a few reports of using the AFM technique to measure the spatial dimensions of localized corrosion,[1.38] no effort to correlate magnetic degradation and degree of corrosion has been made with the MFM method. Both AES and ESCA/XPS are generally applied to gather elemental and bonding information at the surface of a film. The surface and depth profile abilities of both techniques enable them to present elemental and compound distributions of thin film structures and the interfaces between thin film layers.[1.30][1.40] SEM and TEM are structural image tools, which are useful in visual judgments and quantification measurements, have rarely been reported in corrosion studies.

On the other hand, applications of chemical analysis methods, such as IC, ICP-OES, and TOF-SIMS presented in Gao's paper, are also highly beneficial in studying corrosion on magnetic thin film surfaces.[1.41] A direct relationship between rates of corrosion on magnetic thin films and the extracted content of both anions and cations produced on their surfaces was correlated and reported by Westre *et al.*[1.42] using the IC technique.[1.43] TOF-SIMS is a very sensitive tool used to differentiate chemically-bonded compounds, which is most suitable when organic components are encountered in corrosion production or induction.[1.44]

1.3. Motivations and Goals of This Research

Corrosion of thin film materials used in magnetic recording devices is a real concern because it has been observed in many real-life cases. For example, corrosion was observed, as shown in Figure 1.2, on a magnetic sensor, which was virtually in contact with the disk surface.

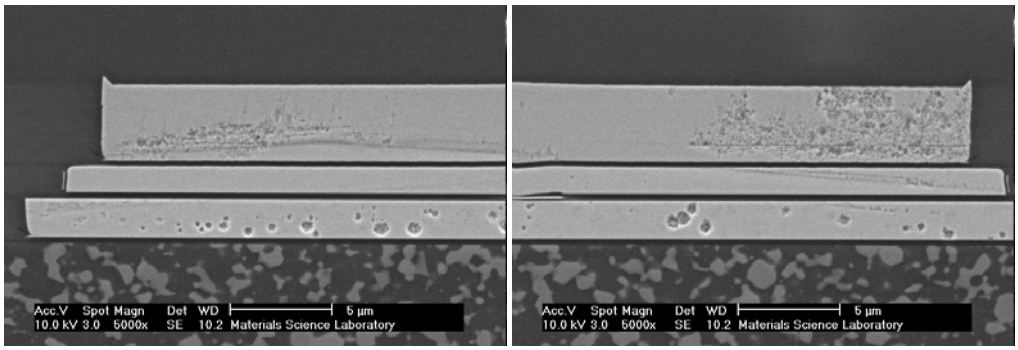

Figure 1.2. Corrosion observed on the surface of a magnetic recording component

Anions, including chlorine, sulfur, and nitride or nitrate, are occasionally detected on component surfaces inside failed devices. Their presences occur constantly in daily failure analysis activities and, thus, urgently require investigation.

Owing to the multilayer structures and multi-elemental alloy compounds of Co thin film alloys, the mechanism of creation of localized corrosion on magnetic thin film surfaces becomes unimaginably complex. Conducting this research is strongly motivated by considerations of unique thin film structures and compositions as well as some of the "mysteries" encountered in diagnosing and analyzing magnetic thin film failures.

First, spatial volume of thin film structures limits their endurance capabilities against corrosion attacks even under environments with low concentrations of contamination.[1.45] Metallic alloys in thin film structures possesses often different material phases than those in bulk materials do.[1.46] Since different phases represent different micro- and macro-structures, corrosion resistance therefore acts differently even with the same stoichiometry.[1.47] Microscopically, the atomistic evolution mechanism creates highly-oriented polycrystalline grain structures[1.48] in columnar shapes[1.49] in thin films, which challenges traditional corrosion theories and presumptions. Because of epitaxially grown, a high density of crystallographic defects via nucleation and atomistic kinetic distribution can greatly impact interactions between metallic elements and anionic species. Therefore, investigations of magnetic thin film corrosion must rely on advanced instrumentation and methodologies.

Second, corrosion studies of magnetic thin film materials could provide insight into and explain some of the "mysteries" encountered in the analysis of some cases of drive

failures. These mysterious phenomena were sometimes detected in partial spectra of either magnetic alloys or underlayer alloys during elemental analysis of debris left on the surface of magnetic sensors. For instance, Co and Pt, which were constituents in commonly used CoCrPtB alloys, were detected without the presence of Cr and B in the spectra of Energy Dispersive X-ray Spectrometry (EDS). Even more puzzling, in some other cases, Pt was detected in the EDS spectra alone, without Co, Cr, and B, as shown in Figure 1.3.

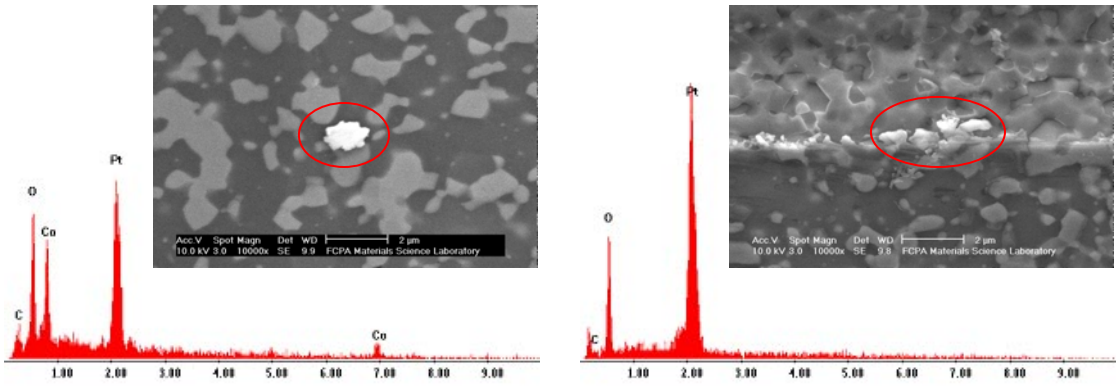

(a) (b)

Figure 1.3. EDS spectra and surface debris images detected on magnetic sensor surfaces with (a) Co and Pt without Cr and (b) Pt only

That the magnetic thin film contained stoichiometry of CoCrPtB alloys and the presence of partial compounds of Co-Pt or Pt only without the presence of Cr and B in EDS spectra was one puzzle needing reasonable explanation. Since there was no other possible external source of Co-Pt or Pt alloys, the dissociation of the magnetic alloy CoCrPtB compound led the case to be linked to possible corrosion-induced structural degeneration.

Furthermore, in some other analyses, the detection of large amounts of Ni or nickel oxides without accompanying magnetic material in CoCrPtB and underlayer compounds, which contain CrMo and Cr alloys, in EDS spectra, as shown in Figure 1.4, is unexplainable.

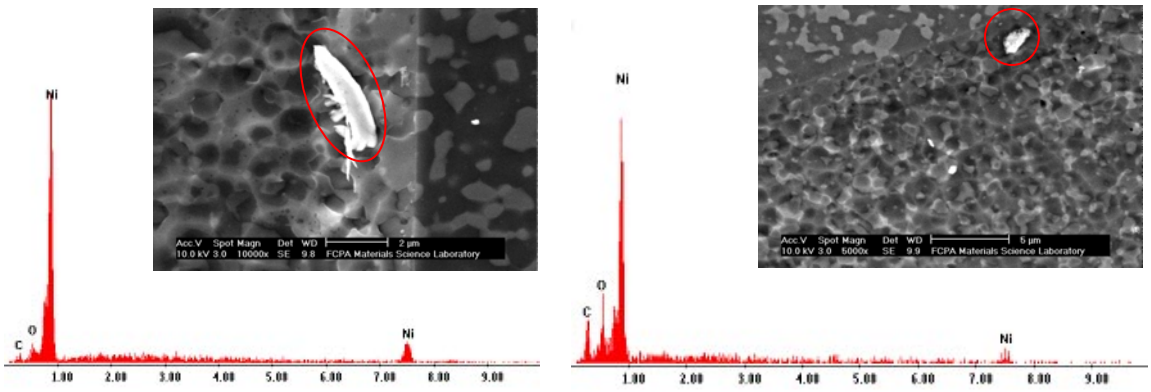

(a) (b)

Figure 1.4. EDS spectra and particulate images of samples with (a) Ni and (b) Nickel Oxides on a magnetic sensor surface, with the background subtracted

The detection of a large amount of Ni without trace elements from the upper thin film layers was beyond common comprehension. In addition, the ratio of Ni to P in the amorphous structure is about 4 to 1. The lack of phosphorous in the spectra made the presence of nickel even more mysterious. If the nickel content was presumably the result of oxidation, noticed oxygen in the above spectra, what could the channels for nickel penetration upward without incorporation with elements from upper layer structures. Importantly, drastic volume changes of nickel during crystallization transformation from nano-crystal structures in amorphous alloy with phosphorous into stoichiometric oxides has been reported.[1.50]

Third, diagnostic magnetic recording electronics encountered increasing amounts of recoverable single bit errors without the observation of surface anomalies, which raised doubts about possible linkages among alloy dissociation, structural changes, and magnetic performance degradation in lieu of corrosion occurrences at the microscopic level. As magnetic recording areal density increased, the size of each individual magnetic transition bit decreased to retain fewer and fewer magnetic grains, and room for error of magnetic responses decreased.[1.51] A corrosion induced correctable error recovery scheme at magnetic transition bits came from considerations of magnetic interference as magnetized particles being generated due to the oxidation of magnetic compounds. Although cobalt and nickel are elements that naturally display ferromagnetic properties,

microscopic amounts of their oxides do not necessarily possess strong magnetization strengths.[1.52][1.53] However, even such subtle interactions between the oxides and primary magnetic field could yield extraordinary field distortion and diminishing original magnetic patterns, which in turn make the magnetic signals of the magnetic sensor deficient. When the interference, along with oxidation obstacles from the surface, is removed using certain external forces, a normal signal is then restored.

The final and most important reason to initiate this study was to elaborate on the discovery of thin film corrosion mechanisms, from an empirical macroscopic understanding up to quantitative microscopic comprehension. Generally, most corrosion studies involving thin film materials have been under the shadows of traditional electrochemical approaches and have treated the corrosion phenomena as surface events.[1.54]-[1.57] Although fundamental theories about thin film technologies have not changed much over the last several decades, thin film performances and features have very much improved. The stagnation and repetition of classic corrosion methodologies have been replaced by modernized analytical operandi, which have been successfully demonstrated in some other crossover fields.[1.58] By developing innovative methodologies and novel techniques with the benefit of expertise in the analytical science community, new territory beyond the limits of many previous corrosion studies can be forged, and new knowledge can be gained that will serve in the future development of advanced magnetic thin film materials and structures with high quality and durability in many applications.

One of the newly-developed methods, which could be potentially suitable and beneficial in studying thin film corrosion, realizes *in-situ* determination of amounts of metallic ions from surfaces during the corrosion processes as a function of electrochemical potential changes.[1.59] By correlating electro-potentials on metal surfaces with amounts of anions in corrosive solutions, this revolutionized concept has had a remarkable impact on understanding corrosion mechanisms and even providing opportunities to amend some misunderstandings about how the corrosion pits are formed and influences of corrosion on property changes. Measurements of electrochemical reactions determined ionic interaction rates, which included movement of all electron transfers from an anode to a cathode. Therefore, in characterizing the overall corrosion process, elemental dissolution

quantification provided a valuable means to create a much more thorough picture of how the electrochemical results were obtained. However, among a handful of promising combinatory techniques, only limited ones could be practically applied to thin film corrosion studies because restrained ionic amounts from thin film structures require extremely high detection sensitivity, and differentiation of multiple elements demand high resolution.[1.60] On-line coupling of electrochemistry and Inductively Coupled Plasma – Mass Spectrometry (EC-ICP-MS) was one of the front runners with its many advantages, which have been reported in many research studies.[1.61][1.62] Unfortunately, none of these achievements were reported in magnetic thin film corrosion studies.

The primary goal of this research was to explore chances for implementing the hyphenated technique, which coupled EC and ICP-MS with methodology development and system construction for magnetic thin film corrosion studies. The methodology development aimed to experimentally determine feasibilities under different conditions over courses of corrosion and to theoretically derive computational algorithms, which apply to specific thin film alloys. Mechanical assembly of an EC-ICP-MS system was carried out over several stages: designing corrosion cells, mechanical retrofitting of instrumentations, synchronizing data acquisition schemes, and optimizing experimental parameters.

The ultimate goal of this research was to truly understand the full course of thin film corrosion processes predominantly based upon results from real-time kinetic electrochemical measurements and *in-situ* ICP-MS quantifications. The depiction of corrosion mechanisms in an illustration concludes this report. The proposed corrosion models were also useful in arguing that the mystery phenomena mentioned previously were direct consequences of or partially induced by corrosion of magnetic thin films. However, the corrosion models could not be firmly established without solid supporting information from research in surface topographic analysis, microstructure characterization, and magnetic performance measurements, which would require a vast amount of effort. Unambiguously, the goal in developing in-depth analytical methods in this research was to uncover the influential consequences of corrosion on the thin film heterogeneous microstructures and galvanic coupling effects between the multiple thin film layers.

1.4. The Scope and Content of This Dissertation

In Chapter 2, a brief development of historical combinatory methods is provided, and their applications are summarized. The EC-ICP-MS technique is emphasized and presented with some of its applications to corrosion studies. Key features in the instrumentation of ICP-MS are simply described. Importantly in this chapter, the design and construction of an instrumental system are detailed, followed by sample specifications and preparation procedures. Because of the nature of mass spectrometry, the development of a calculation algorithm for *in-situ* measurement is necessary to ensure the validity of experimental results. Chapter 3 then provides a detailed derivation of theoretical algorithms, followed by their verification and standardization. In Chapter 4, experimental results using EC-ICP-MS are presented for potentiometric corrosion experiments. Corresponding to the conditions at *in-situ* measurements, some of the samples were produced *ex-situ* in order to reveal specific surface topographic features that required further characterization. Beyond static measurements, potentiodynamic *in-situ* measurements are more intriguing and meaningful in corrosion studies, and the experimental results of using the EC-ICP-MS techniques are thereafter followed in Chapter 5. Chapter 6 and Chapter 7 are devoted to presenting specific important characteristics of microstructures and magnetic properties, respectively, which systematically change during the course of corrosion. Corrosion models for magnetic thin film structures, combining the measurements and analyses of all aspects of thin film corrosion studies, are proposed in Chapter 8, followed by general conclusions and perspectives in Chapter 9. The flow chart below summarizes the general guidelines and contents of this dissertation.

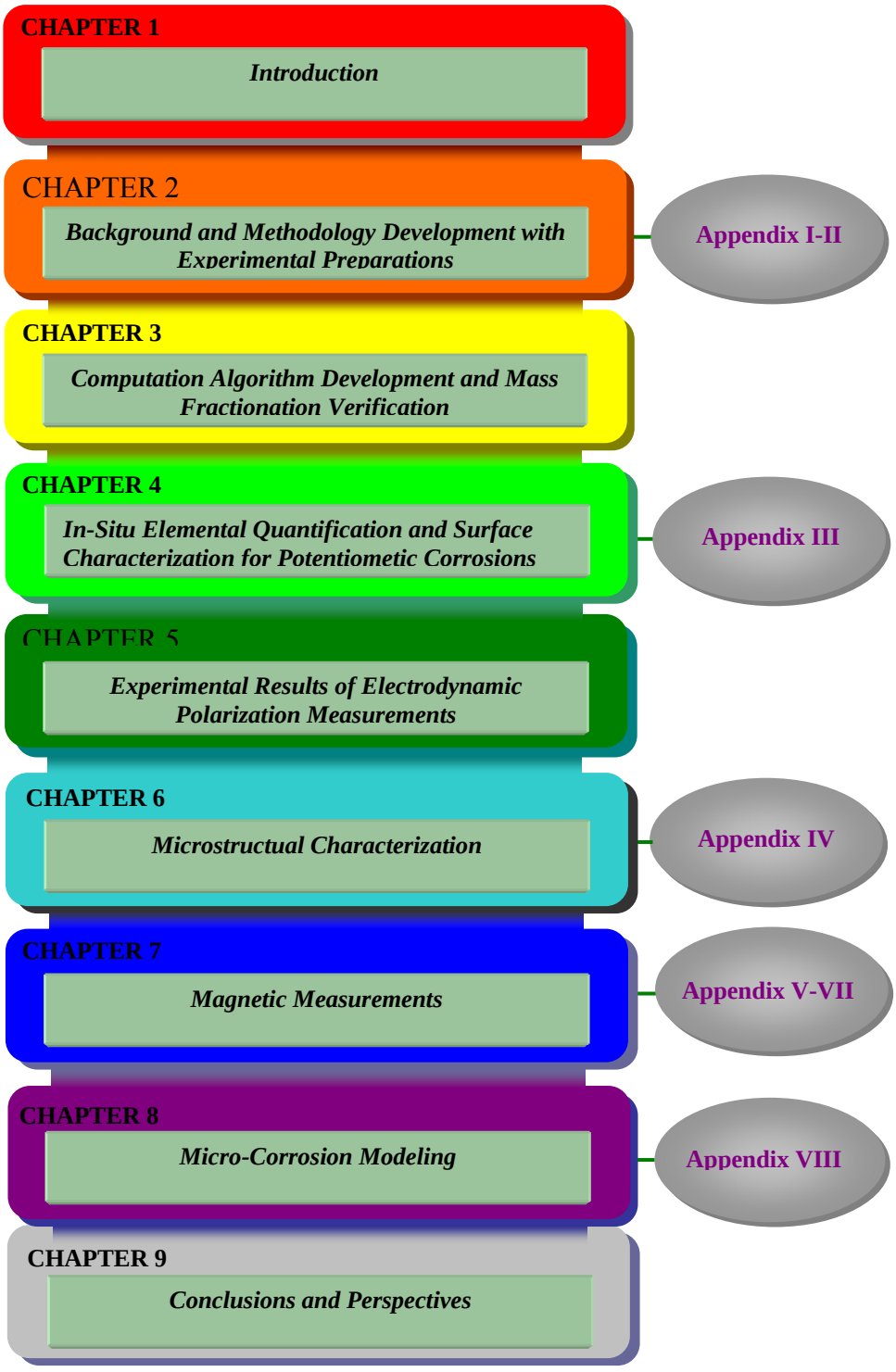

Figure 1.5. Dissertation organization

References:

1.1. "Chapter 9: Magnetic Storage Principles", in *Upgrading and Repairing PCs*, 16th Edition by Scott Mueller edited from Que Publishing, (2003) pp.548-567

1.2. Porter, J., "Disk Drive's Evolution", Keynote Presentation at *100th Anniversary Conference: Magnetic Recording and Information Storage*, Santa Clara University, December 14, 1998

1.3. Kim, J, J. Donovan, and M. Geenen, "2005 HHD Shipments Surpass 380 Million – 2006 Unit Demand Strong Amid Changing Landscape", *Insight*, IDEMA, April 2006, pp.1-5

1.4. Speriosu, V. S., D. A. Herman, Jr., I. L. Sanders, T. Yogi, "Magnetic thin films in recording technology", *IBM Journal of Research and Development*, Vol. 44, No.1/2, Jan/Mar 2000, pp.186-204

1.5. Grundy, P. J., "Thin film magnetic recording media", *Journal of Physics D: Applied Physics*, 31 (1998) pp.2975-2990

1.6. Miura, Y., "Information Storage for the Broadband Network Era - Fujitsu's Challenge in Hard Disk Drive Technology", *Fujitsu Science and Technology Journal*, Vol.37, No.2 (2001) pp.111-125

1.7. Thompson, D. A. and J. S. Best, "The future of magnetic data storage technology", *IBM Journal of Research and Development*, Vol. 44, No.3 (2000) pp.311-321

1.8. Lambeth, D. N., D. E. Laughlin, S. Charap, L,-L. Lee, P. Harllee, and L. Tang, "Present Status and Future Magnetic Data Storage", G.C. Hadjipanayis (ed), *Magnetic Hysteresis in Novel Magnetic Materials*, Kluwer Academic Publishers, (1997) pp.767-780

1.9. Chou, S. Y. and P. R. Krauss, "Quantum magnetic disk", *Journal of Magnetism and Magnetic Materials*, 155 (1996) pp.151-153

1.10. Akimoto, H., I. Okamoto, and M. Shinohara, "Magnetic interaction in Co-Cr-Pt-Ta-Nb media: utilization of micromagnetic simulation", *IEEE Transactions on Magnetics*, Vol.34, No.4 (1998) pp.1597-1599

1.11. Yoshimura, S., D. D. Djayaprawir, H. Shoiji, and M. Takahashi, "Magnetic and structural properties of CoCrTaNiPt longitudinal thin-film media", *Journal of Applied Physics*, Vol.87, No.9 (2000) pp.6866-6868

1.12. Weller, D., A. Moser, L. Folks, M. E. Best, W. Lee, M. F. Toney, M. Schwickert, J-U. Thiele, and M. F. Doerner, "High K_u materials approach to 100 Gbits/in^2", *IEEE Transactions on Magnetics*, Vol.36, No.1 (2000) pp.10-15

1.13. Johnson, K. E., "Magnetic materials and structures for thin-film recording media (invited)", *Journal of Applied Physics*, Vol.87, No.9 (2000) pp.5365-5370

1.14. Gavrilă, H., "New Solutions for Improving Recording Performance of Magnetic Recording Media", *Journal of Optoelectronics and Advanced Materials*, Vol.6, No.3 (2004) pp.891-903

1.15. Abarra, E. N., A. Inomata, H. Sato, I. Okamoto, and Y. Mizoshita, "Longitudinal magnetic recording media with thermal stabilization layers", *Applied Physics Letters*, Vol.70, No.16 (2000) pp.2581-2583

1.16. Novotny, V. and N. Staud, "Correlation between environmental and electrochemical corrosion of thin film magnetic recording media", *Journal of Electrochemical Society*, Vol.135, No.12 (1988) pp.2931-2938

1.17. Klein, D. L., G. H. Vurens, C. L. Jiaa, S. Agarwal, and K-W. Chang, "Corrosion of thin film media and substrate", *Insight*, IDEMA, March/April 2000, pp.28-32

1.18. Smallen, M., P. B. Mee, A. Ahmad, W. Fretag, and L. Nanis, "Observations on electrochemical and environmental corrosion tests for cobalt ally disc media", *IEEE Transactions on Magnetics*, Vol.MAG-21, No.5 (1985) pp.1530-1532

1.19. Asphahani, A. I., "Corrosion of cobalt-base alloys", *Corrosion of Metals Handbook, 9th Edition*, Vol.13, ASM International, (1987) pp.658-668

1.20. Merchant, K., M. Smallen, R. Fisher, and S. Smith, "Physical factors affecting the corrosion resistance of CoCr thin film media", *Journal of Applied Physics*, Vol.67, No.9 (1990) pp.4707-4709

1.21. Huang, L. J., Y. Hung, and S. Chang, "Surface and lubricant/overcoat interface properties of the rigid disks after corrosion", *IEEE Transactions on Magnetics*, Vol.33, No.5 (1997) pp.3154-3156

1.22. Sides, P. J., "The Dependence of the Corrosion Behavior of Rigid Disk Magnetic Recording Media on the Deposition Conditions of the Underlayer, Magnetic Layer, and Carbon Overcoat", *Journal of Electrochemical Society*, Vol.139, No.5 (1992) pp.1352-1358

1.23. Wang, C. C., R. W. J. Chia, J. K. Lee, and W. T. Tang, "Study of substrate bias effect on corrosion susceptibility of thin film magnetic disks by accelerated chemical test", *Journal of Vacuum Science and Technology: A*, 16(3) (1998) pp.1745-1749

1.24. Wang, C.C., R. W. J. Chia, J. J. K. Lee, and W. T. Tang, "Aggressive corrosion tests on thin film magnetic media", Presentation at *Corrosion and Control (Session II)*, International Disk Drive Equipment and Materials Association (IDEMA) Micro-contamination Symposium, March 1998, Santa Clara, CA

1.25. Brusic, V., M. Russak, R. Schad, G. Frankel, A. Selius, D. DiMilia, D. Edmonson, "Corrosion of Thin Film Magnetic Disk: Galvanic Effects of the Carbon Overcoat", *Journal of Electrochemical Society*, Vol.136, No.1 (1989) pp.42-45

1.26. Chung, Y-W. and C. B. Bhatia, "Best bets in protective overcoats for hard disks", *Data Storage*, June 1998, pp.47-48

1.27. Greve, R. J., S. C. Langford, and J. T. Dickinson, "Oxidation and reduction reactions responsible for galvanic corrosion of ferrous and reactive metals in the presence of a perfluoropolyether lubricant: Formblin Z-DOL", *Wear,* 249 (2001) pp.727-732

1.28. Mimani, T. and S. M. Mayanna, "The effect of microstructure on the corrosion behaviour of electroless Ni-P alloys in acidic media", *Surface and Coatings Technology*, 79(1996) pp.246-251

1.29. Nishimori, K., K. Tanaka, and K. Sato, "Surface contamination on sputter carbon coated disks measured by using low energy photoelectron spectroscopy in an ambient atmosphere", *IEEE Transactions on Magnetics*, Vol.26, No.5 (1990) pp.2508-2510

1.30. Brusic, V., J. Horkans, and D. J. Barclay, "Corrosion of Thin-Film Storage Media: A Review", *Electrochemistry in Transition From the 20th to the 21st Century*, O. J. Murphy, S. Srinivasan, and B. E. Conway, Eds, Plenum, New York, 1992, pp.547-560

1.31. Selwyn, G., C. A. Weiss, F. Seqeda, and C. Huang, "Particle contamination formation in magnetron sputtering processes", *Journal of Vacuum Science and Technologies: A*, Vol.15, No.5 (1997) pp.2023-2028

1.32. Teng, E., C. Jiaa, and A. Eltoukhy, "Diamond-lik carbon overcoat for magnetic thin film recording disks", *Surface and Coatings Technology*, 68/69 (1994) pp.632-637

1.33. Mattox, D. M., "Atomistic film growth & resulting film properties", *Vacuum Technology & Coating*, June 2001, pp.32-34

1.34. Wang, T. G. and G. W. Warren, "Corrosion behavior of CoCr films in sulfuric acid", *IEEE Transactions on Magnetics*, Vol.MAG-22, No.5 (1986) pp.340-342

1.35. Tomcik, B., T. Osipowicz, and J. Y. Lee, "Diamond-like film as a corrosion protective layer on the hard disk", *Thin Solid Films*, 360(2000) pp.173-180

1.36. Marcus, P., "Surface science approach of corrosion phenomena", *Electrochemica Acts,* Vol.43, Nos.1-2 (1998) pp.109-118

1.37. Windeln, J. C. Bram, H-L. Eckes, D. Hammel, J. Huth, J. Marien, H. Rohl, C.Schug, M. Wahl, and A. Wienss, "Applied surface analysis in magnetic storage technology", *Applied Surface Science* 179(2001) pp.167-180

1.38. Tomcik, B., T. Osipowicz, and J. Y. Lee, "Diamond-like film as a corrosion protective layer on the hard disk", *Thin Solid Films*, 360(2000) pp.173-180

1.39. Ying, J., T. Anoikin, and C. Martner, "Evolution of the corrosion processes on thin-film media", *Journal of Vacuum Science and Technology. A*, July/August 2000, pp.1804-1809

1.40. Goodson, K. and R. Cormia, "The effect of conversion coated and plated components on the corrosion of cobalt alloy magnetic disks", *Corrosion of Electronic and Magnetic Materials*, P. J. Peterson, ed. ASTM, Philadelphia, PA, 1992

1.41. Gao, C., "Corrosion evaluation of cobalt based magnetic film using various techniques", *Material Research Innovation*, Vol.1, Issue 4 (1998) pp.238-242

1.42. Westre, E. D., S. Lian, and S. Chang, "Measurement of corrosion magnetic recording media by Ion Chromatograhy and Transition Metal Ion Chromatography", Oral Presentation at *Pittscon 2000*

1.43. Vanatta, L. E., "Application of ion chromatography in the semiconductor industry", *Trends in Analytical Chemistry*, Vol.20, Nos.6-7 (2001) pp.336-345

1.44. Fowler, D. E. and R. H. Geiss, "Chemical contamination at the head-disk interface in a disk drive", *IEEE Transactions on Magnetics*, Vol.36, No.1 (2000) pp.133-139

1.45. de Bokx, P.K., S.J. Kidd, G. Wiener, H.P. Urbach, S. De Gendt, P.W. Mertens and M.M. Heyns, "Grazing-Emission X-Ray Fluorescence Spectrometry: A Novel Tool for Surface Contamination Analysis and Thin Film Metrology" *ECS Meeting Abtracts*, Vol. MA 98-1 (1998) pp.387

1.46. Bouchoms, I.P.M., A. Schoonveld, J. Vrijmoeth, and T.M. Klapwijk, "Morphology identification of the thin film phases of vacuum evaporated pentacene on SIO substrates", *Synthetic Metals*, 104 (1999) pp.175–178

1.47. Hemmes, K. W. Lisowski, J. C. Lodder, L. J. Hanekamp, and Th. J. A. Popma, "Surface and bulk magnetic behaviour of sputtered CoCr films", *Journal of Physics D: Applied Physics*, 19(1986) pp.1311-1320

1.48. Thompson, C. V., "Structure Evolution During Processing of Polycrystalline Films", *Amu. Rev. Mater. Sci.* 30, (2000) pp.159-190

1.49. Petrov, I., P. B. Barna, L. Hultman, and J. E. Greene, "Microstructural evolution during film growth*", Journal of Vacuum Science and Technology: A,* 21(5), (2003) pp.S117-S128

1.50. Krasteva, N., V. Fotty, and S. Armyanov, "Thermal Stability of Ni-P and Ni-Cu-P Amorphous Alloys", *Journal of Electrochemical Society*, Vol.141, No.10 (1994) pp.2864-2867

1.51. Bucher, J. P., D. C. Douglass, and L. A. Bloomfield, "Magnetic Properties of Free Cobalt Cluster", *Physical Review Letters*, Vol.66, No.23 (1991) pp.3052-3055

1.52. O'Grady, K. and H. Laidler, "The limits to magnetic recording – media considerations", *Journal of Magnetism and Magnetic Materials*, Vol.200, Issue 1-3 (1999) pp.616-633

1.53. Mentese, S., J-B. Suck and A. J. Dianoux, "Atomic Dynamics of Amorphous and Nanocrystalline $Ni_{80}P_{20}$", *Metastable, Mechanically Alloyed and Nanocrystalline Materials* in Materials Science Forum, Vol.343-346 (1999) pp.671-676

1.54. Choi, H. W., K. H. Kim, J. Kim, S. H. Han, and H. J. Kim, "The Effect of Cr Addition on Structure and Corrosion Resistance in FeTiN Nanocrystalline Soft Magnetic Thin Films", *IEEE Transactions on Magnetics*, Vol.37, No.4 (2001) pp.1773-1775

1.55. Frankel, G. S., "The Growth of 2-D Pits in Thin Film Aluminum", *Corrosion Science*, Vol.30, No.12 (1990) pp.1203-1218

1.56. Senna, L.F., C.A. Achetea, R.A. Simãoa, and T. Hirschc, "Comparative Study Between the Electrochemical Behavior of TiN, TiCxNy and CrN Hard Coatings by Using Microscopy and Electrochemical Techniques", *Materials Research*, Vol.4, No.2 (2001) pp.137-141

1.57. Tullmin, M and P. R. Roberge, "Tutorial: Corrosion of Metallic Materials", *IEEE Transactions on Reliability*, Vol.44, No.2 (1995) pp.271-279

1.58. Lipkowski, J., "Challenges and Opportunities of Modern Electrochemistry: The area of electrochemistry is seeing rapid growth that can benefit other areas of science and humanity as a whole", *Canadian Chemical News*, Vol.1 (2000) pp.12-15

1.59. Davenport, A. J., "In Situ Corrosion Studies", The electrochemical Society, *Interface*, Spring 1998, pp.28-29

1.60. Bulska, E., "Analytical advantages of using electrochemistry for atomic spectrometry", *Pure Applied Chemistry,* Vol.73, No.1 (2001) pp.1-7

1.61. Baca, J., Y. Garcia, A. L. Briseno, and F. Zhou, "Quantification of Metals Released by Metallothionein Adsorbates at Mercury Film Electrodes by Differential Pulse Voltammetry and Electrochemical ICP-Atomic Emission Spectrometry," *Journal of Electroanalytical Chemistry*, 513 (2001) pp.25-35

1.62. Goltz, D., M. Boileau, and G. Reinfelds, "Electroerosion of metal in aqueous solution for sample introduction into an inductively coupled plasma mass spectrometer", *Spectrochimica Acta Part B, Atomic Spectroscopy,* Vol.58, Issue7 (2003) pp.1325-1334

CHAPTER TWO

BACKGROUND OF COUPLING EC AND THE ICP-MS TECHNIQUE AND EXPERIMENTAL PRAPARATIONS

2.1. Historic Overview of EC On–line Coupling Technique with ICP-MS

The realization of coupling electrochemistry (EC) with mass spectrometry (MS) dates back to the early 1970s published by Bruckstein *et al.*[2.1] when volatile and/or gaseous intermediates were produced during electrochemical reactions; the flux of the species were monitored by using an MS system. In this and other early experiments, electrochemical reactions and the measurements of the products were mainly obtained by means of electrospray ionization (ESI) mass spectrometry. Electrospray ionization is capable of gently generating and carrying charged solutions from the molecular to the gaseous phase with a complete vaporization. Because of soft ionization method of ESI, many applications of electrochemical combinatory techniques were focused on organic chemical compounds, molecular biology, and polymerized materials.[2.2]-[2.4]

The success of coupling an ionization unit and mass spectrometer with a chemical reactive module has led to the development of many other hyphenated techniques that can be used in various areas of research and a variety of applications.[2.5] Investigations of coupling the Inductively Charged Plasma – Mass Spectrometer (ICP-MS) technique with other separation mechanisms began in the late 1980's. Unlike the soft ionization process in ESI, plasma in ICP can produce several thousands of degree of temperature, which dissociates not only molecular, but also atomic ions.[2.6] Such an unprecedented vaporization process expanded interest in utilizing ICP for speciation of much wide variety of materials. ICP was not commercially usable until the inductive field was dramatically revolutionized and miniaturized in the early 1980s. Because it combined

ICP with the newly developed mass selective detector, the resulting ICP-MS system attracted extraordinary attention in the 1990's. The birth of the highly accurate and efficient ICP-MS ushered the combined analytical techniques into a new era in the chemical analytical science community.[2.7]

The merits of coupling EC with ICP are simplicity and versatility. Proper conjunction between EC and ICP can be achieved with the straightforward insertion of a micro-tube into an ICP purge inlet to convey electrochemical solutions. By modifying the intake mechanism, nebulizer, spray chamber, and torch of an ICP system, electrochemical solutions can be directly or indirectly introduced without complications.[2.8]

By recognizing the advantages of using ICP-MS for trace or ultratrace concentration determination of metallic elements, Zhou's group first reported several accomplishments in the early to mid 1990's when it coupled electrochemical voltammetry with ICP-MS to determine many types of metallic elements from dissolutions.[2.9]-[2.11] Similarly, an application of using combinatory electrochemistry with ICP-AES or MS for studying electro-erosion of steel and brass in aqueous solution was described in Goltz's paper in 1998.[2.12] The combinatory techniques determined many erosion properties, including rates of erosion as a function of the gap between the conductive samples and solution conductivity. Comparisons of such EC-ICP-MS techniques with others are described and summarized in Zhou's review in 2005.[2.13] Until recently, not only was the EC-ICP-MS technique used for the determination of trace and ultratrace elemental analysis with electrochemical reactions, but it was also extended into some research on corrosion-related subjects to identify corrosion mechanisms and even measurements of corrosion rates. For example, by using the EC-ICP-MS technique, Schiff discovered different surface corrosion mechanisms on alloy wires in two different mouthwash solutions.[2.14] As a result, surface corrosion assessments led them to clearly distinguish the risks associated with certain metallic combinations, which possess not only high corrosion rates but also elemental quantifications that produce detrimental effects in dental applications. Employment of the EC-ICP-MS technique in Hochstrasser-Kurz's research is another example in recent years of a corrosion study, which extended the technique capability into *in-situ* on-line measurements.[2.15]

Using the EC-ICP-MS technique in studying corrosion behavior is a novel approach in attempting to reveal some of the fundamental understandings of corrosion formation, passivation, dissolution, and interaction. Unfortunately, only limited scientific and technological efforts using this method have been made and published in corrosion research. Therefore, cross-references of such a method in applications of thin film corrosion studies are hard to find, which becomes virtually nonexistent in the magnetic thin film subcategory.

2.2. Introduction to ICP-MS Technique and Instrumentation

Developed in the mid 1980's, ICP-MS became one of the most powerful analytical tools and a popular instrument and technique used in determining trace amount of elements in almost every analytical field, such as chemistry, biology, geology and mineralogy, environmental engineering, forensic science, medicine and pharmaceutics, food and nutrition, and microelectronics, *etc*. Its superb instrumentation accuracy, low detection limitation, and fast multiple element determination makes ICP-MS a potential frontrunner in trace and ultratrace detection analytical techniques in atomic spectroscopy [2.16] and has led to an ever-increasing demand for the ICP-MS technique in many applications.[2.17]

2.2.1. Basics of Inductively Charged Plasma and Mass Spectrometer

The key process of ICP is the way that solid or liquid samples can be ionized thermally at atmospheric pressure in a plasma region. Unique potentials of ICP as a high temperature atomization/excitation source for spectral chemical analysis were first achieved by Reed in the early 1960s.[2.18]

At center of an ICP is a plasma zone generated as a result of an electrical discharge into a noble gas in which high thermal energy is inductively supplied by electric current. This current is created by fluctuating magnetic fields at radio frequencies of 27.12 MHz and 40.68 MHz. In a plasma region, temperatures normally measure over 7000 K. Under such high temperatures, almost all materials are simultaneously transformed from neutral forms into ionic species through processes of dissolvation, vaporization, atomization, and

ionization, as shown in Figure 2.1. More than 80 percent of the elements have primary ionization potentials that are attainable using argon plasma as the ionization source.[2.19]

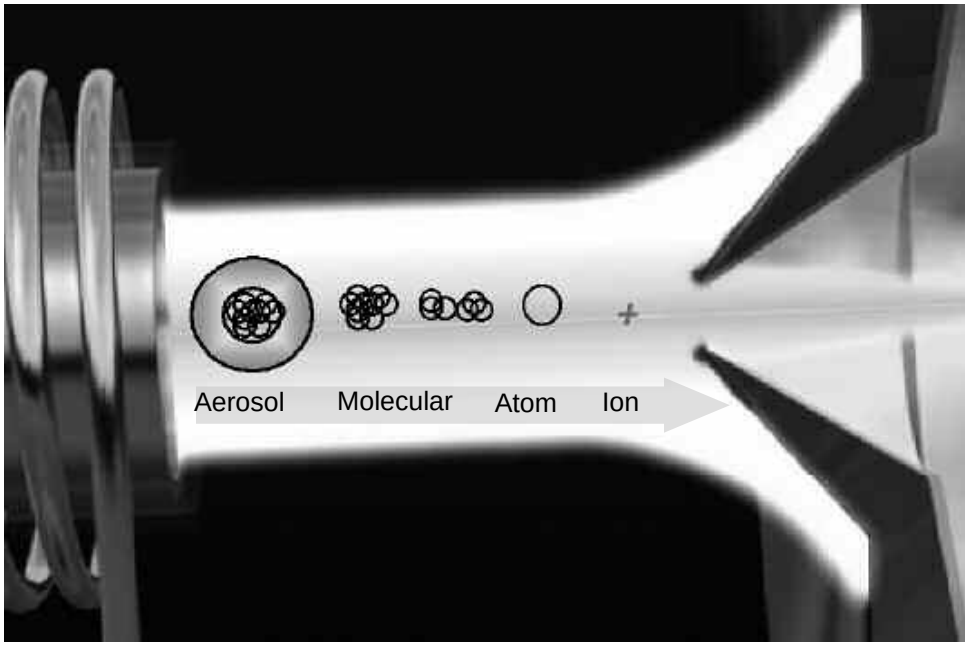

Figure 2.1. Ionization process in plasma region of an ICP (Image courtesy of Agilent Technologies)

Because of such high breakdown efficiency, determination of ionic species based on their mass to charge ratios after entering mass separation chamber is possible. However, ionic interference is a major concern since the mass to charge ratio of a specific element can be redundant with those of other elements. Common interferences come from Ar^+ in combination with C, N, O, and H. Other elements in the matrix can also interfere with analytes, such as Cl, F, and S.

On the other hand, mass selectivity in a mass spectrometry is crucial to optimizing the output of ionic detection ability, which underpins most interpretations of the concept of generic analytical technology. A quadrupole mass spectrometer is the most common mass analyzer because of its high efficiency and sensitivity, great stability and repeatability, and robustness and speed. In a quadrupole mass spectrometer, an electric field accelerates ions out of the source region and into the quadrupole analyzer, in which four electrodes are centrally and symmetrically arranged with alternative electric potentials across each pair, as shown in Figure 2.2.[2.20]

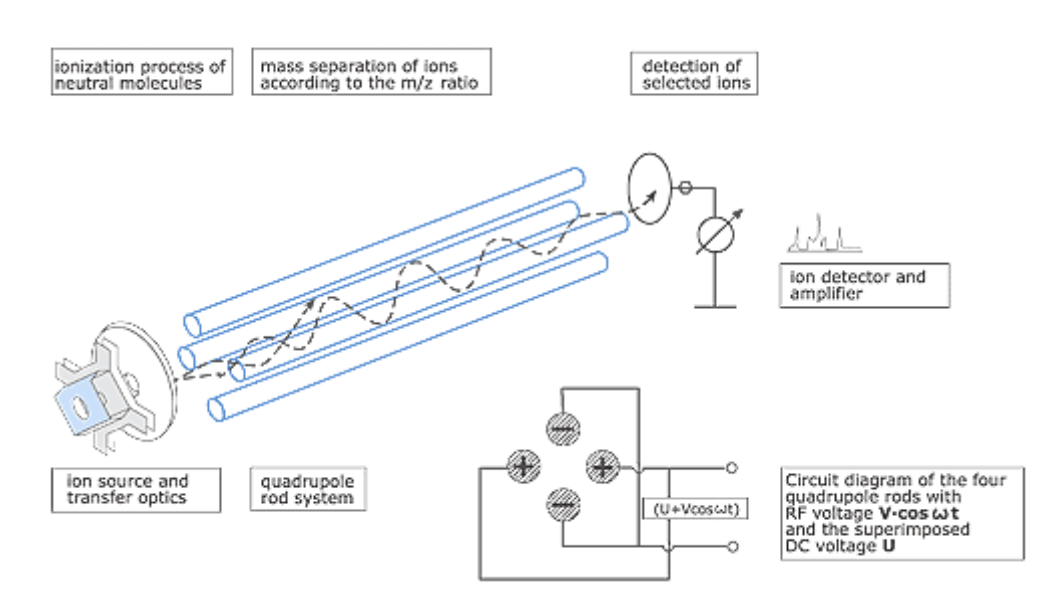

Figure 2.2. Operating principles of a quadrupole mass spectrometer (Picture courtesy of Agilent Technologies)

After passing through transfer optics, ions travel through a quadrupole, which filters ions according to their *m/z* values so that only a single *m/z* value ion can strike the detector. Radio Frequency (RF) and Direct Current (DC) voltages applied to these electrodes alternatively determine the m/z value transmitted through the quadrupole. During the first part of the RF cycle, the top and bottom rods are at a negative potential, as shown in Figure 2.2, while left and right rods are at a positive potential. This squeezes positive ions into the horizontal plane. During the second half of the RF cycle, the polarity of the rods is reversed. This changes the electric field and focuses the ions in the vertical plane. The quadrupole field continues to alternate as the ions travel through the mass analyzer, which causes the ions to undergo a complex set of motions that produces a three-dimensional wave. A conventional ICP-MS instrument equipped with the quadrupole mass spectrometer can provide part per billion (ppb) or even as low as part per trillion (ppt) detection limits for commonly analyzed elements, as shown in Figure 2.3.[2.21]

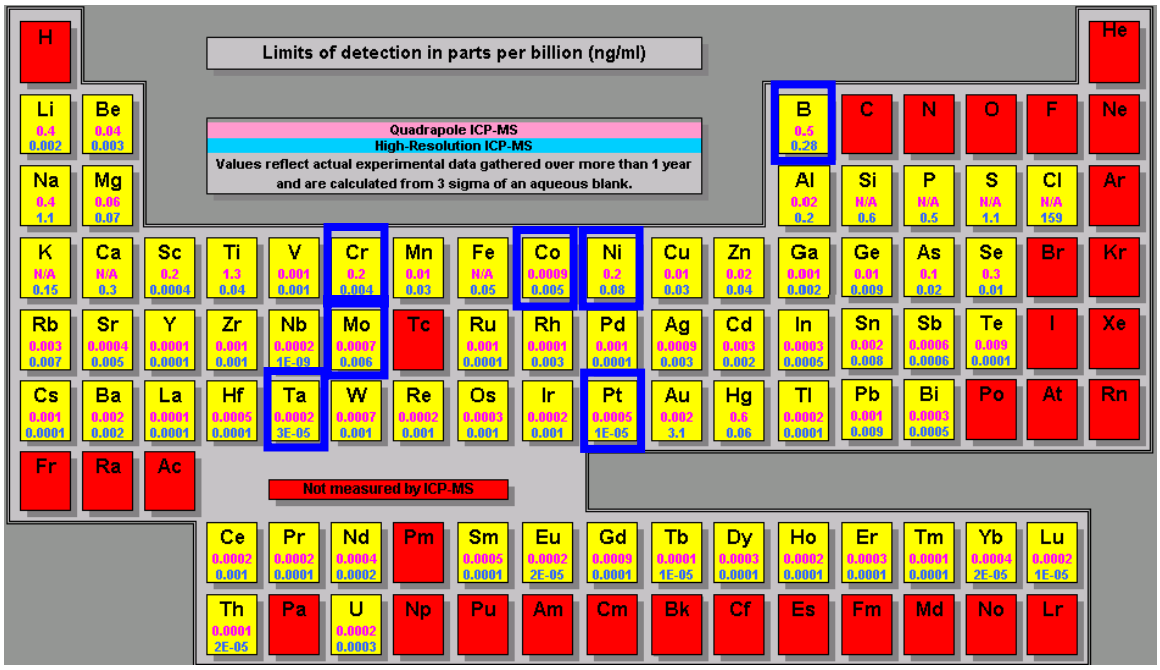

Figure 2.3. Typical detection limits of elements using a quadrupole ICP-MS (reproduced with permission of Elemental Analytical Inc.)

Important elements in this research are Co, Cr, Pt, B, Mo, Ta, and Ni, the main species from thin film alloys in experimental samples, which will be described along with structural characteristics in a later section of this chapter. The quadrupole ICP-MS can achieve sensitivities of 0.2 ~ 0.5 ppb for Cr, Ni, and B and 0.2 ~ 0.9 ppt for Co, Pt, Mo, and Ta. With such unimaginable detection ability, quadrupole IC-MS outdoes many other atomic analytical techniques in thin film corrosion research.[2.22]-[2.24]

2.2.2. Instrumentation of an ICP – MS System

As its name implies, ICP-MS is a synergistic coupling technique, combining a highly efficient ICP for ionic transformation with the accurate and low detection limits of a mass spectrometer. Overall, an ICP-MS system can be dissected into four main processes, including sample introduction and aerosol generation, ionization by an argon plasma source, mass discrimination, and detection. The following is an instrumental sketch of the system.[2.25]

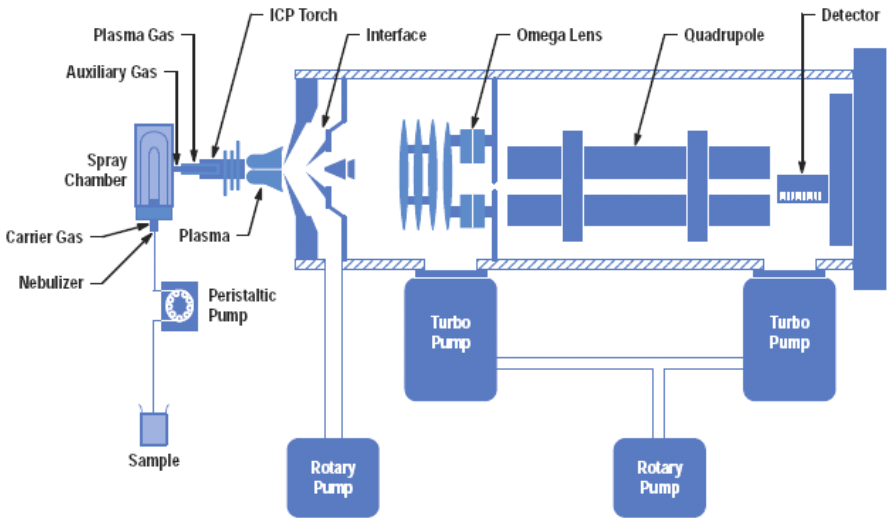

Figure 2.4. Schematic diagram of an ICP-MS system (Picture courtesy of Agilent Technologies)

First, digested solutions are introduced by a peristaltic pump and nebulized in a spray chamber carried with pressurized noble gas, mostly pure helium. When a fine aerosol stream is brought into a plasma region, the majority of sample will be discharged into a drain in large drops. The ionization inside the plasma produces both simple and complex (polyatomic) ions, which include dissociation products of water, the plasma gas, and various solutes. The ions produced are extracted from the plasma into the mass spectrometer region, which is situated in a very high vacuum environment.

At the ICP interface, a pneumatic nebulizer produces aerosols with a broad distribution of droplet diameters up to 100 μm. The main task of a spray chamber, shown in Figure 2.4, placed after a nebulizer is to remove large droplets from the gas stream. When the aerosol enters the spray chamber, it undergoes changes in direction. The large droplets cannot follow, strike the walls of the spray chamber, and turn into waste. With most types of pneumatic nebulizers, 99% of the solution ends up in the waste container.[2.26] Only droplets that are small enough to remain in the gas flow are carried to the plasma.

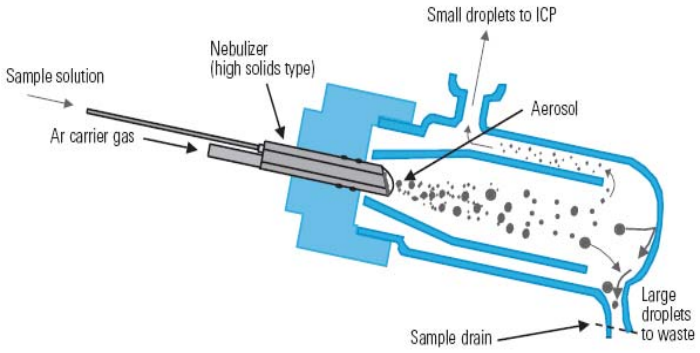

Figure 2.5. Schematic drawing of a double wall spray chamber (Picture courtesy of Agilent Technologies)

After the ionic species pass through the plasma interface, precise mass selection occurs in a high vacuum chamber. The ionic stream flows through a series of offset lenses and is separated by the quadrupole mass spectrometer according to the desired mass to charge ratio. The selected ions then bombard the surface of a mass detector, which amplifies the counts into electric signals known as ion mass counts. In normal mass mode, the single mass count can be individually processed and recorded. However, when the selected ionic species gush out of the mass selector, the overflow of recording signal becomes analog output, which could be biased from digital recording scheme.

2.2.3. ICP-MS Applications on Magnetic Thin Film Studies

ICP-MS as a chemical analytical method has been reported in some magnetic thin film studies.[2.27]-[2.29] Lin *et al.* used ICP-MS to correlate Co quantities from the surface with different acceleration temperatures after magnetic thin film disks were immersed in DI water for 96 hours. According to their ICP-MS measurements, Co extracted from the surface ranged from about 0.05 – 0.10 μg/disk depending on overcoat dimensions and types of overcoat. Chia's study confirmed the previous results in the same general range, finding that the surface quantity of Co in these tests was about 0.1 – 10 $\mu g/m^2$ depending on the thickness and methods through which a hydrogenated carbon overcoat was

deposited. Similar procedures were used in Tsai's study for the samples prepared with different deposition conditions of thin films as well as surface roughness. ICP-MS measurements clearly indicated that corrosion resistance in terms of the extracted amount of Co is highly sensitive to every layer's structure and deposition environments.

Even though ICP-MS measurements have been used in these studies, the results represented only at state when corrosion tests completed. The quantity of Co extracted from the sample surfaces had no indication of when Co release started and how much the increases of Co ions on surfaces during the course of corrosion. The importance of knowing Co extracted amount as well as the others as a timely based event is to associate compositional variations in responding to electrochemical reactions with changes of microstructures and magnetic properties during the full course of corrosion.

2.3. Components of an Online Coupled EC-ICP-MS System

An EC-ICP-MS combinatory system designed in this research is based upon the conceptual integration of an electrochemical reaction apparatus and an ICP-MS unit. Conjoining the two functions is harmonically achieved by balancing chemical compatibility and synchronizing their physical activities. The following is a conceptual diagram of the integration of the electrochemical reaction vessel with ICP-MS in this research.

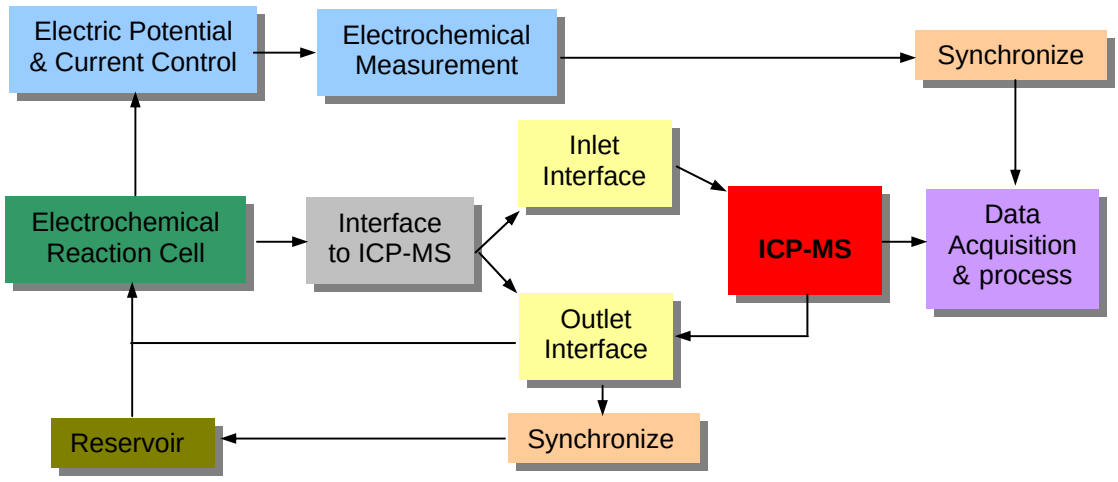

Figure 2.6. Schematic diagram of the EC-ICP-MS system

In this system, a customized electrochemical reaction vessel is designed and fabricated to produce a uniform electric field under potential polarizations and homogenized ionic distribution in electrolytes before they are introduced to the coupling interface. The details of the vessel will be described in following section. Electric currents or potentials are supplied by a source meter (2400 Keithley Instruments Corp.), which can regulate DC voltages in both static and dynamic modes. Also a Keithley 2000 Multimeter is used to measure or monitor corresponding outputs, which are acquired by a computer through a standard interface. The data acquisition of electrochemical measurement is then synchronized with data acquisition of mass measurement from the ICP-MS system.

The electrochemical vessel is connected to the ICP-MS system at both an inlet and outlet, which are modifications from standard ICP-MS setups. A special electrolyte solution reservoir is added to the electrochemical reaction vessel to compensate for quantities lost during ICP nebulization. The following photograph illustrates the experimental setup of the EC-ICP-MS system used in this research.

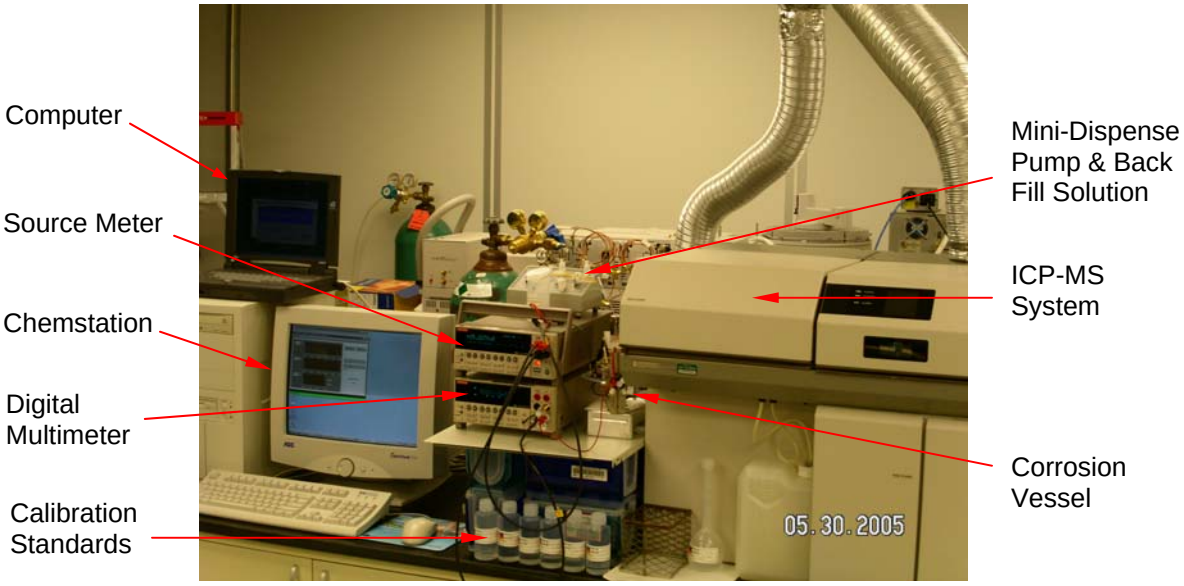

Figure 2.7. Illustration of major components in the EC-ICP-MS system used in this research

2.3.1. Construction of an Electrochemical Reaction Vessel

The construction of a corrosion vessel for the EC-ICP-MS measurements is shown in Figure 2.8. Additional details about the design diagram can be found in Appendix I.

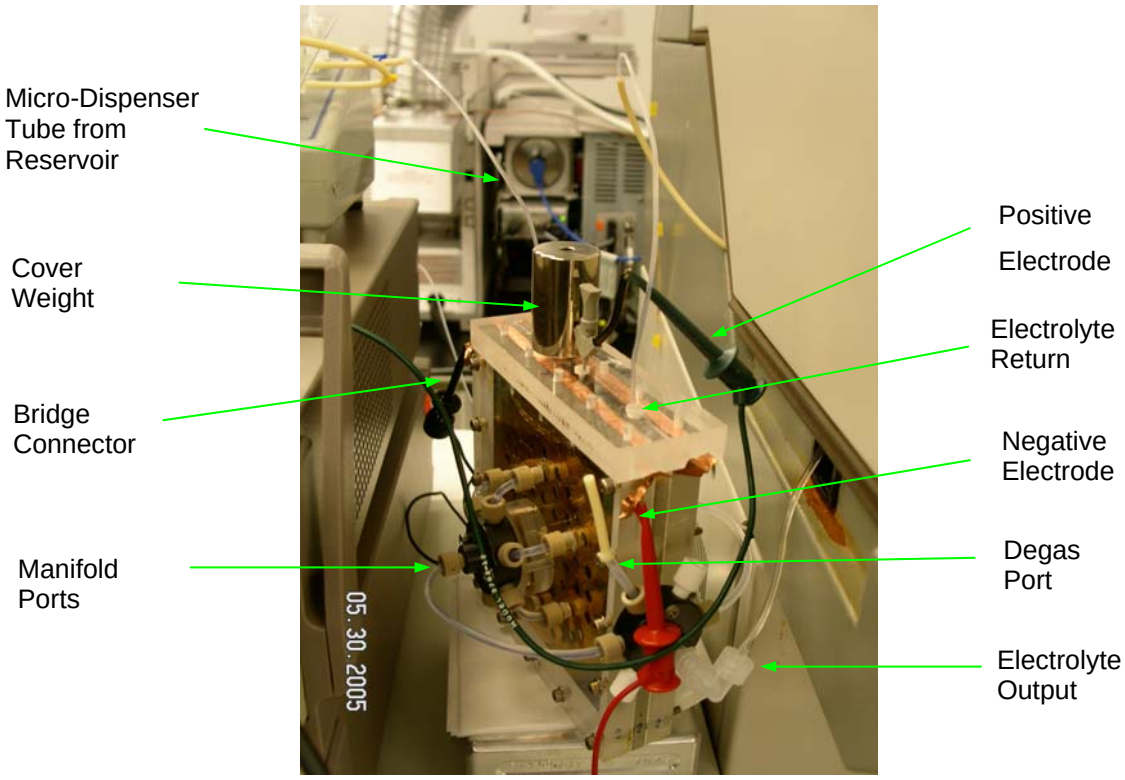

Figure 2.8. Photograph of the corrosion vessel used for EC-ICP-MS measurements

The enclosure of this corrosion vessel is made of clear acrylic plastics, which have the advantage of being easy to clean and highly resistant to most acid solutions. Two pieces of PTFE sheets were inserted as inert gaskets, and stainless steel screws were used for fastening the wall and base. A pure gold mesh, constructed with 0.005 mil gold wire having a square open size of 10 mm (McMaster-Carr), was placed between the inside wall and PTFE gasket. The integration of gold mesh in this cell provides a uniform electric field as counter electrodes, which are connected with metal strips pressed on the mesh extended over top of the vessel wall and aligned with another pair of electric contacts at the bottom of the cover, which is made of copper. Copper contacts are bridged from both sides by alligator connectors.

A disk sample is situated in the center of the vessel and electrolytes flow through 6 flangeless ferrules and merge into a 7-port manifold mounted on each side of the wall (#P-335 and #P-151, Upchurch Scientific Inc.). The materials for the manifold and nuts are made of polyetheretherketone (PEEK), and the 1/8" OD tubing are made of Chemfluor PTFE (#EW-96000-02, Cole-Palmer). The manifold ports are important to the design because they ensure the uniformity and homogeneity of electrolyte flow and reduce accidental over-reaction due to a localized event when concentrations of metallic ions in the electrolytes are in part per billion (ppb) levels. The fluid extracted out of the both 7-port manifolds is converged into another manifold on side of the vessel and is then ready to be delivered to the ICP-MS system. In this manifold, a degas port initially releases backpressure. A spared port might be connected when overflow occurs.

The top cover has several ports for return flow and reservoir connection. Instead of discharging into a waste container, the electrolytes from the corrosion vessel are designed to reflow back to the vessel from the top of cover. On the same cover, another hole was drilled to pass compensated fresh electrolytes from a purge reservoir. In the middle of the cover, a working electrode is inserted with a small clip attachment, which grasps the rim of the tested disk as a working electrode. A cover weight is placed during tests to ensure electric continuity and to reduce structural vibration from the surrounding environment.

2.3.2. EC-ICP Interface Design

The interface connections from EC vessel to ICP contain both input and output. At input where analyzed solutions are conducted from EC into ICP, the connection is straightforward as commonly used ICP setup. The output connection is where the solutions flow out of ICP spray chamber. Instead of dispensing the waste into drain tank, a short Chemfluor PTFE tubing is inserted and recycles the liquid back into corrosion vessel, as shown in Figure 2.8. Both lengths and openness of inner diameter of connection tubing for both input and output are key considerations in the EC-ICP interface design.

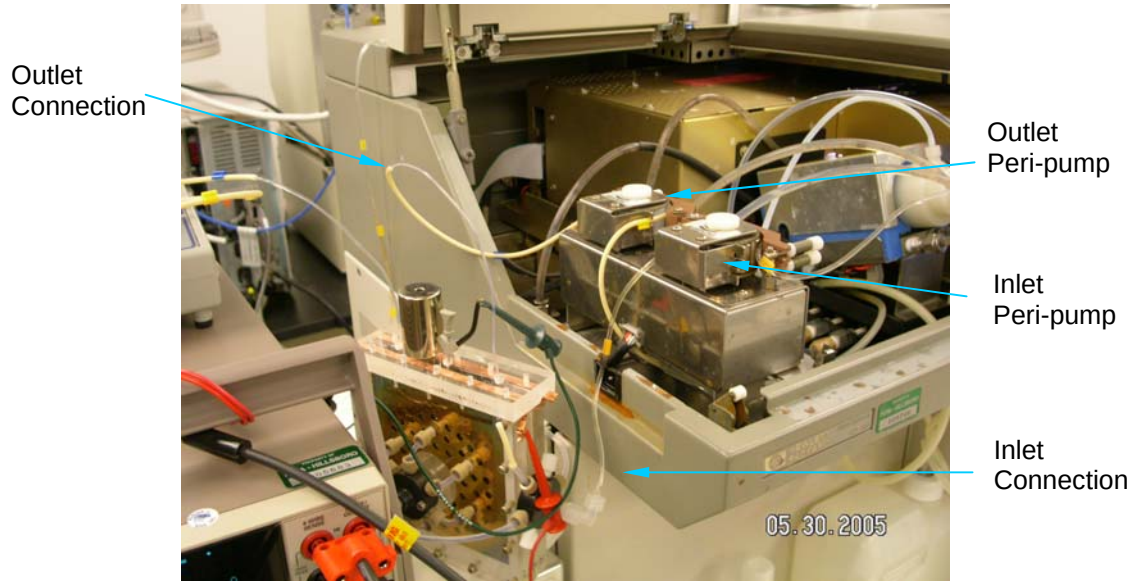

Figure 2.9. Interface connections of the EC-ICP-MS system

The output assembly of the corrosion vessel is an elbow luer clock (HP G1820-65144) made of high-density polypropylene (HDP) with male 1/8" flare end. Instead of connecting to an auto-sampler, as is done in standard ICP setups, a Tygon peri-pump tubing, which has 1.0 mm ID from HP (G1820-65004) fits into the flare end, which feeds analyzed electrolytes into ICP directly. This direct connection of peri-pump tubing from the vessel made measurements of metallic ion concentrations in electrolytes an *in-situ* case.

Rerouted from waste dispensing, the output tubing after the outlet peristaltic pump was connected directly to a 1/32" PTFE tubing (Cole-Parmer 06407-41) and dispenses the "waste" fluid back to the corrosion vessel. As indicated in a previous study, more than 99% of liquid injected into ICP will be dispensed back to the corrosion vessel. The tubing lengths are trimmed as short as possible for effective recirculation.

2.3.3. Incorporation of a Replenishment Reservoir

Adding a mini-dispense pump and back fill solution compensates for the lost portion of electrolyte feeding into the plasma for analysis. In extended *in-situ* analysis process, decreasing re-circulated electrolytes could cause significant unbalances of the amount of dissolution, which could yield an unfavorable environment that further retards depletion

of ions into the electrolytes. Maintaining a constant volume of electrolytes in the corrosion vessel is important to obtaining consistent, meaningful measurement results as the electrochemical reaction preceded over a time period. The feeding tube, connected from the pump, was directly inserted into the corrosion vessel, as shown in the following illustration.

Figure 2.10. Replenishment supply from a reservoir through a micro-pump

The variable speed mini-pump to dispense reservoir solution was acquired from VWR International. An electrolyte solution, which is the same as the background solution for each test, was filled in a clean polypropylene bottle (Corning Snap-Seal #1730) as a replenishment reservoir. The amount of intake from the reservoir can be adjusted by either motor speed of the mini-pump or different ID size tube used. In the experiment, 1/8” ID tubing is used, and slow motor speed is regulated.

Since the mini-pump has different settings and dispense modes, calibration of the dispense rate is critical to ensuring that the correct amount of fluid can be precisely dispensed from the pump to match the amount of solution lost in the course of analysis. By using a digital electronic balance (AB54, Mettler Toledo), DI water dispensed from the pump is weighted for one hour at each setting. The rates are summarized in Figure 2.11.

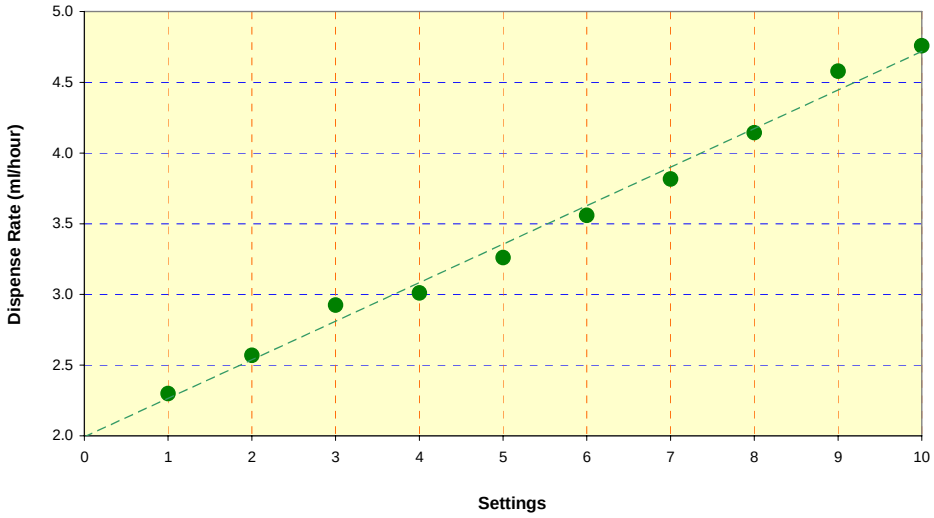

Figure 2.11. Volumetric dispense rate of DI water from a VWR micro-pump

The dispense rate at slow dispense mode is in the range of 2.30 to 4.76 ml/hour. Both fast and prime modes in this pump are other options. Prime pumping mode is used only for purge, and its rate is unregulated. Fast mode in this pump provides a dispense rate of 4.7 to 8.8 ml/hour, which is out of usable range for this study.

Determination of the volume change of electrolytes in ICP is highly dependent on the intake volume of the solution from the cell to ICP, which is controlled by the speed of the peristaltic pump of ICP. Also, the uptake and stabilization times to feed solutions into the spray chamber significantly influence the volume change. However, because the design of the experiment requires continuous circulation of the electrochemical reactive solutions in the system, both uptake and stabilization times in the experiment are set to be zero. Thus, the overall volume of each testing cycle depends only on the uptake speed of peri-pump, through which DI water is passed to experimentally determine the volume change rate. The following graph shows the lost volume rate of DI water as a function of the uptake speeds of the peristaltic pump in this research.

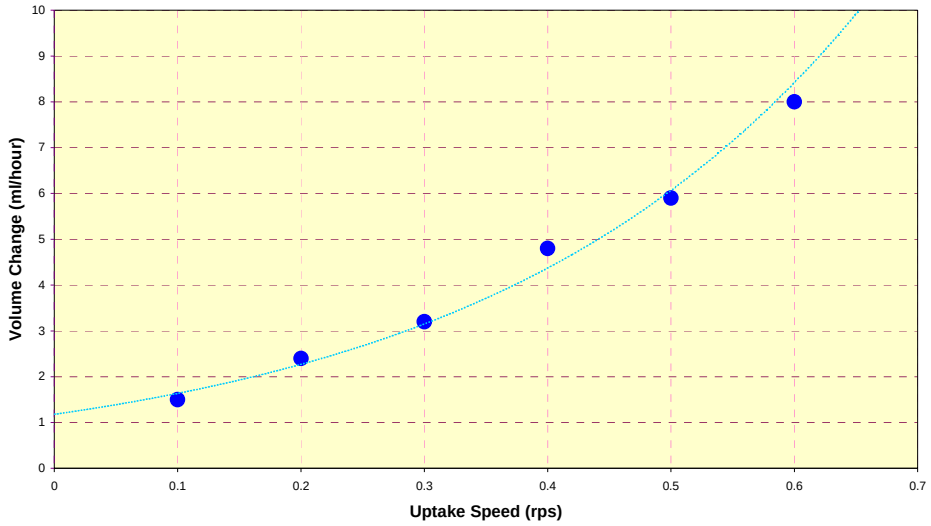

Figure 2.12. Consumed solution volume in ICP as a function of peristaltic pump speed

2.3.4. Setup of the ICP-MS

The ICP-MS system used in this research is an HP 4500 unit with Chemistation 4.0 version software. The key parameters of the ICP-MS setup are summarized in the following table.

Table 2.1. ICP-MS setup parameters

ICP-MS Parameter	Value	ICP-MS Parameter	Value
rf Power (Watt)	1200	Omega Bias (V)	-85
Sampling Depth (mm)	6.5 – 7.2	Omega + (V)	+1
Carrier Gas Flow Rate (L/min)	1.01 – 1.05	Omega - (V)	-20
Plasma Gas Flow Rate (L/min)	0.75	QP Focus (V)	0
Peri-pump Rotation (rpm)	0.11 – 0.13	Plate Bias (V)	-6
Extraction 1 (V)	-300 – -350	Ion Deflection (V)	+60
Extraction 2 (V)	-250 – -180	EM (V)	-2400
Enzel 1, 3 (V)	-150	Discriminator (mV)	+10
Enzel 2 (V)	+11.5		

After being pumped, electrolyte fluid is fed into a Babington Nebulizer (BN), which is made of PEEK. This nebulizer allows the introduction of higher matrix samples because of its large sample orifice. The Ar gas supply pressure is adjusted to be about 300 – 500 kPa, which provides 1.0 L/min carrier gas flow. The same Ar gas is also supplied to ignite and maintain the plasma. Because the Ar gas is from liquefied Ar kept in a low pressure dewar about 210 degree below room temperature, the Ar gas becomes much colder when a long period of vaporization is needed. The temperature fluctuation of Ar gas can cause different emulsification efficiencies of the fluid in the nebulizer and gas density in the plasma. To compensate and stabilize the Ar gas temperature for uninterrupted use, approximately 50 feet of PTFE feed tubing with ¼" ID (McMaster-Carr) is looped inside an incubator oven (Model#12-140, Quincy Lab, Inc.) between Ar dewar and the ICP gas inlet where the Ar gas temperature maintains at 20^{o}C.

In the ICP system, a Fassel type torch is employed as standard setup with three Ar gas purge ports. A platinum injector 1.5 mm in diameter is inserted in the center of the torch. At the interface of the plasma region, standard nickel sample and skimmer cones are replaced by a platinum sample cone on a brass base (HP G1820-65239) and platinum skimmer cone (HP G1820-65237), respectively, in order to avoid interference from the electrolytes with the nickel. Beyond the vacuum gate, all setups are standardized with no major changes from many normal applications.

2.3.5. Preparations of Background and Standard Solutions

The accuracy and precision of ICP measurements depend upon many factors, from the selection of supplies to the preparation of solutions to the calibration techniques applied. As with many other elemental analytical techniques, preparation of aquatic solutions for an ICP-MS measurement is essential because ICP is a matrix-dependant technique for trace and ultra-trace concentration detection. The procedures used in this research to prepare ICP samples for trace elemental analysis mostly follow several standards and recommendations from several well known institutes.[2.30] [2.31]

Before preparation of any aquatic solution, an adjustable-volume pipette (#4910-000-069, Eppendorf Reference®, Germany) used in the full course of this research is calibrated

based upon the E1154-89 (2003) standard from the American Society for Testing Materials (ASTM).

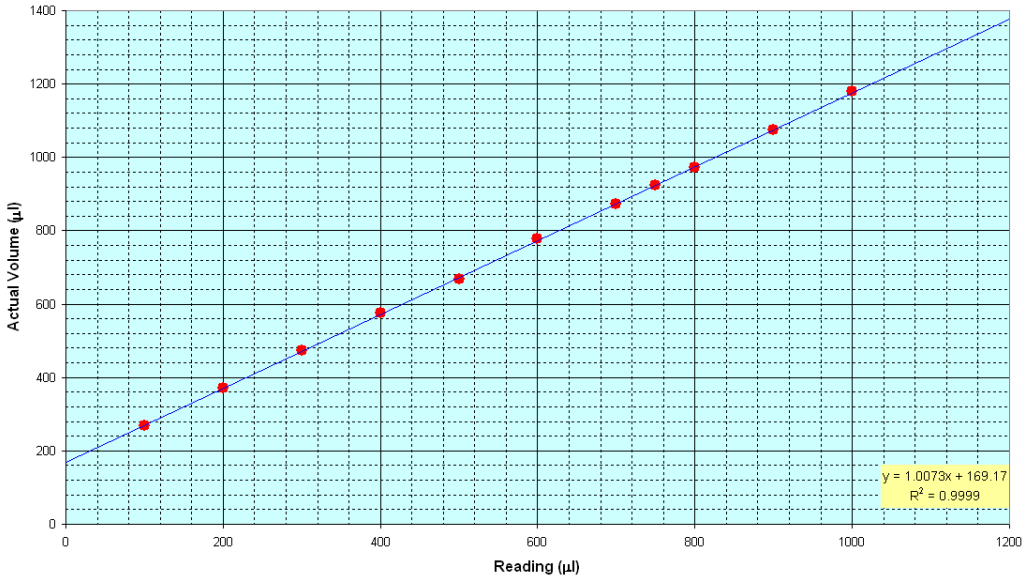

Figure 2.13. Calibration curve of an adjustable-volume pipette

The delivered volume readings of this pipette fall into linear range from 100 µl to 1000 µl and have good correlation with minimum standard error deviation.

2.3.5.1. Aquatic solution supplies

In preparing all aquatic solutions, including standard, background, and reference, *etc*., using de-ionized water with a high purity level, which overwhelmingly dominates the sequential output of the contamination level, is absolutely crucial. The electric conductivity of the DI water supply is between 18.0 - 18.2 MΩ-cm at any given dispensation. Metal contamination of concentrated solutions is specified in mostly part per trillion (ppt) levels, which is necessary to achieve low background noise and to attain less interference in the trace and ultra-trace elemental analysis. The use of aquatic solutions also extends to cleaning, soaking, and rinsing apparatus and fixtures, making digest samples, and generating blanks. Sample preparation and analysis are performed in a class 1000 environment. The following table summarizes the specifications and sources of DI water and other liquids used in the studies.

Table 2.2. Summary of precursor aquatic solutions used in this research

Aquatic Solution	Specification	Catalog #	Source
DI Water	18.2 MΩ-cm	D11951 NanoPure Diamond Ultrapure	Barnstead Corp. Dubuque, IW
Concentrated HNO_3	60.7 wt%	28163-1B (250 ml)	Kento Chemical Co. Inc. Portland, OR
Concentrated HNO_3	55 wt%	AA-10 (500 ml)	Tama Chemical Co. Ltd. Kawasaki City, Kanagawa, Japan
Tuning Solution & Internal Standard (in 2% HNO_3)	Li: 1000 mg/L Y: 1000 mg/L Tl: 1000 mg/L	PLLI2-2Y PLY2-2Y PLTL2-2Y	SPEX Certprep Group, Metuchen, NJ
External Standards (in 2% HNO_3 + Tr HF + Tr HCl) B, Cr, Co, Cu, Li, Mo, Ni, Pt, Ta, Tl, and Y	10 μg/L ± 0.5%	SM-2280-003	High-Purity Standards Charleston, SC
Internal Standards (in 2% HNO_3 + Tr HF) B, Cr, Co, Cu, Mo, Ni, Pt, Ta	10 mg/ml	FCAP-CAL-1	Inorganic Ventures, Inc., Lakewood, NJ

Nitric acid (HNO_3) matrix is preferred due to the solubility of the nitrates, their oxidizing ability, and their relative freedom from chemical and spectral interferences as compared to acids containing Cl, S, F, or P. In addition, HNO_3 is very popular in acid digestion sample preparations. High purity nitric acids have been commercially available for years with the major impurities typically measured in less than several parts per trillions. The following table shows trace element concentrations from Kanto HNO_3 high purity nitric acid.

Table 2.3. Impurity concentration in nitric acid (ppt)

Aluminum(Al)	8.2	Germanium(Ge)	4.0	Rhodium(Rh)	0.3
Arsenic(As)	1.0	Gold(Au)	3.0	Rubidium(Rb)	0.05
Antimony(Sb)	0.5	Iron(Fe)	7.8	Selenium(Se)	10.0
Barium(Ba)	0.08	Lead(Pb)	0.9	Silver(Ag)	0.5
Beryllium(Be)	0.2	Lithium(Li)	0.08	Sodium(Na)	1.3
Bismuth(Bi)	0.3	Magnesium(Mg)	0.5	Strontium(Sr)	0.08
Cadmium(Cd)	1.0	Manganese(Mn)	1.5	Tantalum(Ta)	0.5
Calcium(Ca)	4.0	Mercury(Hg)	0.5	Thorium(Th)	0.005
Chromium(Cr)	4.8	Molybdenum(Mo)	3.0	Tin(Sn)	1.0
Cobalt(Co)	0.3	Nickel(Ni)	1.1	Tungsten(W)	6.0
Copper(Cu)	1.0	Platinum(Pt)	3.0	Uranium(U)	0.002
Europium(Eu)	0.3	Potassium(K)	1.0	Zinc(Zn)	3.2

Selection of a low metal contamination container is another task critical to ensuring a low baseline for the blank. There is much variation in the metal content of different materials for containers, which was studied by Glad *et al*. from Inorganic Ventures (Lakewood, NJ).

Among commonly used materials, perfluoroalkoxy (PFA) contains relatively low concentrations of total metal elements after the elements are extracted for 5 days in 10% ultrapure HNO_3 at 25^{o}C. Thus, containers for transporting ultrapure nitric acid solutions must be made of PFA resin. The sampling bottles, which are made of Nalgene Teflon FEP (2100-0004), are acquired from Nalge Nunc (Rochester, NY). All these bottles are rinsed and soaked in DI water for several hours before being washed in 2% HNO_3 solution. These same procedures are applied to other preparation tools, including the pipette (#5137 from Savillex Corp., Minnetonka, MN), graduate beaker, and flasks, which are made either of PTFE or high-density polypropylene (PP).

2.3.5.2. Preparations of blank and background solutions

Blank solution is a dilution of ultrapure concentrated HNO_3 into 2% (by volume) HNO_3 in mixture of DI water. The background digestions are of 1 %, 2% and 4% (by volume) HNO_3 from ultrapure concentrated HNO_3 in DI water with an addition of the 10 ppb internal standard.

Volume reductions from concentrated 69 wt% of ultrapure HNO_3 were used to produce those background digestions. The properties of ultrapure HNO_3 acid solutions are listed below:

Molecular Weight:	63.05
Density:	1.41 g/ml
Molarities:	15.24

Table 2.4. Preparations for 200 ml background ICP-MS solutions in different concentrations by volume

Background Concentrations	Volume from Concentrated HNO_3 (ml)	Volume from 1 ppm Tuning Solution (ml)	DI Volume (ml)
1%	4.0	2.0	194
2%	8.0	2.0	190
4%	16.0	2.0	182

2.3.5.3. Preparations of standard solutions

Since the response of the mass spectrometer in counts per second is directly proportional to the concentration of a given element in a sample, the system can be calibrated by

incorporating a series of external standards with different concentrations. The challenge, therefore, is to ensure that conditions are identical for each sample, and potential variables that can affect the analysis are recognized and compensated for.

Standard solutions in this research include ICP-MS tuning solution, internal standards, and both single and multiple element external standards. Both external standards and background solutions are useful in confirming the ability of an internal standard calibration curve technique to correct for both nebulizer and plasma-related effects

Tuning solutions for the baseline of an ICP-MS instrument contain 10 ppb of Li, Y, and Tl, which are diluted from 1000 mg/L (ppm) stock solutions. First, 1 ml of each stock solution is added into 500 ml DI water, which is dispensed into a 1000 mL volumetric flask and then shaken well. DI water is filled to the 1000 mL mark, which makes 1 ml/L (1 ppm) tuning solution. This process is repeated by drawing 10 ml of 1 ppm solution and mixing it with DI water in a 1000 mL volumetric flask to make a final concentration of 10 μg/L, which is 10 ppb of tuning solution.

The preparation of external standards starts from diluting 10 ppb standard solution with elements of B, Cr, Co, Li, Mo, Ni, Pt, Ta, Tl, and Y, which are purchased from High Purity Standards Corp. The balance acid is specified to be 2% HNO_3 with traces of HF and HCl, which is consistent with 2% HNO_3 background and tuning solutions. The concentrations of external standards are 0.0, 1.0, 2.0, 5.0, 10, 50, and 100 ppb of all elements required for analysis. But 0.1, 0.5, and 1.0 ppm Ni calibration standards are separately prepared due to the excessive Ni content encountered in some electrochemical reactions. This individual Ni standard is diluted from a single Ni element standard of 1000 μg/L purchased from SPEX Certprep Group.

Internal standards can be incorporated for each sample at known concentrations for the desired element(s) to compensate for any variation in the intensity of the element signal. These internal standards can then be used to correct the measured instrument response to the known concentrations. By applying this same correction to other elements in the matrix solution, the correct element concentrations can then readily be calculated.

Internal standardization is very effective at correcting for ICP-related effects. It is important that the matrix effect influence the internal standard to the same extent as the

catalysts. It may be difficult to find an internal standard that has a similar excitation potential as the catalyst in measurements where several catalysts are involved. That the matrix influences the internal standard and catalyst signal intensities proportionately should be confirmed.

Internal standards are used to trace instrument performance during operation. 10 ppb of solutions containing Li, Y, and Tl in mixture with HNO_3 are used as internal standards to add into the electrolyte in different concentrations of HNO_3 before it is infused into the electrochemical reaction vessel. The difference between tuning solution and internal standards is the percentage of HNO_3, which is set for 2% in tuning solution but is variable in internal standards depending on the concentration of HNO_3, which ranges from 0% HNO_3 to 4% HNO_3 in this report, containing electrolytes in different tests.

A summary of the usage of these aquatic solutions is provided in the following table.

Table 2.5. A summary of specifications and usages of aquatic solutions

Solution	Purpose	Element	Concentration	Balance
Blank	Purge		2% HNO_3	DI Water
Tuning	Instrument Performance	Li, Y, Tl	10 ppb	2% HNO_3
Background	Initial and Final Verification	Li, Y, Tl, B, Cr, Co, Li, Mo, Ni, Pt, Ta,	10 ppb 0.0, 1.0, 2.0, 5.0, 10, 50, and 100 ppb	Variable% HNO_3
External Standard	Calibration	Li, Y, Tl, B, Cr, Co, Mo, Ni, Pt, Ta,	0.0, 1.0, 2.0, 5.0, 10, 50, and 100 ppb	2% HNO_3
Internal Standard	Monitoring	Li, Y, Tl,	10 ppb	Variable% HNO_3

2.3.6. Testing and Measurement Schemes

The measurement of a series of standards and other prepared solutions takes place at both the beginning and end of each testing cycle. The overall scheme is shown in Figure 2.14.

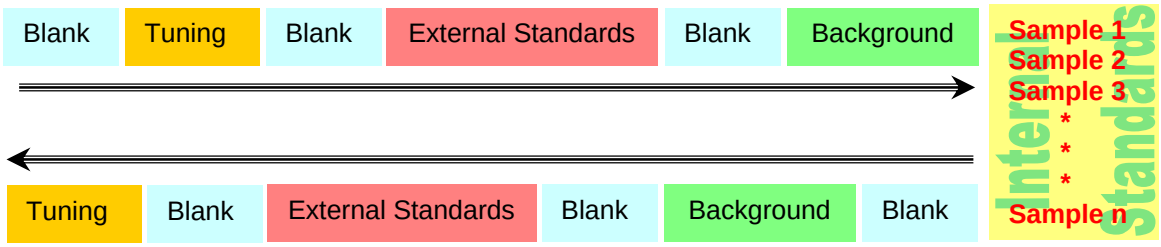

Figure 2.14. Calibration schedule in this experiment

At the beginning of each experiment, blank solution is used to purge the fluid path for approximately 15 minutes. 10 ppb tuning solution is then fed in for instrument adjustment, such as gas flow rate, peristaltic pump speed, bias of lenses, and position of cones, *etc*. to the sensitivity and total response desired. This process can take several minutes to hours depending on instrument performance. Also, the stability of ICP is judged based upon the tuning solution response. When the adjustments of instrument is completed, multi-element external standards with 0.0, 1.0, 2.0, 5.0, 10.0, 50, and 100 ppb are then drawn sequentially from individual container directly followed by blank cleaning. Background solution is dispensed from the pre-filled electrochemical reaction vessel before the sample disk is placed in. At least three cycles are tested for stable readings. All the infusion fluids are drained up to this point. After the test is completed, a reverse calibration process takes place. Instead of drawing background from the vessel, the background solution is taken from the original bottle or reservoir.

2.4. Sample Specifications and Preparations for *Ex-Situ* EC Tests

2.4.1. Sample Specifications

The samples used in this research are made from highly magnetized thin films with multiple layer structures, as indicated in the previous chapter. The major physical

properties and chemical compositional characteristics of these samples are summarized in the following table.

Table 2.6. Major physical and magnetic characteristics of selected samples

Characteristics	Composition and Thickness
Lubricant Layer Composition Thickness (nm)	 AM3100 1.25 ± 0.15
Protective Layer Composition Thickness (nm)	 DLC 8.0 ± 1.2
Magnetic Layer Composition Thickness (nm)	 $Co_{63}Cr_{24}Pt_9B_4$ 20
Seed Layer Composition Thickness (nm)	 $Co_{82}Cr_{13}Ta_5$ 1.0
Underlayer Composition Thickness (nm)	 $Cr_{80}Mo_{20}$ 4.0
Baselayer Composition Thickness (nm)	 Cr 6.0
Substrate Composition Thickness (m)	 Ni_{88}/P_{12} 10
Surface Roughness (nm)	**0.8 ± 0.3**

In these samples, multiple elements exist in different layers. Besides cobalt (Co), chromium (Cr) is the most important major element found in many layers. Minor elements in this multilayer structure include platinum (Pt), boron (B), tantalum (Ta), and molybdenum (Mo). Noticeably, the substrate Ni/P amorphous compound has enormous thickness (measured in micrometers) compared to its deposits in the thin film layers (measured in nanometers). Additionally, hydrogenated diamond-like carbon (DLC) film is to protect magnetic layer and consisted of carbon (C) and hydrogen (H). The lubricant layer at the top of the structure contains mainly fluorine (F).

2.4.2. Assembly of a Diametrical Multiple-cell Aperture

In addition to the corrosion vessel used for *in-situ* corrosion tests, a diametrical multiple-cell aperture for *ex-situ* corrosion tests was also designed and assembled as a part of the experimental preparation. As indicated in many previous studies, surface properties of the magnetic thin film disks vary slightly from surface to surface and location to location. These variations are mainly due to inhomogeneous deposition of thin film structures, surface roughness, cleanness, film thickness, and even magnetization. An example showing the electrochemical variations, when different radial locations on the same surface are tested, is shown in Figure 2.15.

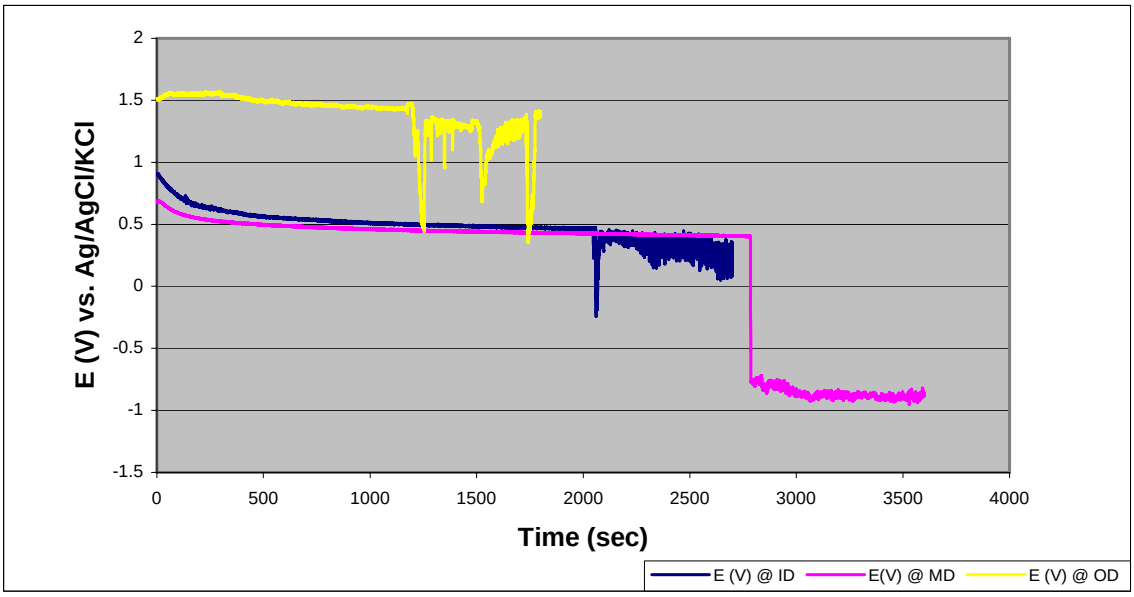

Figure 2.15. Open circuit potentials measured at different radial locations on a disk surface

In this early study, electrochemical properties in terms of corrosion potentials varied at different regions from the inner diameter to the outer diameter. In the middle of the disk, the electrochemical breakdown at the surface commences at about 45 minutes after the disk is immersed into the electrolyte. In contrast, similar electrochemical activities from either side of the center location on the same surface are noticed as early as 19 minutes and 35 minutes.

To minimize variations in electrochemical measurement due to geographic locations on a surface, a diametric multiple cell aperture, in which all corrosion cells are equally radial located, was specially designed and constructed. This aperture enables consistent measurements for electrochemical reactions at the same radius on a disk surface to be obtained, which is especially useful when comparable reaction results are expected. The following photograph shows the structural construction of this unit, and the design diagram can be referred to in Appendix II.

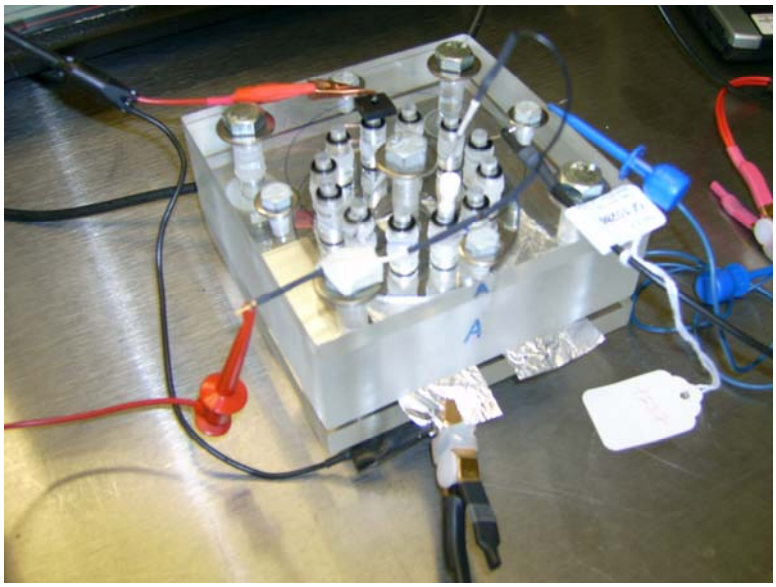

Figure 2.15. Diametric multiple cell fixture used in electrochemical measurements

Three pieces of 4”x4” acrylic plastic plates were assembled with 5 hand tight screws at the four corners and center in this fixture. The test samples was supported by the bottom plate and electrically connected with test instrument through two pieces of aluminum foils placed between sample and the bottom plate. In the middle plate, 12 holes as corrosion chambers were drilled concentrically and equal spaced. In these chambers, PTFE pillars with ¼” inner diameters were placed to support twelve PTFE O-rings on both sides. The bottom O-rings contacted on test surface at same radius of the disk. Correspondingly, there were 12 holes were aligned with the centers of pillars on top plate made for filling electrolytes and inserting electrodes, such as counter electrode or standard reference electrode. Each individual chamber hold 1000 μl of electrolyte solution.

2.4.3. Construction of a Standard Electrode

Besides a working electrode, a commonly used 3-electrode system contains a reference electrode and a counter electrode. Most often a counter electrode is made of an inert metal piece, such as gold or platinum. In this study, a pure platinum wire is used as a counter electrode to pass the electric current without reaction through the electrolyte. However, space considerations make a combination of reference electrode and counter electrode is highly desirable.

The purpose of a reference electrode is to complete the measuring circuit and provide a stable and reproducible potential against electrode from which potential is measured. The contact is made through a liquid junction that allows the reference electrolyte to contact the sample. The reference electrode is designed to produce the same potential no matter in what solution it is placed. Many types of reference electrode can be selected and used in electrochemical measurements. Reference electrodes are composed of four distinct parts: an inert outer body, a reference element, an electrolyte, and a liquid junction.

The silver/silver chloride electrode is the most common due to its ease of fabrication and superior temperature range. The electrode is a silver wire that is coated with a thin layer of silver chloride through electroplating or by dipping it in molten silver chloride. When the electrode is placed in a saturated potassium chloride solution, it develops a potential of 197 mV versus the standard hydrogen electrode. For the silver-silver chloride reference electrode, the half reaction is:

$$AgCl_{(s)} + e^{-} \Leftrightarrow Ag_{(s)} + Cl^{-}{}_{(sat)} \qquad (2.1)$$

where *(s)* indicates a soluble compound and *(sat)* stands for saturated state. The potential of the electrode remains constant as long as the chloride concentration remains constant. But the potential is a function of the concentration of Cl ions, as indicated in the following table.[2.32]

Table 2.7. Potentials of an Ag/AgCl reference electrode vs. a standard reference electrode as a function of KCl concentration at 25°C

Concentrations	Potential @ 25°	
	vs. NHE	vs. SCE
Ag/AgCl, KCl (0.1*M*)	*0.2881*	*0.047*
Ag/AgCl, KCl (3.5*M*)	*0.205*	*-0.039*
Ag/AgCl, KCl (sat'd)	*0.199*	*-0.045*
Ag/AgCl, NaCl (3*M*)	*0.209*	*-0.035*
Ag/AgCl, NaCl (sat'd)	*0.197*	*-0.047*
Ag/AgCl,Seawater	*0.250*	*0.01*

NHE and SCE stand for *normal hydrogen electrode* and *saturated calorimetric electrode*, respectively. Different approaches can be used to construct the Ag/AgCl reference electrode.[2.33] In this study, a close-end construction of the Ag/AgCl reference electrode was used, as shown in the following figure.

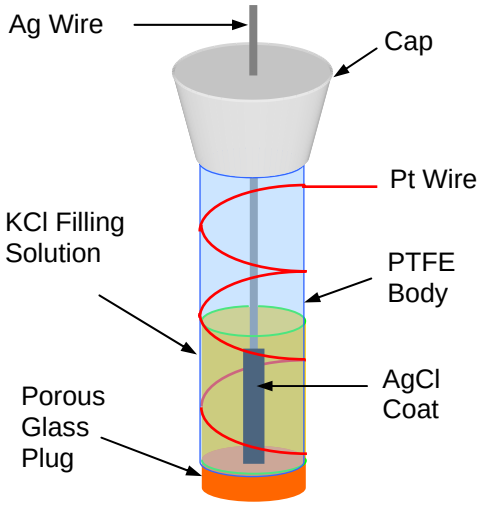

Figure 2.16. Construction of an Ag/AgCl reference electrode

The body of this construction, like the cap, is made of PTFE tube. At the end of the electrode, a porous glass plug, which is made of Vycor glass (MF2078, Bioanalytical System, Inc.), is inserted and glued with epoxy at the rim. AgCl coated silver wire is acquired from A-M Systems, Inc. (Carlsborg, WA)

Using the Nernst equation, we can evaluate E^{o}_{cell} for Ag, and the relationship simplifies to following equation:

$$\Delta E_{cell} = \Delta E^{o}_{cell} + \frac{0.05916}{n} \log\left[Ag^{+}\right] \qquad (2.2)$$

where *n*, the moles of electrons transferred by silver, is 1. The concentration of silver, $[Ag^{+}]$, can be determined as a function of ΔE_{cell} by measuring ΔE_{cell} for various standard solutions of Ag^{+} and generating a calibration curve. A linear plot indicates that the slope of the line is 0.05916 and the *y*-intercept is ΔE^{o}_{cell}, when ΔE_{cell} is graphed against $\log[Ag^{+}]$.

References:

2.1. Bruckenstein, S., and J. Comeau, "Electrochemical mass spectrometry: Part 1. - Preliminary studies of propane oxidation on platinum", *Faraday Discussions of Chemistry Society*, 56 (1973) pp.285-292

2.2. Bolzan, A.E., T. Iwasita, and W. Vielstich, "On the electrochemical oxidation of glucose identification of volatile products by on-line mass spectroscopy", *Journal of Electrochemical Society*, Vol.134, No.12 (1987) pp.3052-3058

2.3. Wasmus, S., E. Cattaneo, and W. Vielstich, "Reduction of carbon dioxide to methane and ethene, an on-line MS study with rotating electrodes", *Electrochim. Acta* 35 (1990) pp.771-775

2.4. Cattaneo, E., B. Rasch, and W. Vielstich, "Anodic stability of propylene carbonate electrolytes at potentials above 4 volts versus lithium, an on-line MS and in-situ FTIR study", *Journal of Applied Electrochemistry*, Vol.21, No.10 (1991) pp.885-894

2.5. Chang, H., D. C. Johnson and R. S. Houk, "*In situ* coupling between electrochemistry and mass spectrometry — a literature review", *TrAC Trends in Analytical Chemistry*, Vol.8, Issue 9 (1989) pp.328-333

2.6. Bradshaw, N., E. F. H. Hall, and N. E. Sanderson, "Inductively Coupled Plasma as an Ion Source for High - Resolution Mass Spectrometry", *Journal of Analytical Atomic Spectrometry*, 4(8) (1989) pp.801-803

2.7. Ward, A.F. "Inductively coupled argon plasma spectroscopy: development, technique, and applications", *American Laboratory*, Vol.10 (1978) pp.79-87

2.8. Yanes, E.G., N. J. Miller-Ihli, "Use of a parallel path nebulizer for capillary-based microseparation techniques coupled with an inductively coupled plasma mass spectrometer for speciation measurements", *Spectrochimica Acta Part B*, Vol.59, Issue 6 (2004) pp.883-890

2.9. Pretty, J.R., E.H. Evans, E.A. Blubaugh, W-L. Shen, J.A. Caruso, and T.M. Davidson, "Minimisation of Sample Matrix Effects and Signal Enhancement for Trace Analytes Using Anodic Stripping Voltammetry With Detection by Inductively Coupled Plasma Atomic Emission Spectrometry and Inductively Coupled Plasma Mass Spectrometry." *Journal of Analytical Atomic Spectrometry*, 5 (1990) pp.437-443

2.10. Zhou, F., "Stripping Analysis Combined On-Line with Inductively Coupled Plasma-Atomic Emission Spectrometry and with Inductively Coupled Plasma-Mass Spectrometry," *Electroanalysis*, Vol.8, Issue 10 (1996) pp.855-861

2.11. Hwang, T-J. and S-J. Jiang, "Determination of Copper, Cadmium, and Lead in Biological Samples by Isotope Dilution Inductively Coupled Plasma Mass Spectrometry After Online Pre-Treatment by Anodic Stripping Voltammetry." *Journal of Analytical Atomic Spectrometry*, 11 (1996) pp.353-357

2.12. Goltz, D., M. Boileau, and G. Reinfelds, "Electroerosion of metal in aqueous solution for sample introduction into an inductively coupled plasma mass

spectrometer", *Spectrochimica Acta Part B, Atomic Spectroscopy*, Vol.58, Issue 7 (2003) pp.1325-1334

2.13. Zhou, F., "Electrochemistry combined on-line with atomic mass spectrometry and related techniques for trace-metal analysis and electrode-reaction studies", *TrAC Trends in Analytical Chemistry*, Vol.24, Issue 3 (2005) pp.218-227

2.14. Schiff, N., M. Boinet, L. Morgon, M. Lissac, F. Dalard, and B. Grosgogeat, "Galvanic corrosion between orthodontic wires and brackets in fluoride mouthwashes", *The European Journal of Orthodonti*cs 28(3), (2006) pp.298-304

2.15. Hochstrasser-Kurz, S., "Mechanistic Study of the Corrosion Reactions on WC-Co Hard metal in Aqueous Solution – An Investigation by Electrochemical Methods and Elemental Solution Analysis", A dissertation from *SWISS FEDERAL INSTITUTE OF TECHNOLOGY ZURICH*, 2006

2.16. Bings, N. H., A. Bogaerts, and J. A. C. Broekaert, "Atomic Spectroscopy", *Analytical Chemistry*, 76 (2004) pp.3313-3336

2.17. Date, A. R. and A. L. Gray, eds., "Applications of Inductively Coupled Plasma Mass Spectrometry", Blackie and Sons, London, (1989) pp.254

2.18. Reed, T. B., "Induction-Coupled Plasma Torch", *Journal of Applied Physics*, Vol.32, No.5 (1961) pp.821-824

2.19. McCurdy, E. and D. Potter, "Optimising ICP-MS for the determination of trace metals in high matrix samples", *Spectroscopy Europe*, 13/3 (2001) pp.14- 20

2.20. Skoog, D. A., F. J. Holler, and T.A. Nieman, "*Principles of Instrumental Analysis*", 5th edition, Saunders College Publishing, 1997, pp.253-271

2.21. Copy with permission from website www.elemenalanalysis.com of Elemental Analysis, Inc., Lexington, KY

2.22. Zoorob, G. K., J. W. McKiernan, and J. A. Caruso, "Fundamental Review: ICP-MS for Elemental Speciation Studies", *Mikrochimica Acta*, 128 (1998) pp.145-168

2.23. Fisher, A., P. Goodall, M. W. Hinds, S. N. Nelms, and D. M. Pennye, "Atomic spectrometry update – Industrial analysis: metals, chemicals and advanced materials", *Journal of Analytical Atomic Spectrometry*, 19 (2004) pp.1567-1595

2.24. Rojas, F. S. and C. B. Ojeda, "Effluent analysis in analytical chemistry: an overview", *Analytical & Bioanalytical Chemistry*, 382, (2005) pp.978–991

2.25. Kishi, Y., "A Benchtop Inductively Coupled Plasma Mass Spectrometer", *Hewlett-Packard Journal*, Article #9, August 1997

2.26. Jarvis, K.E., A.L. Gray, and R.S. Houk, "Handbook of Inductively Coupled Plasma Mass Spectrometry", Chapman and Hall: New York, 1992

2.27. Lin, M-S., C. Tsai, Y. Sun, W. Huang, C. M. Wang, and C. Dong, "An accelerated test for cobalt migration in thin-film rigid disks", *IEEE Transactions on Magnetics*, Vol. 35, No. 5 (1999) pp.2703-2705

2.28. Chia, R. W. J., J. Edwards, M. Geisler, C. Wang, "Effect of disk roughness and carbon impact energy on corrosion protection of magnetic recording films", *Tribology International*, 33(2000) pp.323-327

2.29. Tsai, C., J. Liang, H. H. Liang, C. M. Wang, "Sputtering parameters affecting the corrosion resistance of CoCrPtTa thin film media", *Journal of Magnetism and Magnetic Materials*, 209(2000) pp.157-159

2.30. Talbot, J. and A. Weiss, "Laboratory Methods for ICP-MS Analysis of Trace Metals in Precipitation", *Hazardous Materials Lab, Hazardous Waste Research and Information Center*, Volume 3, Chapter 1, March 1994

2.31. Wasser, K. "Guide for volume determination within the scope of reference measurement procedures in medical reference measurement laboratories, Part 1: Calibration liquid water", *PTB-Mitteilungen* Vol.112 No. 2 (2002) pp.139-149

2.32. Janz, G.J., "Silver-silver halide electrodes", in *Reference electrodes: theory and practice*, Edited by D.J.G. Ives and G.J. Janz, Academic Press, NY (1961) Ch 4, pp.179-230

2.33. Ahn, M. K., D. J. Reuland, and K. D. Chadd, "Electrochemical measurements in general chemistry lab using a student-constructed Ag/AgCl reference electrode", *Journal of Chemical Education*, Vol.69, Issue 1 (1992) pp.74-76

CHAPTER THREE

DEVELOPMENT OF COMPUTATION ALGORITHMS AND MASS FRACTIONATION VERIFICATION

3.1. Introduction

One of the issues that analysts face while using ICP-MS techniques is that ICP outputs are extremely matrix-dependent, which directly results from the atomization and ionization processes. Therefore, quantification of an individual element in a matrix is greatly dependent on the standardization of the known elemental amount present in the solutions or on the calibration of the element with known concentrations of interested elements. These two common technique options for ICP-MS measurements are called *internal* and *external calibrations*. Internal standard calibration is commonly used in ICP-MS when a quantification measurement is needed. Because of drifts of physical dimensions of some components in an ICP-MS instrument due to thermal factors, internal references are necessary to provide a baseline for correction of variations during the course of experiments. On the other hand, external calibration is carried out before and after the experiments to ensure that the instrumental parameters are within normal limits. Normally, deviations of measured concentrations of elements of interest from their concentrations in a known solution indicate successful calibration. The known solution is typically prepared from single or multi-element stock solutions.

Although these calibration techniques have been well established and integrated into many ICP-MS systems for quantitative or semi-quantitative analysis, applications of a time-resolved measurement are not well suited to these schemes. A variation on the external calibration method called Standard Addition, or Method of Standard Additions (MSA), has been developed for use when high purity materials are analyzed. MSA utilizes the same sort of synthetic elemental calibration standard mix as external

calibration, but the calibration solution is spiked at multiple levels directly into the unknown sample, giving a calibration of response against added concentration, rather than response against absolute concentration. The added concentrations give the slope of the calibration line for each element.

With knowledge of these calibration techniques, a time-resolved calibration algorithm was derived in this research, which was based upon known concentrations of internal, external, and background solutions. A detailed derivation was given in this chapter. Similarly, the background noise of signal outputs was subtracted from calibrations of blank solutions, which were also included in the calculations.

In order to verify the correctness of experimental results and to identify an effective measurement range, the computational algorithm was then applied to several solutions with known concentrations. The results of time-resolved measurements on repeatability and reproducibility of isotopic redundancy with errors were summarized in this chapter.

3.1.1. Basic Computational Algorithm

The electronic outputs of an ICP-MS rely on both the mass analyzer and detector. The quadrupole mass analyzer in an ICP-MS system is responsible for separating ions in a selective mode according to mass-to-charge ratio. The sensitivity and resolution of the selectivity highly depends on the design of the quadrupole analyzer geometrically and electronically. However, the yield of mass counts of a selected ion depends not only on the efficiency of the quadrupole analyzer but is also related to the function of the electron multiplier detector. Trace element concentrations are then generally calculated using the following relationships:

$$C = (Y) \times \left(\frac{I}{A} \right) \tag{3.1}$$

where

C = concentration of an elemental isotope

I = mean intensity of mass counts of the elemental isotope

A = abundance of the elemental isotope

Y = efficiency of instrumentation in detecting the element isotope

If standards and unknown species in an ICP yield the same efficiency, the concentration of the unknown elemental isotope can be calculated simply with the following equation:

$$C_{Unknown} = \frac{\left(I_{Unknown} - I_{Unknown}^{Background}\right)}{\left(I_{Std} - I_{Std}^{Background}\right)} * C_{Std} \tag{3.2}$$

where $C_{Unknown}$ and C_{std} are concentrations of the elemental isotope in unknown and standard electrolytes, respectively. I denotes mean intensities acquired from mass counts from unknown and standard solutions with their backgrounds.

The linear relationship between the concentration of elemental isotopes in digested electrolyte and the intensity of mass counts in the ICP-MS system is because of the high resolution of mass separation in quadrupole and the discrete dynode detector which counts electrons hitting on multiplier up to approximately 1 million times. Even though the mass discretion of a quadrupole mass detector possesses high efficiency and resolution, system drift as temperature, pressure, airflow rate, and plasma spacing, *etc.* can cause measurement outcomes to change. Thus, mass intensity measurements corresponding to their known concentration samples must be used, as shown in the above equations. Such comparative measurements are the bases of internal or external calibration techniques mentioned above.

Both methods of imprinting known concentration samples with corresponding mass counts (intensity) are excellent practices to obtain valid concentrations of unknown samples in most cases of stationary measurements. However, when mass counts are acquired as a function of time, using the external calibration method is, unfortunately, impossible because of continuous data acquisition. Meanwhile internal calibration practice could also be invalid when instrument encounters unpredictable hardware drifts. However, applying both external and internal calibration process with standard additions

could overcome the difficulties and computational development of a time-resolved algorithm is necessary in this research as the time factor is introduced in the mass count for solutions with unknown concentrations.

3.1.2. Development of Time-resolved Computational Algorithm

Concentrations of external standard solutions are expressed as $C(\varepsilon)^n$, in which the element is expressed as ε, and superscript n represents the specific concentration for calibrations. In this research, external standard solutions are made of 0.5, 1.0, 2.0, 5.0, 10.0, 50, and 100 ppb. Correspondingly, the intensity of mass counts of each known standard is measured as $I_o(\varepsilon)_a^n$ and $I_o(\varepsilon)_b^n$ before and after the course of corrosion test, respectively. This dual external calibration (before and after each experiment) scheme is illustrated as follows:

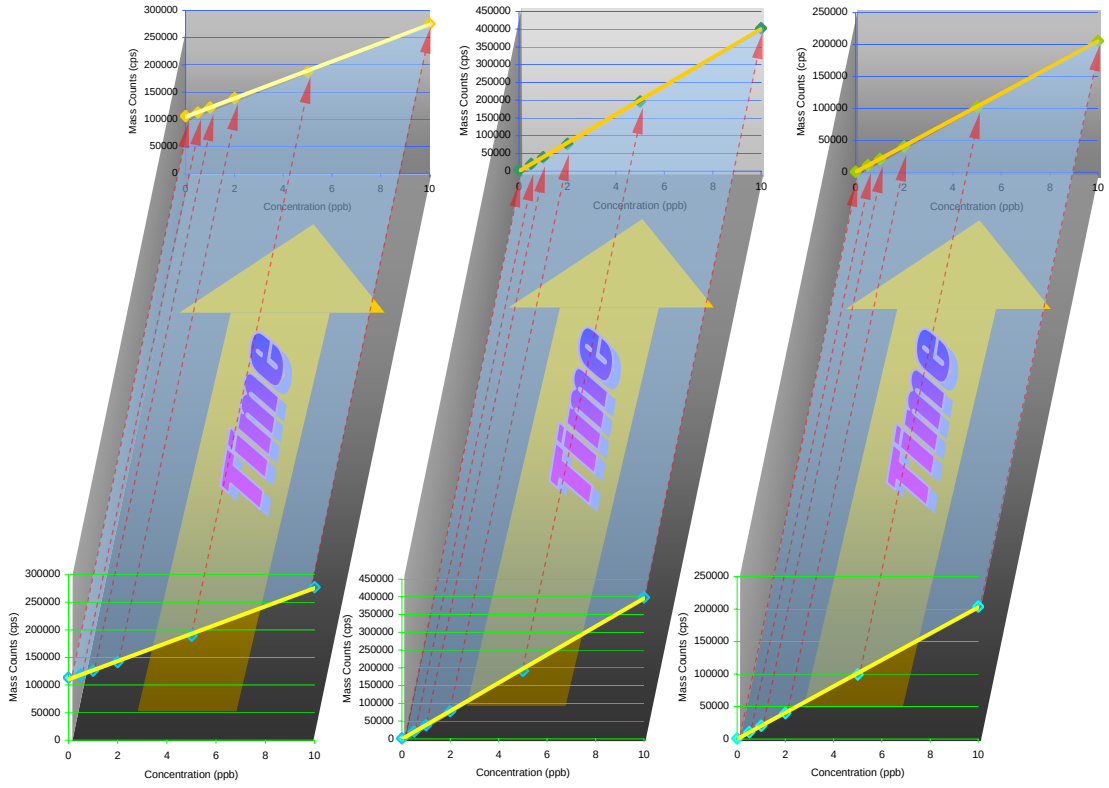

Figure 3.1. A time-resolved calibration algorithm scheme

First, to derive the time-resolved calibration algorithm scheme, initial and final external calibrations are performed with external standard solutions for which the various concentrations of interested elements are known. For example, in the above figure, the intensity of mass counts of Li, Y, and Tl are measured before and after a test run. Concentration of the element in the solutions corresponding to the mass counts is then linearly extrapolated. Using a mass count with 10 ppb standard with internal 10 pp spikes as a comparative value, the critical normalized factor is obtained to result variation of polynomial progression of other isotopes. Initial external calibration with different concentrations $C(\varepsilon)^n$ yields corresponding mass count (intensity) of $I(\varepsilon)_a^n$, which can then be written as:

$$I_o(\varepsilon)_a^n = \alpha(\varepsilon)_a * C_o(\varepsilon)^n + \beta(\varepsilon)_a \tag{3.3a}$$

where the slope of the calibration curve is expressed as:

$$\alpha(\varepsilon)_a = \frac{\left(\sum_n \left(C_o(\varepsilon)^n * I_o(\varepsilon)_a^n \right) - \frac{\left(\sum_n C_o(\varepsilon)^n * \sum_n I_o(\varepsilon)_a^n \right)}{n} \right)}{\left(\sum_n \left(C_o(\varepsilon)^n \right)^2 - \frac{\left(\sum_n \left(C_o(\varepsilon)^n * I_o(\varepsilon)_a^n \right) \right)^2}{n} \right)} \tag{3.4a}$$

and the interception of the curve is then:

$$\beta(\varepsilon)_a = \left(\frac{\sum_n I_o(\varepsilon)_a^n}{n} \right) - \alpha(\varepsilon)_a * \left(\frac{\sum_n C_o(\varepsilon)^n}{n} \right) \tag{3.5a}$$

Similarly, the calibration curve after testing is calculated using:

$$I_o(\varepsilon)_b^n = \alpha(\varepsilon)_b * C_o(\varepsilon)^n + \beta(\varepsilon)_b \tag{3.3b}$$

where

$$\alpha(\varepsilon)_b = \frac{\left(\sum_n \left(C_o(\varepsilon)^n * I_o(\varepsilon)_b^n \right) - \frac{\left(\sum_n C_o(\varepsilon)^n * \sum_n I_o(\varepsilon)_b^n \right)}{n} \right)}{\left(\sum_n \left(C_o(\varepsilon)^n \right)^2 - \frac{\left(\sum_n \left(C_o(\varepsilon)^n * I_o(\varepsilon)_b^n \right) \right)^2}{n} \right)} \tag{3.4b}$$

and

$$\beta(\varepsilon)_b = \left(\frac{\sum_n I_o(\varepsilon)_b^n}{n} \right) - \alpha(\varepsilon)_b * \left(\frac{\sum_n C_o(\varepsilon)^n}{n} \right) \tag{3.5b}$$

The expressions of the external calibration equations are suitable for all elements in the external standard solutions. Practically, the curve slopes and interceptions of all elements of interest slightly change due to a shift of system configurations during operation. Therefore, a presumption of linear drift of parameters with time is made. The calibration curve could be then extrapolated as the expression:

$$I_o(\varepsilon)_t^n = \left[\alpha(\varepsilon)_a - \frac{\left(\alpha(\varepsilon)_a - \alpha(\varepsilon)_b \right)}{T} * t \right] * C_o(\varepsilon)_t^n + \left[\beta(\varepsilon)_a - \frac{\left(\beta(\varepsilon)_a - \beta(\varepsilon)_b \right)}{T} * t \right] \tag{3.6}$$

where *t* is the time when the $C_o(\varepsilon)_t^n$ is measured, and *T* represents total running time for the experiment. The effective slope and interception could be given as:

$$\tilde{\alpha}(\varepsilon)_t = \left[\alpha(\varepsilon)_a - \frac{\left(\alpha(\varepsilon)_a - \alpha(\varepsilon)_b\right)}{T} * t \right] \tag{3.7}$$

and

$$\tilde{\beta}(\varepsilon)_t = \left[\beta(\varepsilon)_a - \frac{\left(\beta(\varepsilon)_a - \beta(\varepsilon)_b\right)}{T} * t \right] \tag{3.8}$$

The mass intensity in standard solutions based upon this double calibration method is then simplified as follows:

$$I_o(\varepsilon)_t^n = \tilde{\alpha}(\varepsilon)_t * C_o(\varepsilon)_t^n + \tilde{\beta}(\varepsilon)_t \tag{3.9}$$

3.1.3. Algorithm of Internal Standard Conversion

When internal standards, sometimes also called spikes, are added into the calculations, the normalizations of the concentrations of these elements are needed. The calculation algorithm with internal spikes can be expressed linearly or retrofitted nonlinearly to the overall calculations.[3.1] In this research, the linear inversion approach was applied. Based upon Eq. (3.9), the standards of Li, Y, and Tl internal spikes with 10 ppb are then expressed as:

$$I_o(\varepsilon)_t^{10} = \tilde{\alpha}(\varepsilon_p)_t * C(\varepsilon)_t^{10} + \tilde{\beta}(\varepsilon_p)_t \tag{3.10}$$

The normalized factors of these internal spike elements are then expressed as:

$$\delta(\varepsilon_p)_t^{10} = \frac{I(\varepsilon_p)_t^{10}}{I_o(\varepsilon_p)_t^{10}} \tag{3.11}$$

where ε_p represents Li, Y, and Tl. The normalized factors of primary elements are considered to be independent of concentrations in the calibration process because the similarity between standards and extrapolated values depends on system performances.[3.2] Therefore, the normalized factors of primary elements are written as:

$$\delta(\varepsilon_p)_t = \frac{I(\varepsilon_p)_t}{I_o(\varepsilon_p)_t} \tag{3.12}$$

However, the normalized factors are functions of element yields, which are closely related to the mass range of isotopes, due to mass selectivity and sensitivity. In this research, to simplify the relationship between normalized factors of interested elements and primary elements, secondary polynomial extrapolation is then used:

$$\delta(\varepsilon)_t = A_1(\varepsilon_p)_t * \phi(\varepsilon)^2 + A_2(\varepsilon_p)_t * \phi(\varepsilon) + A_3(\varepsilon_p) \tag{3.13}$$

where $\phi(\varepsilon)$ is the mass of element ε. The coefficients of the equation can be expressed as:

$$\begin{aligned} A_1(\varepsilon_p)_t &= \frac{\frac{\delta(Tl)_t - \delta(Li)_t}{205-7} - \frac{\delta(Y)_t - \delta(Li)_t}{89-7}}{205-89} \\ &= 6.16*10^{-5} * \delta(Li)_t - 1.05*10^{-4} * \delta(Y)_t + 4.35*10^{-5} * \delta(Tl)_t \end{aligned} \tag{3.14}$$

$$A_2(\varepsilon_p)_t = \frac{\delta(Y)_t - \delta(Li)_t}{89-7} - A(\varepsilon_p)_t$$
$$= -0.00628 * \delta(Li)_t - 0.00211 * \delta(Y)_t + 0.00418 * \delta(Tl)_t \quad (3.15)$$

$$A_3(\varepsilon_p)_t = \delta(Li)_t - A(\varepsilon_p)_t * 7^2 - B(\varepsilon_p) * 7$$
$$= 1.00326 * \delta(Li)_t + 0.00726 * \delta(Y)_t - 0.006312 * \delta(Tl)_t \quad (3.16)$$

The corrective mass intensity of an interested analyte at time *t* is then given as:

$$\tilde{I}(\varepsilon)_t = \left[I(\varepsilon)_t - I_b(\varepsilon)_t\right] * \delta(\varepsilon)_t \quad (3.17)$$

where $I_b(\varepsilon)_t$ is the background mass intensity measured at time *t*, which is derived based upon initial and final background calibrations with:

$$I_b(\varepsilon)_t = \left[I_b(\varepsilon)_a - \frac{t}{T} * I_b(\varepsilon)_b \right] \quad (3.18)$$

Reversely, the concentration of electrolyte in elements of interest is expressed as:

$$C(\varepsilon)_t = \frac{\tilde{I}(\varepsilon)_t - \tilde{\beta}(\varepsilon)_t}{\tilde{\alpha}(\varepsilon)_t} \quad (3.19)$$

The concentration of a specific element is a function of time and mass counts measured by ICP-MS in relation to mass counts from external calibrations, background, and the internal standard at 10 ppb level.

3.2. Verification of Mass Fractionations

The changes of the mass fractionations in the *in-situ* process are herein calculated using the time-resolved calibration algorithm, for which a series of verifications are essentially needed to ensure the correctness and validity of correspondent to concentrations of unknowns in real measurements. In order to verify the fitness of the time-resolved computation algorithm, a series of verification solutions with standard 1.0, 2.0, 5.0, 10, 20, 50, and 100 ppb in balance in 2% HNO_3 and DI water were made out of dilution from 10 ppm known solutions supplied from Inorganic Venture Inc. The algorithm was first applied to stability measurements, in which time was a core parameter. In this research, different operation times would be set for different experiments; it was important that the instrument became stable in a timely fashion so that insight into instrumentation fluctuation could be obtained. Satisfactory correlations of the measurements with the verification solutions were then provided to show confidence in using the mathematics for future quantification of unknown concentration of elements. Error rate estimations and a brief summary are presented thereafter in this section.

3.2.1. Stability Verifications of ICP-MS Measurements

Stability measurements were performed for solutions containing 1.0, 2.0, 5.0, 10, 20, 50 and 100 ppb of elements of interest in balance with 2% HNO_3 and DI water. Each test lasts for one hour in a sequence of increasing concentrations. Between each test, calibrations and purges were employed to minimize interferences. Figure 3.2 shows the stability of ICP counts of internal standards with 10 ppb of each element in an hour interval measurement for a total of 6 hours. The actual time of the experiment was much longer since calibrations were implemented in between.

Mass counts of 10 ppb Li, Y, and Tl in the blends were first obtained, which showed fairly linear during each course of test. The standard deviation of acquired data indicated that mass counts of Y stay fairly constant in all types of concentrations of matrix, while Li mass counts increased. Conversely, Tl decreased its mass counts as the concentration of analytes increases. However, in general, standard deviations of mass counts of all three internal standards were less than 2%. The stability of internal standards regardless of the

variation of operational parameters, such as pressure, temperature, and flow rates of carrier gas, *etc*., was a key factor to ensuring valid output and success for trace and ultra-trace analysis.

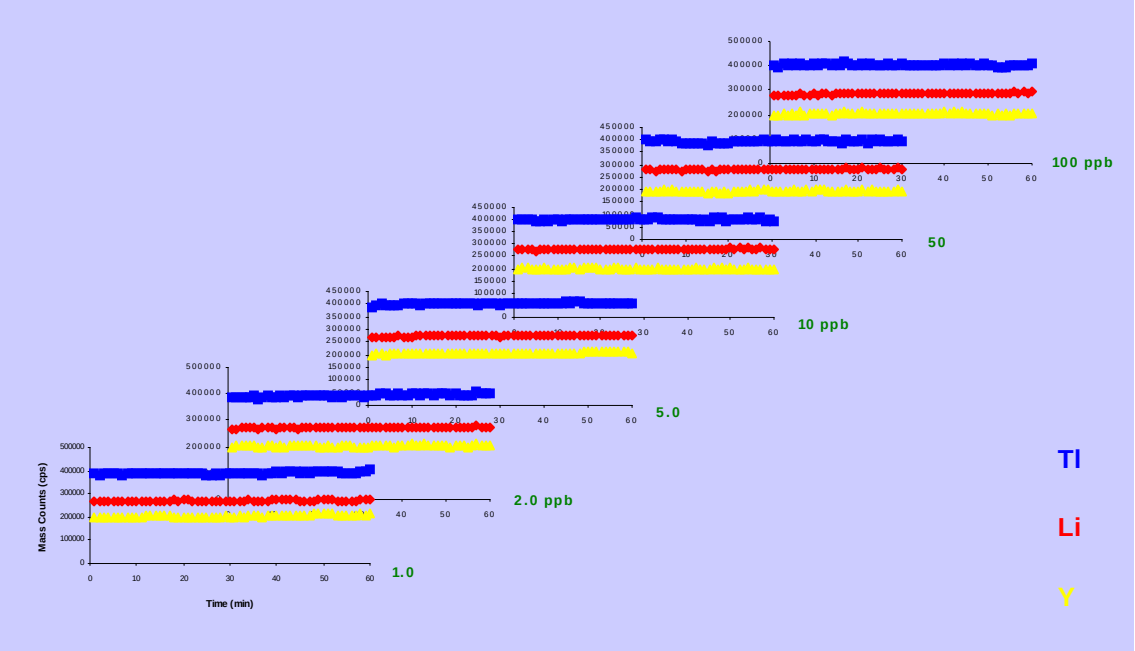

Figure 3.2. Mass counts of internal standards at 10 ppb concentrations as a function of time in different matrix concentrations

Derived from ICP-MS counts, concentrations of these internal standards from the time-resolved mathematic algorithm are presented in Figure 3.3, which show good matches to their known concentrations of 10 ppb regardless of matrix concentrations.

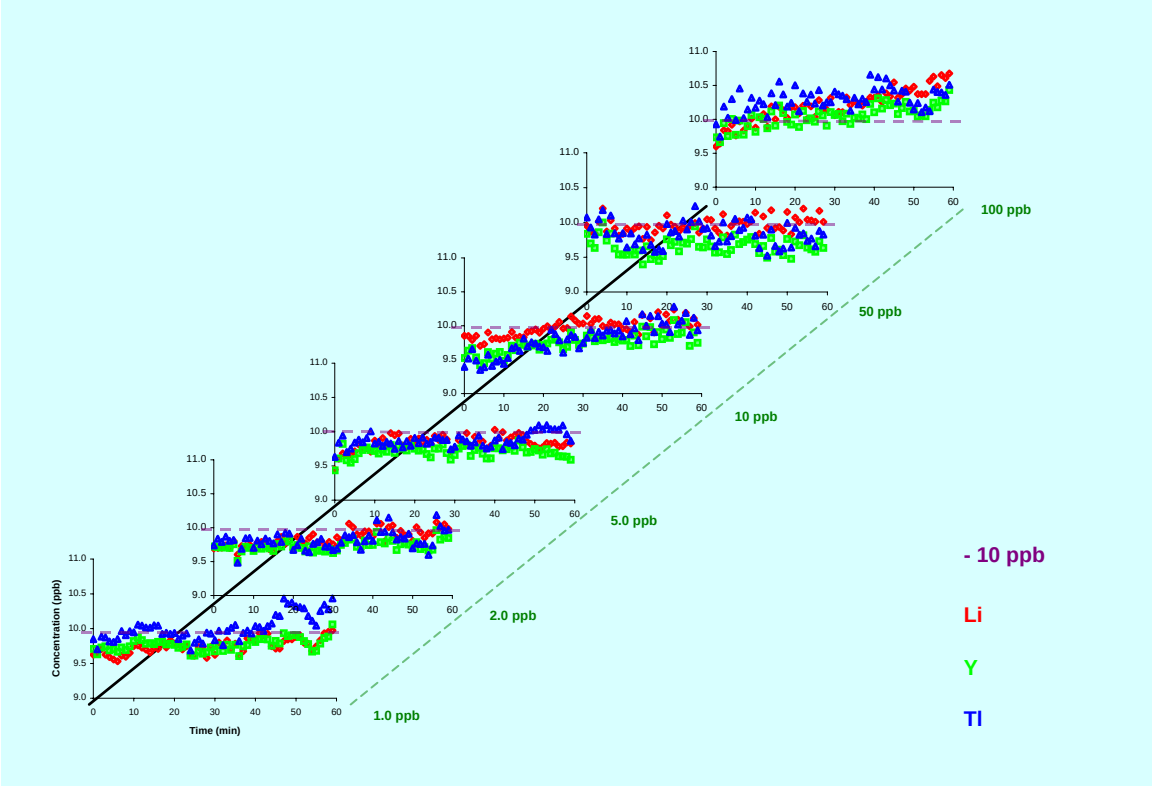

Figure 3.3. Calculated 10 ppb internal standard spikes based upon time computation algorithms

Though general trends of the ICP counts for each element were slightly up swung, satisfactory stability within each hour measurement was demonstrated, which was critical to achieving stable and consistent real time measurements. Accordingly, other interested elements were also charted. The calculated concentrations of each element of interest within the same time period are showing in the following chats.

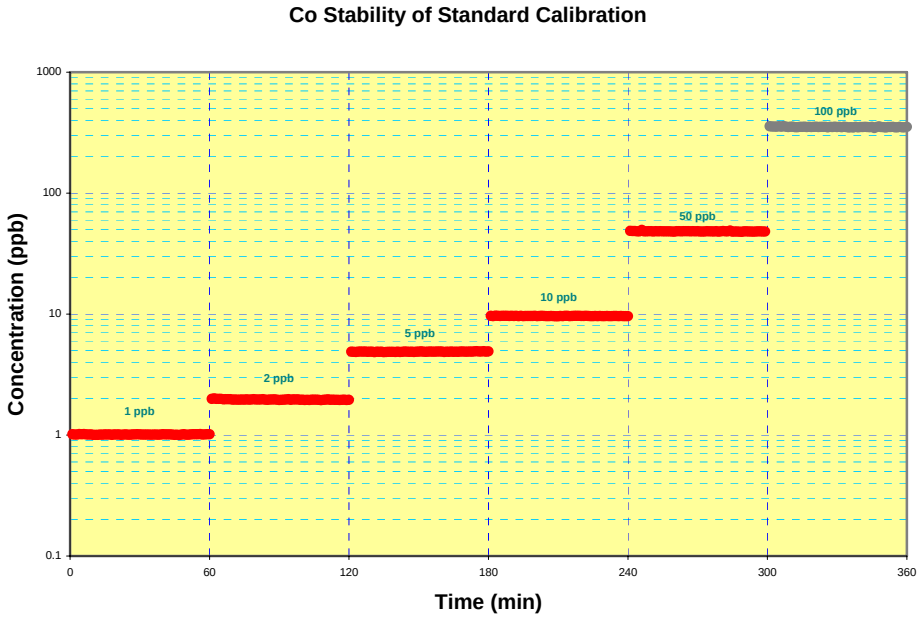

Figure 3.4(a). Per hour stability of standard calibration curves for Co with different standard concentrations

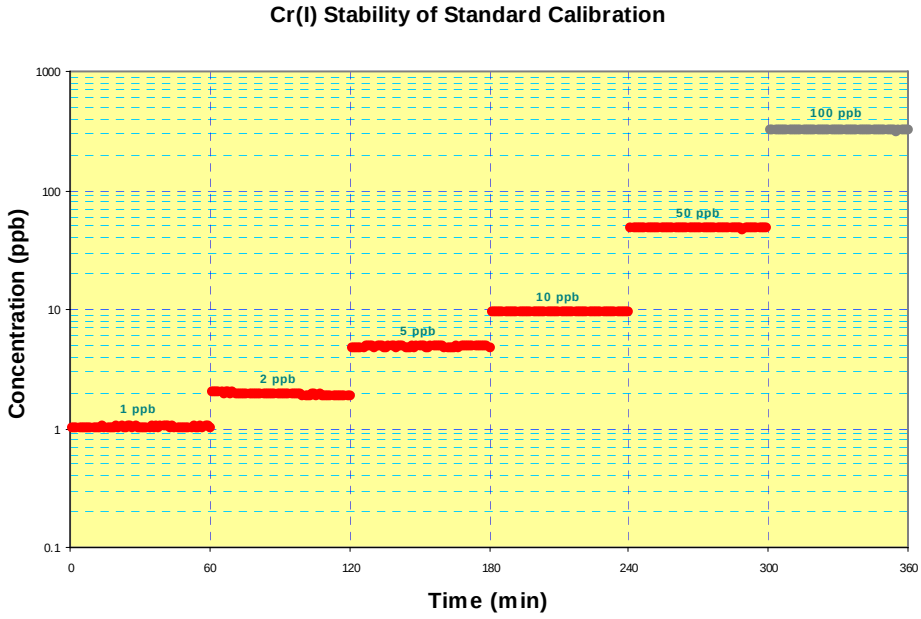

Figure 3.4(b). Per hour stability of standard calibration curves for Cr(I) with different standard concentrations

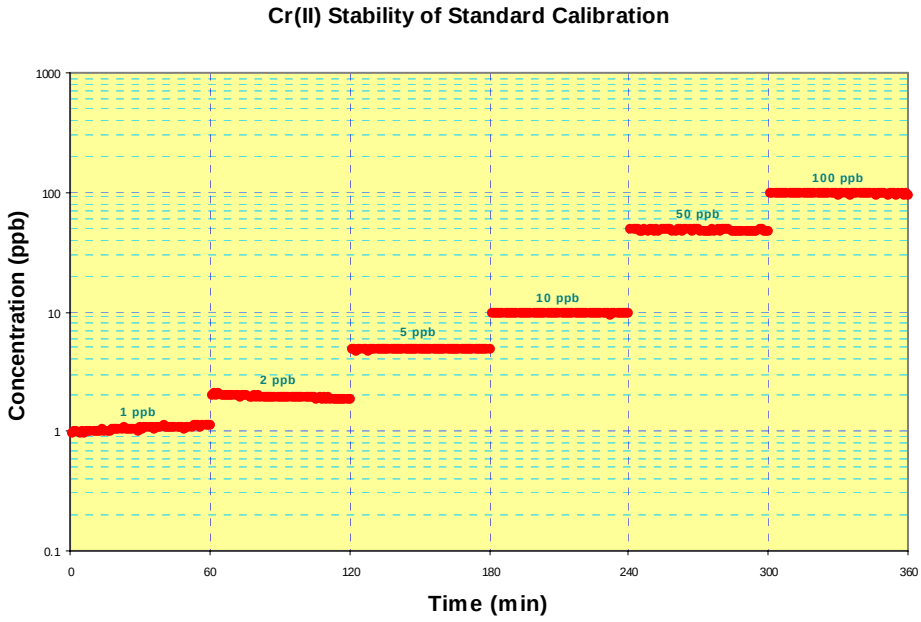

Figure 3.4(c). Per hour stability of standard calibration curves for Cr(II) with different standard concentrations

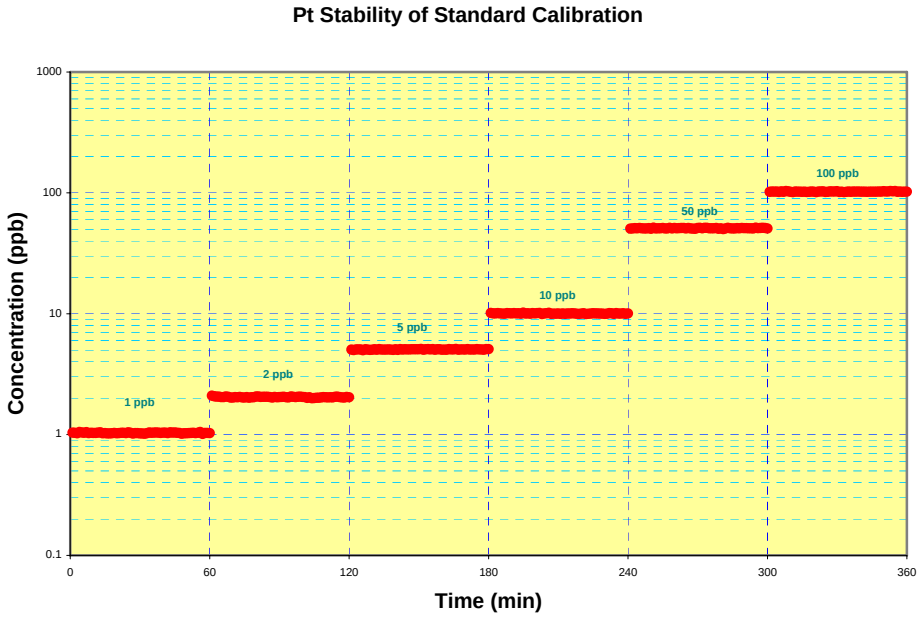

Figure 3.4(d). Per hour stability of standard calibration curves for Pt with different standard concentrations

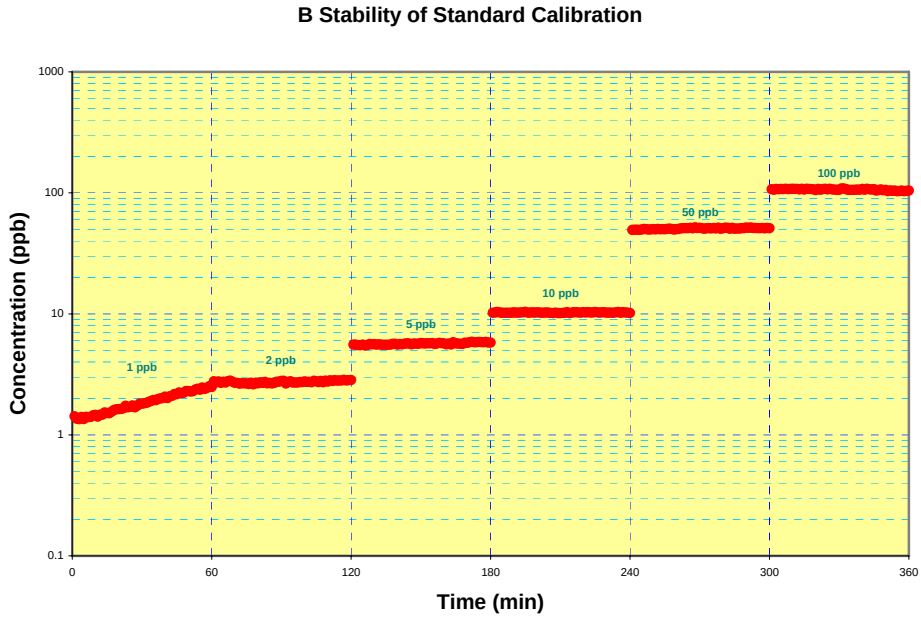

Figure 3.4(e). Per hour stability of standard calibration curves for B with different standard concentrations

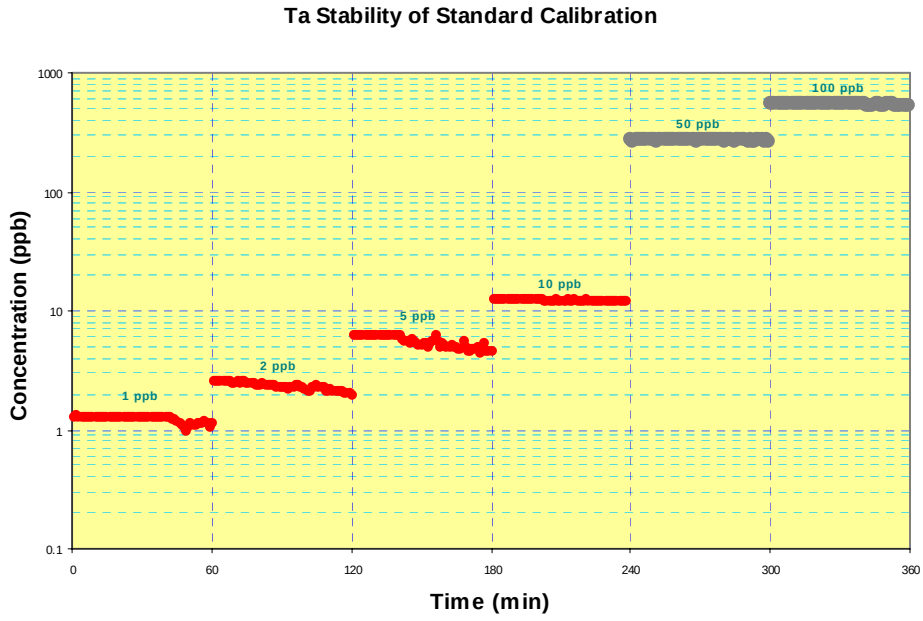

Figure 3.4(f). Per hour stability of standard calibration curves for Ta with different standard concentrations

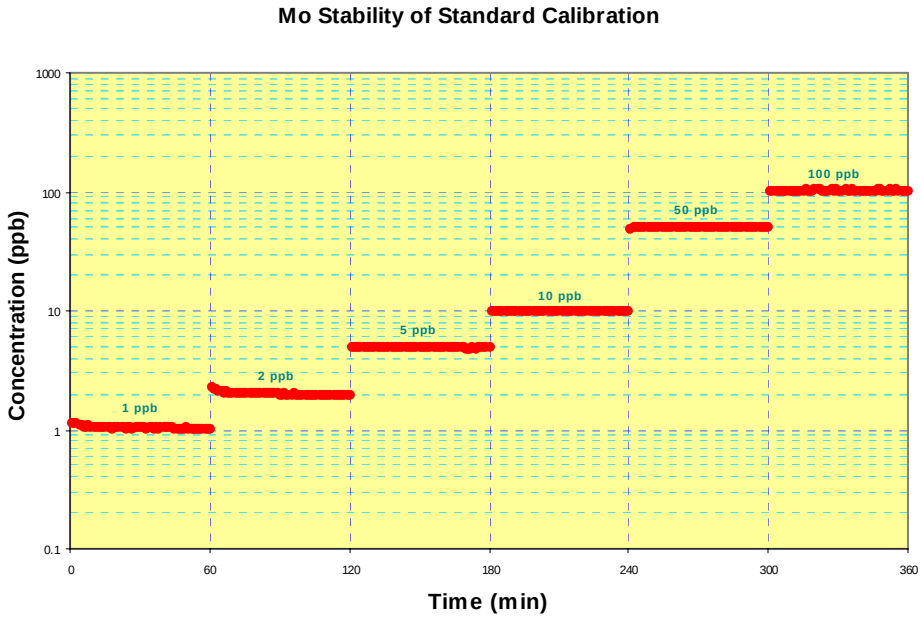

Figure 3.4(g). Per hour stability of standard calibration curves for Mo with different standard concentrations

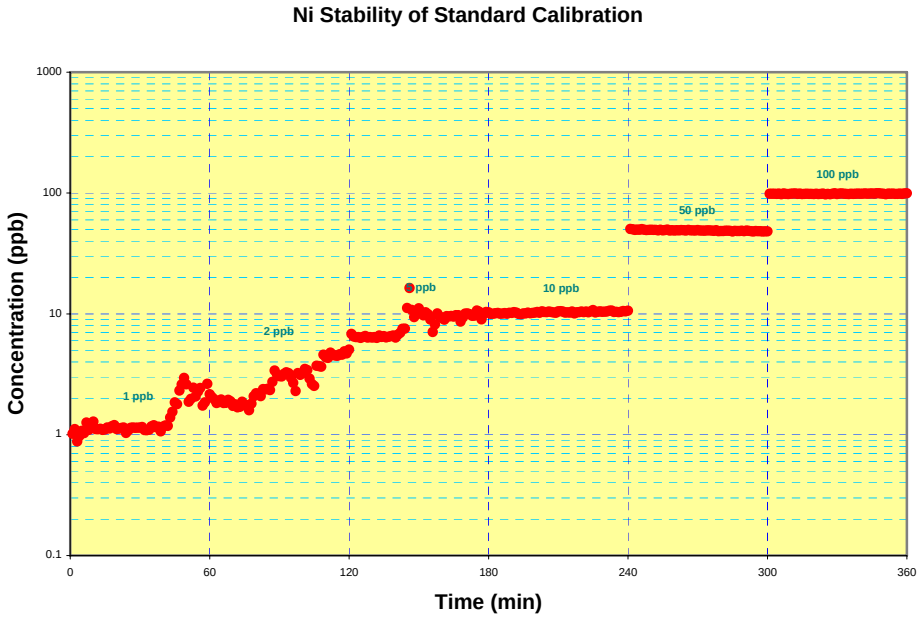

Figure 3.4(h). Per hour stability of standard calibration curves for Ni with different standard concentrations

The digestion stability of the ICP system was very promising for the elements of interest, Cr(II), Pt, B, and Mo, over an hour period at different concentration ranges from 1 ppb to 100 ppb. Slight deviations from the centerlines of B and Ta digestions at low concentrations, as well as fluctuations for Ni at concentrations below 10 ppb, caused minor perturbations in the correlations. It was important to notice in these experiments that the mass resolution of ICP-MS was no longer in the digital reading range at high concentrations of Cr(I), Co, and Ta, which were shown in gray color lines are shown in above charts. These limitations in each elemental correlation provided an important guideline: digestions were better detected and quantified with minimum distortion of the measurement results.

3.2.2. Standard Correlation Measurements

By averaging the measured concentrations of individual element from each hourly segment, the following graphs show the calibration curves of this system with known concentration standards.

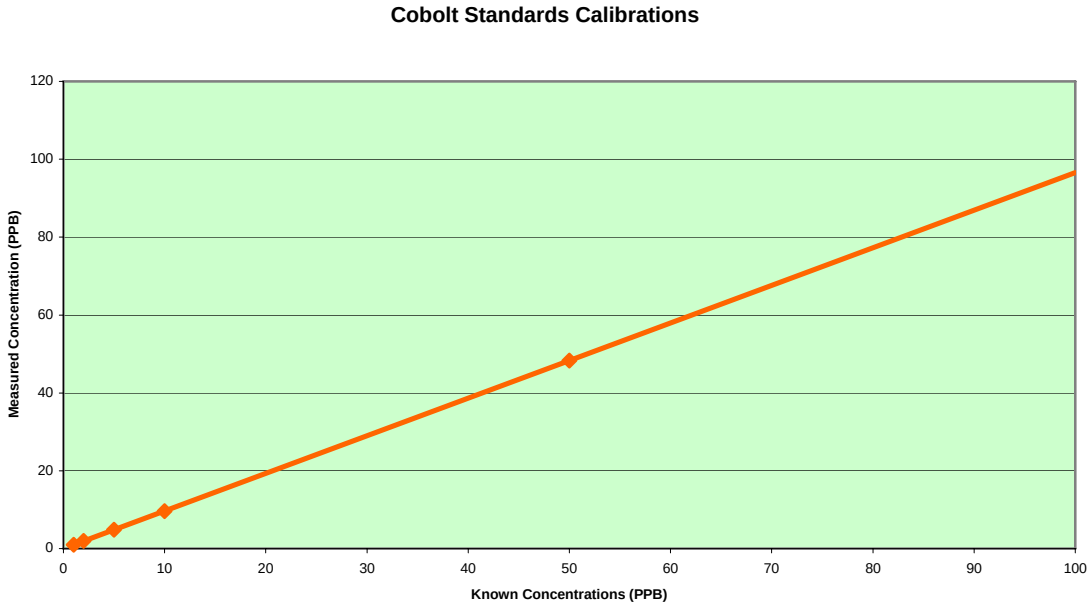

Figure 3.5(a). Correlation between known concentration standard and measured concentration for Co by the ICP-MS system

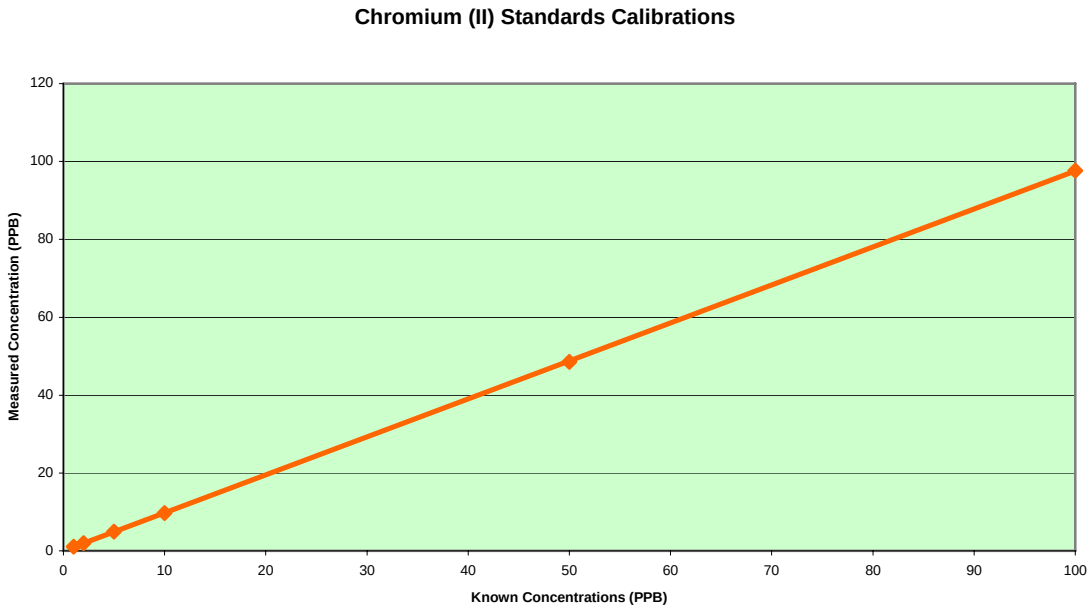

Figure 3.5(b). Correlation between known concentration standard and measured concentration for Cr(II) by the ICP-MS system

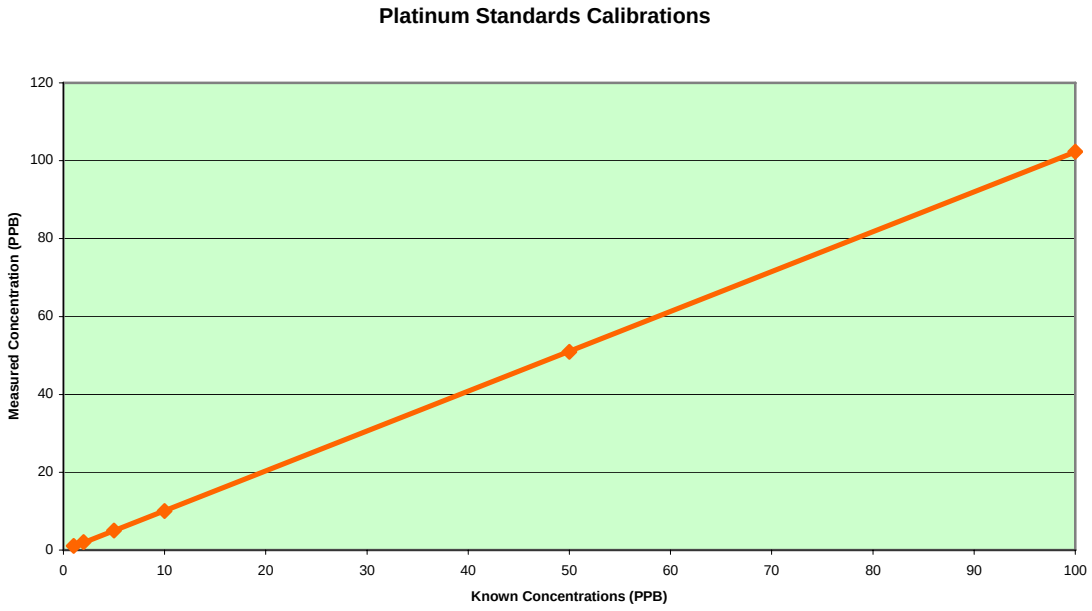

Figure 3.5(c). Correlation between known concentration standard and measured concentration for Pt by the ICP-MS system

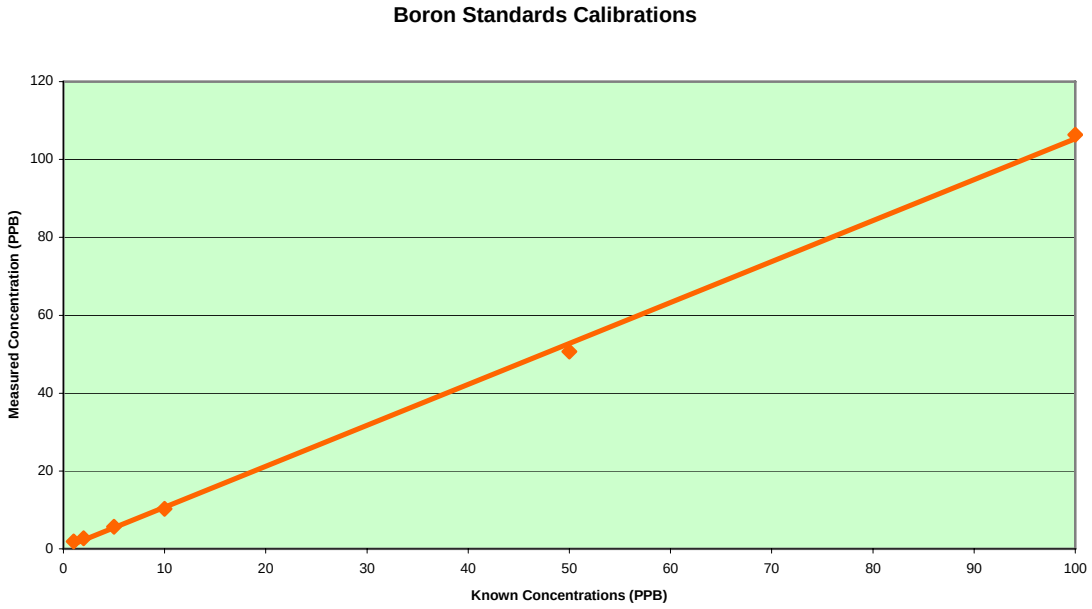

Figure 3.5(d). Correlation between known concentration standard and measured concentration for B by the ICP-MS system

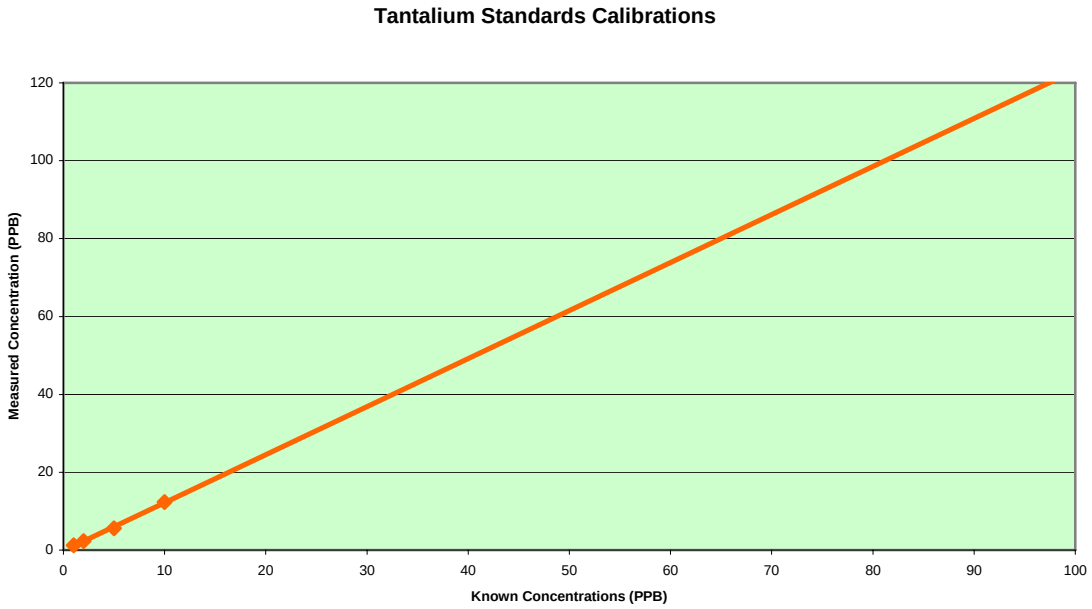

Figure 3.5(e). Correlation between known concentration standard and measured concentration for Ta by the ICP-MS system

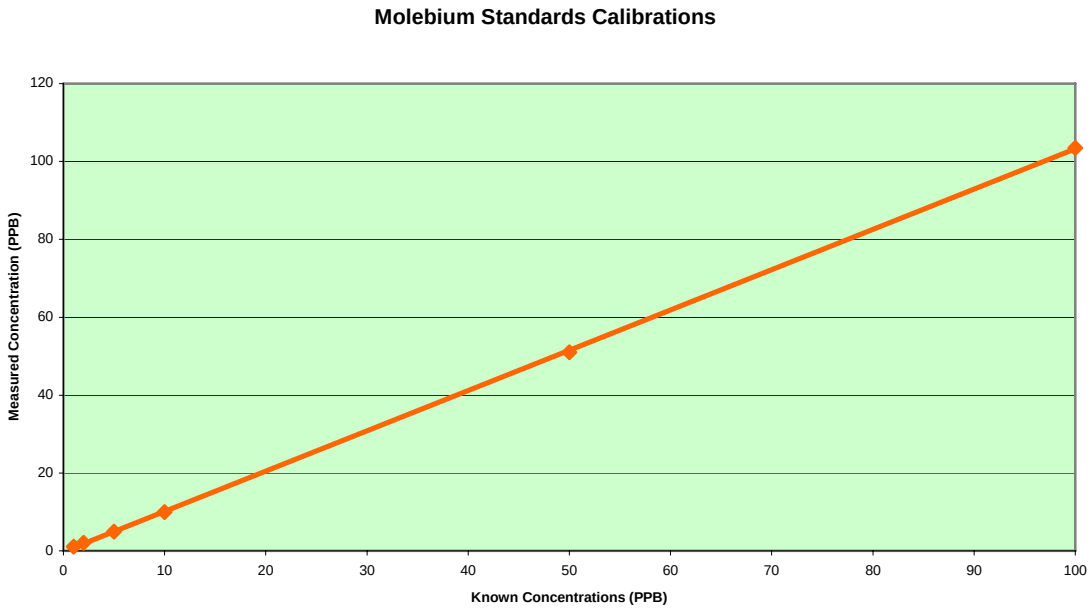

Figure 3.5(f). Correlation between known concentration standard and measured concentration for Mo by the ICP-MS system

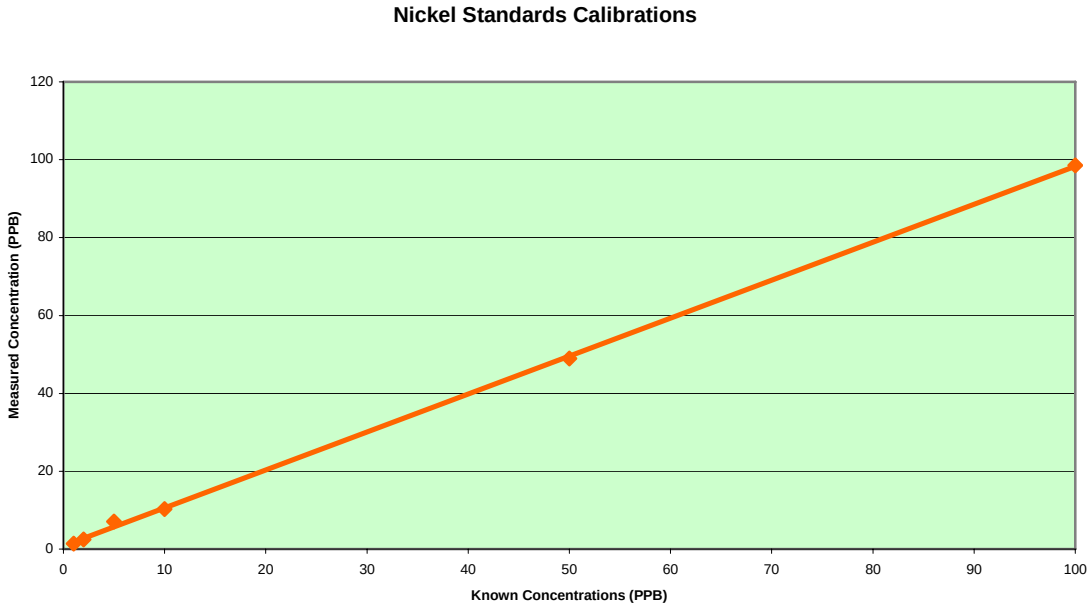

Figure 3.5(g). Correlation between known concentration standard and measured concentration for Ni by the ICP-MS system

The elements Cr(II), Pt, B, Mo, and Ni had strong correlations between known standards and measured concentrations with the ICP-MS system. In the Co chart, a correlation at

very high concentrations over 50 ppb was unsustainable and out of the linear range. However, at very low range of concentrations, the linear correlations were satisfactory. A nonlinear regression could be found in the Ta chart when the content exceeds 10 ppb. The reason for such a deviation from a linear correlation was due to the transformation of the digital signal output into an analogue signal. The mass count data in the above-described experiments were mostly collected in a digitized signal mode at low concentrations range. The digital output depended strongly on how much the element needs to be counted into the mass spectrometer. When the amount of an element gushing into the detector exceeded a threshold, the digital mass counting became saturated, and analogue output was turned on, which resulted in high concentration calibrations for Ta and Co. This transformation yielded non-linear regression in standard calibrations. The limitation of Co and Ta provided measurement guidance that proper instrumentation adjustment for these elements might be needed to ensure that the measured concentrations of these elements were controlled under these counting thresholds.

3.2.3. Specificity and Errors

The standard deviation of linear regression calibration curves are then calculated as:

$$r_a^2 = \frac{\left(\sum_n C_o(\varepsilon)^n * I_o(\varepsilon)_a^n\right)^2}{\left(\sum_n \left(C_o(\varepsilon)^n\right)^2 * \sum_n \left(I_o(\varepsilon)_a^n\right)^2\right)} \tag{3.21a}$$

and

$$r_b^2 = \frac{\left(\sum_n C_o(\varepsilon)^n * I_o(\varepsilon)_b^n\right)^2}{\left(\sum_n \left(C_o(\varepsilon)^n\right)^2 * \sum_n \left(I_o(\varepsilon)_b^n\right)^2\right)} \tag{3.21b}$$

Based upon error calculations, the relative deviations of standard elements at different internal spike concentrations are summarized in the following figure.

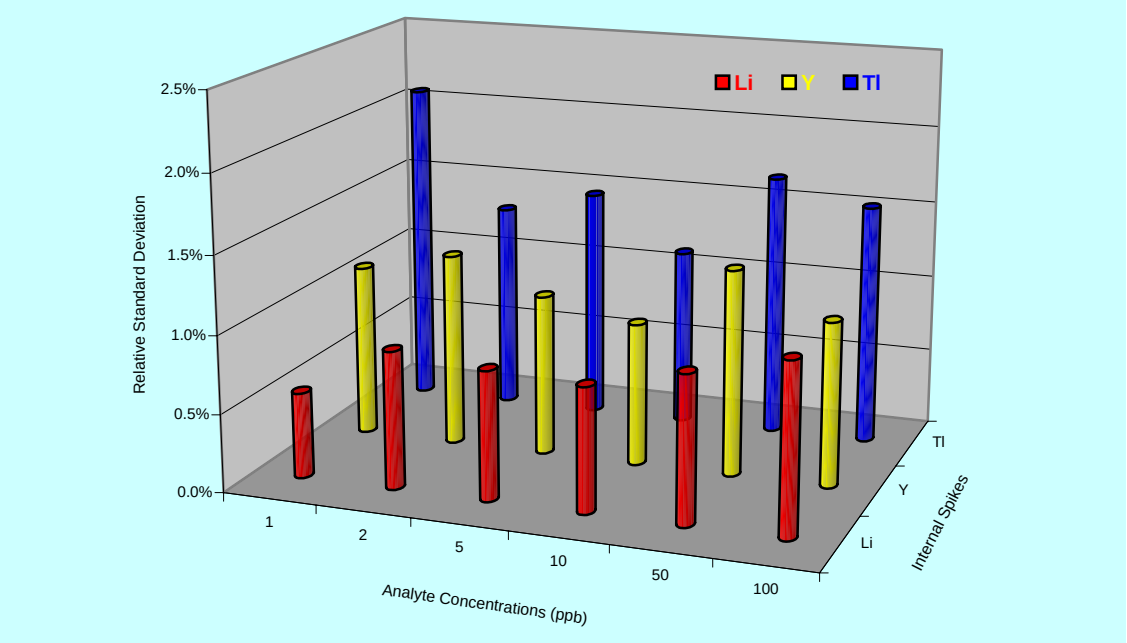

Figure 3.6. Standard deviations of three internal spikes in different concentrations of analyte-containing solutions

Showing how mass counts responded to internal standards of concentrations of analytes was important to demonstrating the interference of analytes in solutions having minimum or no scaleable affects on readings. The independence of mass counts from internal standards mixed in analytes was critical in calculations transforming mass counts into real concentrations of each analyte in a time base. Also, it was important to have stable and less interferential spikes when different concentrations yielded similar stability and low variation of mass counts.[3.3]

3.2.4. Standard Correlation Summary

The following table summarizes the correlations of concentration and deviations for the measurements of these elements.

Table 3.1. Summery of standard calibration results with correlation factors, standard deviations, and recovery rates at different ppb levels for all elements

Element	Correlation Factors		Standard Deviation (R^2)	Recovery Rate (%) at 1 ppb	Recovery Rate (%) at 10 ppb	Recovery Rate (%) at 100 ppb
	a	b				
Co	**0.9655**	**0.0315**	**1.0000**	**101.0**	**96.4**	**96.6***
Cr(I)	**0.9675**	**0.0475**	**1.0000**	**103.1**	**97.2**	**96.7***
Cr(II)	**0.9753**	**-0.0114**	**1.0000**	**106.0**	**96.9**	**97.6**
Pt	**1.0231**	**-0.0799**	**1.0000**	**103.1**	**100.4**	**102.3**
B	**1.0517**	**0.1443**	**0.9993**	**186.2**	**102.5**	**106.5**
Ta	**1.2335**	**-0.1791**	**0.9966**	**124.5**	**123.4**	**122.9***
Mo	**1.0346**	**-0.2244**	**0.9999**	**105.2**	**99.2**	**103.5**
Ni	**0.9744**	**0.8417**	**1.0000**	**142.7**	**103.0**	**98.6**

As indicated in the above table, all elements except for Ta had fairly good dynamic correlations in a range from 1 ppb to 100 ppb. Ta consistently measured about 20% over known concentrations with regard to recovery rates. In the recovery rate at 100 ppb column, recovery rates with asterisks indicate that the values were estimated due to analogue signal recorded instead of digital integrated signal.

3.3. Reproducibility and Interferences

3.3.1. Isotopic Reproducibility Measurements

Due to the natural existence of isotopic abundances of all elements, reproducibility measurements and verification were important. In the group of elements of interest, Cr had the most distinguished two isotopic abundance under plasma excitation, namely Cr(I)

and Cr(II), which had atomic masses of 52 and 53, respectively, and relative isotopic abundances of 83.8% and 9.5%, respectively. Figure 3.7 shows a negligible difference in the measurements at different concentrations between Cr(I) and Cr(II) regardless of their isotopic abundance differences. Therefore, from the isotopic reproducibility point of view, the measurement results of Cr(I) and Cr(II) were equally valid.

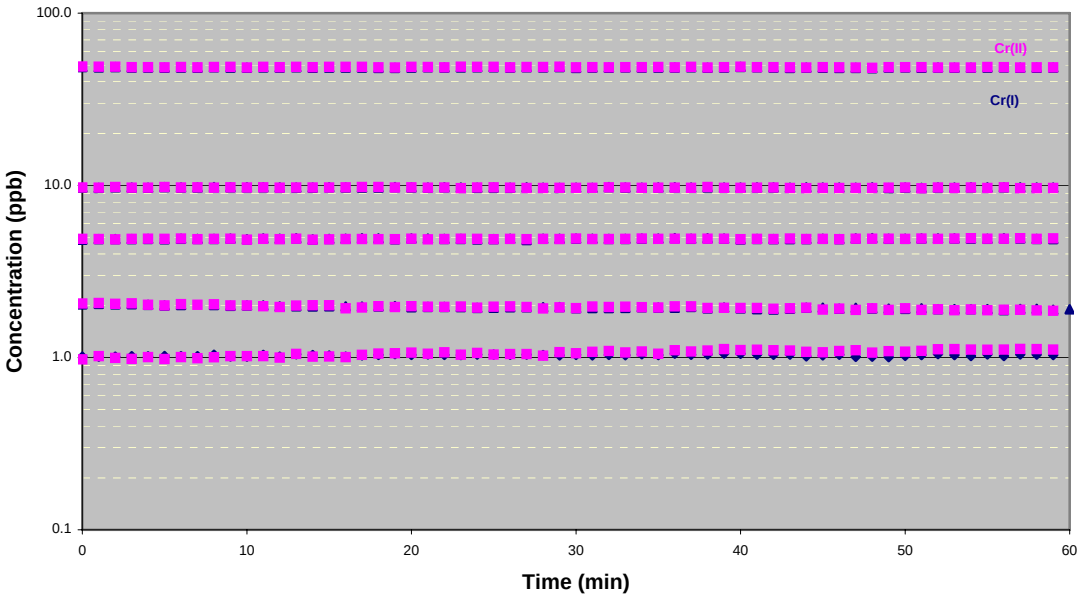

Figure 3.7. Very close matches between isotopic Cr(I), shown with purple squares, and Cr(II), shown with dark blue triangles, at different concentrations

This high correlation between Cr isotopic abundances provided solid support for representing Cr concentrations with Cr(I) or Cr(II) measurements. Unlike Cr, the isotopic abundances of most other elements had only a single response in plasma excitations. Thus, one mass selection was the only choice for elements other than Cr.

3.3.2. Plasma-generated Interferences

The interference of Cr(I) with ArC is commonly known and inevitably encountered in ICP analysis. Ar in the ICP system is the main purge gas used to sustain plasma in this system, and the existence of carbon from the degeneration of surface carbon film is unavoidable. Also, the organic lubricant layer on the sample surface could be another

potential carbon source. Fortunately, Cr(II) exhibited no carbon related interferences with a mass of 53, which then selected to be used in this research consistently.

Phosphorous was the only element in the group showing strong interferences with nitric acid matrices due to the same mass to charge ratio. The mass of 31 of phosphorus (P) matched that of nitrogen hydroxide (NOH), which combined masses of 14 (N), 16 (O), and 1 (H). When concentrations of nitric acid were increased in ICP solutions, ICP counts for phosphorus increased dramatically, and the correlation of the standard of P to nitric acid became nonlinear. Figure 3.8 shows the relationship between ICP counts and different concentrations of nitric solutions.

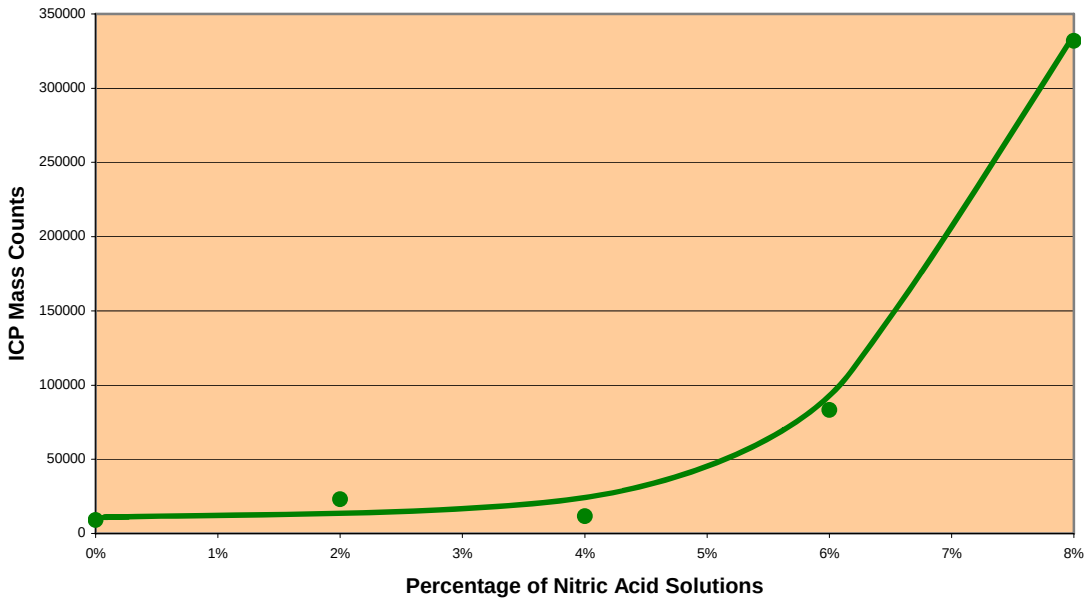

Figure 3.8. Dependence of Phosphorous ICP counts on nitric acid concentrations

Even though the changes in ICP counts for phosphorous at low nitric acid concentrations, say less than 4%, were not as dramatic as in high nitric concentration solutions, to quantify amount of phosphorous in this study was not desirable .

3.4. Potentiodynamic Parameter Optimization

Under potential polarization, potential sweeping rate was one of the critical parameters in controlling outcomes of electrochemical reactions kinetically. By altering the potential

scan rate, the corrosion current density changed because of kinetic equilibrium. In this part of work, potential polarization experiments were performed with different scanning rates at 0.278, 0.139, and 0.069 mV/sec, which corresponded to 3.6, 7.2, and 14.4 sec/mV, respectively, in 2% HNO_3 solution, and the results are presented in this section.

3.4.1. Electrochemical Characteristics

Initial potentials in the experiments were set up at equilibrium potentials obtained from potentiometric measurements, and all scans are terminated at 1000 mV relative to the initial potentials. The current densities as a function of potential applied are shown in Figure 3.9.

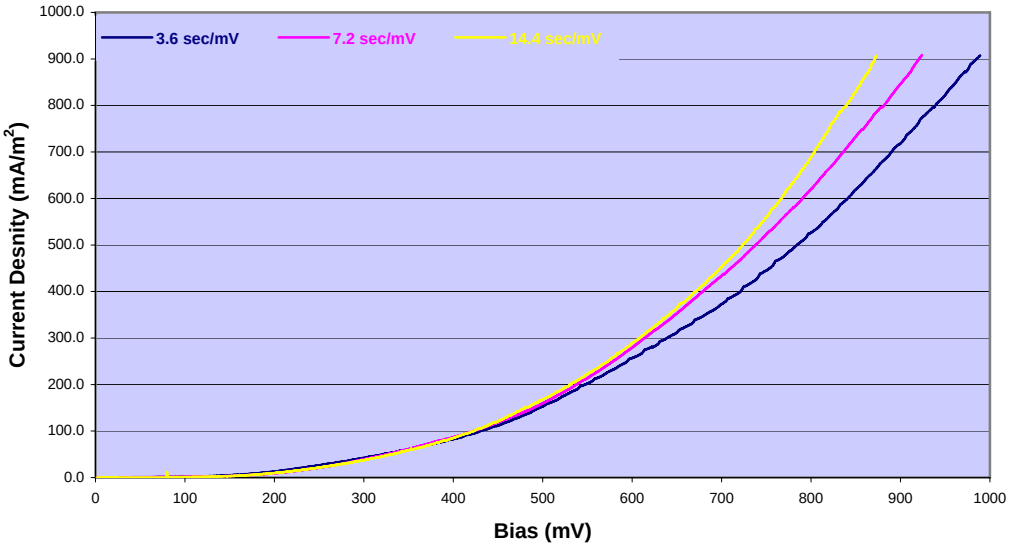

Figure 3.9. Dependence of current density on potential applied to thin film surface with different scan rates

When anodic polarizations were applied with different scanning rates, overall dissolution rates of metallic ions generally followed the same trend. At low bias region less than 450 mV, current densities measured at different scan rates were indistinguishable. But when the potential is applied over 450 mV, variation was presented. Using a fast scan rate of 3.6 sec/mV, electric current density reached 900 mA/m^2 levels at 1000 mV after one hour. By comparison, the slow scan, which was two times slower at 7.2 sec/mV, reached

the same level of current density with about 900 mA/m^2 at 910 mV bias potential. When the scanning rate was further reduced to 14.4 sec/mV, which ideally completed a 1000 mV scan in four hours, the current density reached maximum testing limits at 900 mA/m^2 at about 850 mV applied potential. This fact indicated that the slow scan created equilibrium in electrochemical reactions and brought about a greater number of electric conductive ions in solutions. Meanwhile, concentrations of each cationic element were measured corresponding to the potential applied with increase of bias voltage.

3.4.2. ICP-MS Measurements

Figure 3.10(a) to (g) summarized the elemental concentrations in 2% HNO_3 solutions when polarization potentials were incrementally scanned from 0 to 1000 mV.

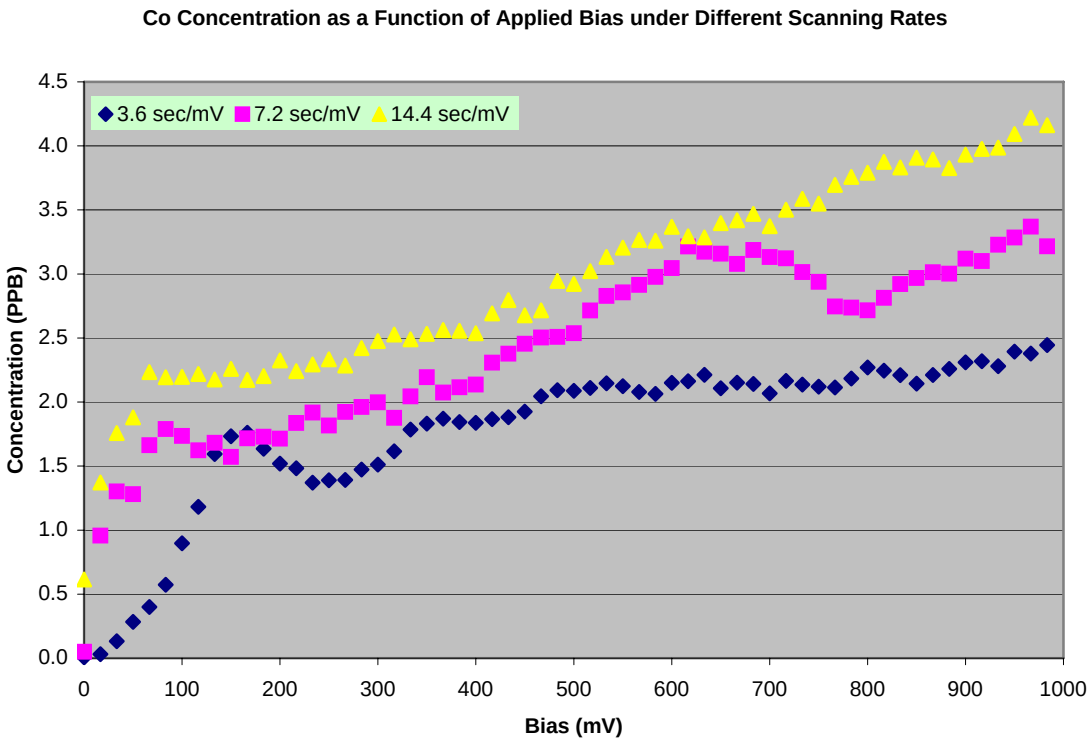

Figure 3.10(a). Dependence of Co concentration in 2%HNO_3 solution on potential applied with different scanning rates

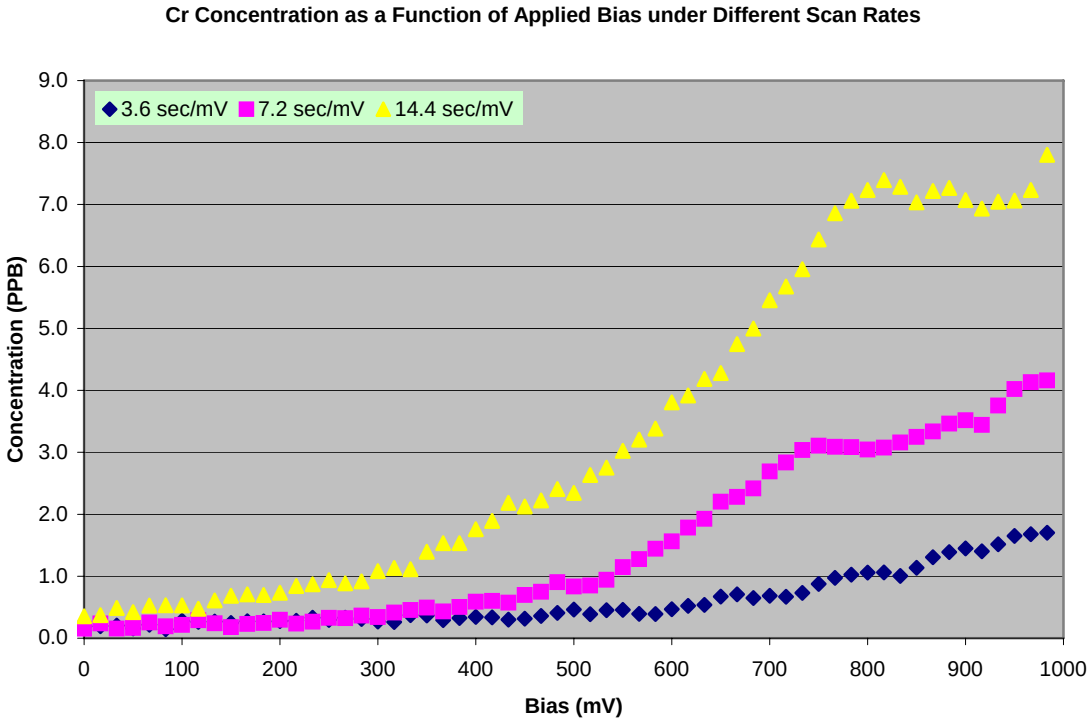

Figure 3.10(b). Dependence of Cr concentration in 2%HNO_3 solution on potential applied with different scanning rates

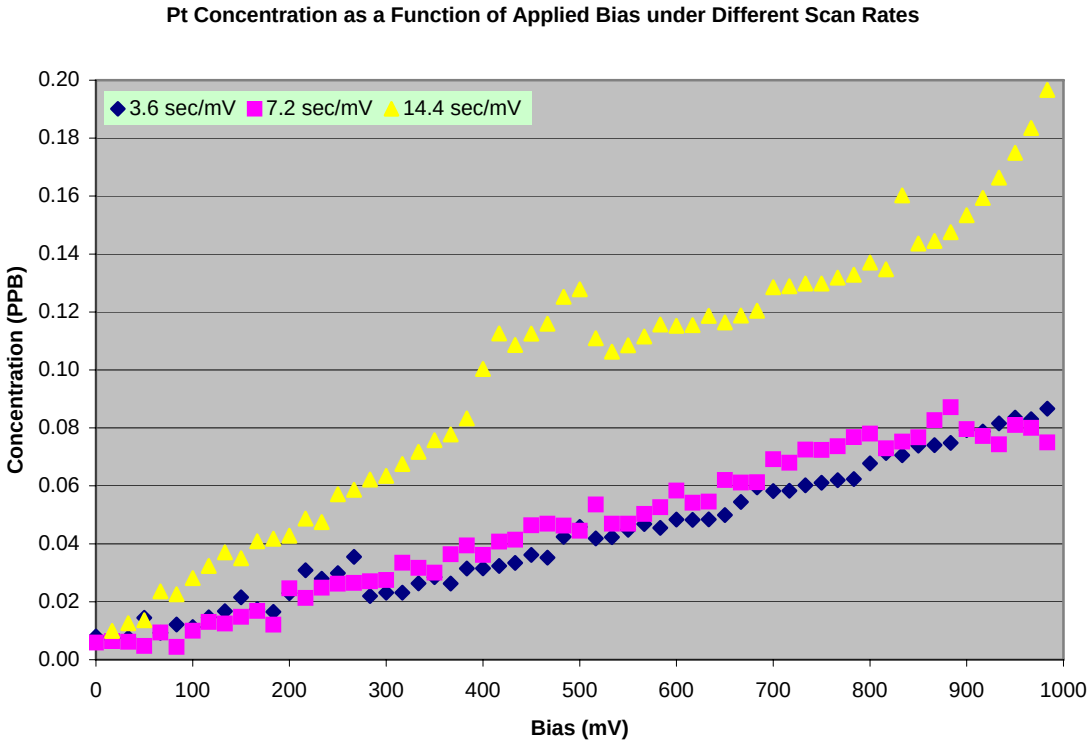

Figure 3.10(c). Dependence of Pt concentration in 2%HNO_3 solution on potential applied with different scanning rates

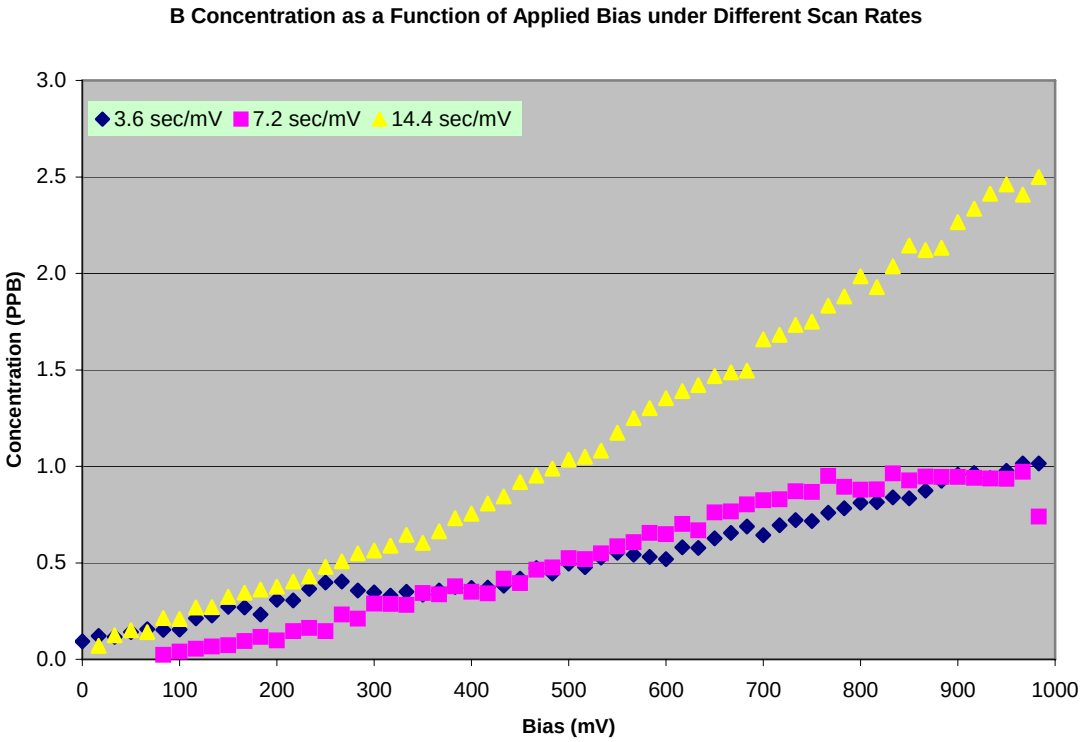

Figure 3.10(d). Dependence of B concentration in 2%HNO_3 solution on potential applied with different scanning rates

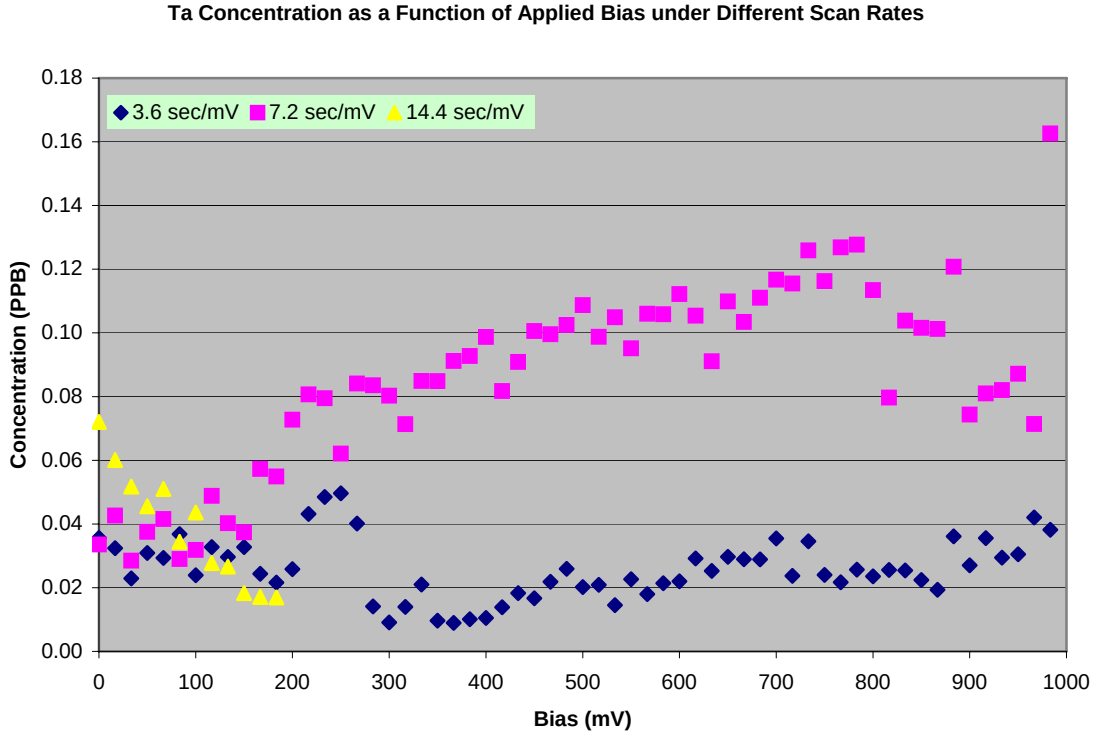

Figure 3.10(e). Dependence of Ta concentration in 2%HNO_3 solution on potential applied with different scanning rates

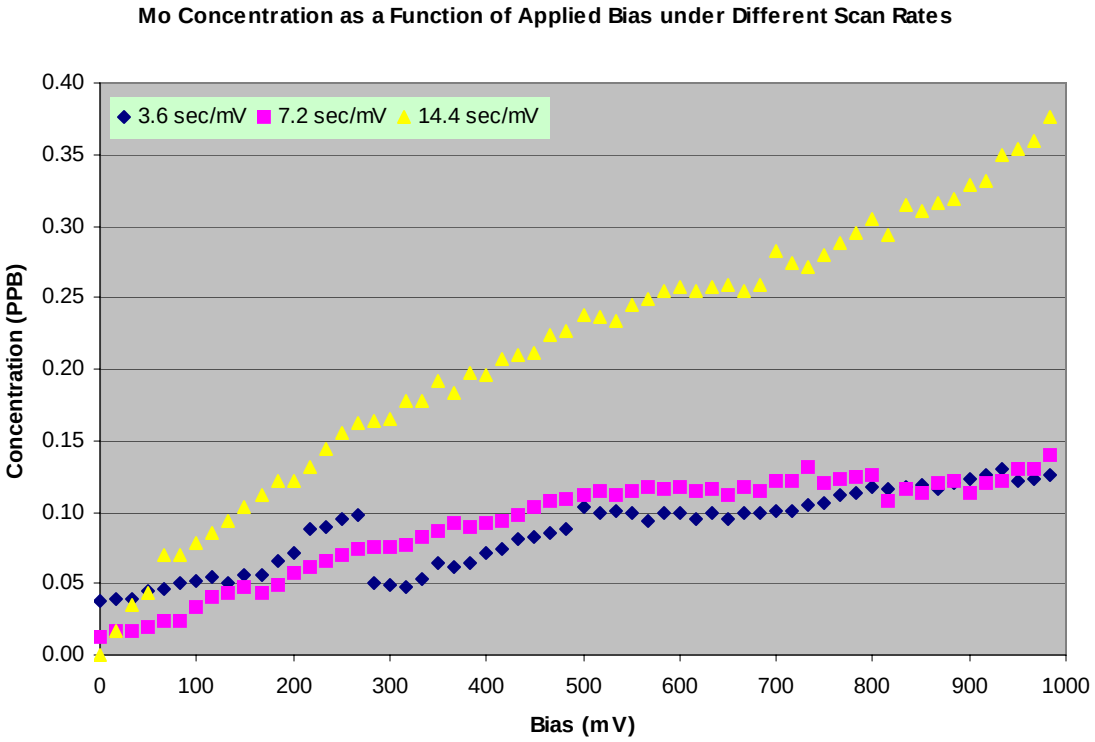

Figure 3.10(f). Dependence of Mo concentration in 2%HNO_3 solution on potential applied with different scanning rates

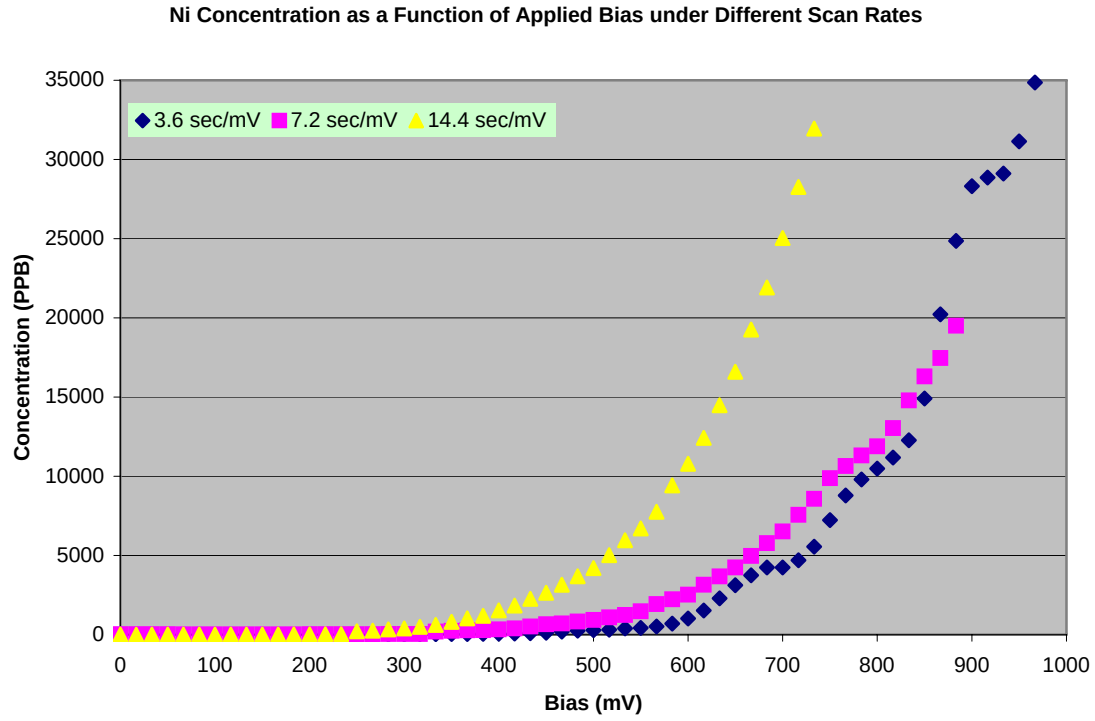

Figure 3.10(g). Dependence of Ni concentration in 2%HNO_3 solution on potential applied with different scanning rates

Using a fast scan rate, Co dissolved to 2.5 ppb at 1000 mV, while its dissolution at low scan rates reached more than 4.0 ppb under the same bias condition. This occurrence indicated that Co dissolution from the thin film structure was retarded at the equilibrium oxidation state. High dissolution rates for Co under low potential bias implied that cobaltous compounds, such as CoO, were highly produced and increased as potential supplied increased suggesting that dissociation of cobaltous compounds was limited by some intrinsic reason.

Slowly increasing Cr concentrations during all scanning modes suggested the existence of Cr passivity at the low potential range, and acceleration of Cr dissolutions at high potentials indicated that the passivity of Cr in reduction reactions pushed the limits of the element's oxidation tolerance. The total concentration of Cr in the solutions could reach 2.0 ppb, 4.0 ppb, and 8.0 ppb when 1000 mV reached 3.6 sec/mV, 7.2 sec/mV, and 14.4 sec/mV in 2% HNO_3 solution, respectively.

Concentrations of Pt precipitates in 2% HNO_3 solution increased linearly for all scan rates. But their quantities could be measured at double or even triple the magnitude at slow scan rates, which indicated that reaching the equilibrium of corrosion potential is very important in the breakdown of Pt immunity during oxidation process. Boron and Mo, which could have outputs of 1.0 and 0.15 ppb, respectively, at high scan rates, exhibited similar trends to that of Pt, while a slow scan rate yielded up to 2.5 and 0.4 ppb, respectively, for these elements. Although concentrations of those elements were detected in the low parts per billion, these quantities were significantly higher in comparison to their normal limits of detection, as shown in the last chapter.

Quantitatively, Ta concentrations in the solutions were lower than the concentrations of other elements, even at 1000 mV of potential applied at fast scan rates, which could be a result of the limited quantity of the element in thin CoCrTa film only one nanometer in thickness, as presented in Chapter 2. When using a slow scanning rate, no Ta content was detected in the solutions, which suggested that even Ta could be released from its structure but also that it would unfavorably compete with the movement of other elements.

Unexpectedly, Ni concentrations increased exponentially as a function of electric potential applied, and the quantities of Ni in the solutions were charted out of digital counting ranges under these scanning conditions. The increase of Ni concentrations in the solutions was consistently independent of the scan rate, which produced about 35 ppm of Ni up to 1000 mV applied. The same amount of Ni could be introduced at 750 mV when the scan rate was reduced to 14.4 sec/mV. Exponential increases in Ni content in the solution due to overwhelming electrochemical agitation generates interesting arguments about the corrosion mechanism that describes how Ni migrates in such enormous quantities from the substrate. The predominant presence of Ni in the solution suggested that the electrical current largely contributed to this Ni migration by dissolving Ni ions.

References:

3.1. Lee, C.-T., Q.-Z Yin, and T.-C. Lee, "An internal normalization technique for unmixing total-spiked mixtures with application to MC-ICP-MS", *Computers & Geosciences*, 27(2001) pp.577-581

3.2. Watters, R.L. Jr., K. R. Eberhardt, E.S. Beary, and J. D. Fassett, "Protocol for isotope dilution using inductively coupled plasma-mass spectrometry (ICP-MS) for the determination of inorganic elements", *Metrologia* 34(1997) pp.87-96

3.3. Gray, J. R., C. Homescu, L. R. Petzold, and R.C. Alkire, "Efficient Solution and Sensitivity Analysis of Partial Differential-Algebraic Equation Systems: Application to Corrosion Pit Initiation", *Journal of The Electrochemical Society*, Vol.152, Issue 8 (2005) pp.B277-B285

CHAPTER FOUR

IN-SITU QUANTIFICATION FOR POTENTIOMETRIC CORROSIONS AND SURFACE CHARACTERIZATION

4.1. Electrochemical Potentiometric Experiments

Potentiometric measurements are to determine surface potentials at which there is no electric current involved. Sometimes, this measuring technique is also called open circuit potential measurements. Although such measurements are very simple, they have many important applications because metal surface potentials are governed by many intrinsic and extrinsic variations of surface structure and chemical composition. Any surface deviation can thus greatly alter surface potential. In applications of corrosion studies, the knowledge drawn from monitoring potential changes over the period of time that the sample undergoes electrochemical transformation is fundamental importance, which provides both quantitative and qualitative guidance for further experiments.

4.1.1. Electric Potential Determination

Measurement of the thin film surface potentials was referred to as the standard potential of Ag/AgCl. Different concentrations of nitric acid solutions were used as electrolytes. The measurement results of surface potential changes for six hours are shown in Figure 4.1.

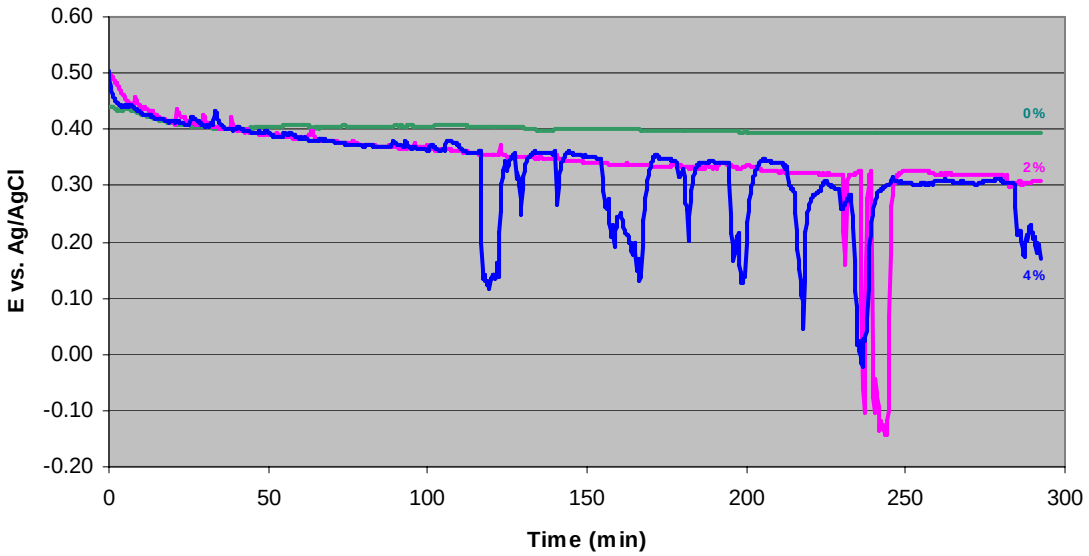

Figure 4.1. Surface potentials in different concentrations of HNO_3 solutions

In these experiments, initial surface potentials against the standard potential were found to be slightly different in responding to different pH levels in electrolyte solutions. These potentials were measured about 450 mV, 500 mV, and 504 mV for the liquid containing 0%, 2%, and 4% HNO_3 solutions, respectively. In general, the potentials at the surface measured against the standard Ag/AgCl electrode decreased gradually. The decrease of surface potentials signaled certain changes of electrical states on a conductive surface. These changes could be structural variations from the initial stage or chemical alterations of surface coverage. Approaching a potential plateau suggested that a thin film surface achieved electrochemical equilibrium, with dissolution rate of metallic ions in electrolytes equal to their solidification rate. Therefore, the potential plateau was also known as corrosion equilibrium potential. As shown in Figure 4.1, equilibrium potentials of 370 mV, 320 mV, and 318 mV were measured for the thin film surfaces in 0%, 2%, and 4% HNO_3 solutions, respect of the metallic thin film surface possesses. Thus Figure 4.1 suggested that the thin film surface was relatively inert in acid-free solution. However, when nitric acids were added into the electrolytes, the surface potential changes dramatically.

Unlike the smooth graduation of the surface potential in 0% HNO_3 solution, the potentiometric measurements recorded important surface electrochemical events at 225 minutes and 110 minutes in 2% and 4% HNO_3 solutions, respectively, as shown in Figure 4.1. These drastic potential slumps indicate that thin film surface conditions have been abruptly altered due to interfacial reactions between surface materials and electrolytes. Furthermore, multiple drastic potential drops in the 4% HNO_3 solution at irregular intervals of time provided another important indication that these surface phenomena were recoverable. The recovery of potential loss indicated that surface electrochemical immunity to the environment could be reached again as the surface was percolated electrochemically. Although only a single potential drop was recorded over a six-hour potentiometric test in 2 % HNO_3 solution while none was discovered in acid-free solution, it was reasonable to extrapolate that the multiple surface potential irregularities would occur on surfaces in low acidic concentration solutions as time progresses.

4.1.2. Potentiometric ICP-MS Measurements

ICP-MS measurements gained quantity information of most important constituents of thin film elements Co, Cr, Pt, B, Mo, and Ni in corrosion solutions directly. Commonly, the mass counts were directly related to concentrations of the ions in the solutions. In order to obtain meaningful comparison, the mass counts measured by ICP-MS were mathematically converted into ionic surface density. The conversion of concentrations measured in ICP-MS was simply to multiply total volume of solutions for each test run and divided by total surface of a specimen disk. Even though each experiment could hold slightly different volume of solutions, ions leached out per unit specimen surface area in individual potentiometric experiments could be quantitatively compared. The results are summarized in Figure 4.2(a) to (f). Other elements were filtered and considered as background contaminants without being recorded.

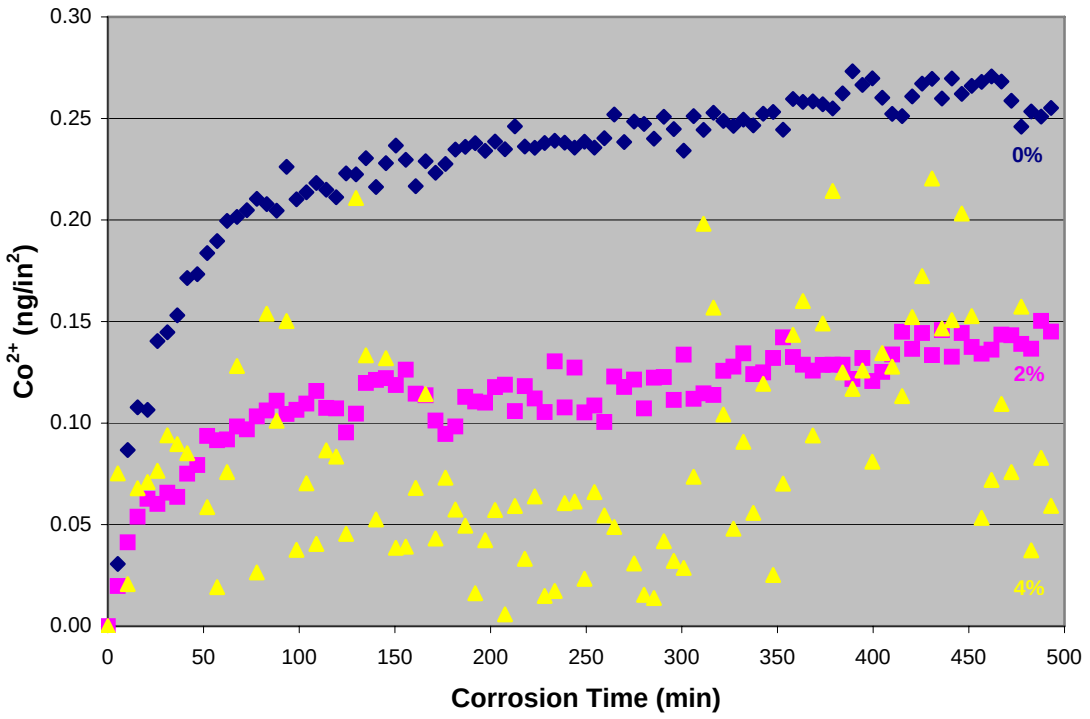

Figure 4.2(a). Dissolution concentration trends of Co ion per surface area of a disk specimen in various nitric acid solutions

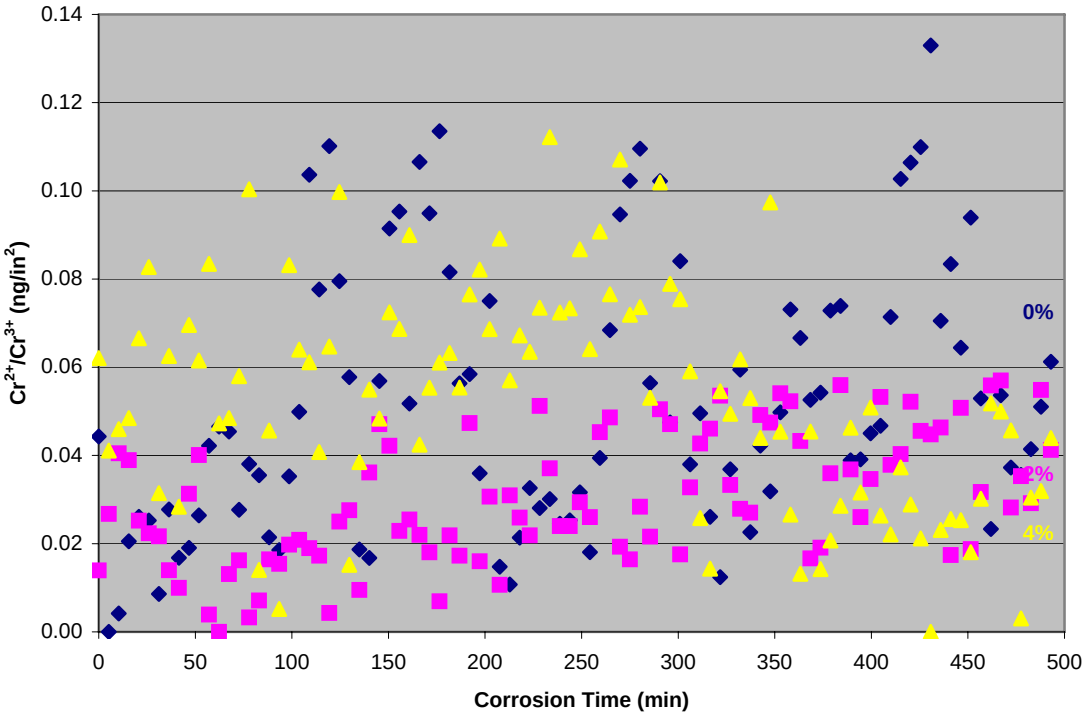

Figure 4.2(b). Dissolution concentration trends of Cr ions per surface area of a disk specimen in various nitric acid solutions

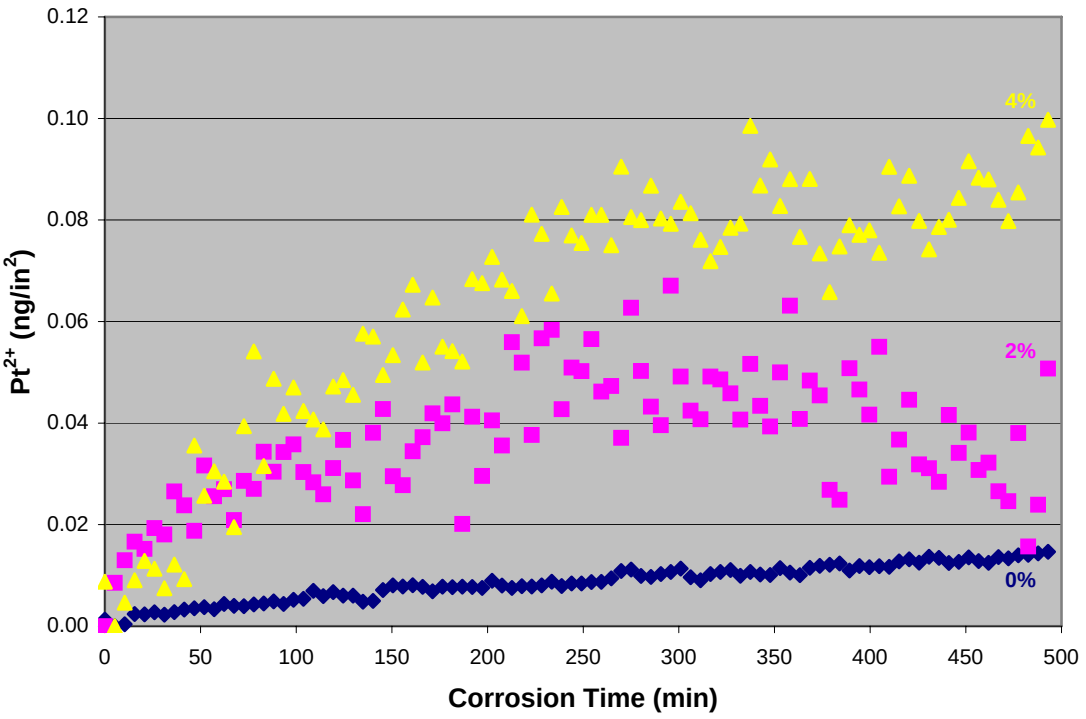

Figure 4.2(c). Dissolution concentration trends of Pt ion per surface area of a disk specimen in various nitric acid solutions

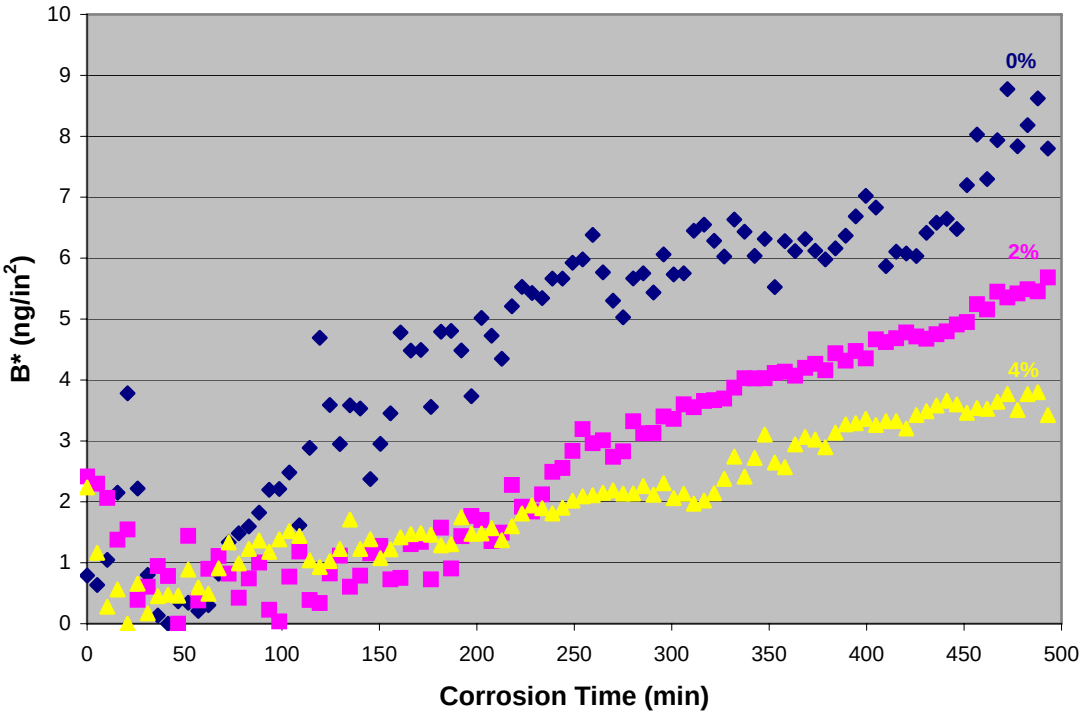

Figure 4.2(d). Dissolution concentration trends of B ion per surface area of a disk specimen in various nitric acid solutions

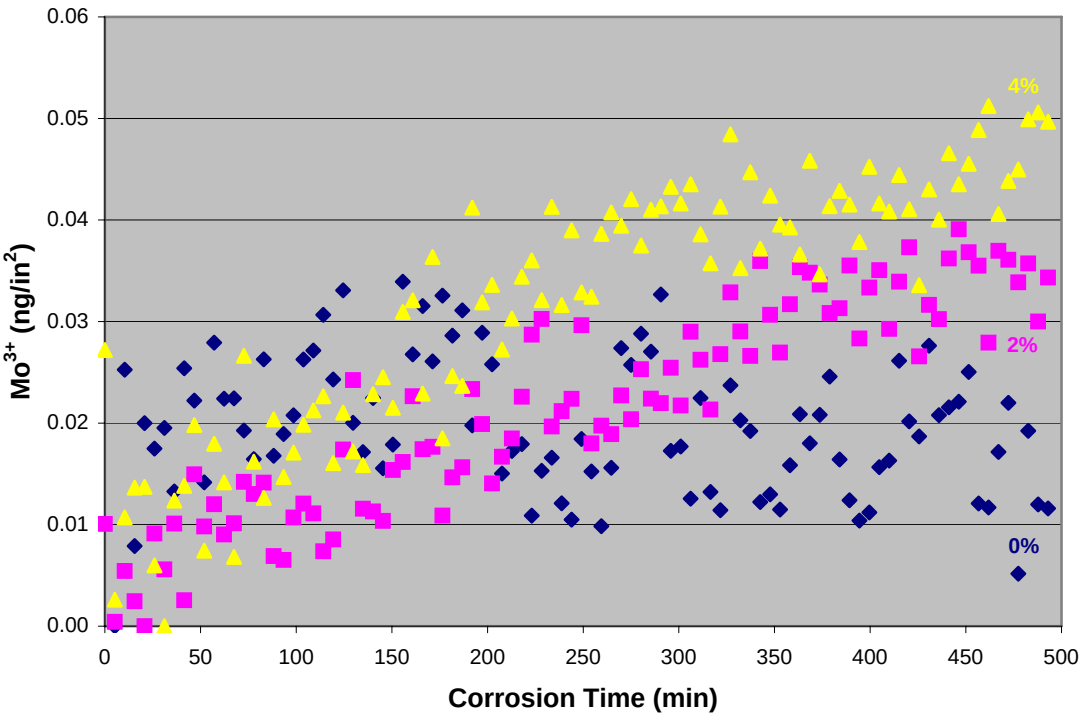

Figure 4.2(e). Dissolution concentration trends of Mo ion per surface area of a disk specimen in various nitric acid solutions

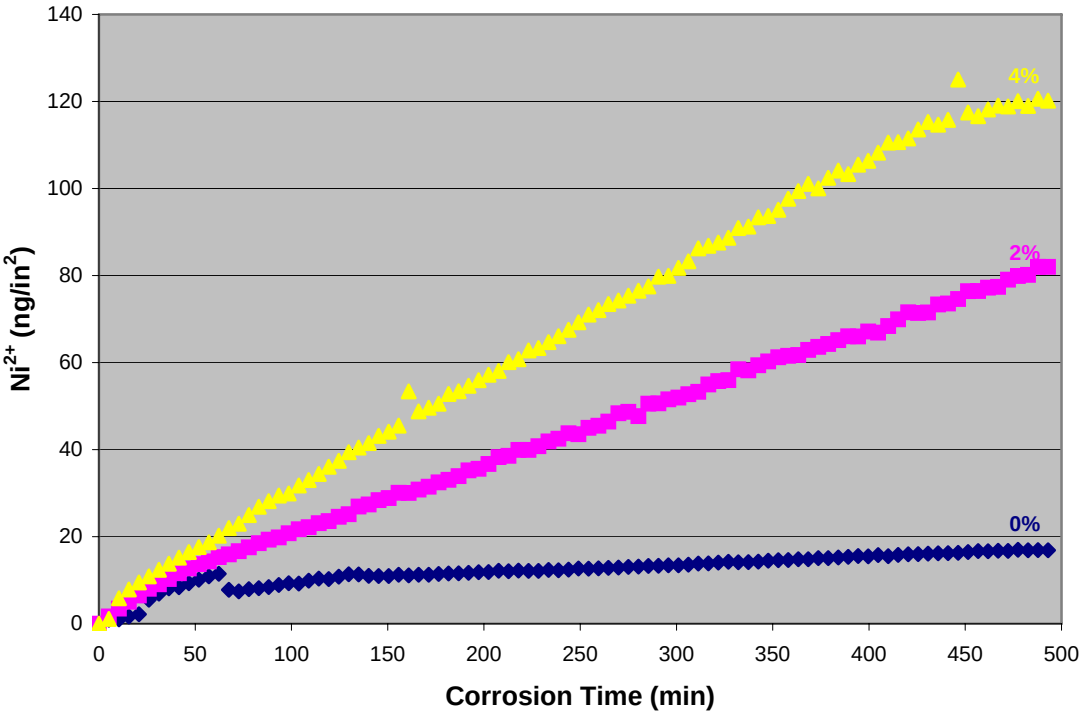

Figure 4.2(f). Dissolution concentration trends of Ni ion per surface area of a disk specimen in various nitric acid solutions

Under unbiased conditions, mass counts of all elements were in the digital reading range, and Co, Cr, Pt, and Mo were all measured in sub-nano grams per square inch, which is the same as the sub-ppb concentration ranges. B concentrations were in the ppb level, which were measured to be in nano-grams per unit area from the disk surfaces. An quantity of Ni, which was hundreds or even thousands of times larger than that of all other element quantities combined, was astonishing. In general, dissolution concentrations of all elements increased as immersion time and matrix concentrations increased. But the elemental dissolution behaviors were time-dependent and relied on matrix concentrations. For example, non-linear increases in Co dissolution rates in the electrolytes initially followed logarithmic patterns and then reached plateaus of 0.22 and 0.12 ng/in^2 of surface density in 0% and 2% HNO_3 matrices, respectively. It could be clearly seen in the Co plot that acid-free solution, such as DI water, resulted in almost double the amount of Co in the solution from the unit surface than in 2% HNO_3 solution. In a matrix solution with an even higher concentration, i.e. 4% HNO_3, the change in Co dissolution density highly fluctuated. This inverse relationship between Co dissolution rate and electrolyte concentration indicated that Co became oxidized much more quickly and easily in low pH solutions, and consequently, passive Co film could be produced and further dissolution halted. This finding was extremely important since Co was the most magnetic and magnetically predominant element in the magnetic thin film structure. Unveiling the electrochemical behavior of Co mitigations and reactions underscored the need for further studies of magnetic characteristics and microstructural changes.

Chromium, as the main elemental species not only incorporated with Co in magnetic thin film structures but also alloyed with Mo in the underlayer, on the other hand, had no distinguishable and meaningful dissolution trends regardless of matrix concentration. Cr was commonly known to act as a corrosion inhibitor by forming chromites or chromium oxides, which could provide structural protection to the other elements in the alloy. In its oxidation state, Cr often showed both 2+ and 3+ states, and, unfortunately, mass spectrometry/a mass spectrometer could not distinguish them. Therefore, in this research, both states of chromium were counted together.

In the magnetic thin film layer, platinum and boron shared very similar dissolution characteristics, with a relatively linear trend as a function of corrosion time. However, the

rates of dissolution density increase trended in opposite directions for Pt and B. B dissolved faster in low concentration matrix solutions, while Pt responded more vigorously in high concentrations of matrix solutions. Quantitatively comparing these results to the dynamic potential measurements described in the previous chapter, Pt concentrations had relatively low readings, while B concentrations dramatically increased, indicating that electrochemical reactions of the magnetic thin films were electro-affinity dominated events.

Incorporated in the underlayer alloy, molybdenum showed a general upward trend as corrosion time increased, but the changes in Mo dissolution rates in these electrolytes were insignificant. The overall amount of Mo dissolution could be measured as less than 0.05 ng/in^2.

Unexpectedly, these non-polarized *in-situ* corrosion measurements produced very similar results to polarized experiments, namely that the majority of ionic dissolutions in the electrolytes belonged to nickel, which exhibited a linear trend under all these situations. With several thousand more times the elemental amount than all the other elements combined, the fact that an excessive amount of Ni was found in the electrolytes raises serious concerns about the corrosion mechanism of thin film structures since Ni was an underlayer alloy beneath multiple magnetic thin films.

One of the important results from the *in-situ* potentiometric measurements was to relate ionic activities with electric potential changes in the thin film surface in response to environmental conditions. As shown in the *in-situ* elemental dissolution trends, metallic ions were continuously present in the electrolytes. However, surface potential irregularity was identified, especially in high concentrations of the matrix. Therefore, loss of thin film constituents from thin film structures was not fully responsible for surface potential changes. In order to resolve the discrepancy between continuous ionic dissolution rates and interrupted surface electro-potentials during the corrosion courses, analyses of chemical compositions and surveys of surface conditions were encouraged.

4.2. Surface Corrosion Topography

Corrosion on magnetic thin films has been commonly acknowledged to be a localized phenomenon that produces surface pits in corrosive environments. However, no literature can be found that demonstrates how the surface pits are created and explains what the driving force producing the surface changes is. Based on the *in-situ* experimental results in this research that ionic levels are detected in electrochemical reaction solutions, metal oxides are presumably produced microscopically. The transition of the metal oxidation from the metal surface is gradual and uninterrupted over the course of the corrosion process. Therefore, studies of surface features and chemical composition changes of corrosion pits can be beneficial, which ties the amount of metal ions from alloy structures to physical and chemical changes and eventually leads to the postulation reasonable thin film corrosion models.

4.2.1. *In-situ* Digital Optical Microscopic Measurements

Optical *in-situ* technique is a powerful tool, which can record surface images continuously when the surface undergoes physical changes. With the advancement of CCD technology, micrographic images can be consistently and precisely recorded digitally and processed later with varieties of imaging software.

4.2.1.1. Setup of a digital optical microscope system

In this study, a digital optical microscope from Keyence (VH-8000, Keyence Corp., Osaka, Japan) was used because of its versatility and adaptability with long focus optical lenses. A 200X Zoom lens (VH-Z35) was selected in this part of the work. Direct photographing was conducted on exposed surfaces in corrosion chambers from the diametric corrosion cell under potentiometric conditions. Due to comparable corrosion conditions, both optical analysis and EC-ICP-MS results can be then correlated. Figure 4.3 shows the actual setup.

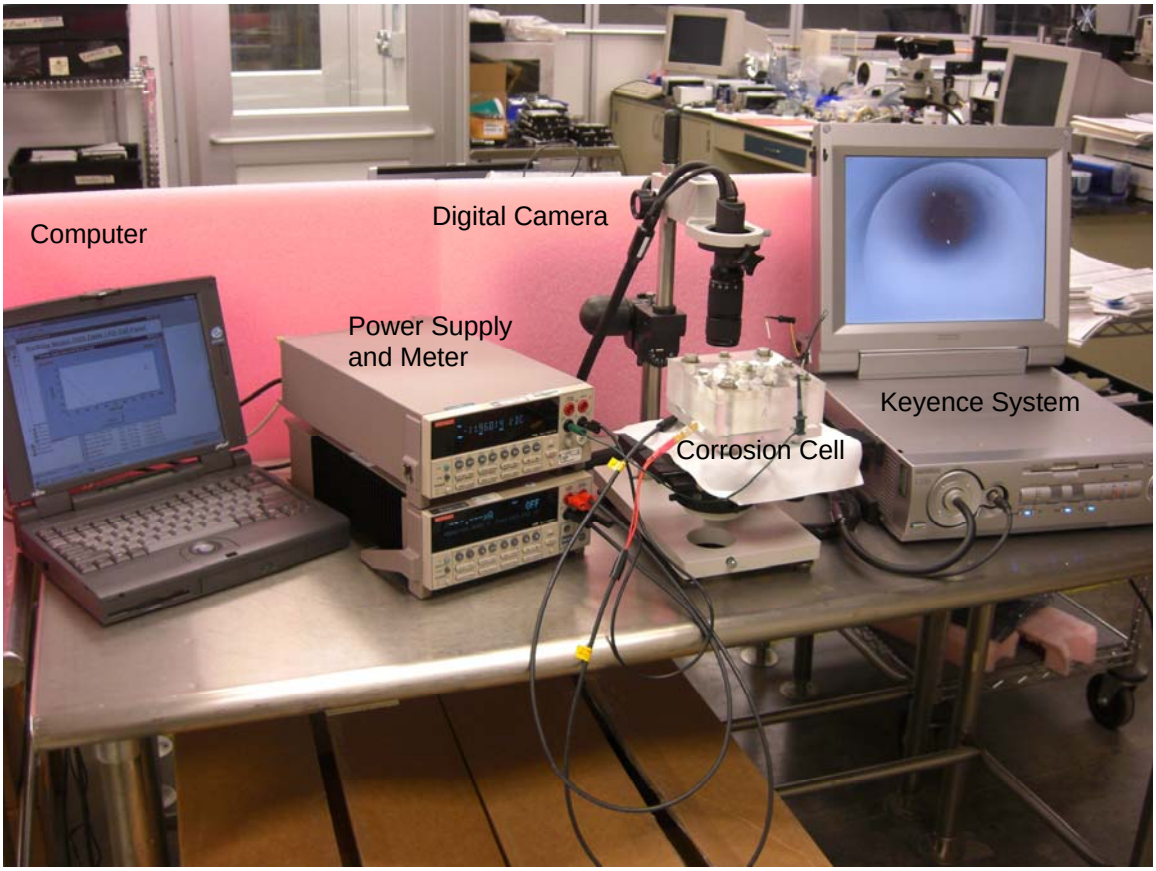

Figure 4.3. An optical system setup for *in-situ* optical measurements

The key component in this system is a Keyence digital camera, which was synchronized with electric voltage or current measurements from Keithley source meter and multi-meter. The optical images captured by Keyence system were then processed frame by frame using the UTHSCSA *ImageTool* program (developed at the University of Texas Health Science Center at San Antonio, Texas and available from the Internet by anonymous FTP from maxrad6.uthscsa.edu).

4.2.1.2. *In-situ* measurement results

Samples of recorded optical micrographic images taken by using this system in the experiments can be referred in Appendix III. The following figure shows recorded counts of corrosion occurrences in 2% and 4% HNO_3 solutions over 6 hours under potentiometric conditions. Corrosion images in acid free solution are not processed since the counts are in single digits over this period of time.

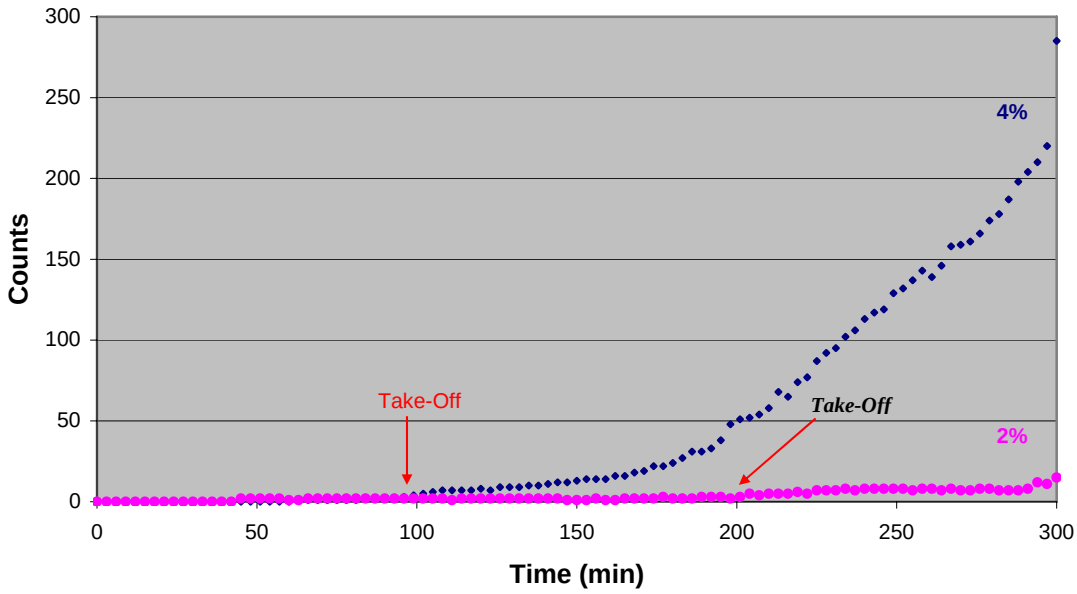

Figure 4.4. Optical corrosion spot counts as a function of immersion time in different HNO_3 solutions

The comparison of counts of the spots indicated that the occurrence of corrosion in 4% HNO_3 solution was dramatically better than what happened to the surface in 2% HNO_3. It was noticed that a take-off time about 100 minutes after immersion in 4% HNO_3 solution and such take-off time was almost doubled at 190 minutes when the same sample was in the 2% HNO_3 solution. The drastic increase of visible corrosion spots under optical microscopic observations meant that corrosion spots appeared in multiple locations were because of surface structural homogeneity and uniformity.

Meanwhile, the size of each corrosion spot was also optically measured, and the average corrosion defect size was shown in the following graph.

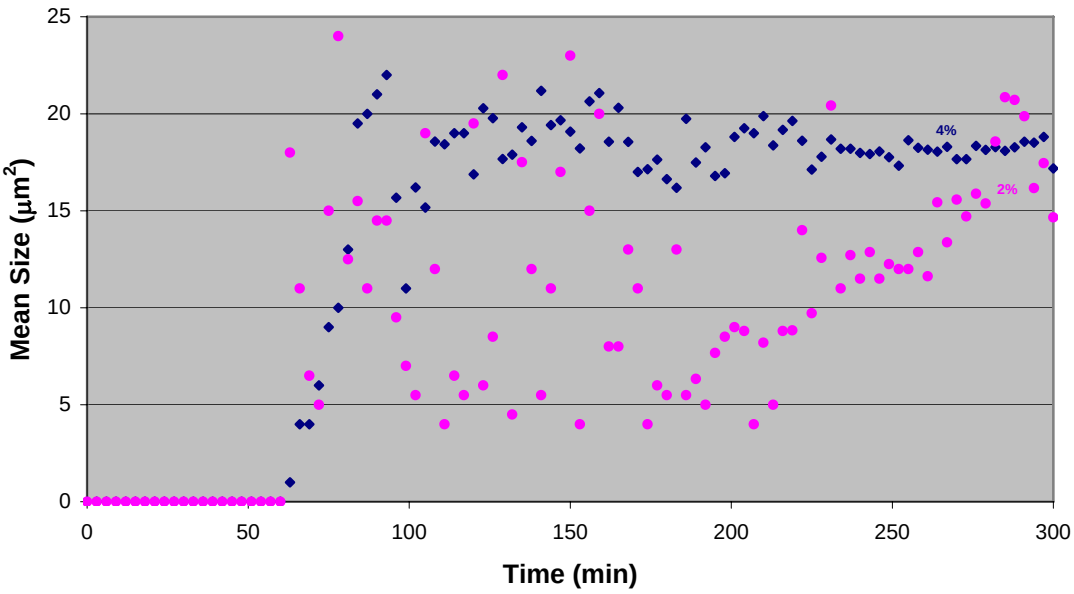

Figure 4.5. Mean size of corrosion spots in different HNO_3 solutions

The mean size of corrosion spots was calculated by taking an average of the integrated area of all corrosion spots recorded on an optical image. In both solutions of 2% and 4% HNO_3, 60 minutes was a magic time, as seen in Figure 4.6, during which growth of corrosion spots began. The mean size of these corrosion spots reached a plateau of about 18 μm^2 after 100 minutes in 4% HNO_3 solution. Similarly, the mean size in 2% HNO_3 eventually reached also approximately 18-20 μm^2. For the most part, low count numbers in the calculations caused a large variation in the mean size in 2% HNO_3 solution.

Interestingly, leverage of differences between counts and size changes along with time axis indicated that the creation of individual island spots in the acidic solutions was firstly happened up to an hour. Next, the growth of some of the island spots accelerated, and the spots form much larger visible corrosion spots, which could be optically differentiated from the surrounding background. These individual enlarged sites became active polarized electrodes with different potentials and combine with other micro-open pores to form new electrochemical cells. Then these cells promote more aggressive electrochemical reactions and become optically visible corrosion spots.

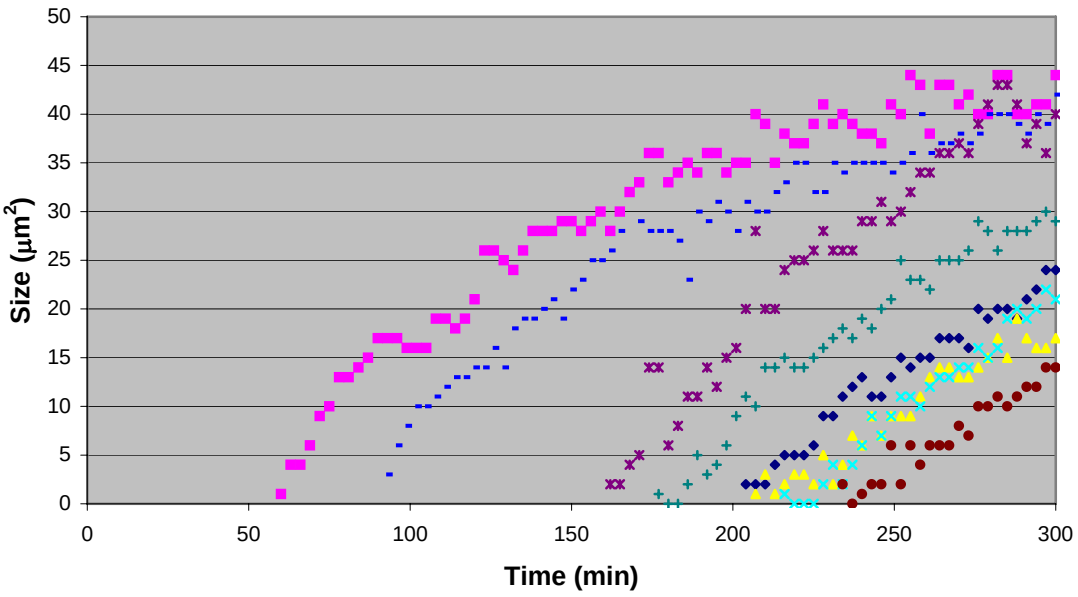

Figure 4.6. Several examples of growing corrosion spots in an optical distinguishable range

The corrosion defects grown at all times after the surface breakdown occurred. The optical lateral size increases linearly during the early stage, which implied that mass transport corrosion behavior took places during this stage. The size growth then leveled off, as can be seen for some large growing spots in Figure 4.6; this trend was less dependent on time. This fact indicated that the electro-migration mechanism overcame mass transport corrosion behavior to predominate the overall control of the corrosion process.

Similarly, *in-situ* optical analysis was also used to observe the occurrence and growth rate of corrosion spots in potentiodynamic corrosion conditions, during which electric potential was applied. In general, quantitative occurrences of corrosion spots under optical micrographic imaging were very much like what has been shown in the potentiometric experiments. However, dissimilar to the potentiometric results, individual corrosion spots showed that size growth increased nonlinearly with time, and statistic measurements showed the spots had the potential to decrease after reaching a certain size.

4.2.2. Surface Structural Profile by AFM

Atomic Force Microscopy (AFM) is a scanning profile technique[4.1] that provides a number of advantages over conventional microscopy techniques in many applications because of its sensitivity and resolution. An AFM probes the sample and makes measurements in three dimensions and thus enables the presentation of three-dimensional images of a sample surface. The theories and principles of AFM are referenced in much of the literature on surface analytical techniques.[4.2]-[4.4] AFM used in this part of research is based on model DI3100 (Digital Instruments of Veeco Metrology Group, Santa Barbara, CA), which has a tapping mode[4.5] with a cantilever (MESP-70 from Digital Instruments). Image acquisition and data processing are achieved by using software version 4.18r. The advantages of utilizing AFM technique are to compensate analytical inadequacies of using optics, which have limited spatial resolution and no capability to determine subtle changes of surface topographic features.

The following 3-D AFM images were obtained from a surface with a series of potentiometric tests for one hour in a 2% HNO_3 solution. Surprisingly, instead of discovering a corrosion pit, the formation of a corrosion nodule was clearly seen in these *ex-situ* images.

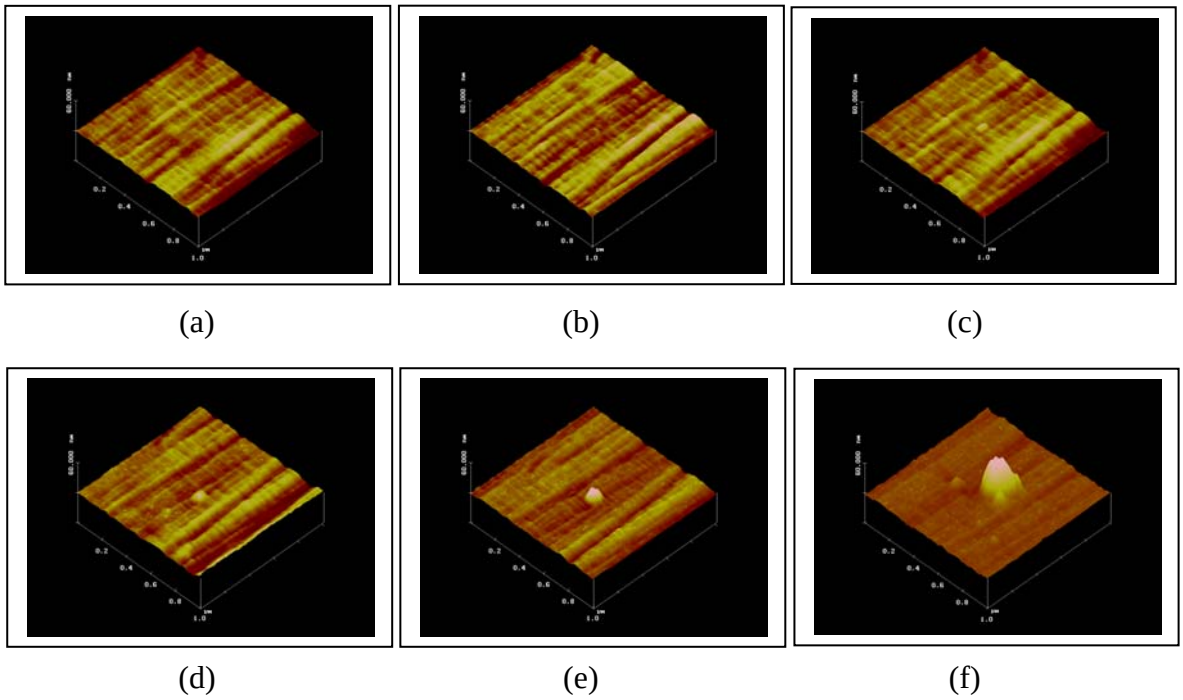

Figure 4.7. Pit growth in 2%HNO_3 at (a) 5 min, (b) 10 min, (c) 15 min, (d) 30 min, (e) 45 min, and (f) 60 min

This example clearly showed that growth of corrosion nodules at very early stages occurred directly on a clean and defect-free location on the thin film surface. The transformation of a corrosion nodule was gradual, with increases in both lateral size and height. This demonstration of the evolution of corrosion nodules inspired more statistical measurement of formed corrosion nodules. However, during measurements, some corrosion pits developed instead of corrosion nodules, at which point the emphasis of nodule growth measurement shifted to examining how corrosion nodules became pits and to identifying the relationship between nodules and pits with regard to geographic volume.

About 30 corrosion nodules were measured on a specimen surface after a potentiometric test, and the locations were marked. This disk was then clamped on a high-speed motor spindle, which revolves 10,000 rpm. A clean polyester swab was gently rubbed on the surface during spinning. AFM re-measurements at these locations were performed, and depths were observed at most of the nodule areas, which indicated that corrosion pits

result from removing nodule materials from the surface. Figure 4.8 shows an example of a localized corrosion nodule before the cleaning process and its pit image thereafter.

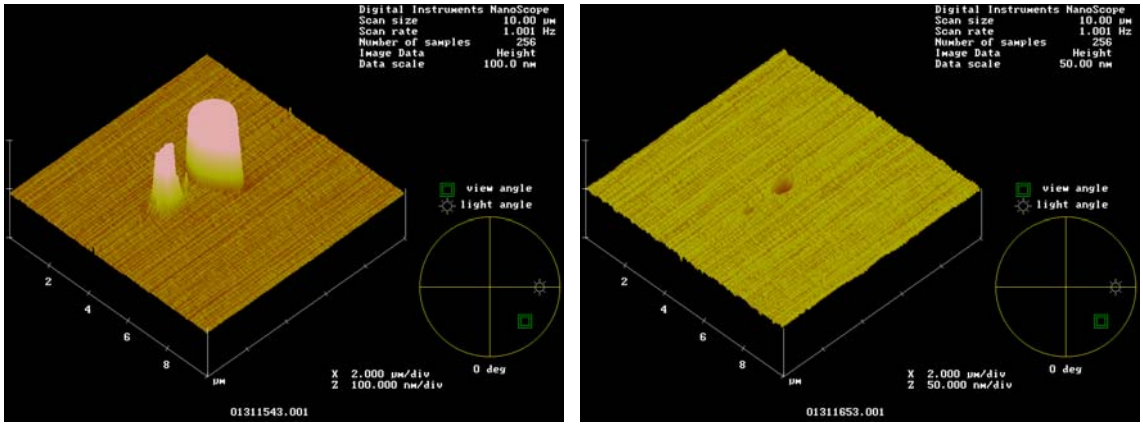

Figure 4.8. Surface topographic AFM images of (a) nodules before and (b) pits after the surface is cleaned

Topographically, two corrosion nodules were produced on the clean surface with a height of several hundred nanometers and a diameter of several micrometers. Corresponding pits showed surface depression in the thin film surface. The correlations between nodule height and pit depth are summarized in Figure 4.9.

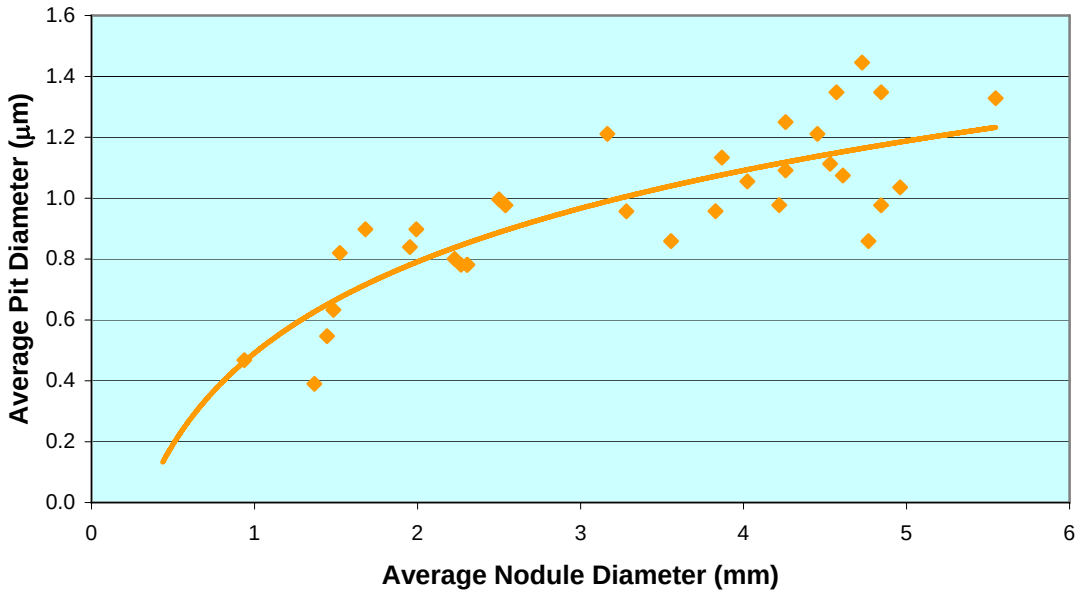

Figure 4.9. Correlation of average corrosion nodule and pit diameters

Since the formation of nodules and pits was slightly asymmetrical along the radial and circumferential orientations, the average of the diameters was used for the plot. In general, the larger the nodules, the larger the pits, which led to the conclusion that most of the material used in the formation of nodules came from the pit. As indicated in the Figure 4.9, corrosion nodules were detected without the formation of measurable pits for about half of the micrometers. Thus, it was important to notice that pitting corrosion on a thin film surface under potentiometric conditions could be potentially invisible. The following graph shows the volume ratio of nodules and pits.

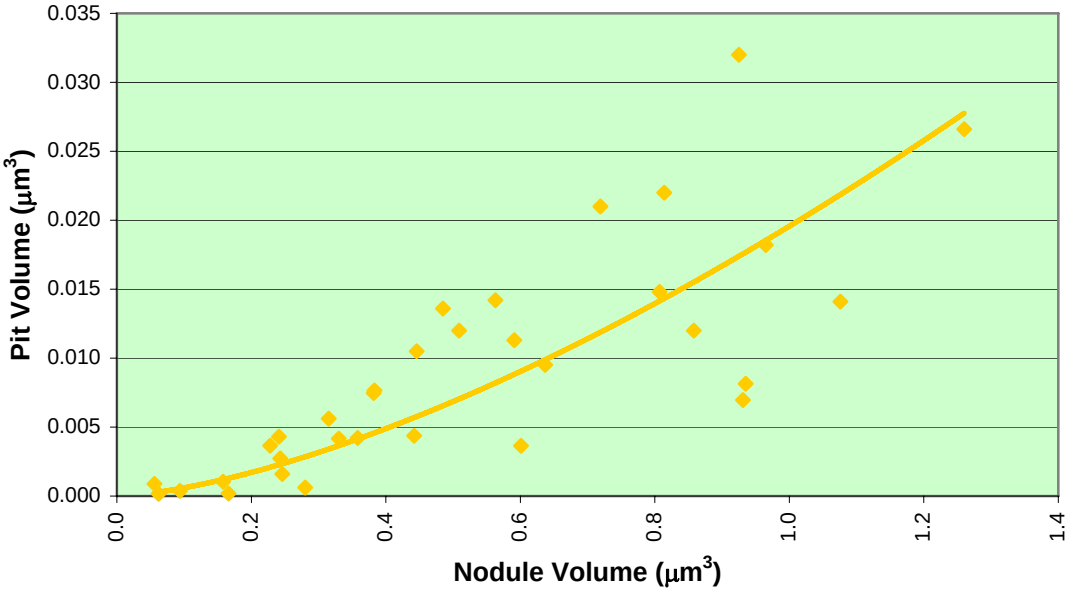

Figure 4.10. Correlation of volume of 30 corrosion nodules and pits

The nodule volume can be almost 900 times the pit volume in some cases, as shown in the above plot, but corrosion made the majority of nodules have 40 ~ 70 times the volume that pits have. This study indicated that thin film pitting corrosion caused not only compositional changes but significant structural changes as well. The extraordinary volume increase of corrosion nodules compared to the volume of pits indicated a dramatic transformation of metal alloy compounds into oxides. As is commonly known, thin film metallic constituents undergo oxidation reactions to form oxides or hydroxides.[4.6]

No literature can be found to directly relate all these elements to drastic volume changes. However, some studies[4.7] suggest that the crystallization of Ni during the amorphous phase could increase its volume. The following SEM graphs show a needle-like crystal of Ni oxides, identified with X-ray Energy Dispersive Spectrometer (EDS), on some sample surfaces as a result of aggressive corrosion reactions.

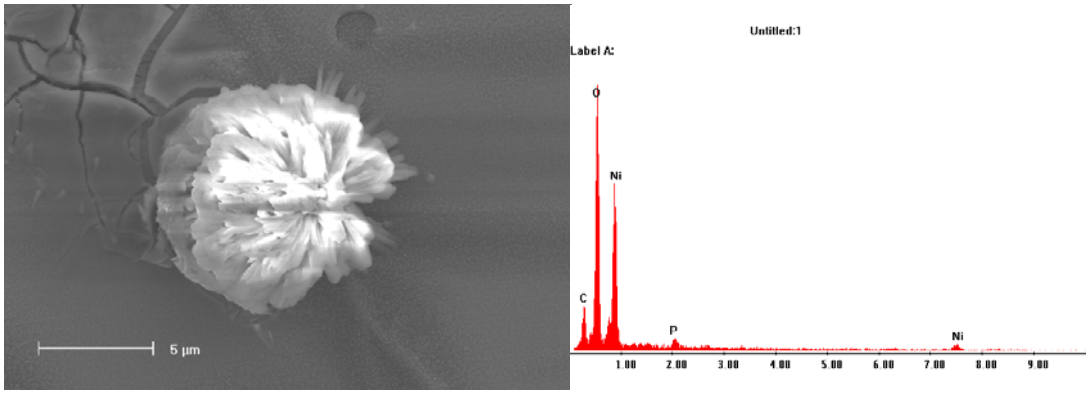

Figure 4.11. (a) A SEM image of a nickel oxide product identified with (b) EDS spectrum as a result of an aggressive corrosion reaction

That an increase in corrosion nodule volume due to nickel transformation into crystal oxides took place during the amorphous phase is not hard to conclude because an extremely high amount of Ni has been observed by EC-ICP-MS. Other elements in the alloy thin film stack have smaller quantities compared to that of Ni. It was logical to presume that the majority of the corrosion nodule is made of Ni oxides.

Since pitting corrosion is a recognized occurrence on thin film surfaces, the study was then extended to understand pit characteristics, which is critical to relating magnetic and microstructural changes during and after corrosion processes. Another 50 pits were created through the same process described above, and AFM measurements of their geographic dimensions are summarized in Figure 4.12.

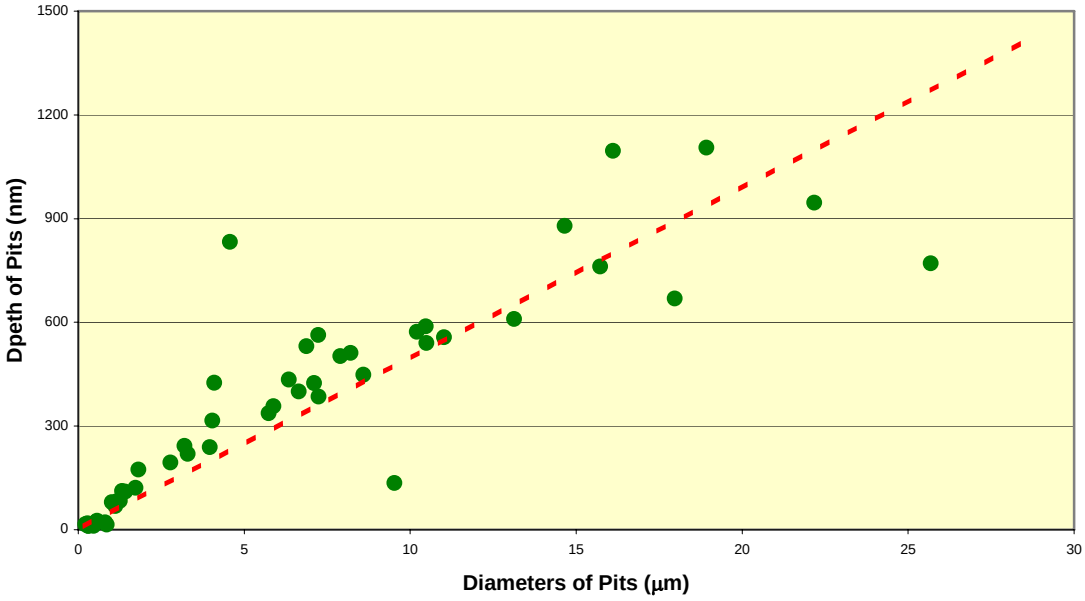

Figure 4.12. Geographic corrosion pit dimensions measured with AFM

As the lateral size of these corrosion pits increased, the depths of the pits increased fairly linearly. The importance of uncovering the depth range of pits was to understand the effects of corrosion on functional thin film structures, namely the Co alloy layer. Well-defined in deposition processes, the thickness of the functional magnetic thin film structure was only several hundred to a thousand angstroms, which meant that pits with depths of less than 10 nanometers theoretically affect the film structure and properties. Statistically from Figure 4.12, only few small corrosion pits could be survived in magnetic thin film without causing magnetic distortions. .

4.3. Elemental Compositional Distribution by EDS

The extended corrosion time makes changes not only the size of corrosion spots but also the distribution of metal concentrations, as determined by X-ray florescence spectroscopy. The following SEM and EDX mapping images are of a medium size nodule 2 μm in diameter.

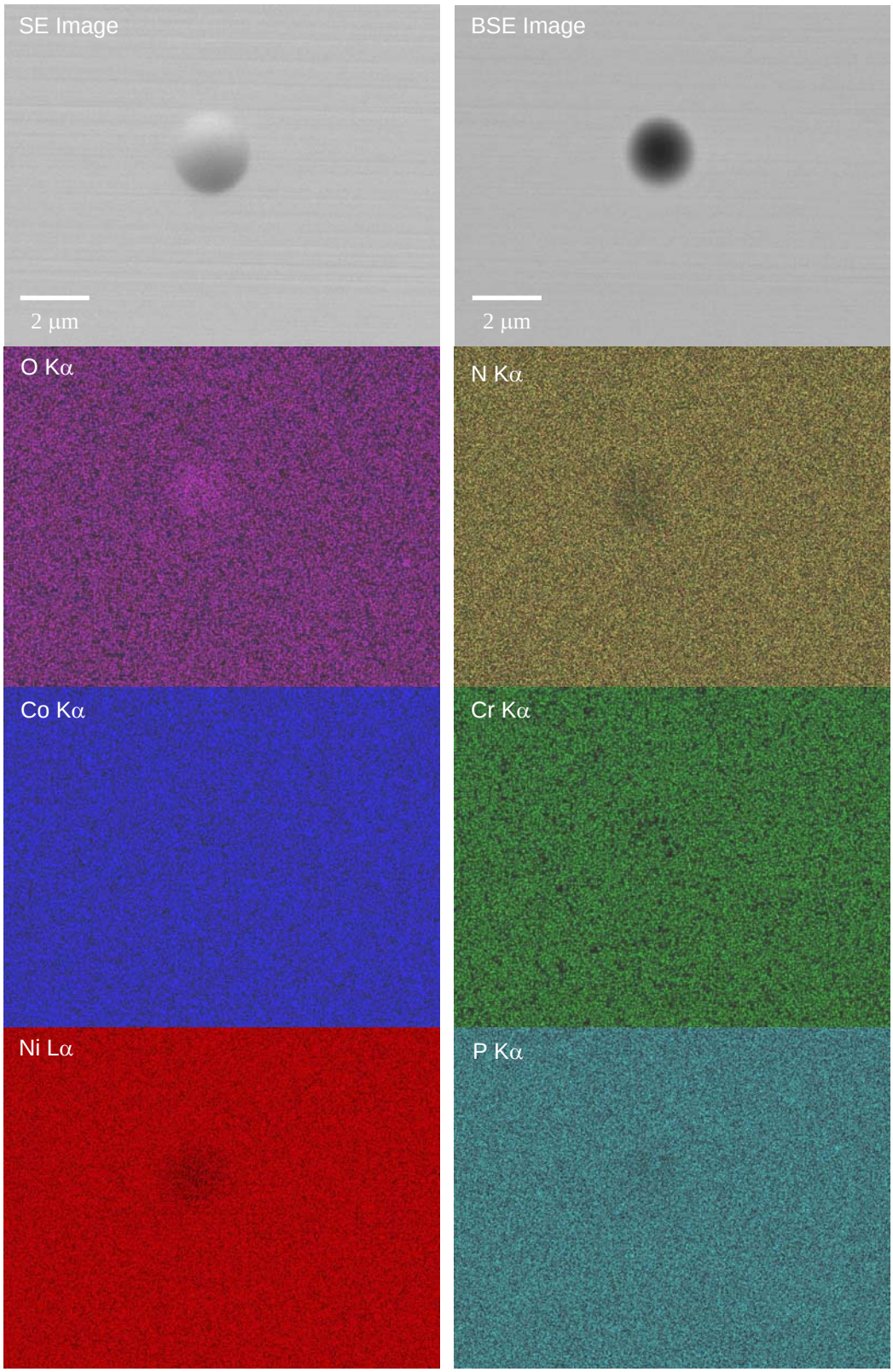

Figure 4.13. SEM micrograph of a corrosion nodule on the surface after a 2-hour soaking in 4% HNO_3 solution and EDS mapping images for X-ray detectable elements

Besides the enrichment of oxygen, as shown in the early stage of the corrosion process, depletion of nickel and nitrogen from the center of the corrosion nodule was clearly seen. Importantly, even though the formation of corrosion nodule was physically established, both cobalt and chromium content was still uniformly distributed over the corrosion nodule.

Furthermore, increases in corrosion nodule size could be easily found in many areas when the testing was prolonged under the same conditions. Not only do changes to surface topography, but also depletion of metal elements became detectable, and eventually the microstructure and magnetic property of the thin film structure deteriorate were negatively affected. An example of an individual corrosion nodule from the same batch of open circuit potential testing in 4% HNO_3 solution for more than 6 hours is shown in Figure 4.14.

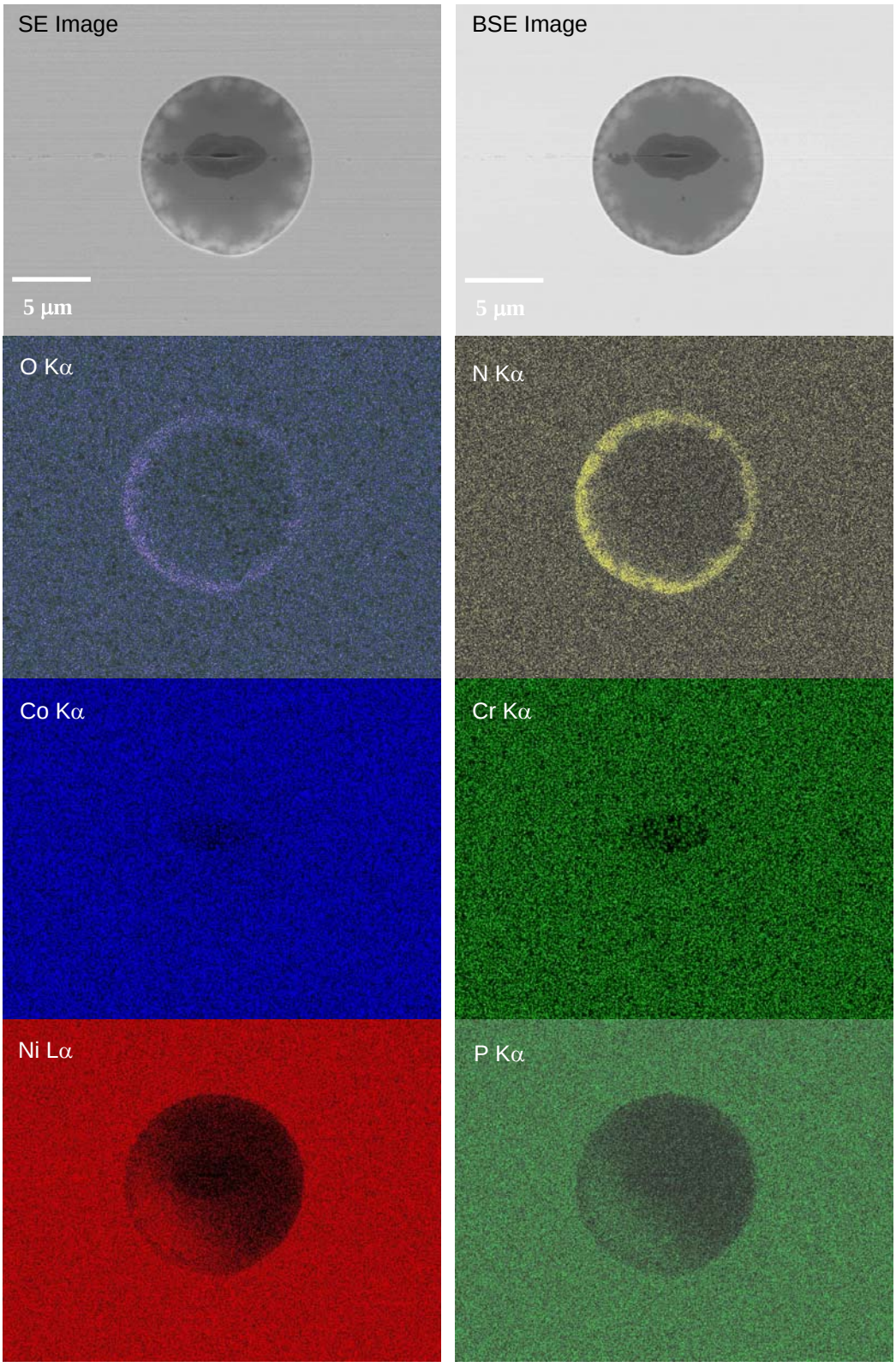

Figure 4.14. SEM micrograph of a corrosion nodule on the surface after soaking in 4% HNO_3 solution for over 6 hours and EDS mapping images for X-ray detectable elements

This individual corrosion nodule demonstrated that the center of the magnetic film layer ruptured due to corrosion process, with the existence of minimal quantities of cobalt and chromium, which were the key elements in excursing magnetic characteristics from the surface. Underneath the magnetic thin film, nickel and phosphorous contents were diminished from the center. In contrast, the segregation of oxygen, nitrogen and phosphorous at the rim of the spot in the form of a ring band indicated that high levels of oxides and nitrides migrate from the center to the edge of the corrosion nodule .

These comparisons suggested that the formation of corrosion nodules started with metallic oxidation processes, which resulted in high oxygen concentrations at the center of corrosion nodules. By increasing exposure of metallic thin film surfaces to corrosive environments, the geographic size of corrosion nodules increased, as seen under micrographic analysis. Meanwhile, the nickel concentration at the center of the corrosion spots was lower while critical elements Co and Cr remained unchanged. The depletion of Ni from the corrosion surface suggested that the migration of underlayer materials through the surface was possibly driven by different electrochemical potential responses in the corrosive solutions.

References:

4.1. Bottomley, L. A., "Scanning Probe Microscopy", *Journal of Analytical Chemistry*, 70 (1998) pp.425R-475R

4.2. Blanchard, C. R., "Atomic Force Microscopy", *THE CHEMICAL EDUCATOR*, Vol.1, No.5 (1996) pp.1-8

4.3. Hansma, H. G. and L. Pietrasanta, "Atomic force microscopy and other scanning probe microscopies", *Current Opinion in Chemical Biology*, 2 (1998) pp.579–584

4.4. Nie, H.-Y. and N. S. McIntyre, "A Simple and Effective Method of Evaluating Atomic Force Microscopy Tip Performance", *Langmuir*, 17 (2001) pp.432-436

4.5. Manning, L., B. Rogers, M. Jones, J. D. Adams, J. L. Fuste, and S. C. Minne "Self-oscillating tapping mode atomic force microscopy", *Review of Scientific Instruments*, Vol.74, No.9 (2003) pp.S4220-4222

4.6. Ying, J., T. Anoikin, and C. Martner, "Evolution of the corrosion processes on thin-film media", *Journal of Vacuum Science and Technology. A*, July/August 2000, pp.1804-1809

4.7. Karis, T. E., X.-C. Guo, B. Marchon, V. Raman, and Y.-L. Hsiao, "Cobalt Oxalate Formation on Thin-Film Magnetic Recording Media", *IEEE Transaction on Magnetics*, Vol.42, No.10 (2006) pp.2507-2509

CHAPTER FIVE

EXPERIMENTAL RESULTS OF ELECTRODYNAMIC POLARIZATION MEASUREMENTS

5.1. Electro-polarization Measurements and Analyses

Theoretically, potentiometric methods control the spontaneous occurrences of corrosion events on metal surfaces, and electro-polarization measurements study dynamic reactions, such as oxidation and reduction rate, surface passivity, re-passivation behavior, formation of localized corrosion, etc. However, thin film metallic surface applications, these variable parameters and surface phenomena are not so simply obtained because of the complexity of corrosion responses from each of the elements and different layers of thin films. But applying electro-polarization technique to magnetic thin film structures can provide significant kinetic information, which are generated via electrochemical reactions.

Generally, electro-polarization refers to a method in which an external driving force, either potential or current, is employed. When a potential is applied, the determination of the resultant current is called potentiostatic measurement. Vice versa, measurement of potential as a consequence of current applied is denoted as galvanostat. Furthermore, dynamic scanning of applied voltage or current is described as potentiodynamic and galvanodynamic, respectively.

5.1.1. Basics of Electrochemical Measurements

Electrochemistry is the study of the chemical response of a system to an electrical stimulation. Electrochemical measurements quantify and study the loss of electrons

(oxidation) or gain of electrons (reduction) that a material undergoes during electric provocation, which is described by the following general equation:

$$Me(s) \underset{\text{Reduction}}{\overset{\text{Oxidation}}{\rightleftharpoons}} Me^{+n} - ne^{-} \tag{5.1}$$

where *Me(s)* represents the solid phase of metal or alloy materials, which lose numbers of electrons e^{-}, to form metallic ions in electrolytes when the oxidation process, or *anodic* reactions, occurs. Conversely, reduction or *cathodic* reactions result in the consumption of electrons, and for corrosion, these typically correspond to the oxygen reduction or hydrogen evolution reactions, which can be described as:

$$O_2 + 2nH_2O + ne^{-} \rightleftharpoons 4nOH^{-} \tag{5.2}$$

or

$$2nH_2O + 4ne^{-} \rightleftharpoons nH_2 + 2nOH^{-} \tag{5.3}$$

Therefore, electrochemical measurement is a powerful tool in studying corrosion reactions. The depictions of oxidation and reduction reactions can be seen in Figure 5.1, which shows what happens when a potentiodynamic polarization is applied to a passive metal surface.

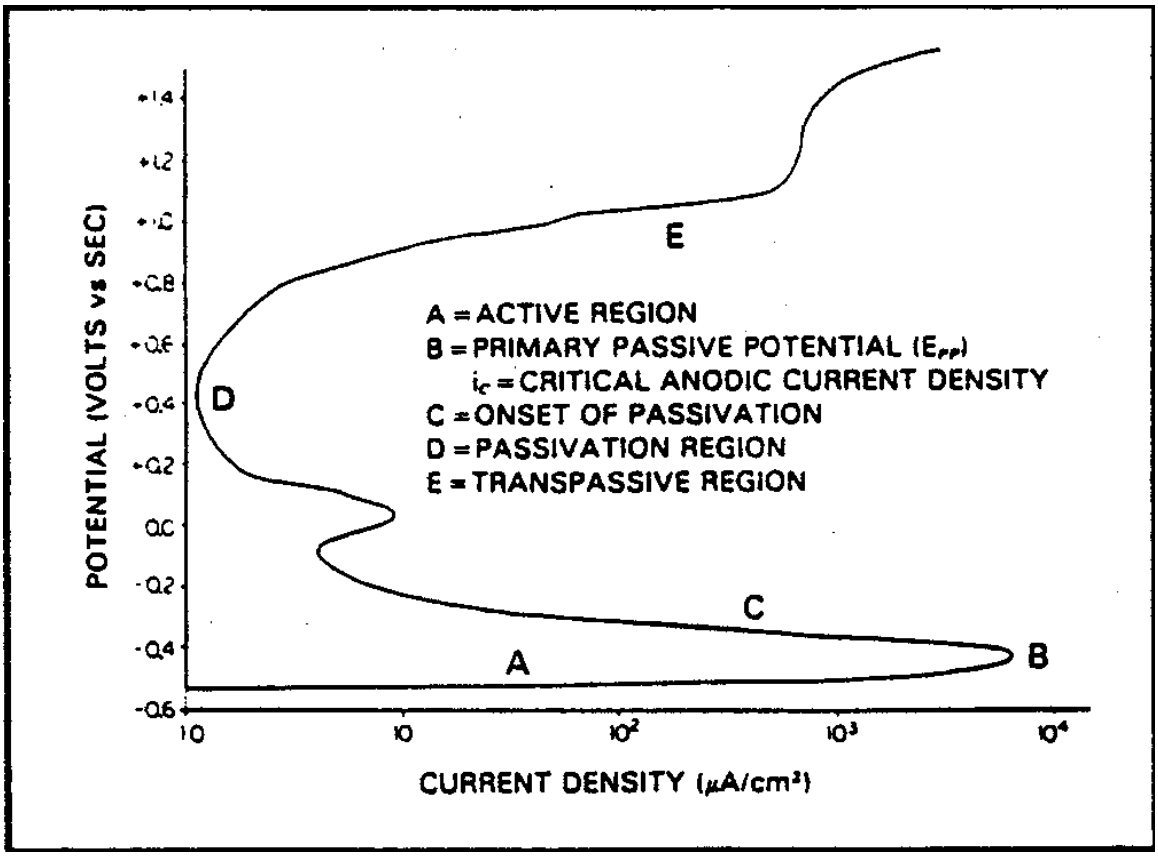

Figure 5.1. Standard potentiodynamic polarization plot (reproduced with permission from Princeton Applied Research, Inc.)

It is important to obtain the potentiodynamic curve of a metal or alloy because it reveals electrochemical behaviors at different stages. When an anodic bias is applied to a metal surface, the metal surface starts to engage in an active dissolution process, which results in increased current density. Generally the increase of current density has a linear trend with increasing of potential, seen in region A called active region. When the current density increases enough to reach value B, called the primary passive potential (E_{pp}), the dissolution of metal ions will stop. The metal surface undergoes a transformation from an active dissolution state into a passive state, passing through an onset passive region, which is indicated by region C. At this point, the current decreases dramatically as potential increases. When the surface of the metal is continually polarized, the current density will only slightly change as passivity is achieved, shown in region D. The passive metal surface is usually not unbreakable, and transpassive processes occur when potential exceeds certain limitations as result of the breakdown of the passive layer, indicated by

region E. Common understanding of a corrosion process is generally followed the curve in this plot and as a guideline in study corrosion mechanism.

5.1.2. Traditional Electrochemical Polarization Measurements

Electrochemical potentiodynamic measurements were first achieved in traditional setups with potentio/galvanostatic generators. The following graph shows the results from examples taken at different locations on the same disk surface and measured up to 2000 mV with a scan rate of 1.3 mV/sec.

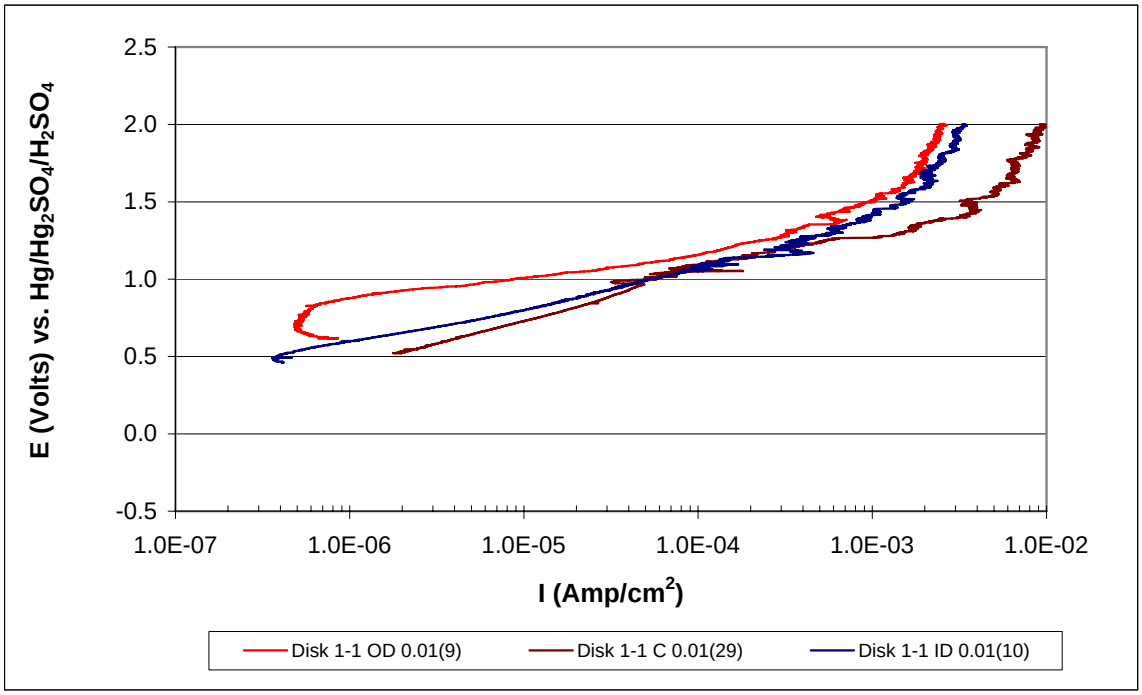

Figure 5.2. Potentiodynamic measurements at different locations on the same disk surface with traditional potentio/galvanostatic setups

In comparison to the theoretical potential responding curve shown in Figure 5.1, the direct measurements obtained using the potentiodynamic process show the corrosion mechanism is predominately in anodic dissolutions. However, the dissolution rates at different locations on the same surface showed slight variations up to 1000 mV, which could be caused by different surface conditions and topographic changes. Besides, nonlinear dissolution rates suggested that concentrations of elements dissolved in

electrolytes could be the major factor governing the corrosion mechanism in the thin film structure. When applied potentials exceed the breaking point at 1000 mV, the electric current densities responded with high noise levels, and a possible break down of surface coverage was encountered. Under such circumstances, no obvious passivation was greatly noticed, which raises questions about which thin film layer was a dominant material and structure in controlling the dissolution and whether any transpassivity could result.

5.2. Effect of Electrolyte Concentrations

The oxidation state of a metallic element in an electrochemical reaction process is one of the most fundamental parameters in corrosion studies because the oxidation state of an element governs its chemical characteristics in such reactions. Oxidation state is a function of concentrations of electrolytes, which are gauged by pH levels.

5.2.1. Electrochemical Characteristics

In these experiments with potential polarization, voltages are applied at a scan rate of 16.7 mV/min (equivalent to a milli-volt increment for every 3.6 sec), and the concentrations of HNO_3 solutions are 0%, 2%, and 4%. Current density is then calculated by dividing the current measured by the total surface areas of the disk. The increases in current densities from these experiments are plotted against the bias potential applied, as shown in Figure 5.3.

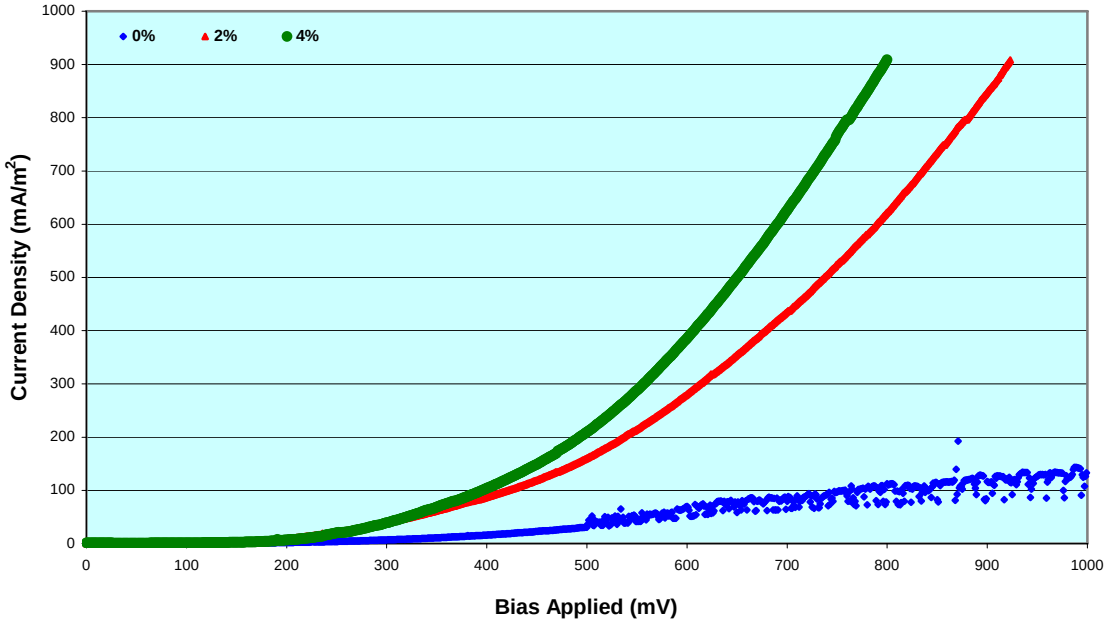

Figure 5.3. Dependence of current density on applied bias in different concentrations of media solutions

As expected, current densities measured in the solutions containing nitric acids increased pseudo-exponentially. In non-acidic liquids, the pseudo-exponential increase of current density was largely diminished, which suggested that surface reactions in such solutions are resistant to anodic reactions. Large fluctuations in current density when the potential bias exceeds 500 mV suggested that surface integrity is constantly compromised but it was restored itself thereafter, repetitively.

5.2.2. Potentiodynamic ICP-MS Measurements

The following series of graphic charts plot the analytical results from ICP-MS measurements when potentials sweep in the cell with different concentrations of electrolytes in 0%, 2% and 4% HNO_3 solutions.

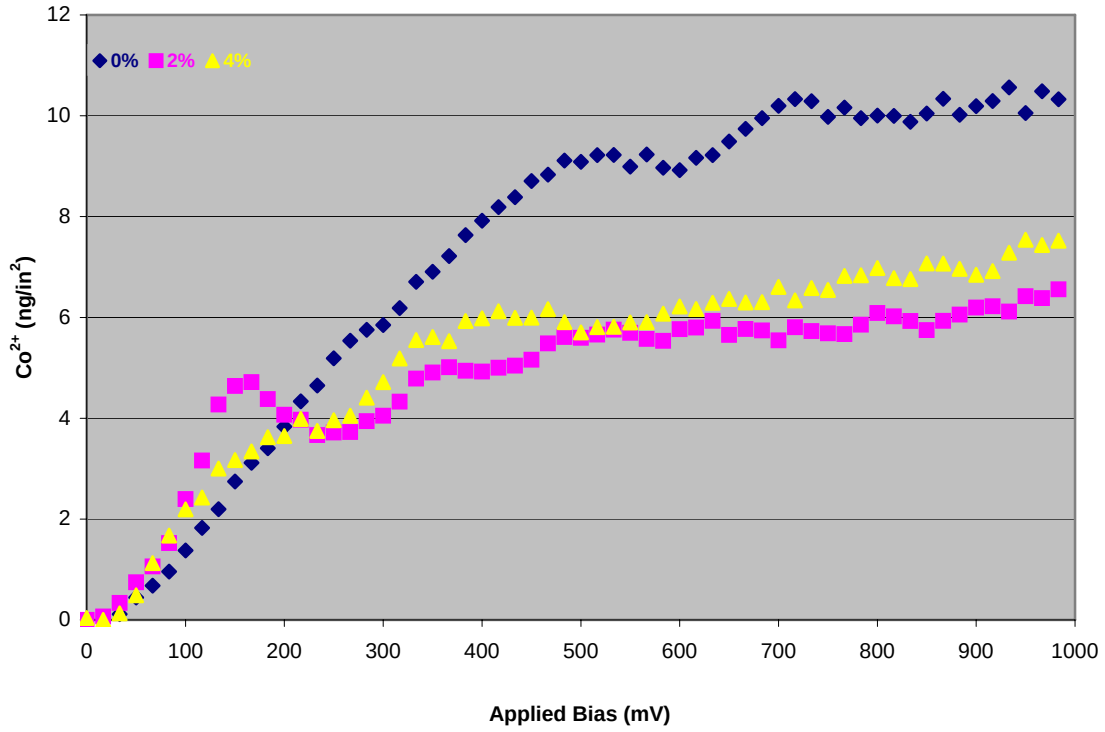

Figure 5.4(a). Surface density of Co dissolutions in different electrolytes as a function of polarization potentials

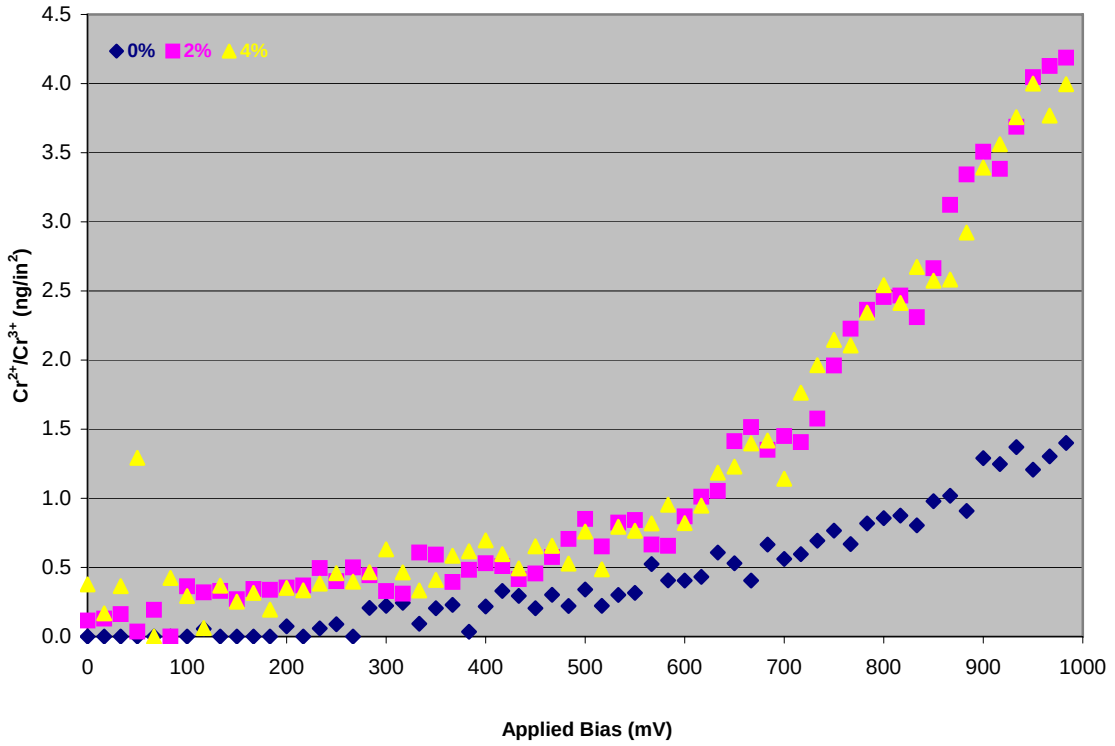

Figure 5.4(b). Surface density of Cr dissolutions in different electrolytes as a function of polarization potentials

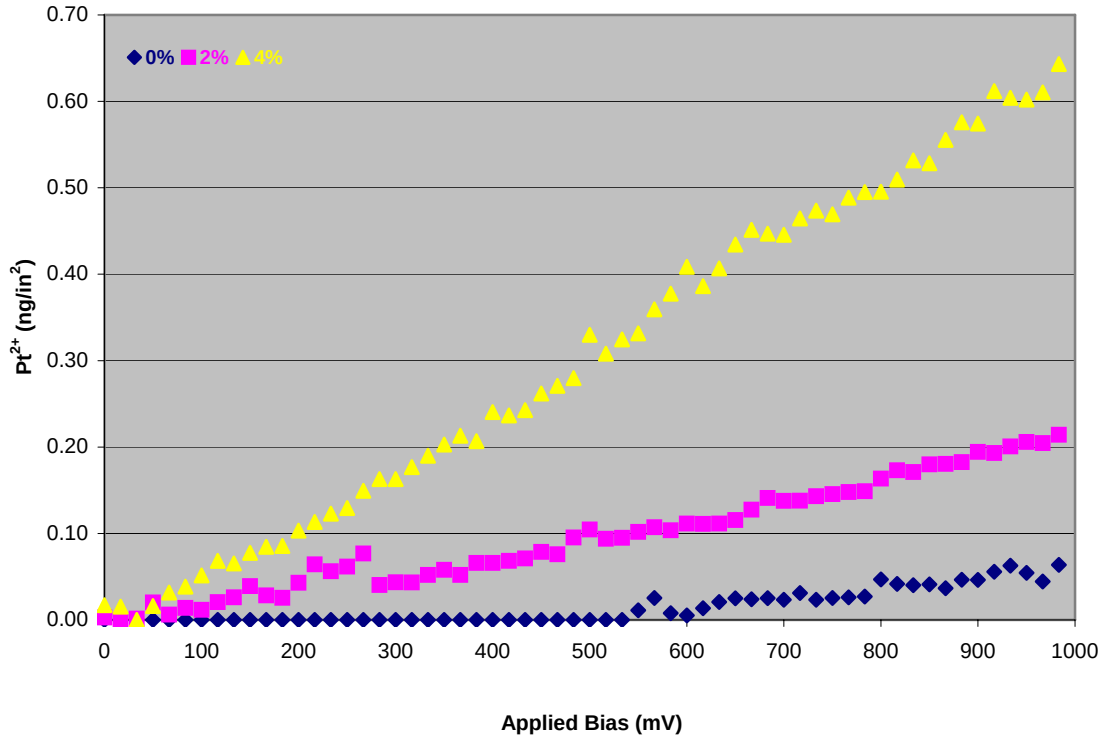

Figure 5.4(c). Surface density of Pt dissolutions in different electrolytes as a function of polarization potentials

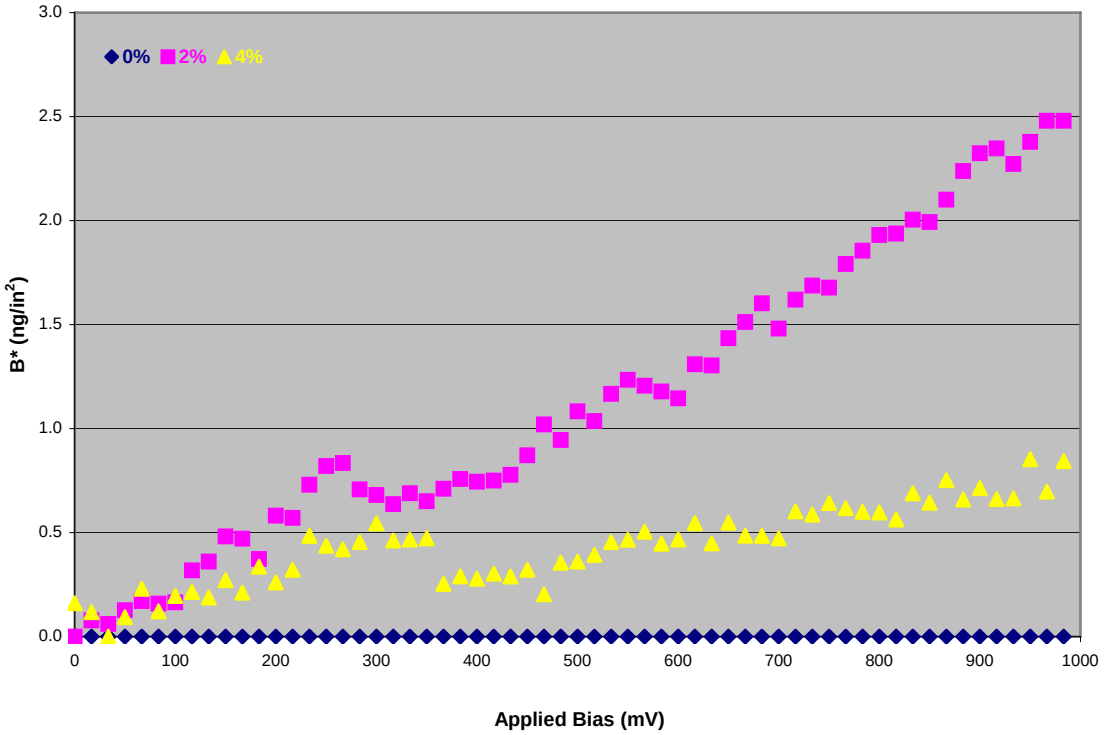

Figure 5.4(d). Surface density of B dissolutions in different electrolytes as a function of polarization potentials

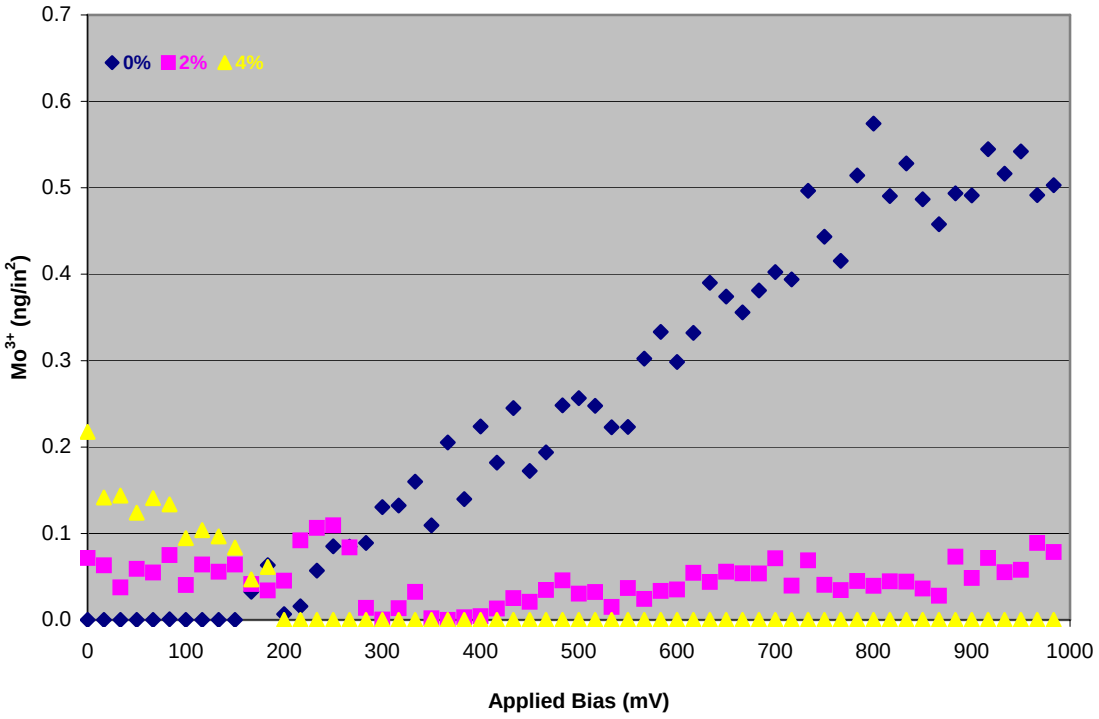

Figure 5.4(e). Surface density of Mo dissolutions in different electrolytes as a function of polarization potentials

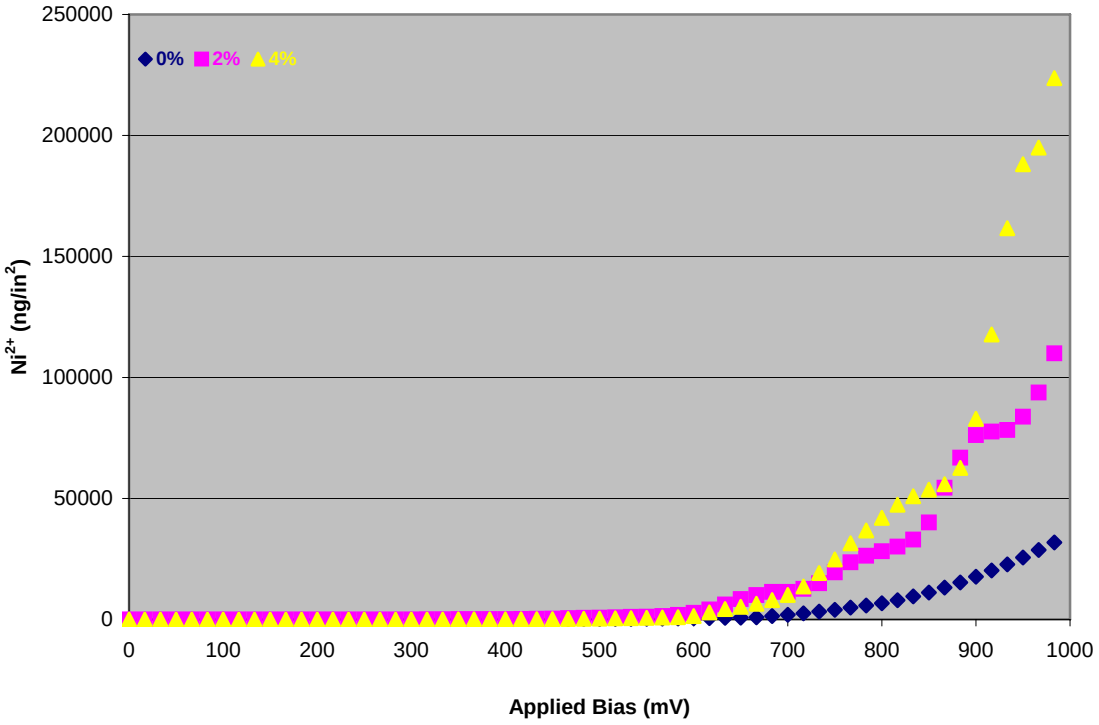

Figure 5.4(f). Surface density of Ni dissolutions in different electrolytes as a function of polarization potentials

Surprisingly, the quantity of Co dissolved in low concentrations of electrolytes was greater than those in high concentrations of electrolytes with the same polarization potentials. For example, a 1000 mV bias potential drew 10 ng/in^2 of Co in acid-free solution but only 6 ~ 8 ng/in^2 in low pH solutions regardless of the percentage of nitric acid. The low dissolution rates in acidic environments suggested that the anodic oxidation process of Co might be a key factor in enabling cobalt oxide to reach more stable atomic states.

In comparison with potentiometric measurements, formations of Cr in solutions were no longer in the background; Co clearly showed an increase in dissolution rate proportional to polarization potential applied as well as the concentration of electrolytes. However, there were two different stages representing different increases in Cr concentration in electrolytes. The potentials at transitions depended on the concentration of electrolytes. In acid-free solution, the transition potential occurred at 200 mV, while 600 mV of bias potential was needed to make such transitions in acidic solutions. When the applied potential was below these transition bias voltages, Cr content in the solutions changed only minimally, which implied that the passivity of Cr was a dominant factor. Total dissolution densities in the magnetic thin film surface in both 2% and 4% HNO_3 solutions had almost identical trends. The independence of pH levels from Cr dissolution suggested that oxidation of Cr in the alloy matrix could take place at specific locations, such as surface or grain boundaries.

Predictably, the increase of Pt concentration in the electrolytes was linearly proportional to the electric potential applied, and its rates of dissolutions increased as the concentration of anion content in the electrolytes increased. Having a linear relationship with polarization potentials of up to 1000 mV meant that oxidation of Pt compounds commenced as soon as the thin film surface contacted acidic electrolytes. Pt dissolution as a function of the linear increase in electric bias was repeatedly found in previous studies.

No detectable amount of B was found in the acid-free solution, but the increasing presence of B in acidic electrolytes was demonstrated. However, with regard to the concentration of electrolytes, B showed a higher constant dissolution in 2% HNO_3 than in

4% HNO_3. The inverse dissolution behavior of B might be explained by the formation of complex and versatile boron oxides, hydroxide, and other forms of borates.

Interestingly, Mo from the underlayer alloy showed an initial decrease in concentration and was virtually undetectable after polarization potentials reached 400 mV and 200 mV in 2% and 4% HNO_3 solutions, respectively. However, in an acid-free solution of electrolytes, a detectable amount of Mo was obtained until the potential reached 200 mV, at which point Mo continued to increase proportionally with the potential applied.

The amount of Ni released from the substrate into the electrolyte solution was extremely high at 1000 mV, which masked natural trends in low potential situations based upon a linear scale, as shown in Figure 5.4(f). By modifying a logarithmic scale plot, shown in Figure 5.5, an exponentially increasing relationship between Ni dissolution surface density and potential applied was clearly observed.

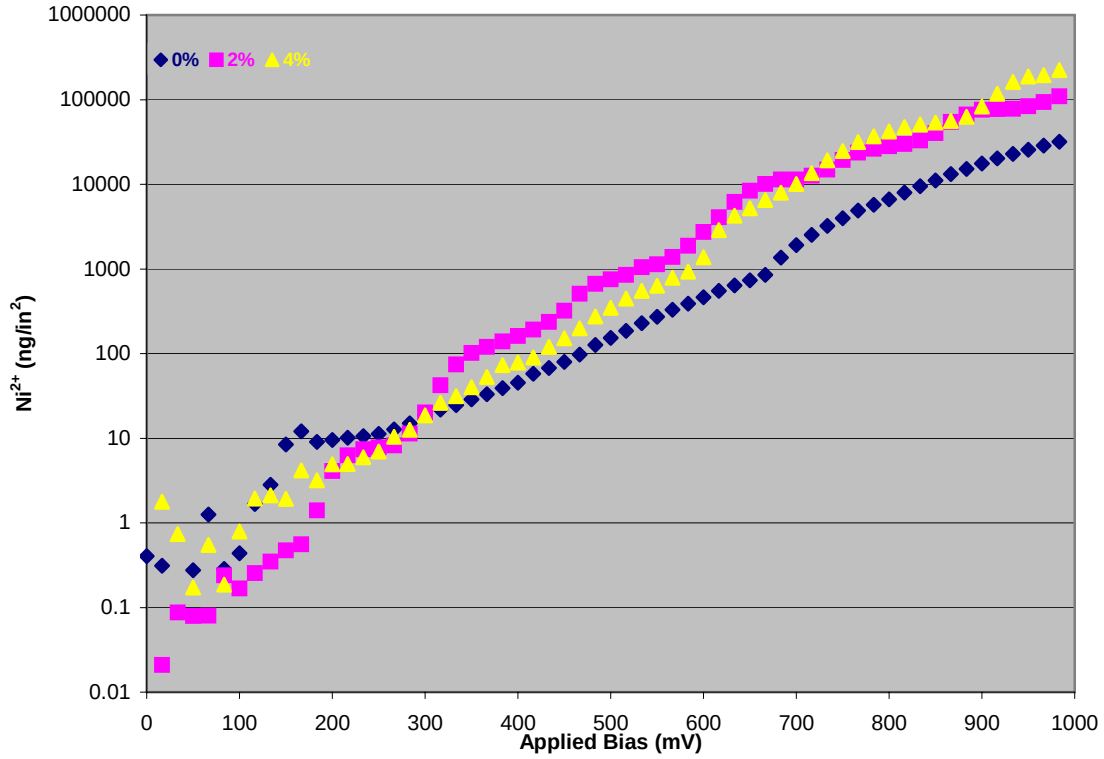

Figure 5.5. A logarithmic scale plot of Figure 5.4(f)

When the biased potential applied was over/greater than 250 mV, Ni dissolution rates well-fitted the linear trend in acid-free solution on the logarithmic scale, while, in the acidic environments, the trends better fit a power trend line, which implied that there were different dissolution mechanisms as corrosion conditions changed. The equations and their standard deviation values are summarized in the following table:

Table 5.1. Retrofitted equations for Ni dissolution and standard deviations

HNO_3 Concentrations	Derived Equation	Standard Deviations (R^2)
0%	$C = 0.5046 * EXP(0.1106E)$	0.9975
2%	$C = 10 - 16 * E^{7.0}$	0.9933
4%	$C = 80 - 19 * E^{7.8}$	0.9751

In the table, *C* represents the amount of Ni dissolved in electrolytes from unit surface area and *E* represents voltage applied.

Figure 5.6 is a graph showing the relationship between current density and total ionic dissolution density in electrolytes.

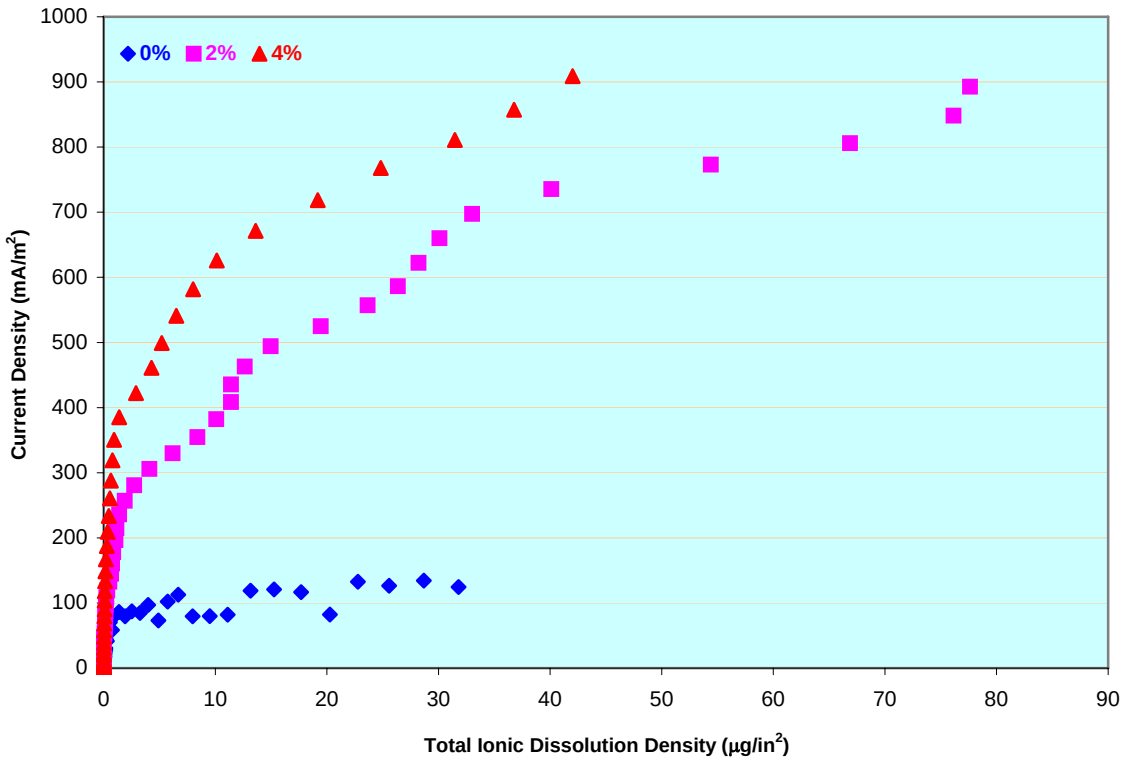

Figure 5.6. Current density as a function of total ionic concentration measured by ICP-MS from the disk surface

Clearly, as total ionic amount increased, current density increases. This proportional relationship meant that the current measured is the result of ion flow into the electrolyte.

5.3. Voltammetry Measurements

Similar to potentiometric measurements, voltammetry polarization is one electrochemical method used to obtain chemical reactions under equilibrium conditions. The voltammetry polarization technique applies a constant potential over a period of time and the changes in the electric currents are then monitored and recorded, which is also sometimes called potentiostatic electrochemical method. The selection of potential to apply on the corrosion systems in this study is based upon potentiodynamic results presented in previous sections of this chapter. In this research, 250 mV, 500 mV, and 750 mV were used because the voltammetric characteristics of thin film structures at these bias

conditions are representative both in terms of electrochemical responses and elemental yields from ICP-MS analyses.

5.3.1. Electrochemical Voltammetry Responses

In voltammetry measurements, constant potentials were exerted between the disk surface and a counter electrode, and changes in the electrical current through the solution as a function of time were monitored, as shown in Figure 5.7. Figure 5.7(a) shows the experimental results for samples in 0% HNO_3 solution at 250 mV, 500 mV, and 750 mV biases, while the same measurement results in 2% HNO_3 solution are shown in Figure 5.7(b).

Changes in electrical current densities in all cases indicated that disk surfaces encounter ionic release with potential biases. In low ionic concentration solutions, a low voltage applied to the disk surface could cause the slow migration of ions from under the surface into the surface. The current density was close to linearly increasing as the applied potential increased. However, the current density shifted upward swiftly as the bias applied was large enough or was in high concentration solutions, i.e. 2% HNO_3. The initial transition of current density was mostly due to initial surface degradation, and localized surface breakdown might be present. After the surface breakdown, the metallic thin film layer was exposed to fresh anionic interactions and forms corrosion spots. A constant release of metal ions followed, and the current density then reached a plateau, as can be seen for 0% HNO_3 at 750 mV. A very similar pattern was seen for the sample in 2% HNO_3 solution but for biases less than 250 mV.

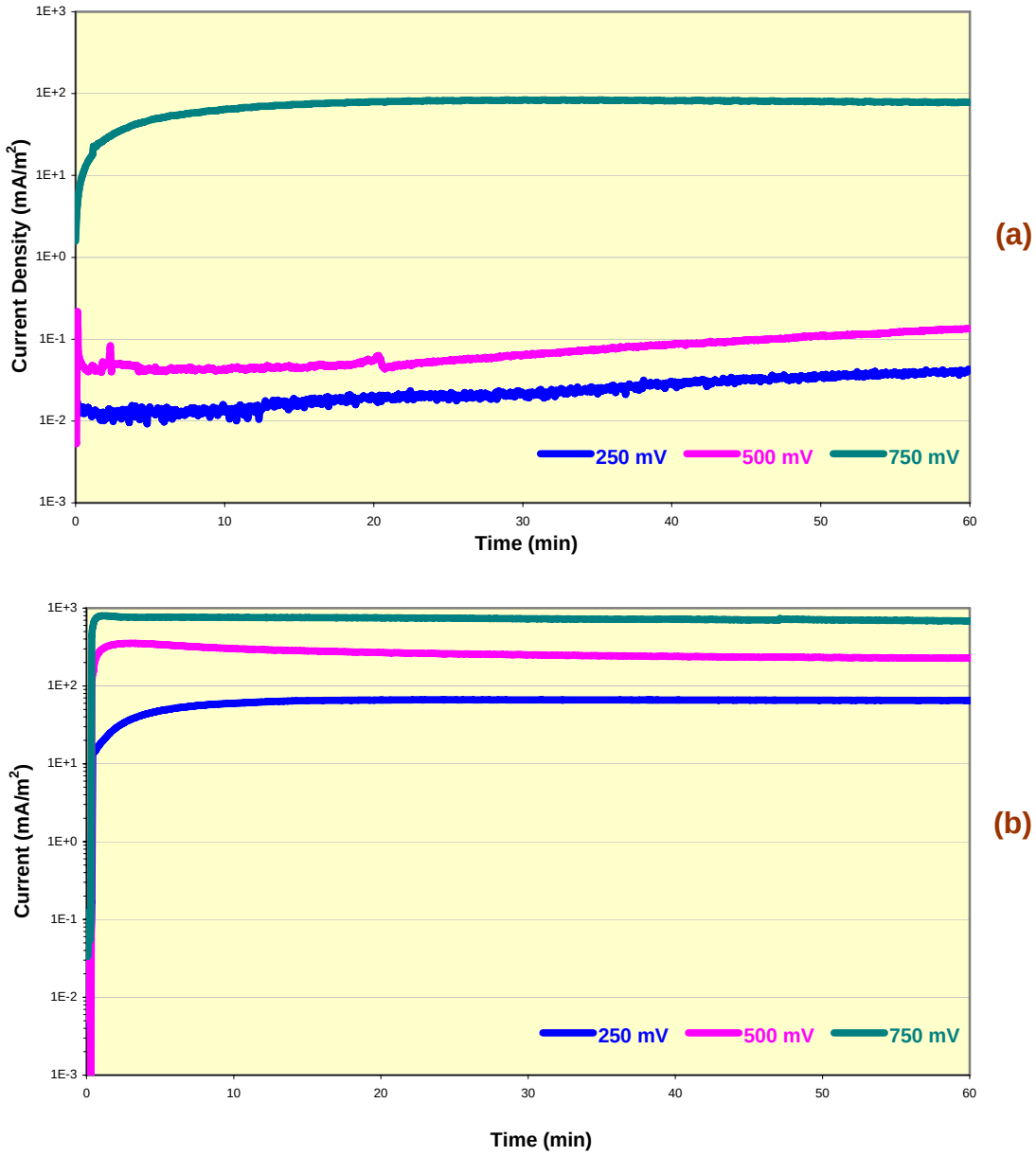

Figure 5.7. Voltammetry measurement results for one hour in (a) 0%HNO_3 solution and (b) 2% HNO_3 solution at constant potential biases of 250 mV, 500 mV, and 750 mV

5.3.2. Voltammetry ICP-MS Measurements

The following graphs show the measurement results of elemental dissolutions in 0% HNO_3 (DI water with trace HNO_3 solution) and 2% HNO_3 at polarization of 250 mV, 500 mV, and 750 mV, respectively. The metal ions measured were Co, Cr, Pt, B, Mo, and Ni.

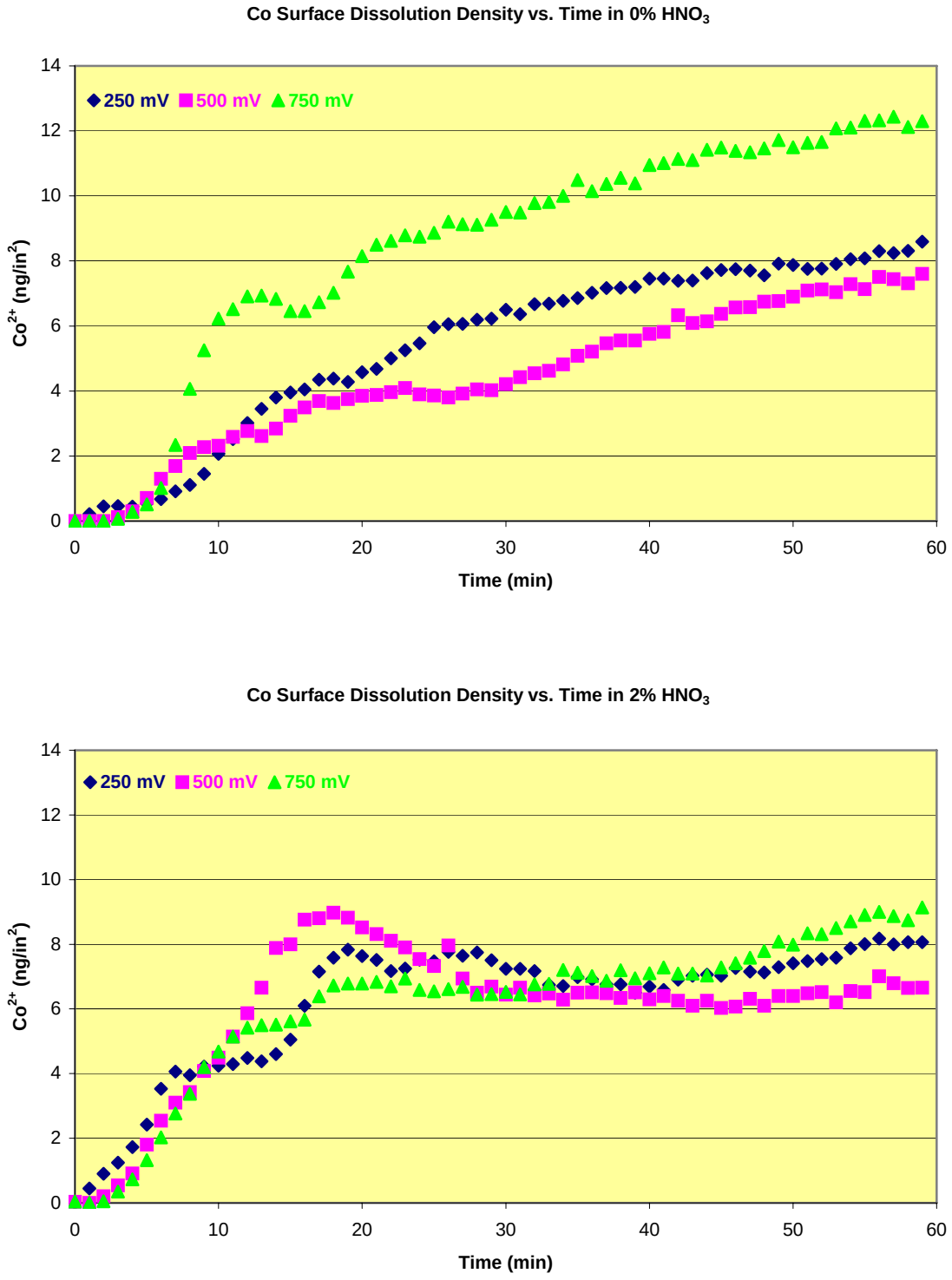

Figure 5.8(a). Co dissolution per surface square inch measured in different solutions at polarizations of 250, 500, and 750 mV for one hour

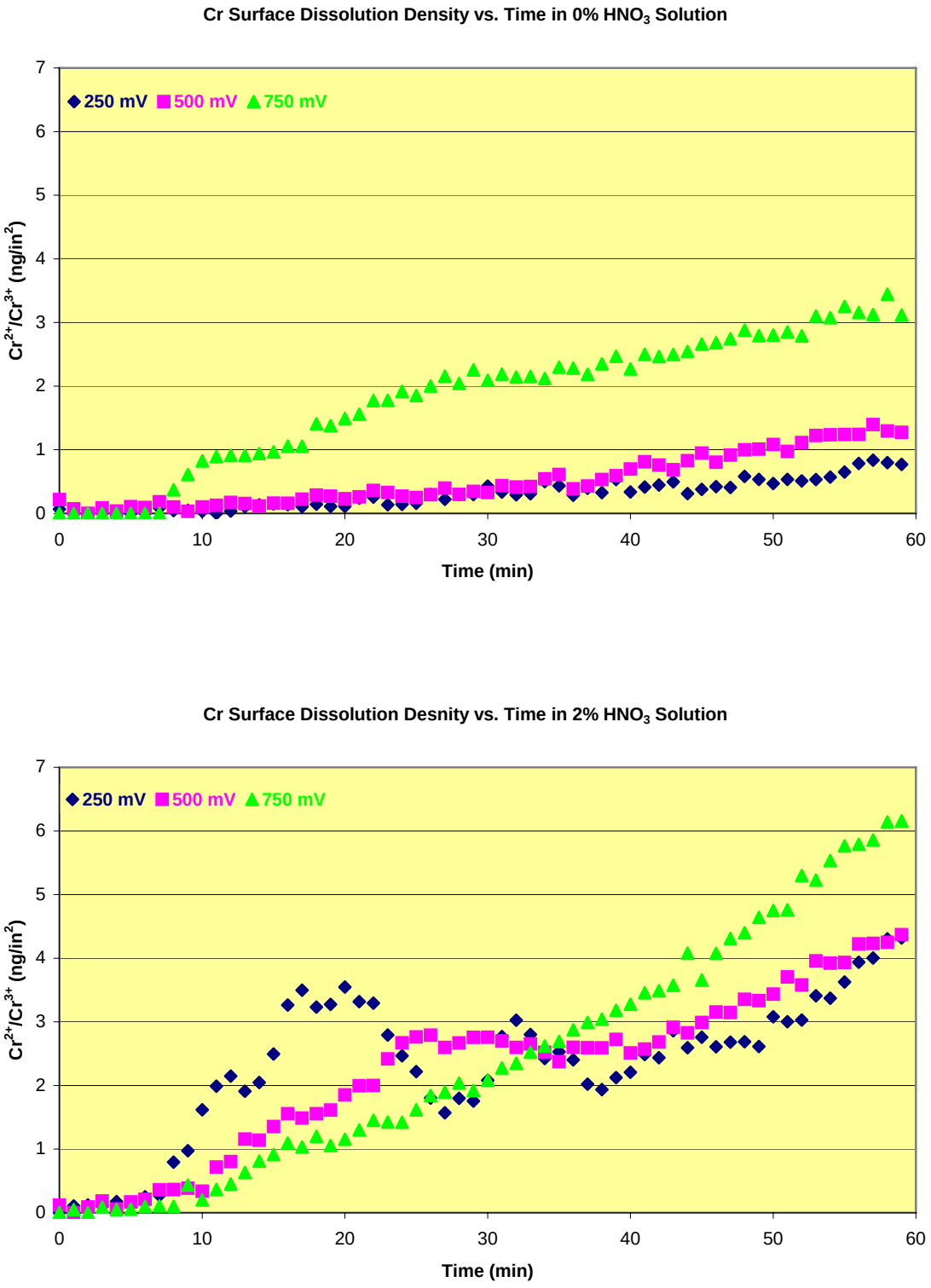

Figure 5.8(b). Cr dissolution per surface square inch measured in different solutions at polarizations of 250, 500, and 750 mV for one hour

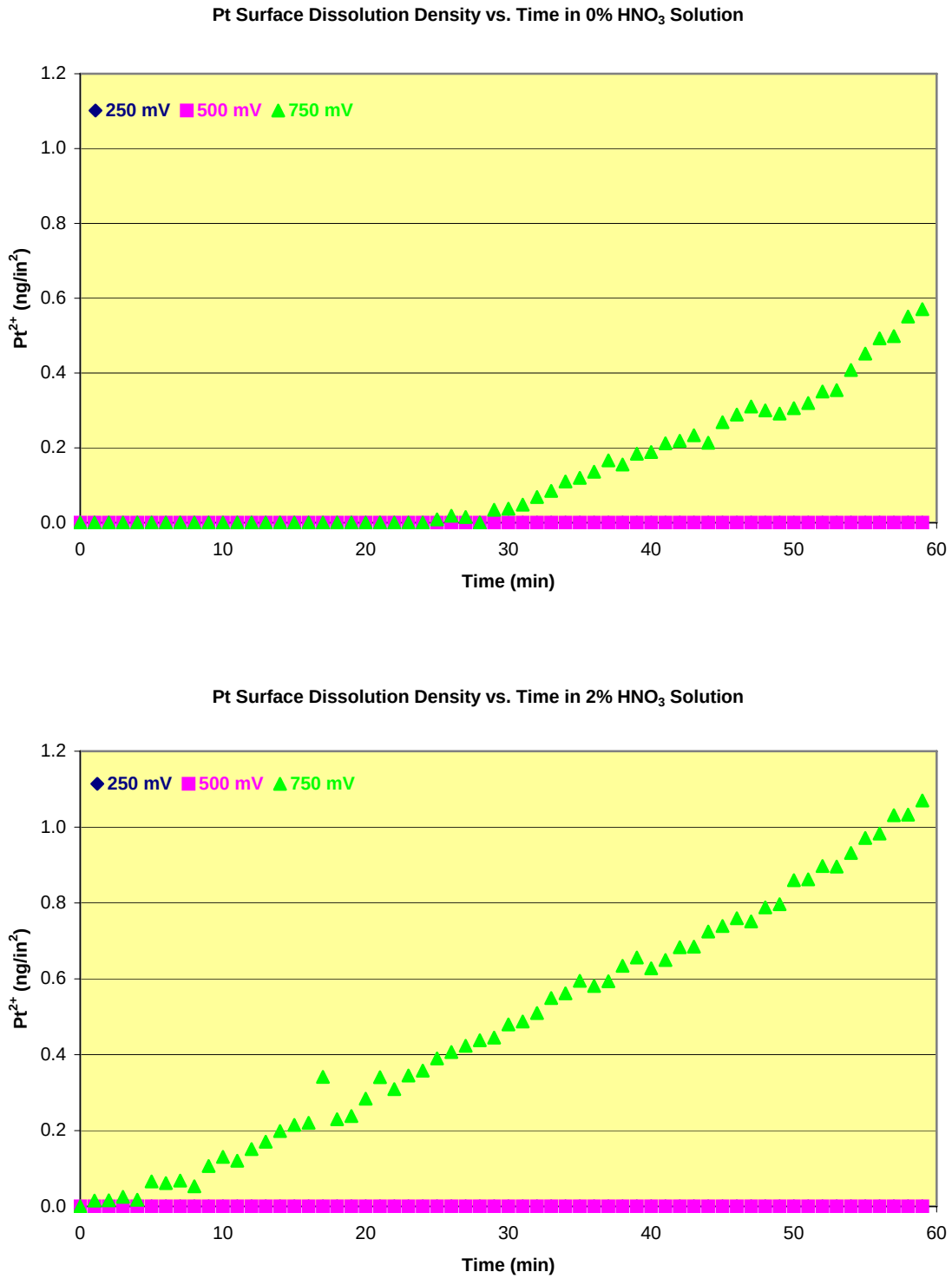

Figure 5.8(c). Pt dissolution per surface square inch measured in different solutions at polarizations of 250, 500, and 750 mV for one hour

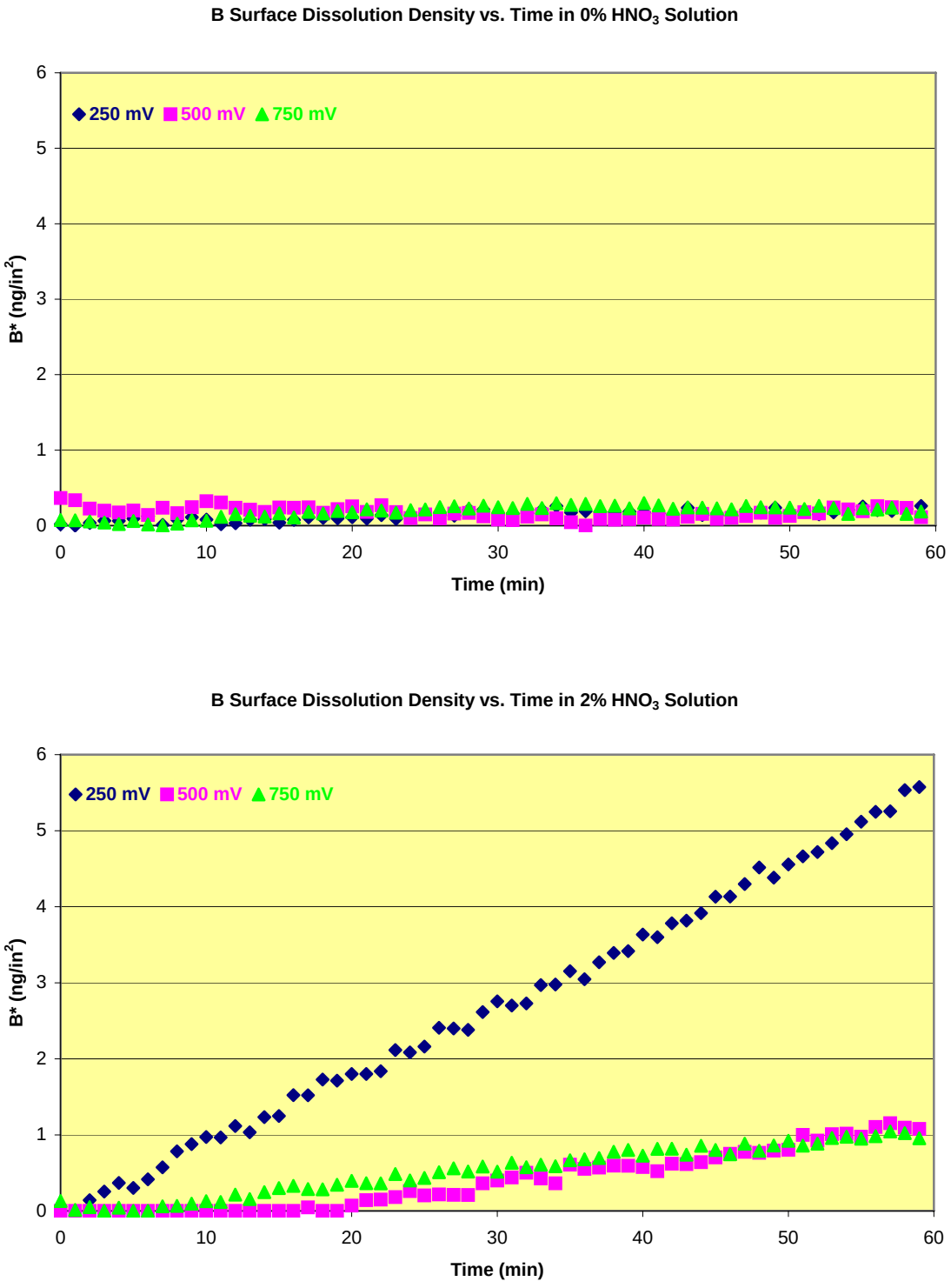

Figure 5.8(d). B dissolution per surface square inch measured in different solutions at polarizations of 250, 500, and 750 mV for one hour

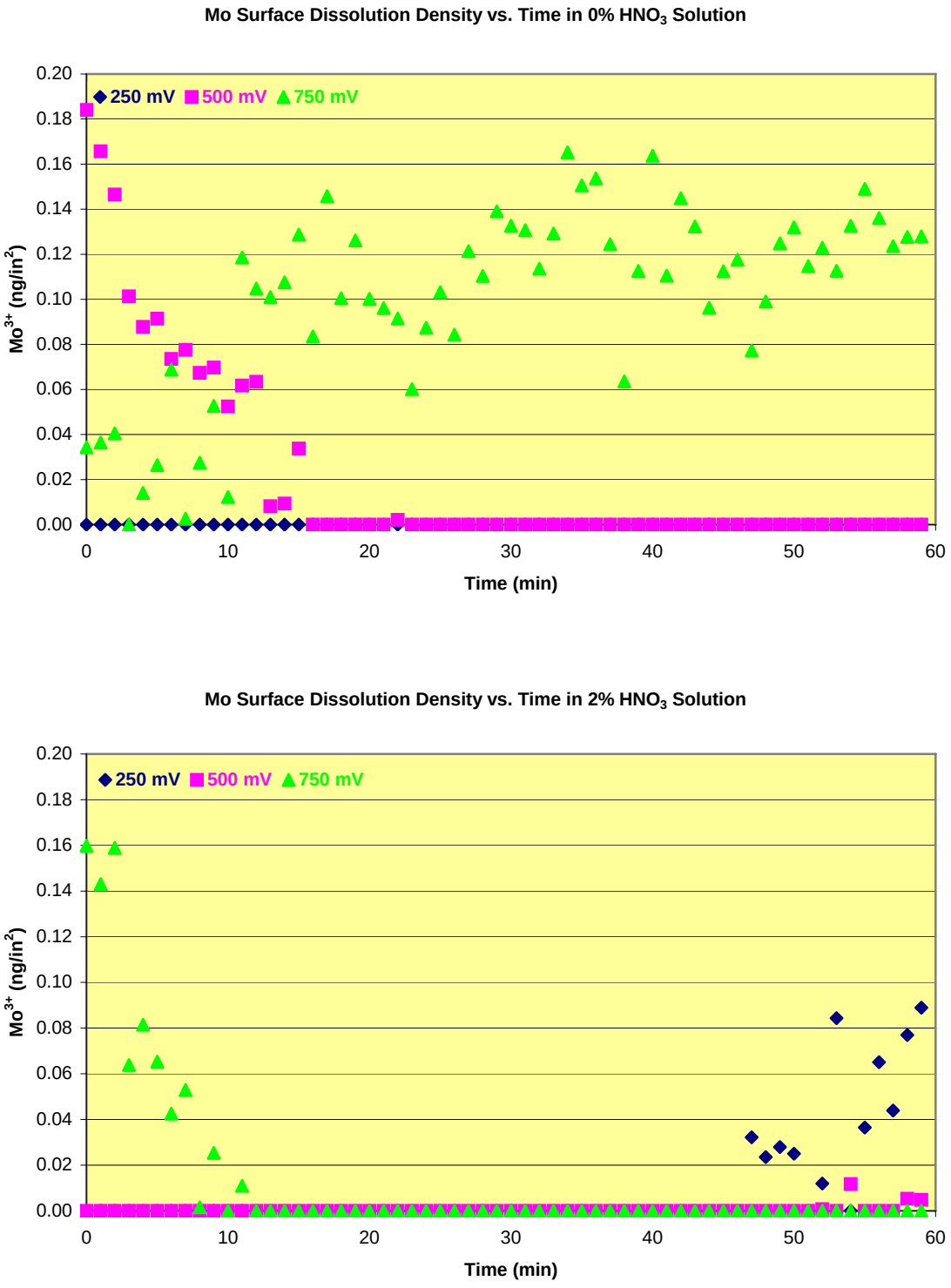

Figure 5.8(e). Mo dissolution per surface square inch measured in different solutions at polarizations of 250, 500, and 750 mV for one hour

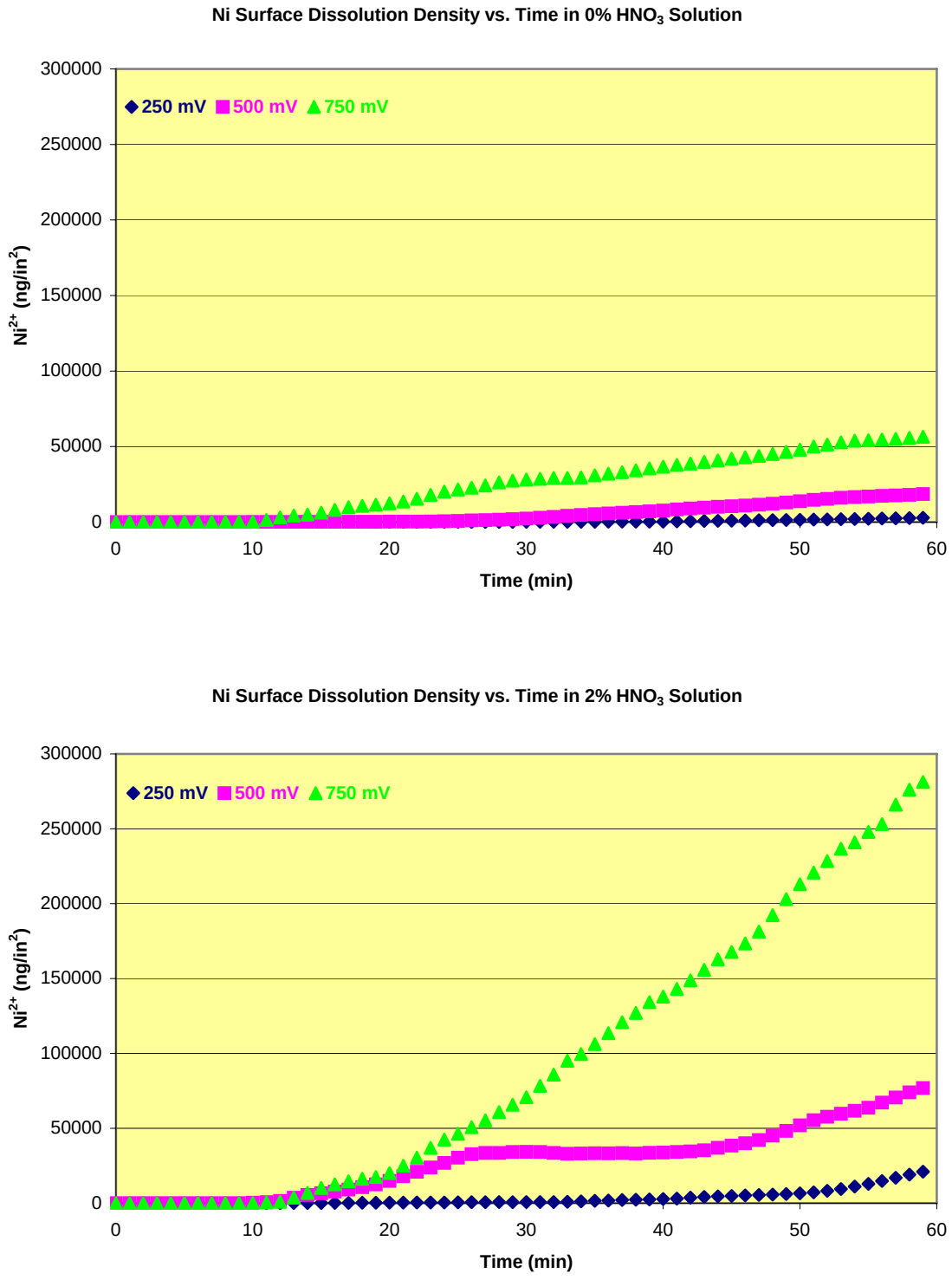

Figure 5.8(f). Ni dissolution per surface square inch measured in different solutions at polarizations of 250, 500, and 750 mV for one hour

Co release rates into electrolytes with and without nitric acids showed similar trends when various voltages were applied, which can be seen in Figure 5.8(a). In non-acidic electrolytes, Co dissolved to about 8 ng/in^2 at 250 and 500 mV bias applied, but 12 ng/in^2 could be achieved at 750 mV for one hour. These values were closely matched to those measured out in potentiodynamic studies. The similar trending of dissolution surface densities is related to different corrosion parameters suggested that either concentrations of corrosive solutions or potential biases acted in very similar way to Co dissolutions. In addition, slow dissolution rates of Co in acid-contained electrolytes, such as in 2% HNO_3, was coincided with findings in potentiometric measurements, which was suggested that Co oxidation state was very sensitive to existence of anions in corrosive environments. The time between 15 and 20 minutes were the moment for transition of the Co dissolution rates at all these potentials. After then, the changes of Co concentrations were insignificant, which suggested that further dissolutions of Co were largely delayed. The reasons for low dissolution of Co from the alloy were possible either because Co could be formed non-ionic product via electrochemical reactions or movements of Co ions could be suppressed by other elements. Since Co is the most important element in magnetic thin film structure, the compound formation and structural variation must be studied further.

Unlike the common understanding of the passivity behavior of Cr, potentiostatic ICP-MS measurements revealed linear increases in the dissolution of Cr in electrolytes regardless of pH levels in the solutions. The linear increase of Cr concentrations in electrolytes was found to be proportional to nitric acid concentrations. With 250 and 500 mV potentials in 0% HNO_3 solutions, Cr dissolved less than 1 ng/in^2 in one hour, while a 750 mV bias accelerated the dissolution more than tripled the amount in the same time period. Correspondingly, these numbers were more than quadrupled to 4 ng/in^2 for 250 and 500 mV and doubled to 6 ng/in^2 for bias of 750 mV when the thin film surface was in contact with 2% HNO_3 solution under the same conditions. Besides the timely increase of concentrations of Cr in electrolytes, it was important to notice that concentrations change only minimally during the first 10 minutes in both cases, which might imply that in the early stage, passivity exists. However, the discovery of constant precipitations of Cr in the electrochemical reactions encouraged more studies of the role of Cr in the structure and characteristics of thin film. The same behavior of Cr dissolution in both types of

polarization experiments suggested that chromium oxides produced under influence of corrosion were not as strongly bonded either on surface or inside of alloy structures as expected. With its significant role in thin film magnetism, Cr in changing microstructural characteristics under corrosion processes was much needed to comprehend the thin film corrosion mechanisms.

As a minor substitute in CoCrPtB alloy, Pt dissolution was all about its quantity. In all *in-situ* EC-ICP-MS experiments, very small amounts of Pt in a general range of several parts per billions (*ppb*) have been detected, which was less than a tenth of nano-gram per inch square from a disk surface. But extra-driving forces could accelerate the output of Pt from noble state into high mobility. As demonstrated in the voltammetric measurements, in both low and high acidic electrolyte environments, a high bias potential at 750 mV could break the oxidation barrier to cause Pt runoff from thin film surfaces. The timing of the runoff events depended on the pH levels in the solutions. In acid free solution, 30 minutes was the magic number needed to drive Pt out of the thin film structure, while instantaneous precipitation occurred from the beginning in 2% HNO_3 solution.

Boron is an element that shows different valances depending on its binding targets and environmental factors, which made explanations of B dissolution mechanisms most complicated of all the metallic elements. In this experiment, Boron behaved inertly in low concentrations of electrolyte regardless of the potential applied. However, in 2% HNO_3 solutions, the higher the potential applied, the lower the measured concentrations, which indicated that B had a tendency to form a negative ionic state. Since the purpose of adding boron into thin film structures was to control grain size and stabilize grain boundary movement, it was interesting to find out how excessive boron within the structure affects magnetic properties.

Detection sensitivity for Molybdenum (Mo) in ICP-MS was limited to the total quantity contained in the thin film structure. The precipitations of Mo in electrolytes were well below the parts per billions (ppb) range. Therefore, using the instrumentation of ICP-MS, which was in the parts per trillions (ppt) range, to differentiate Mo was very difficult, and the reliability of the measurements encountered many challenges from sample surface stability to contamination control on the nano-gram level.

Again, the Ni quantity had a large range from a few to several hundreds of nano-gram per unit area at maximum in these experiments. In 0% HNO_3 solution, Ni concentrations increased to 2.8, 18.5, and 56.5 $\mu g/in^2$ at potentials of 250 mV, 500 mV, and 750 mV applied, respectively. These numbers increased dramatically to 21.0, 76.9, and 281.3 $\mu g/in^2$ at the same applied voltages in 2% HNO_3 solutions. The amount of Ni measured in acidic solutions was in generally five to eight times more in acidic free solution, which confirmed the results from previous polarization experiments. These concentrations were several thousands to even millions larger than the measured concentrations for other elements. Once more, the activation of Ni under corrosion influences demonstrated not only its reactivity but also structural instability as will be further demonstrated in the microstructural characters in a later Chapter. Additionally, with substitution of the linear with logarithmic scale as done before, the trends of all these Ni dissolution rates were found to be the power relationship between the surface density and polarized corrosion time.

5.4. Summary of EC-ICP-MS Measurements

The combination of using the ICP-MS technique with conventional electrochemical polarization measurements has been demonstrated to be powerful in the discovery of the corrosion history and characteristics of magnetic thin film structures. Although electrochemical reactions in terms of potential and current changes were evidenced in most conventional behaviors, *in-situ* ICP-MS measurements produced many interesting and surprising results.

In comparison to the potentiometric EC-ICP-MS measurements, the elemental concentrations in the same electrolyte solutions were much lower than those demonstrated in the potentiodynamic and voltammetric measurements. The increase in elemental concentrations of electrolyte solutions meant that the metallic elements in the magnetic thin film structures underwent anodic electrochemical reactions to form cations. The high concentration output from ICP-MS provided much more reliable degree of confidence in the quantification analysis.

First, all elements from the magnetic thin film structure had different responses to electrochemical environments. ICP-MS analyses showed, for example, that the amount of Co dissolution was inversely proportional to the concentrations of electrolytes as well as polarization speed. But it was proportional to voltammetric potential applied. Thus, the oxidation of Co was believed to take place at an early stage in the electrochemical reaction, and the rate of oxidation slowed down as other elements overcame precipitation barriers.

Second, specific elements could undergo the oxidation process at different stages and with different mechanisms under certain favorable conditions. For example, the passivity of Cr described in traditional theories was challenged by the ICP-MS results in the potentiodynamic studies. In these studies, the passivity of Cr was realized only in a short period during the early stage of corrosion. The increase of Cr dissolution in the electrolytes after an inactive period suggested that the passive state was broken by potentials, concentrations of electrolytes, or increases in the length of time under polarized potentials. Since Cr is contained in all layers of magnetic thin film structures, identification of the layer from which the Cr came during each stage of the Cr dissolution process could not be made. However, the transition of Cr from inactive to positive dissolution had been well demonstrated in the polarization experiments.

Third, the *in-situ* EC-ICP-MS technique had demonstrated in all these experiments that corrosion responses from minor constituents in an alloy matrix could also be determined during the same corrosion processes. This statement was particularly true with regard to the measurements of Pt and B, which were minor additions to the CoCrPtB alloy. Because of their low percentages in the structures, Pt could only dissolve in very low concentrations, in the sub-ppb level, in the electrolytes, for which the ICP-MS instrumentation was the chosen method of quantification. In addition, the *in-situ* EC-ICP-MS method provided vital information about the trends of the minor elements during the course of corrosion, which was meaningful and important. Variations in the linear dissolutions of low concentrations of Pt in electrochemical reaction solutions under certain circumstances were good examples of the subtle changes.

Interestingly, with the ability to both quantify and demonstrate trends in *in-situ* EC-ICP-MS electro-polarization measurements, judgments about anodic and cathodic reactions could be made based upon relationship between amount of elements and electro-potential applied. The response of boron to corrosion was an example of showing cathodic reaction tendencies under anodic polarization was applied resulted dissolution decrease. Oxidation states of B changed due to pH levels in the environment. Because boron possesses different valances, oxidation formation becomes unpredictable, and there is no guarantee that a reduction product would not be formed. Present in ICP-MS, B was mostly inactive in acid-free solutions, but the anodic behavior of B in high concentrations of nitric acid solutions was not as strong as in low concentrations of electrolytes, which could be seen in both potentiodynamic and voltammetric measurements.

Due to atomic quantity limitations, no significant dissolution data for Ta could be traced in this part of study. Even though Mo showed low dissolution concentrations in electrolytes, a general trend of Mo dissolutions was that they generally required high potential, high electrolyte acidic concentrations, and a slow scan rate to be released from the thin film structure. Mo oxidation states and passivation processes were probably as uncomplicated as the others since its mono-oxidation state is relatively simple.

Finally, a surprising discovery was the finding of excessive Ni in the electro-polarization experiments. Since Ni is a substrate constituent in association with phosphorous, the extremely high dissolution rates and amounts were areas for future study. Because the electric current crossed the body of electrolytes, Ni content was believed to be a major contributor to the current, and its chemical interferences with other elements must be studied.

CHAPTER SIX

MICROSTRUCTUAL CHARACTERIZATION

6.1. Microstructures of Magnetic Thin Film Alloys

Which Co alloy thin films exhibit magnetic properties depends on not only the microstructures of magnetic thin film but also structural characteristics and chemical composition distributions of underlayer and substrate alloys. Any structural imperfection and compositional abnormality will result in the impairment of magnetic performance. Corrosion can seriously deteriorate and be destructive to the quality of these characteristics. How corrosion changes the microstructures of the Co alloy thin films are the focus of this work.

6.1.1. Introduction to the Grain Structures of CoCrPtB Thin Films

Most Co alloys, including CoCrPtB thin film deposited on the Cr underlayer, were polycrystalline structures. Figure 6.1 shows an example of one of these structures.[6.1][6.2]

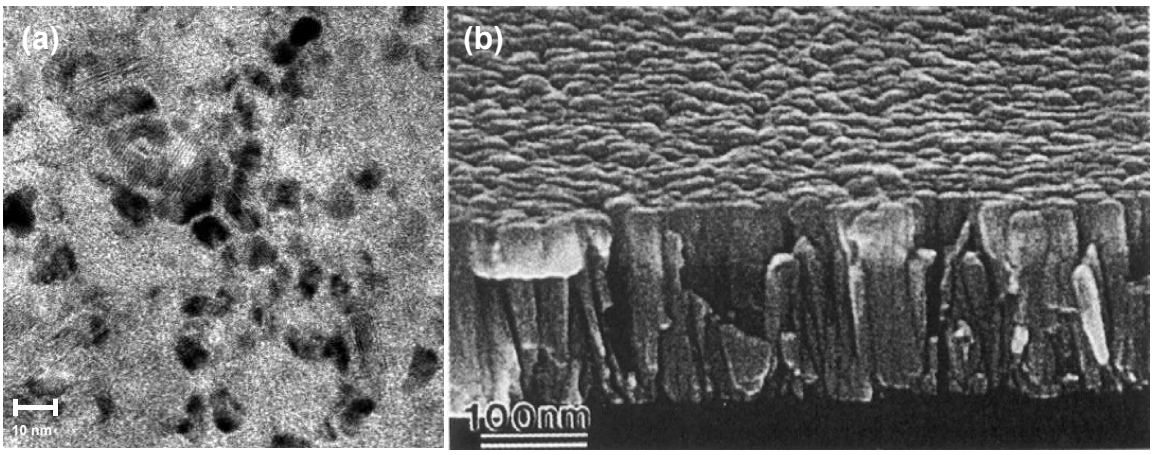

Figure 6.1. (a) Plane view TEM micrograph of CoCrPtB alloy film and (b) SEM micrograph of the cross-section showing the columnar shape of grain growth and vertically-oriented grain boundaries (Images reproduced with permission)

The plane view of this type of film, which showed multiple grain structures using TEM, had been presented in many reports.[6.3]-[6.5] Vertically in cross sectional TEM views, columnar grain structures are typically observed as shown in Figure 6.1(b), which are resulted from thin film growth history [6.6]-[6.8] and had also been reported in many publications.[6.9]-[6.11] Unlike randomly-oriented grain boundaries, this perpendicular orientation of grain boundaries could largely increase risk of corrosion induced structural deterioration and even degeneration because the diffusion process could occur from the top of the surface.

The average grain size of CoCrPtB was several nanometers in diameter and has 1 ~ 1.5 nm thick grain boundaries in between in most consensus.[6.12] High Cr content in such Co-based alloy is mainly to improve magnetic anisotropy by decoupling interactions between grains.[6.13] Addition of Pt into the alloy matrix is to optimize structural orientations and compatibility with underlayer, which results high magnetic coercivity.[6.14][6.15] Bending small amount of B into CoCrPt thin film structures has been realized to decrease physical grain sizes, which effectively suppress magnetic intergranular exchange via chemical segregation to the grain boundaries.[6.16] Grain boundaries perpendicular to the substrate of the underlying thin film provided a rapid diffusion path into the thin film stack. Grains with this orientation and continuous grain boundaries extending from bottom to top surface of the thin film stack were referred to as "prismatic grains."

Both grain and grain boundary structures of epitaxially grown CoCrPtB depend strongly on structural orientations of the underlayer. Nucleation of adatomic Cr-alloy film, such as Cr and CrMo, occurs randomly due to body centered cubic (*bcc)* structures on the smooth surface of the substrates. Therefore, control of grain size distribution of CoCrPtB alloy was realized by controlling the nucleation and growth of the Cr underlayer and CrMo seed layer on the Ni/P substrate.[6.17] Significant influences of both compositional and structural characteristics of CrMo underlayer on grain boundary structures of CoCrPtB alloy has been recognized in several studies. Less structural distinct grain boundary of CoCrPtB alloy was reported as it deposited on top of single layer of $CrMo_{30}$,[6.18] which corresponded to what amorphous phase at grain boundary of CoCrPtB structures was reported.[6.19]

6.1.2. Compositional Segregation of Grain Boundaries

Grain boundaries of Co alloys were particularly important primarily because of their effects on magnetic transition noise and thermal stability.[6.20] But, they could serve as a pathway for corrosion. It was not difficult to imagine that the grain boundaries could play a vital role as a consequence of epitaxial thin film growth.[6.21] Compositional segregation at grain boundaries had been demonstrated by many studies.[6.22]-[6.24]

Compositional segregation had been found to occur in binary CoCr thin films. Co and Cr segregation occurs inside grains and at grain boundaries and was critical for stabilizing the thin film magnetization. Inside grains, rich Co content was often detected, while grain boundaries were Cr-rich. Using the energy-filtering TEM technique, these atomic segregation phenomena were confirmed by Grogger's study when $CoCr_{16}PtB$ alloys were used. In a large TEM plane view with an energy filter, the Cr composition along the grain boundaries could be clearly seen, as in Figure 6.2.[6.25]

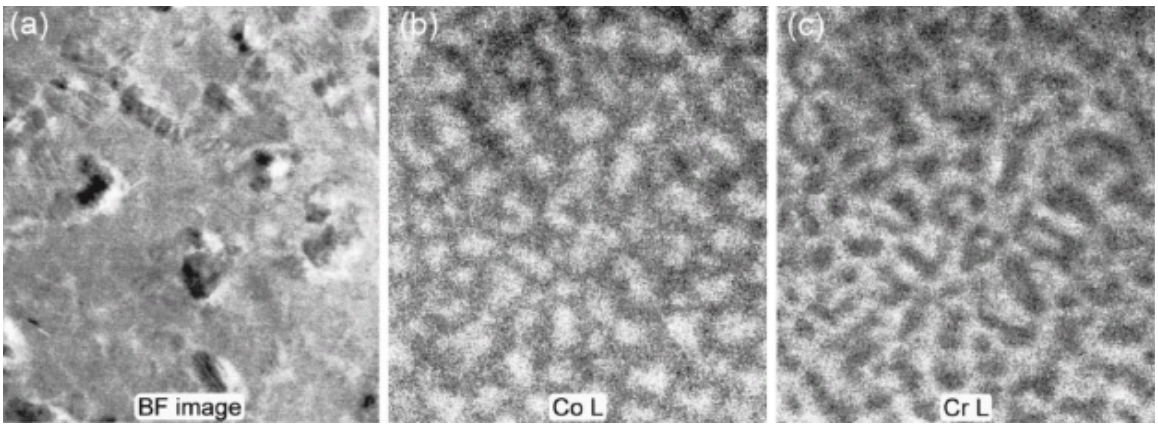

Figure 6.2. (a) Bright field TEM image of $CoCr_{16}PtB$ media with (b) Co elemental mapping and (c) Cr elemental mapping as comparisons (Images reproduced with permission)

Quantitatively, in CoCrPtB alloys used as samples in this research, average amount of Co inside grains was about 86% comparing 64% of Co at grain boundaries. Inversely, Cr content inside grains was measured 14% while 36% is counted in average at grain boundaries. The shell thickness of grain boundary phases was estimated to be approximately 0.8 nm with an average grain size of 7.5 nm.[6.1]

In additions, with X-ray absorption analysis, Kemner, *et al.* concluded in their report that preferential site distribution of dilute Pt in CoCr based films was mostly inside Co-rich grains.[6.26] Because of the face centered cubic (*fcc)* structure of Pt, which has a larger lattice structure, prevention of the segregation of Pt to the grain boundary was probably due to low diffusion rate during film growth. The difference in the diffusion rates of Cr and Pt might be the result of many factors, such as sputtering rate, deposition method, and vacuum conditions.[6.27] Meanwhile, TEM and magnetic studies had shown that adding 3-8% of boron causes a wider grain boundary phase and smaller effective magnetic squareness (S*) and magnetization value (ΔM) peak. These results indicate that better exchanging de-coupled magnetic grains could be achieved by adding boron to the CoCrPt alloy because B segregates to the grain boundaries.[6.28]

6.1.3. Lattice Crystallographic Alignments and Orientations

Microstructures of grains and grain boundaries are governed by lattice crystallographic compatibility during thin film growth. The crystallographic structures of CoCrPtB constructed in both *bcc* and *hcp* have been reported in many studies depending on types of underlayer materials and structures.[6.29]-[6.32] However, ferromagnetism of CoCrPtB has been recognized in hcp structures resulted from deposition on *bcc* structured materials, such as Cr, which exhibited the closed lattice geometric matches as shown in Figure 6.3.[6.33]

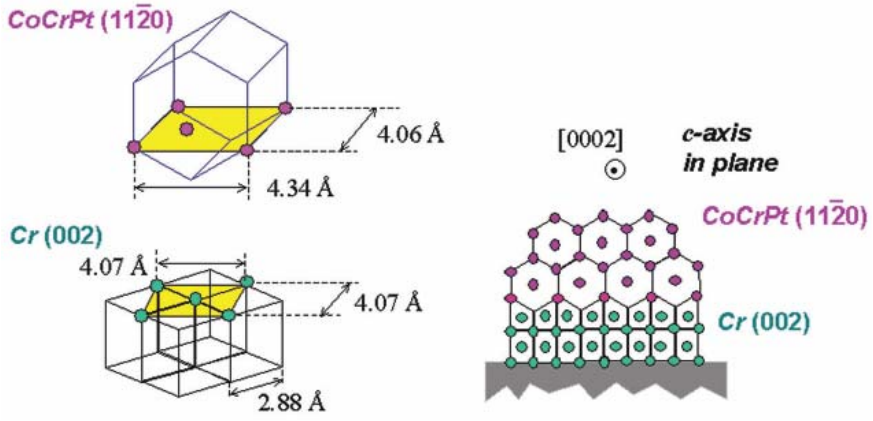

Figure 6.3. Commonly achieved *hcp* Co-based crystallographic structures in matching Cr underlayer lattice structures for magnetic thin film applications (Graphs reproduced with permission)

Co alloy with *hcp* structures retains strong magnetic anisotropy in *c*-axis. Therefore, in order to realize in-plane magnetization, the lattice orientation of Co-alloy is forced to lay its *c*-axis in parallel to surface of thin film by incorporation with *bcc* Cr lattice spacing underneath. Such ideal crystallographic alignment and orientation can be skewed when different content of other elements are incorporated.[6.34] Though there was no report on how much the changes of high percentages of other elements in resulting Co lattice structures, several studies suggested that incorporation of extra elements into Co matrix can change not only structural *hcp* arrangements but also compound phase in different region of the microstructures during epitaxial growth. Because grains and grain boundaries of CoCrPtB have been demonstrated with differentiated amounts of Cr, Pt and B as mentioned before, the structural characteristics at both regions are expected to differently, which effects on corrosion resistance are then postulated with different potentials.

6.2. Sample Cross Sectional Preparations for TEM

Cross section sample preparation for TEM analysis could be found in many references using mechanical preparation or focused ion beam milling.[6.35]-[6.37] In this research, a combination of these two methods was utilized to optimize TEM sample quality for cross sectional TEM analysis. The mechanical sample preparation included cutting, dicing, grinding, polishing, and dimpling followed by FIB milling at corrosion spots to obtain electron transparency. Illustrations of sample preparation procedures for TEM analysis of a cross sectional surface were provided in Appendix IV.

By identifying corroded areas, two coupons half an inch in diameter were cut using a steel metal hole-cutter (MTN7430, Mountain Cutting Tools Company). A thin layer of adhesive (M-Bond 610, Vishy Micro-Measurements) was applied between the surfaces of interest. Pressure was applied when it was heated at 160^{o}C for several hours as recommended to reach complete curing. Excessive base materials were trimmed off using a diamond saw (Isomet Low Speed Saw, Buehler, Illinois). A rectangle bar was then cut out of the middle of the coupon. Meanwhile, a stainless steel tube 3 mm in diameter was filled with 2-part fast curing room temperature adhesive, F-30 from Alteco, Osaka, Japan. After the epoxy was hardened with the bar inside, dicing was performed to slice a cross

sectional sample 2 - 3 mm in thickness. Next, normal mechanical thinning procedures were followed to reduce the thickness down to 80 - 100 μm. A mechanical dimple with 1 μm diamond paste could achieve 5 – 10 μm in thickness at the center of the samples. Thereafter, an FEI Altura 835 dual beam Focused Ion Beam (FIB) system was used to further reduce the thickness to be electron-transparent by milling off surface materials. The final thickness is less than 100 nm and 20 μm wide, which are shown in a TEM image in Figure 6.4.

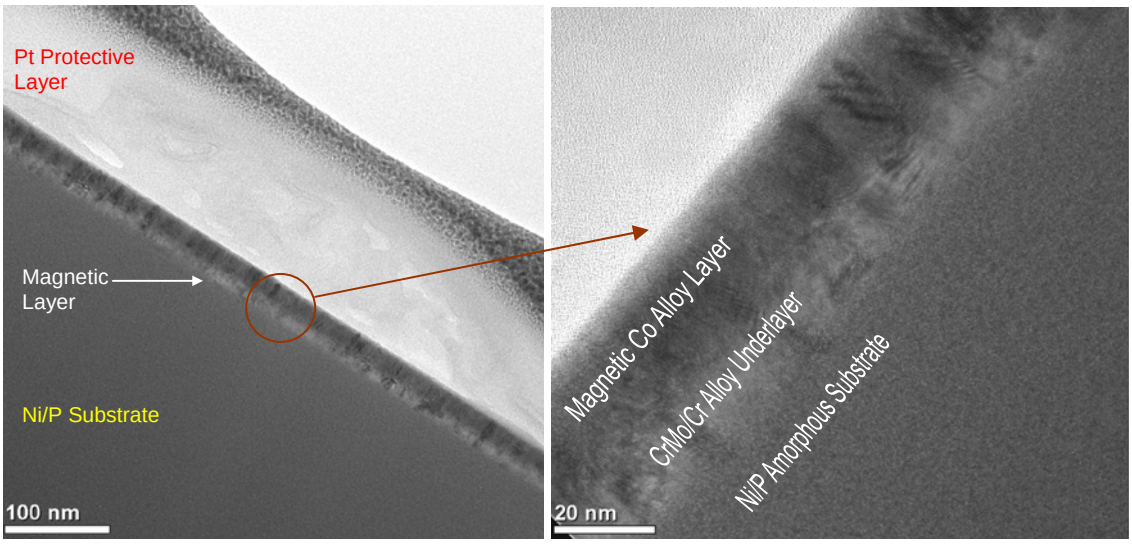

(a) (b)

Figure 6.4. (a) TEM image of an area of interest after thinning using FIB and (b) the same image, enlarged to show the thin film layer structures

6.3. Microstructural Analysis Results

TEM analyses of magnetic thin film microstructures that were reported in much of the relevant literature focus mainly on planar section analysis but cross-sectional images were limitedly presented.[6.38][6.39] In this research, a majority of the microstructural analysis was devoted to cross-sectional TEM analyses, including bright field images of the film stacks, macrostructures and surfaces, and grain and grain boundaries. Electron FFT diffraction pattern analysis and electron nano-probe profiling with EDS comparing elemental abundances in grains and along grain boundaries from cross-sections were also part of this work and presented in this section. These valuable results were achieved

using a 200 KeV FEI Tecnai G2 TEM system located in the TEM laboratory of the Microelectronic Research Center of the J. J. Pickle Research Campus at The University of Texas in Austin, Texas.

6.3.1. Cross sectional TEM Micrography

Cross-sectional microstructural images of the samples that were polarized at 750 mV in a 2% HNO_3 solution for 5 minutes, 15 minutes, 30 minutes, and 60 minutes, respectively, are shown in the following micrographs, Figure 6.5(a) – (d).

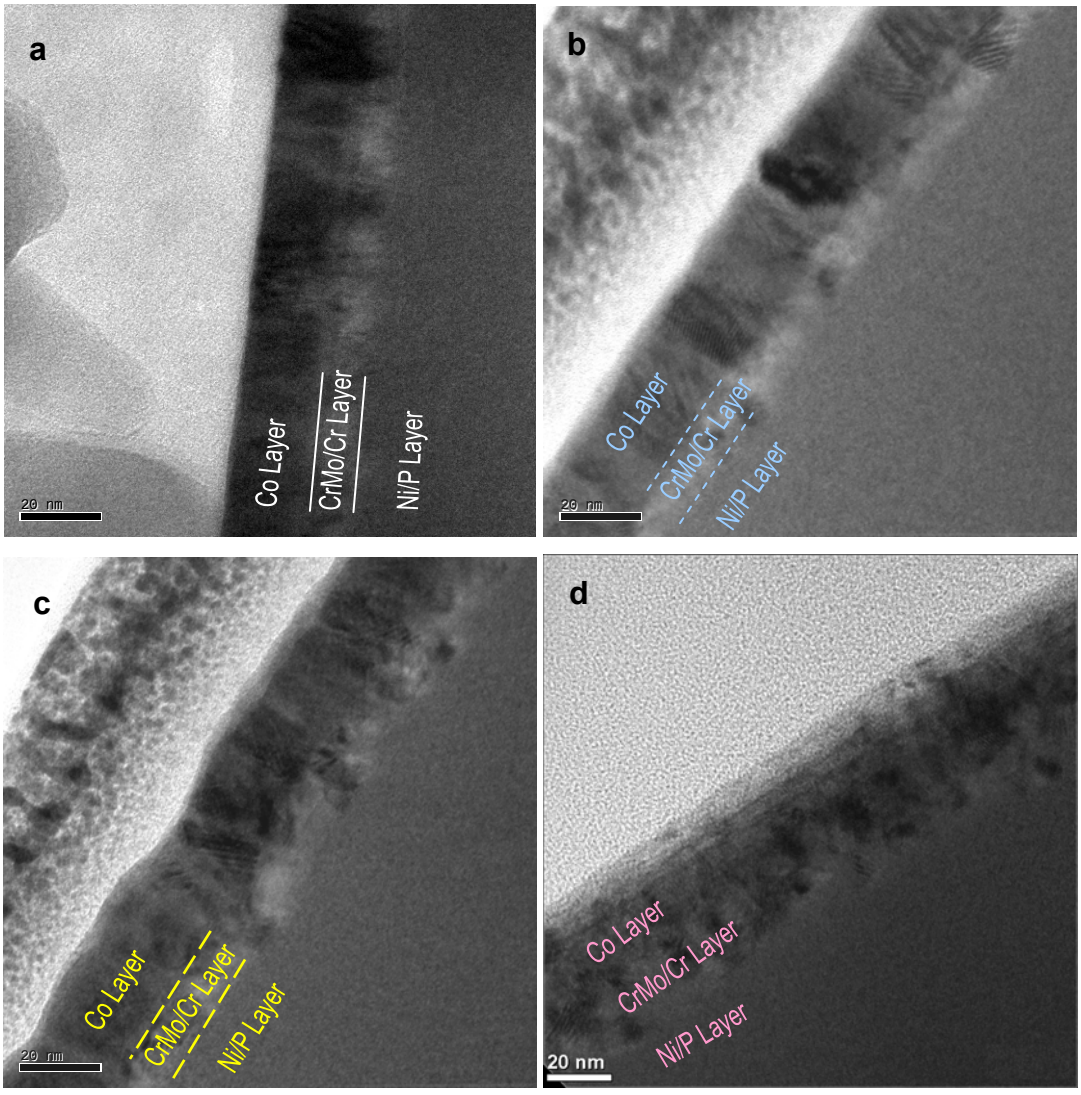

Figure 6.5. Cross sectional TEM micrographs of samples that underwent 750 mV polarization corrosion tests at (a) 5 min, (b) 15 min, (c) 30 min, and (d) 60 min

These four samples were *ex-situ* made under the same conditions as the one in an *in-situ* corrosion polarization experiment, which EC-ICP-MS results were presented in Figures 5.8(a)-(f). In the very early stage of polarization, microstructural change was not visible. In Figure 6.6(a), deformities in grains, along grain boundaries, at the surface, or the interfaces cannot be observed. However, shortly thereafter, with a 750 mV bias, the specimen showed a uniform distinguishable layer only 1 ~ 2 nm in thickness on the surface. Several previous studies performing surface compositional analysis on magnetic thin film suggested that surface oxidation containing mostly CoO and Cr_2O_3 could be naturally formed under normal conditions environment.[6.40] When Co alloys contact an aqueous surface, complex cobalt hydroxides could be produced in many phases.[6.41] As can be seen in Figure 5.8, the most prominent amount of ion detected in the solutions at this stage was cobalt. Therefore, cobalt oxide was the most probable compound grown on the surface under aggressive polarization.

Under the surface, changes to microstructures in both the grains and grain boundaries of the magnetic Co layer became noticeable, while minor variation was seen in the Cr underlayer. Lattice fringes from Co grains became clear, and grain boundaries were less distinguishable from the grains to which they were adjacent. Continuing to polarize specimens not only caused serious degradation of grain and grain boundary structure but also increased surface roughness, as shown in Figure 6.5(c). These changes indicated that the microstructure of the magnetic thin films experienced significant deterioration as a result of the corrosion polarization conditions that took place in a short period of time. Of note is the fact that the nodules produced in the Cr underlayer could be the result of the oxidation of Cr, which indicated that the corrosion process had penetrated to the lower layers. Such quick, diffusive penetration suggested that grain boundaries and thin film interfaces possessed a crucial ability to conduct anodic ions during the oxidation reaction. When corrosion caused a high level of structural damage, shown in Figure 6.5(d), all layers of the thin film stack became indistinguishable, due to the inter-diffusion of metallic ions and anodic corrosion reactions. Average grain size, as a function of corrosion time for the Co magnetic thin film and Cr underlayer, was measured using the TEM bright field images in Figures 6.5(a)-(d) and is summarized in Figure 6.6.

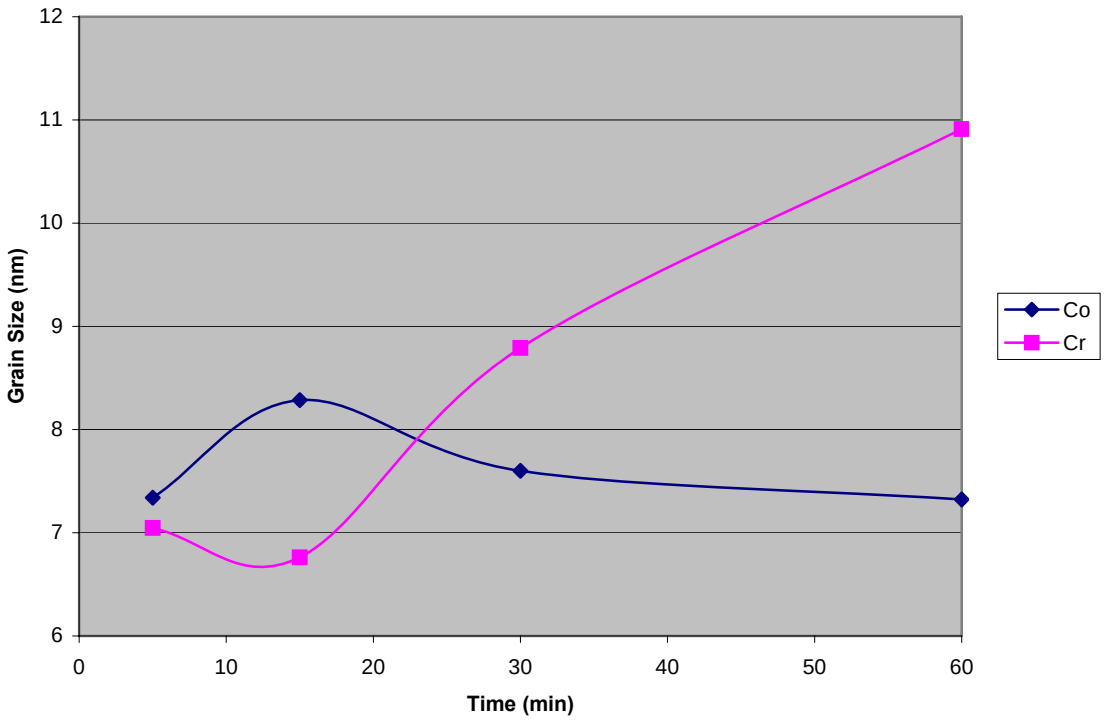

Figure 6.6. Average grain size in thin films of both Co alloy and Cr alloy, shown in the TEM bright field images, as a function of corrosion time under polarization

Because geometric changes in grains were the results of anodic reactions involving metallic thin films during the course of corrosion, knowing the kinetics of such changes provided important insight into the relationship between elemental migration rate and direction, compound formation, and microstructural changes. Interestingly, both magnetic and underlayer grains showed non-linear variations during the corrosion process. Co grains reached a maximum size during the first 15 minutes of biased corrosion, followed by a rapid decrease and then slow decrease over time during which grains return to their original sizes. Conversely, Cr grains shrank before a dramatic expansion occurred. With reference to EC-ICP-MS quantification results, in order to explain the phenomenon of grain size changes in both magnetic thin film layer and underlayer, attentions were focused to changes of grain boundary structures. During the corrosion process, inter-diffusion rates of elements were different. Co had a rapid diffusion rate away from grain boundaries. The flux of Co from the grain boundaries yielded structural vacancies, which could cause Co or Pt to move from inside the grains to segregate at the grain boundaries,

which resulted in swollen grains in bright field TEM images. Meanwhile, the shrinkage of Cr grains in the underlayer could be explained by the redistribution of Mo inside the CrMo structures, which corresponded to the low Mo content detected in EC-ICP-MS experiments under such potential conditions.

As corrosion time increases, the segregation rates of Co and Pt elements from the grain boundaries decreased, and "swollen" grains then subside. In the same time frame, most anodic reactions were associated with the oxidization of Cr, which created passivity around the Cr grains. Another reason for the dramatic size expansion of Cr grains was possibly due to the excessive amount of Ni diffusion from the substrate, which could form a reaction layer along the grain boundaries of the underlayer and caused the grain sizes to appear to be enlarged.

6.3.2. Grain and Grain Boundary Structural Analysis

Under high magnification, grain orientations in different thin film layers could clearly be seen in TEM images. Grain boundaries were then located based upon changes in the grain structures. Interfaces between thin film layers could be also viewed under high magnification of the TEM micrographs. In Figures 6.7(a)-(d), the high magnification images of the above samples were shown at 1.25 MX.

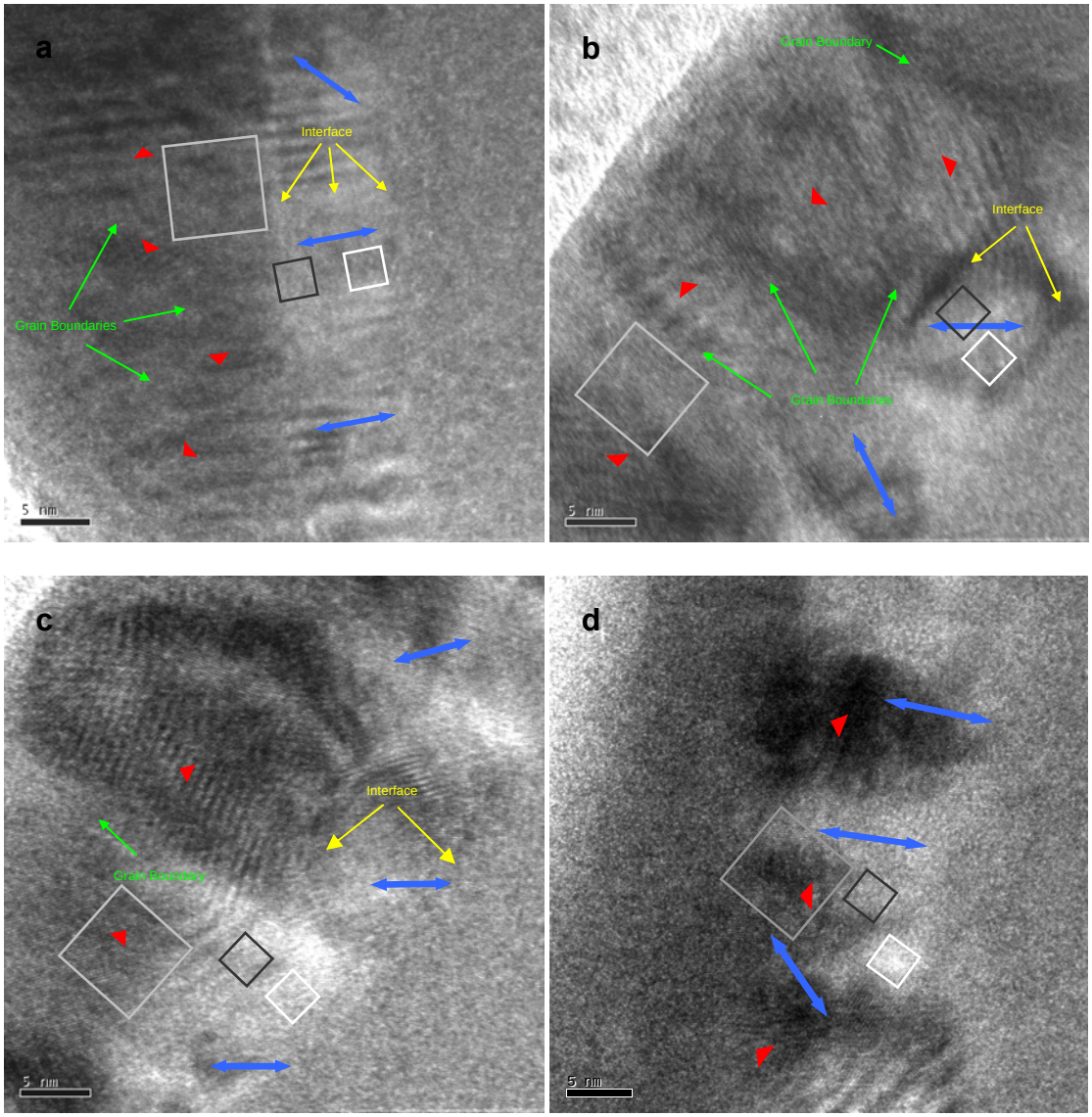

Figure 6.7. TEM cross sectional micrograph of samples with 750 mV polarization potential in 2% HNO_3 solution for (a) 5 min, (b) 15 min, (c) 30 min, and (d) 60 min

In the TEM micrographs shown above, the red triangle arrows represent *c*-axies of Co hexagonal grain orientation, while blue arrows indicate the grain orientation of *bcc* Cr structures. Green arrows point to grain boundaries in the Co layer, and yellow arrows indicate interfaces between the Co and CrMo layers as well as the CrMo and Cr layers. The identifications of lattice orientations of crystallographic structures are based upon measurements that were compared to published data.[6.31][6.34] Squares in grey color are

the areas that electron diffraction patterns are taken in Co layer while squares in black and white are for same applications in the CrMo and Cr underlayers, respectively.

Clearly, for a short time under potential polarization, as shown in Figure 6.7(a), the microstructures of the magnetic thin films maintained a high degree of integrity in the layer boundaries between the Co magnetic layer, Cr underlayer, and Ni/P base layer. The orientations of Co grains were shown to be mostly perpendicular to surface, which indicated the in-plane orientation of the magnetic layer. As expected, the grain had columnar shapes in both the Co and Cr layers. The grain boundaries between the two differently oriented grains were closely aligned from the surface layer to the underlayer. The parallel interfaces between layers tightly bond without delamination.

When the corrosion process continues up to about 15 minutes, as shown in Figure 6.7(b), the microstructures within the layers showed deterioration but maintain the general microstructure of the layer. However, large structural disengagement at the grain boundaries and interfaces indicated that corrosion attacks strongly permeate from the surface of the thin film structures along these paths possibly due to the low energy barrier. According to quantification measurements, depletion of Co during the early stages of corrosion, up to 15 minutes at 750 mV polarizations outpaced other elements, which proved here that this amount of Co could exist well away from the grain boundaries and interfaces.

Severe structural degeneration in CoCrPtB grains became more visible, which could be seen in Figure 6.7(c). The enlargement of lattice structures in the grains indicated fundamental crystallographic changes occur as a result of corrosion progression. Supported by the EC-ICP-MS measurement results, the large amount of ionic release out of the magnetic thin film structures under a longer-lasting corrosion environment mainly consisted of Cr and Pt; this release could leave larger lattice spaces in Co crystallographic structure. The similar increase in lattice spacing of the CrMo underlayer was seen, which could be caused by the presence of Cr, identified in quantification measurements.

Closely examined, grain boundaries had fewer crystallographic features, as can be seen in Figure 6.7(c), and the presence of residues of amorphous structural materials were presumed. One of the main sources of amorphous phase materials is from substrate of

Ni/P. Migration of Ni/P from the substrate up to the surface via the deconstructed grain boundaries and thin film interfaces could be assumed because an extremely large amount of Ni had been measured in the channels, as was presented in previous chapters.

An extended corrosion process severely damaged the structural integrity of film, as all thin film layers showed no distinguishable characteristics, as shown in Figure 6.7(d). Though the Co layer and Cr layer still maintain certain grain structural characteristics, the interfaces were much less clear, especially at grain boundary locations. Miscibility of thin film structures was probably caused by the inter-diffusion process of metallic ions in each thin film layer under strong corrosion influences. The penetrations of anodic ions produced oxidized products along the easiest path at grain boundaries, which could be revealed using electron diffraction techniques.

6.3.3. Electron Diffraction FFT Patterns on Grains and Grain Boundaries

Electron diffraction patterns of Fast Fourier Transform (FFT) were created as a result of the interference between the transmitted and diffracted electron beams in high-resolution images and had been applied in some studies with TEM analysis.[6.28],[6.37] Applications of FFT in electron diffraction patterns, abbreviated as FFT patterns thereafter, in this framework included detecting and characterizing structural degradation and changes to the samples during the corrosion process. The FFT patterns were acquired using DigitalMicrograh ™ version 3.9.2 software from Gatan Inc., Pleasanton CA. Figures 6.8(a)-(d) show FFT patterns on Co grains from the surface of the areas marked in grey squares in Figure 6.7(a)-(d), respectively.

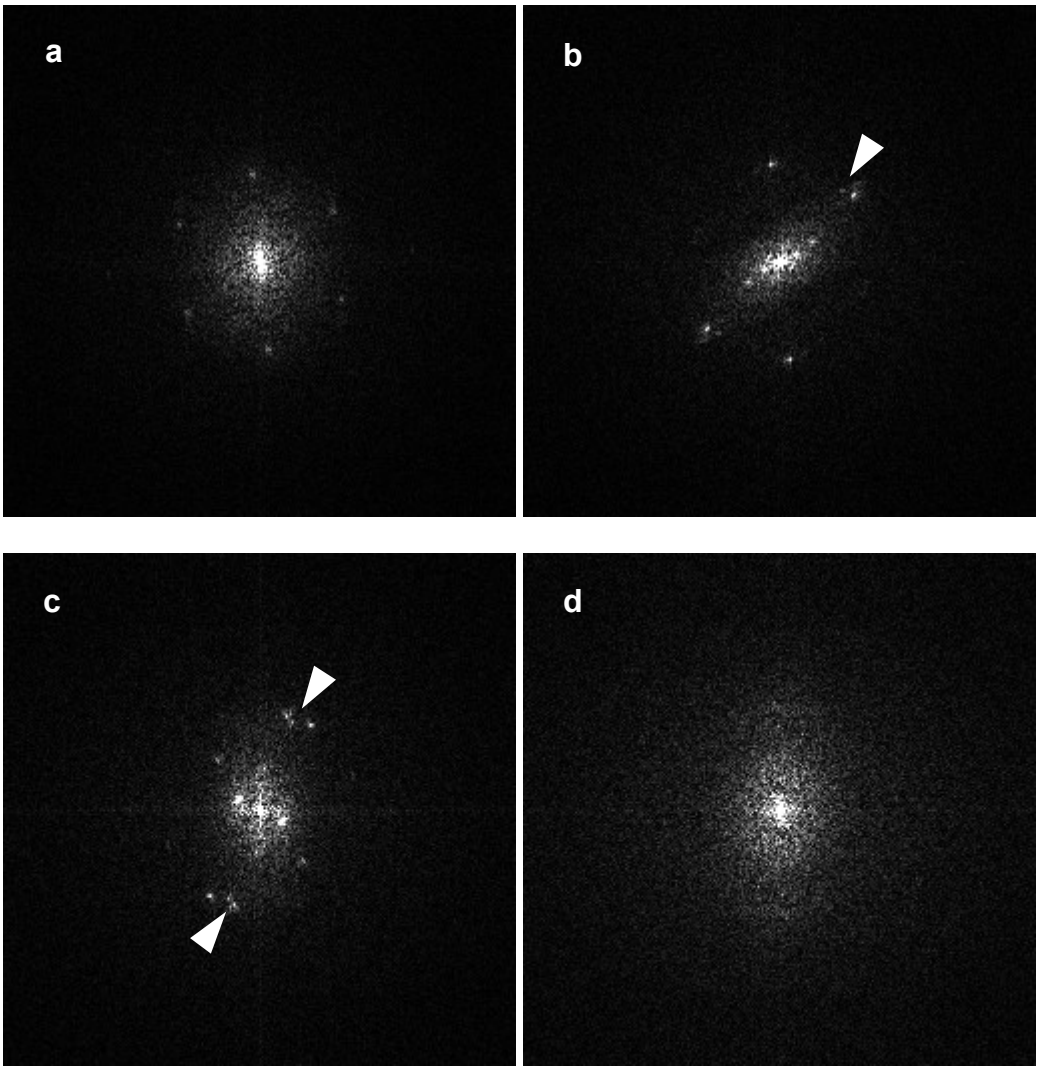

Figure 6.8. Electron diffraction FFT patterns on CoCrPtB grains from samples with 750 mV bias in 2% HNO_3 solution for (a) 5 min, (b) 15 min, (c) 30 min, and (d) 60 min

Within the grain structures, structural degradation of Co thin films showed only minor changes up to 15 minutes of corrosion, at which point the Co depletion reached a minimum as determined by electron microanalysis. A hexagonal diffraction pattern could be clearly seen in this FFT image, as shown in Figure 6.8(a). The structural changes of Co grains were noticed after 30 minutes of corrosion, when hexagonal formation disappeared gradually. Complete transformation of the hexagonal Co structure into a non-crystalline structure could be seen in the last picture of Figure 6.8(d). In between these two stages of early and late corrosion processes, extra diffraction spots, marked in white

arrows, were incorporated into the Co lattice structure, which could be from the diffraction of cobalt oxides.

Similarly, FFT patterns of the CrMo and Cr underlayer from the areas indicated in Figure 6.7are shown in Figure 6.9 in the top and bottom rows, respectively.

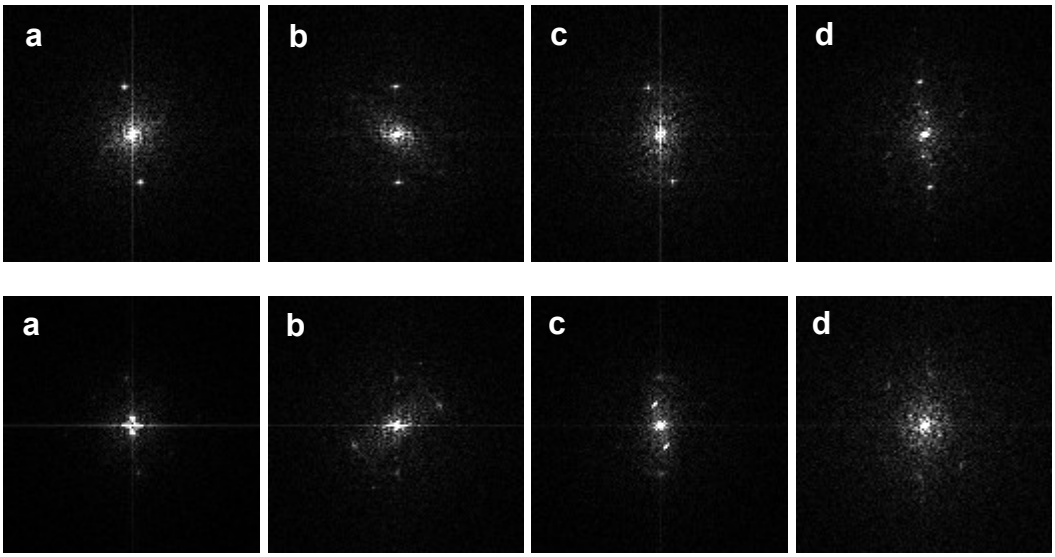

Figure 6.9. FFT patterns of the underlayer of CrMo (upper row) and Cr (below row) from samples with 750 mV bias in 2% HNO_3 solution for (a) 5 min, (b) 15 min, (c) 30 min, and (d) 60 min

The transformation of crystallographic structures of the underlayer demonstrated in the FFT pattern tells an interesting story that the degradation of CrMo was not as severe as it was to the Cr layer underneath during the course of corrosion. Since both CrMo and Cr lattice structures resembled cubic structures, changes to the symmetric FFT patterns of CrMo only occurred during the last stage, while structural dissociation of Cr began at a much earlier time, which corresponded to quantitative measurements of Cr content. In a further study of some samples, the lattice space of CrMo remained fairly constant at 2.02 ~ 2.08 Å, but Cr crystallinity changed from 2.05 ~ 2.85 Å. Furthermore, FFT images of crystallographic lattice variations have been produced for adjacent grains, an example of which is demonstrated in Figure 6.10. In the Co layer, both *hcp* and *bcc* lattice structures were identified with a spatial distance of 4.82 Å and 2.48 Å, respectively. In the Cr underlayer, a grain with an amorphous phase (identified in blue) between crystalline grains was identified based upon FFT patterns, which suggested the above presumption

was reasonable. An *hcp* crystal structure in a Cr grain was also detected in this sample, which suggested lattice site by O or Ni occupation might occur from either implementation of oxygen or out-diffusion of Ni from the substrate.

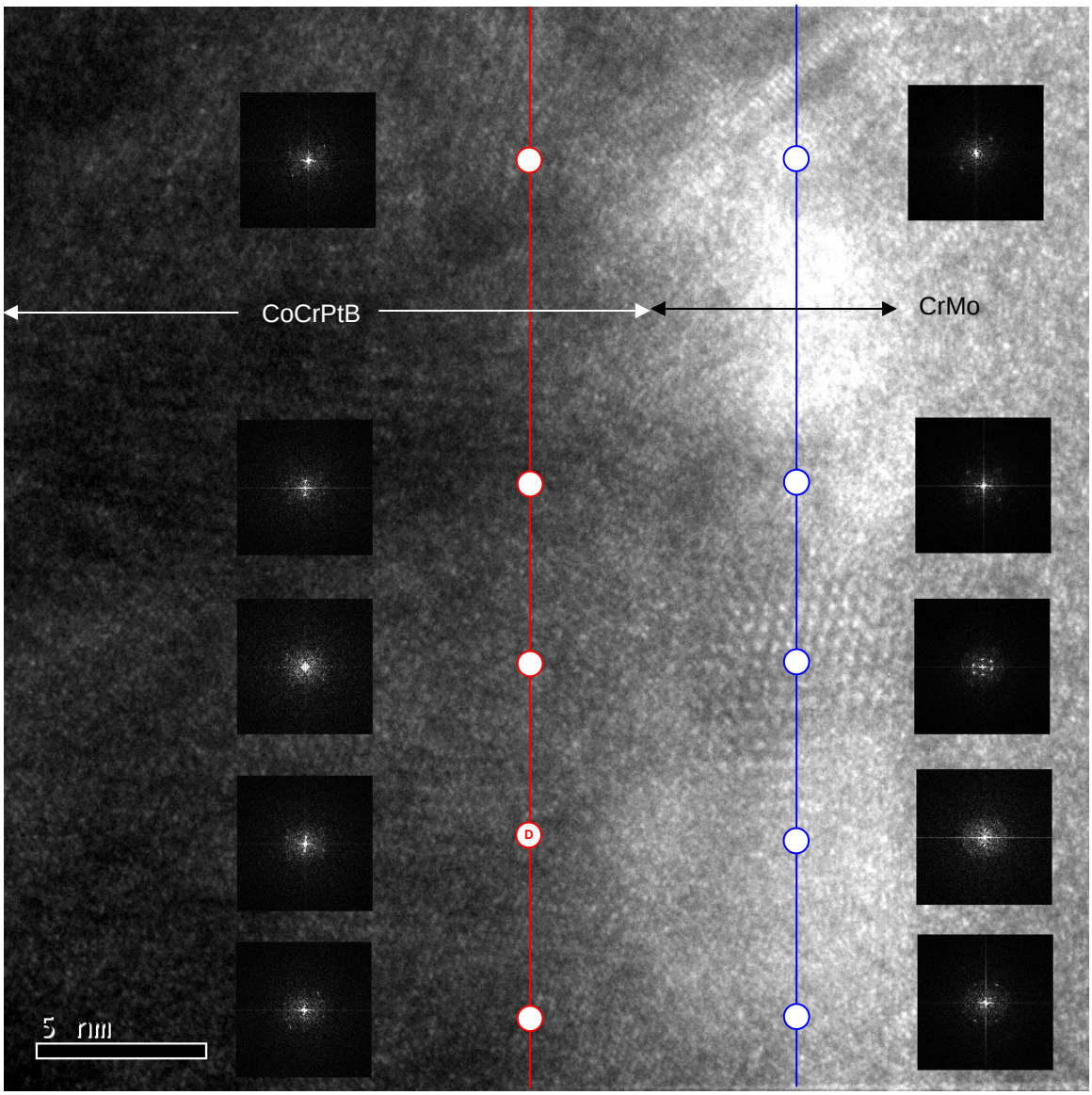

Figure 6.10. Comparison of FFT patterns on adjacent grains in both Co and CrMo layers in a corroded sample

Evidence of Ni diffusion through the grain boundary region was obtained through TEM images and FFT analysis, as shown in Figure 6.11.

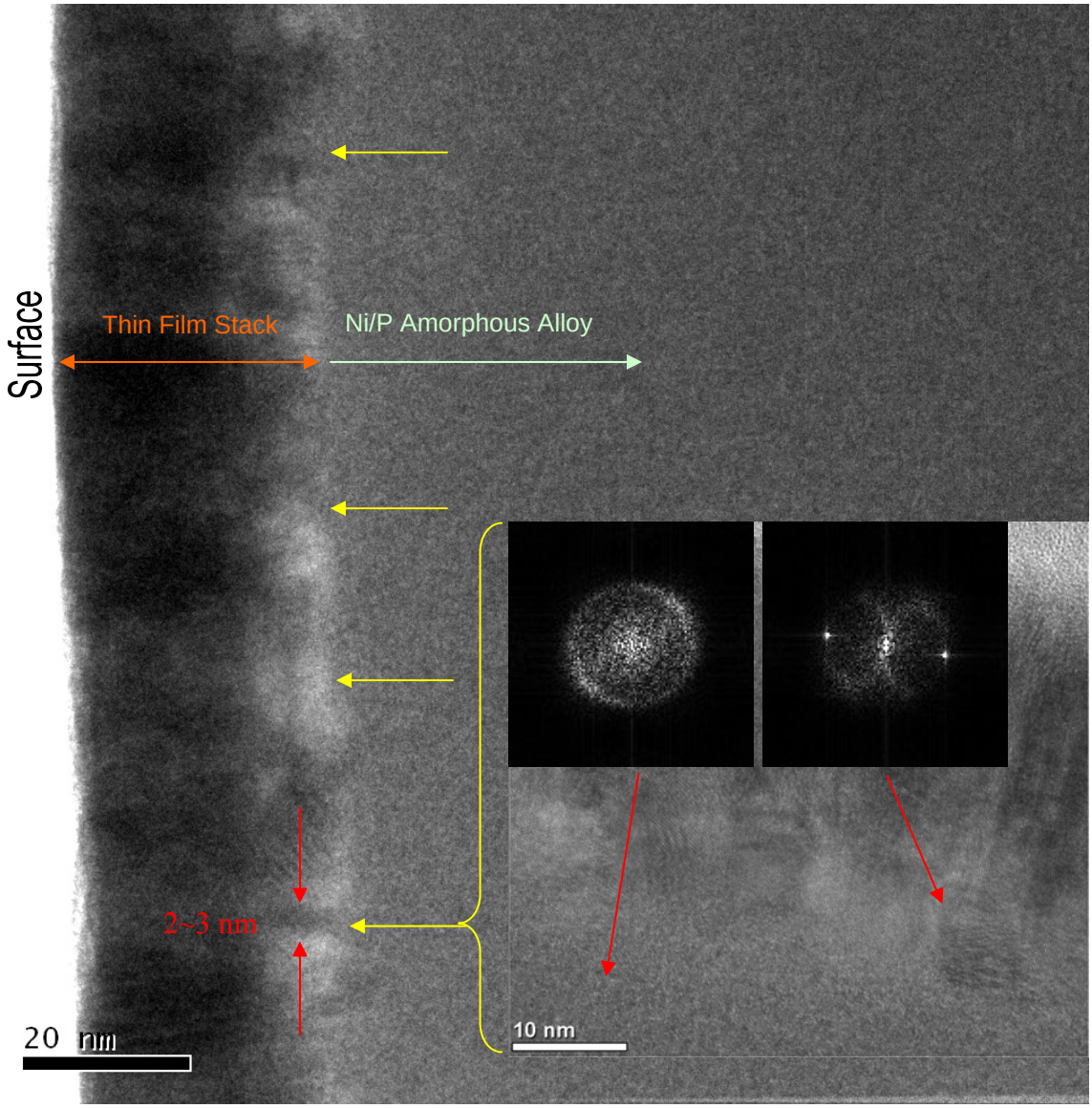

Figure 6.11. Ni diffusion through a grain boundary at a possible texture region with crystalline phase identified by FFT patterns

TEM analysis of one of the corroded samples revealed Ni penetration path through the underlayer grain boundaries. The lateral measurement showed that the reaction layer at the grain boundary was between 2 and 3 nm, which was normally around 1 nm in many similarly reported results.[6.42] Using an High Resolution Transmission Electron Microscopy (HRTEM) image as shown in inserted illustrations in Figure 6.11, a cluster of crystallized Ni was seen by comparison of the FFT patterns with amorphous FFT pattern in a normal Ni/P area. This finding greatly supports the theory that formation of

Ni oxidation was mainly through anodic penetration via the grain boundary and interface regions. The crystallinity of Ni was mostly because of electrochemical transformation by dissociation with phosphorus from an amorphous phase into crystal oxides or a hydroxide compound. Also, from the cross section image, a driving force promoting Ni penetration might be in surface imperfection characteristics, such as texture or micro-waviness, which have been understood to pose low energy barriers to anodic reactions.[6.43]

6.3.4. Textural Structure Influence on Corrosion

Texturing the magnetic thin film surface is designed to enhance magnetic performance and thermal stability.[6.44] Over the years of corrosion studies, the phenomenon of aligning corrosion spots with surface textures has long been recognized to be important, especially at locations with relatively deep grooves, but no explanation for the use of this phenomenon in publications could be found. The mystery of such preference is highly related to thin film microstructural features at uneven surfaces, which provide orientation selections.

Crystallographically, the epitaxial grain growth of CoCrPtB thin film on top of the CrMo layer creates different orientations due to microscopic surface stress and tension, which yields different lattice preferences, as shown in Figure 6.12. [6.45]

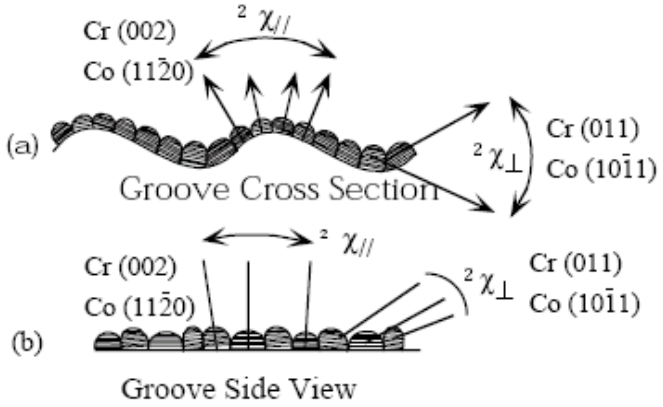

Figure 6.12. A model for the effect of texture lines in magnetic media (Graph reproduced with permission)

At the bottoms of cross sectional grooves, Co prefers to grow in $(10\bar{1}1)$ orientation, but because of lattice mismatch, Cr orientation is mostly (011). On the other hand, at the top

of grooves, Co($11\bar{2}0$) is mostly identified to exist on top of Cr(002) lattice structures. Different grain growth orientations produce different grain size and grain boundary density. Structurally, sparse density at low groove regions with less defensive ability to corrosion is demonstrated in surface topographic measurements of corrosion samples using AFM, shown in the following images.

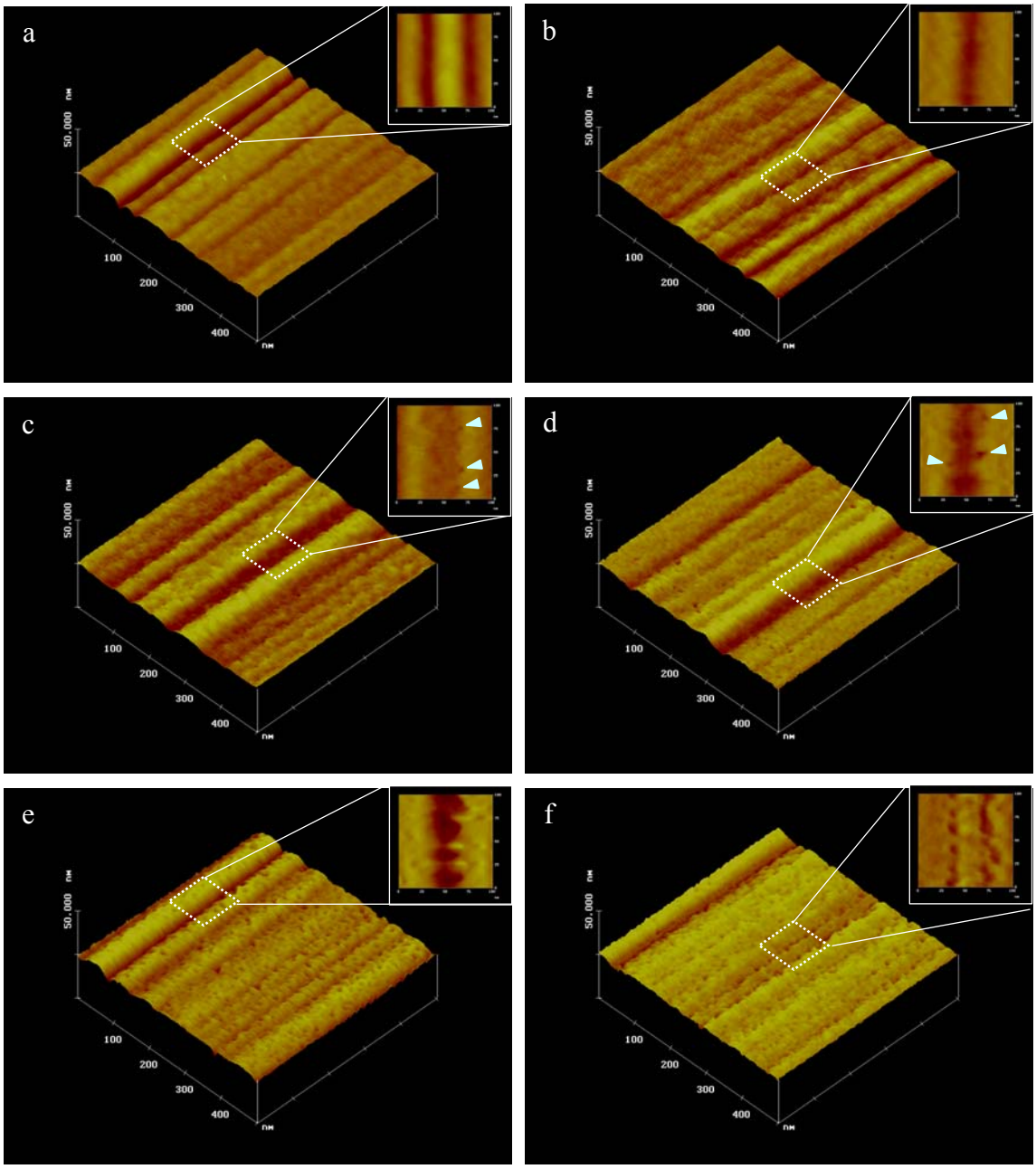

Figure 6.13. A series of micrographs of AFM measurements at texture grooves for (a) an as-received sample, the surface of which underwent potentiodynamic corrosion tests in 2% HNO_3 solutions at (b) 50 mV, (c) 150 mV, (d) 300 mV, (e) 600 mV, and (f) 1000 mV

As can be seen in the images above, the most distinguishable changes to the texture grooves were that the edges go from being clean-cut to rough and that the groove width was gradually enlarged. Formation of irregularities at locations between hills and valleys of texture lines, arrows mark them in some of images, provided support for the strong linkage between microstructural features and corrosion progression. Corrosion was neither at the top nor the bottom of grooves; that the corrosion process was noticeable only at the slope of rocking hills indicated that the grain boundaries at the transition zone between grains of Co($10\bar{1}1$)/Cr(011) and Co($11\bar{2}0$)/Cr(002) played a critical role not only because of grain size distribution but also the existence of stacking fault.[6.46] The explanation for such microstructural deviations could be expanded into understanding many other experimental results, such as the off-centered corrosion spots obtained using AFM measurements presented in Chapter 3.

6.3.5. Electron Nano-probe Profiles

Spatial profiles of elemental distribution by using an electron nano-probe with X-ray Energy Dispersive Spectrometry (EDS) in the thin film structures have been demonstrated to be an effective method for relative comparisons of elemental quantities. The profile results were based upon central X-ray emission energies of either Kα or Lα lines with a 0.1 KeV window and are presented in the following table.

Table 6.1. Selected X-ray emission energies of elements of interest

Element	X-ray Emission Kα (KeV)	X-ray Emission Lα(KeV)
Co	6.93032	
Cr	5.41472	
Pt		9.4423
B	0.1833	
Mo		2.29316
Ni	7.47815	
P	2.0137	
N	0.3924	
O	0.4749	

Figures 6.14 and 6.15 show profile paths along grains and grain boundaries in STEM mode, and the results for the samples are shown in Figures 6.6(a)-(c), respectively.

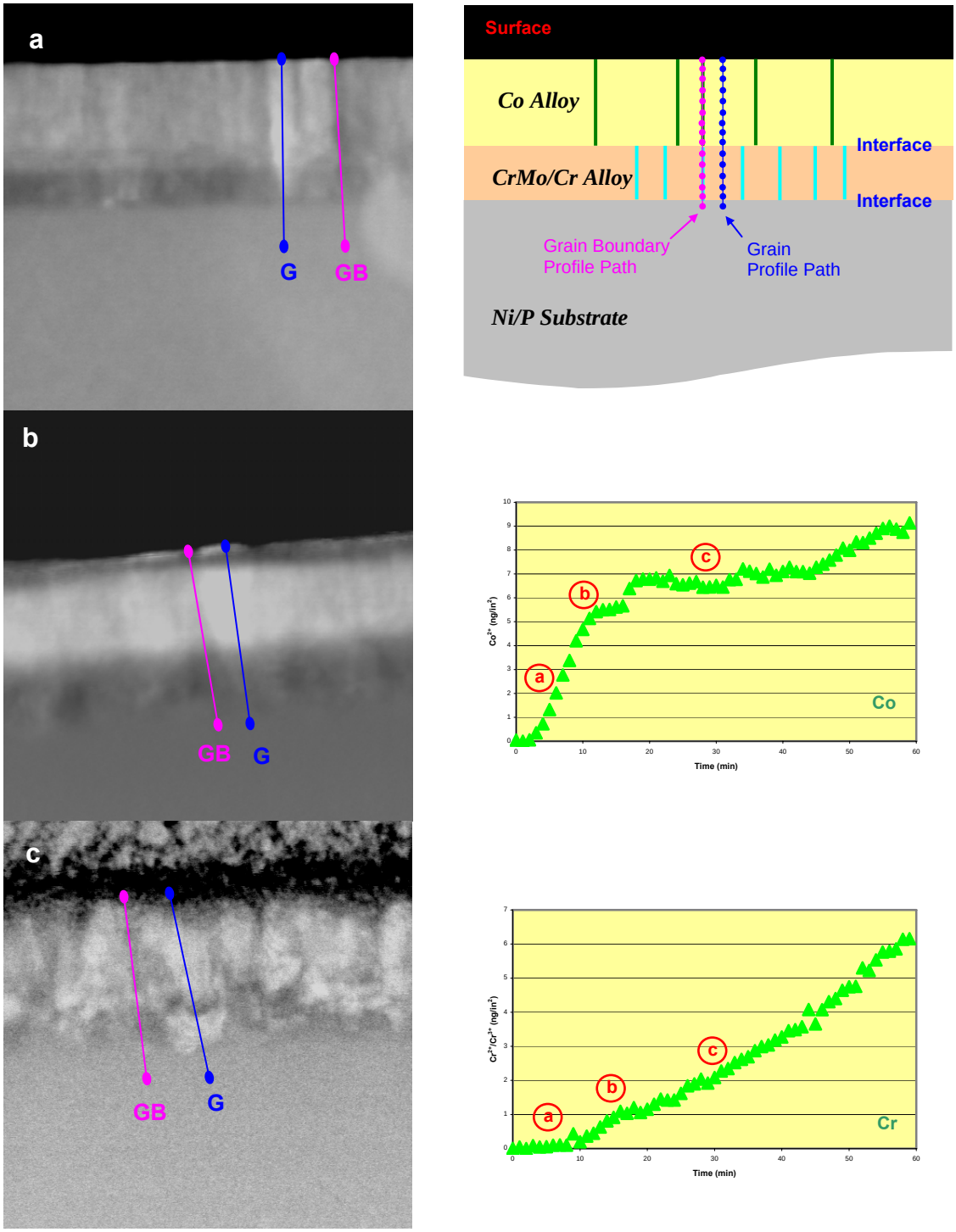

Figure 6.14. Electron nano-probe profile paths in STEM mode along (a) grains (blue) and (b) grain boundaries (pink) for the sample shown in Figures 6.5(a)-(c)

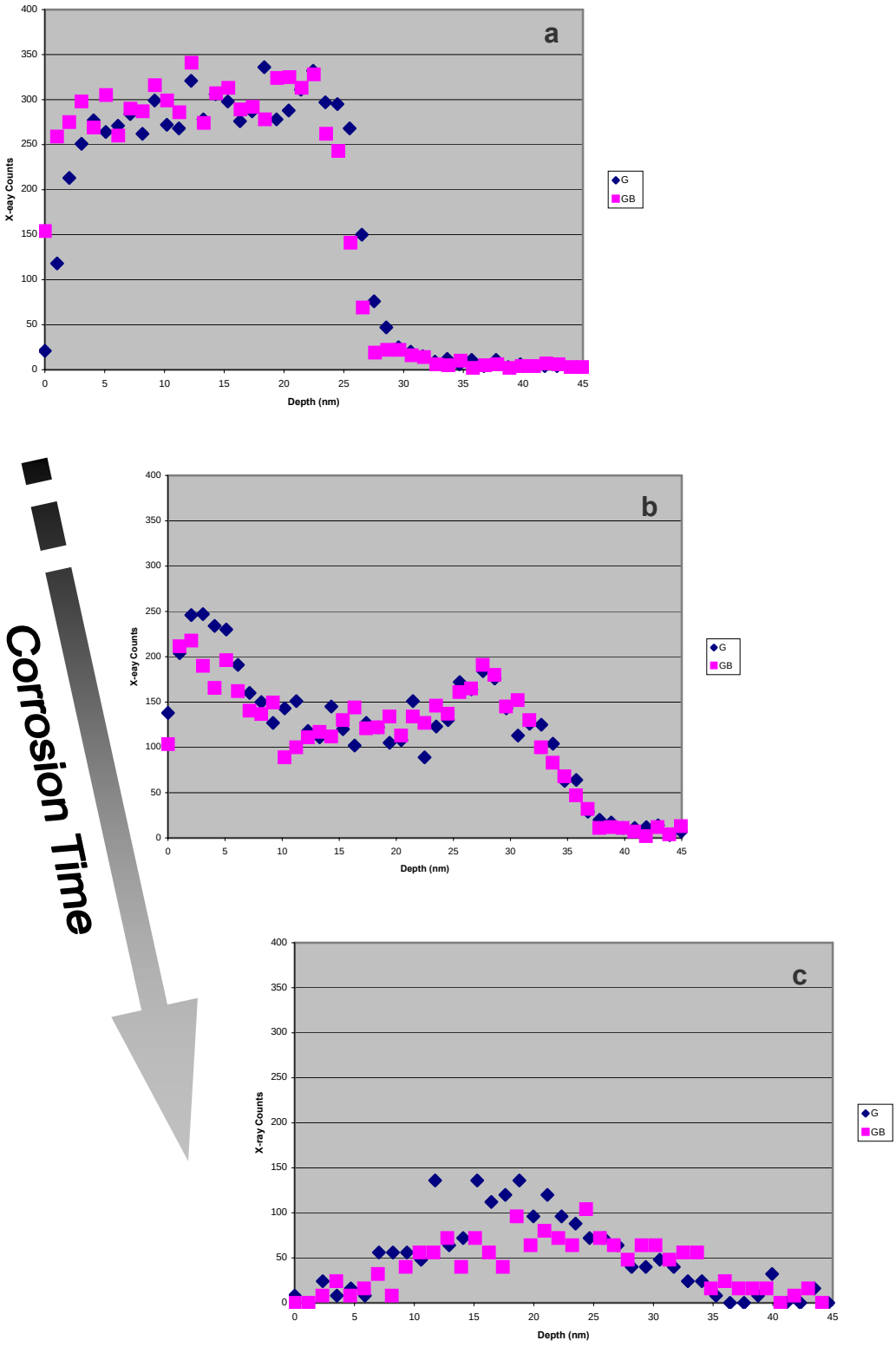

Figure 6.15(a). Comparison of X-ray emission profiles of Co along a grain and a grain boundary for regions a, b, and c in the electrolyte shown in Figure 6.14

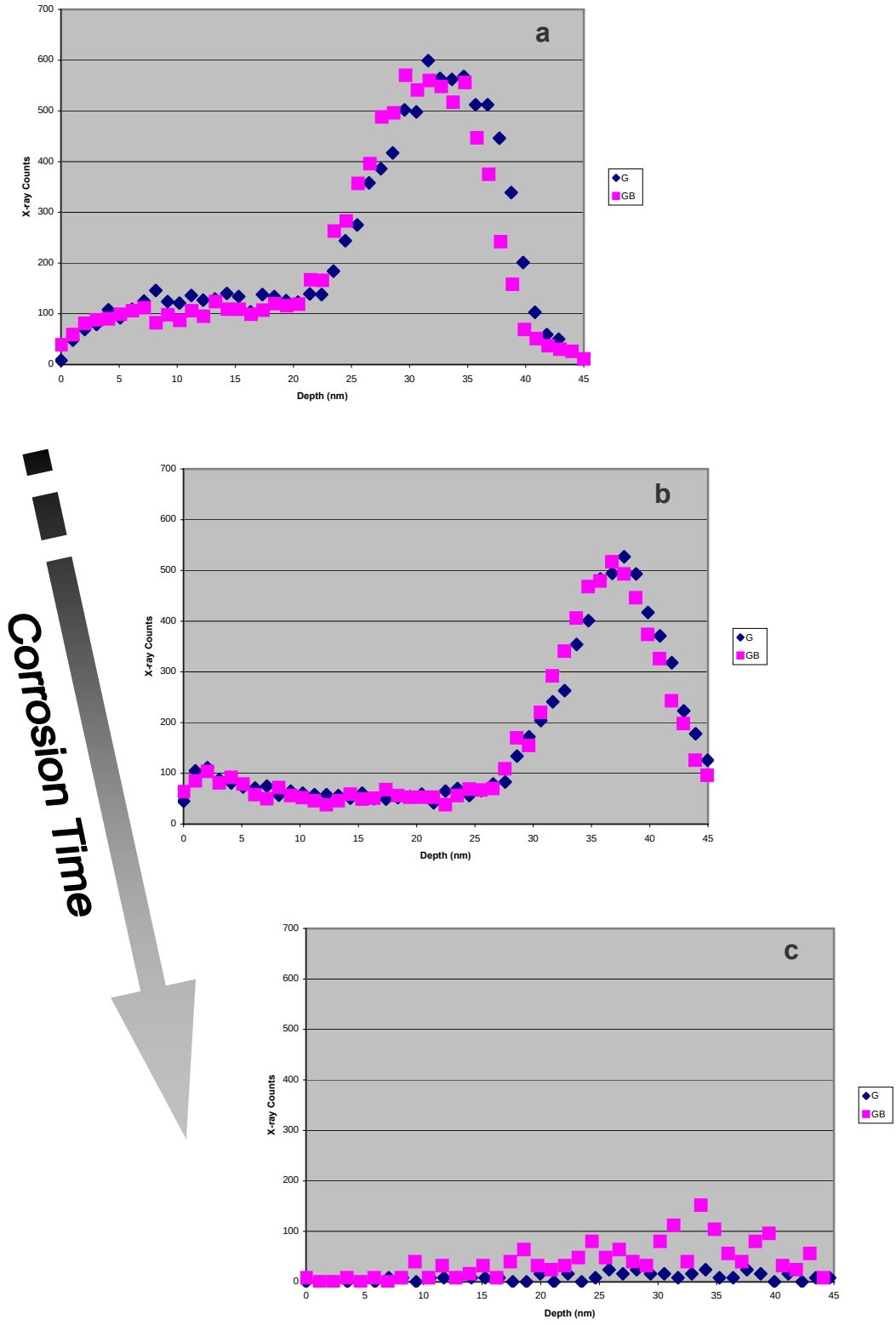

Figure 6.15(b). Comparison of X-ray emission profiles of Cr along a grain and a grain boundary for regions a, b, and c in the electrolyte shown in Figure 6.14

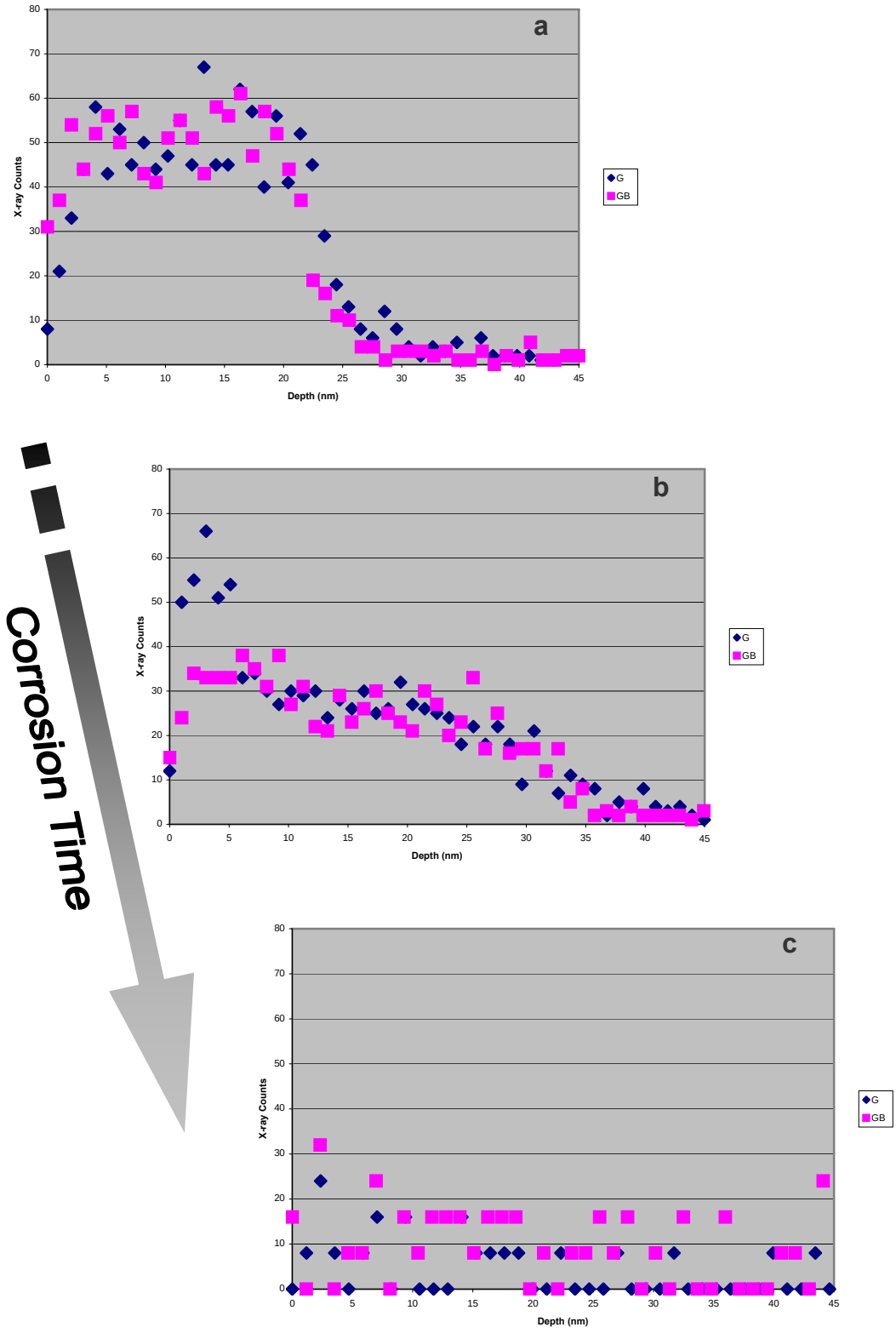

Figure 6.15(c). Comparison of X-ray emission profiles of Pt along a grain and a grain boundary for regions a, b, and c in the electrolyte shown in Figure 6.14

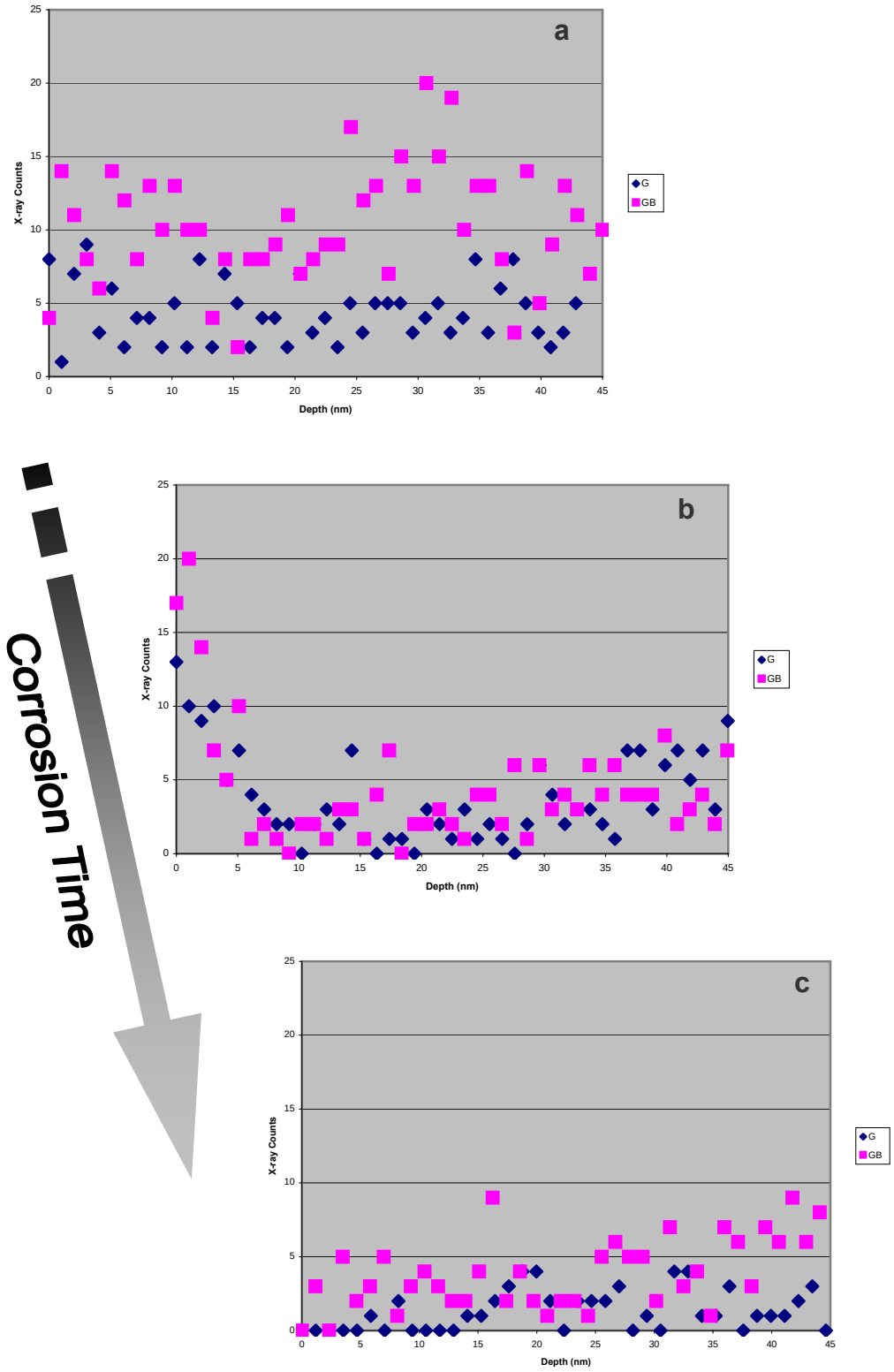

Figure 6.15(d). Comparison of X-ray emission profiles of B along a grain and a grain boundary for regions a, b, and c in the electrolyte shown in Figure 6.14

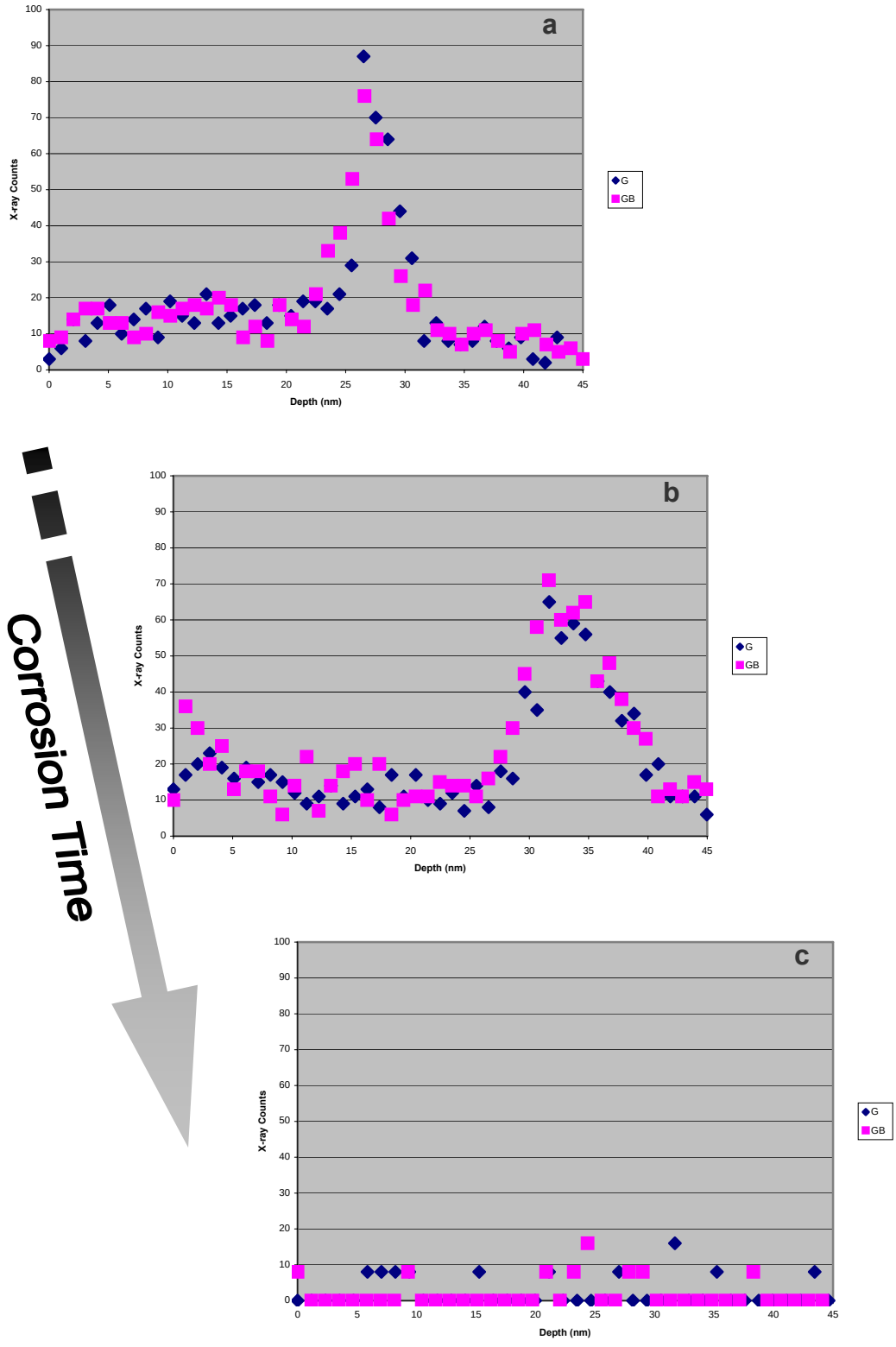

Figure 6.15(e). Comparison of X-ray emission profiles of Mo along a grain and a grain boundary for regions a, b, and c in the electrolyte shown in Figure 6.14

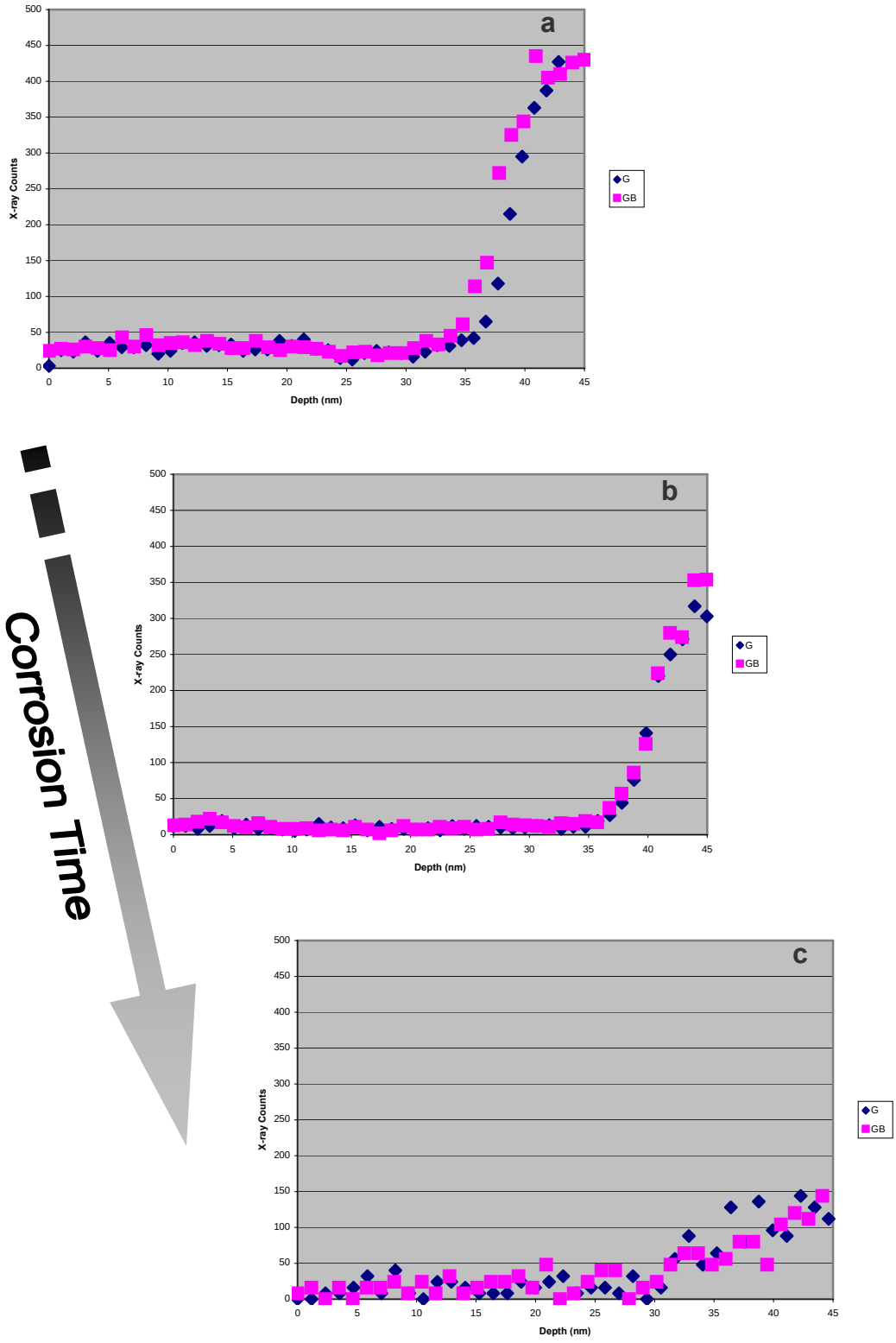

Figure 6.15(f). Comparison of X-ray emission profiles of Ni along a grain and a grain boundary for regions a, b, and c in the electrolyte shown in Figure 6.14

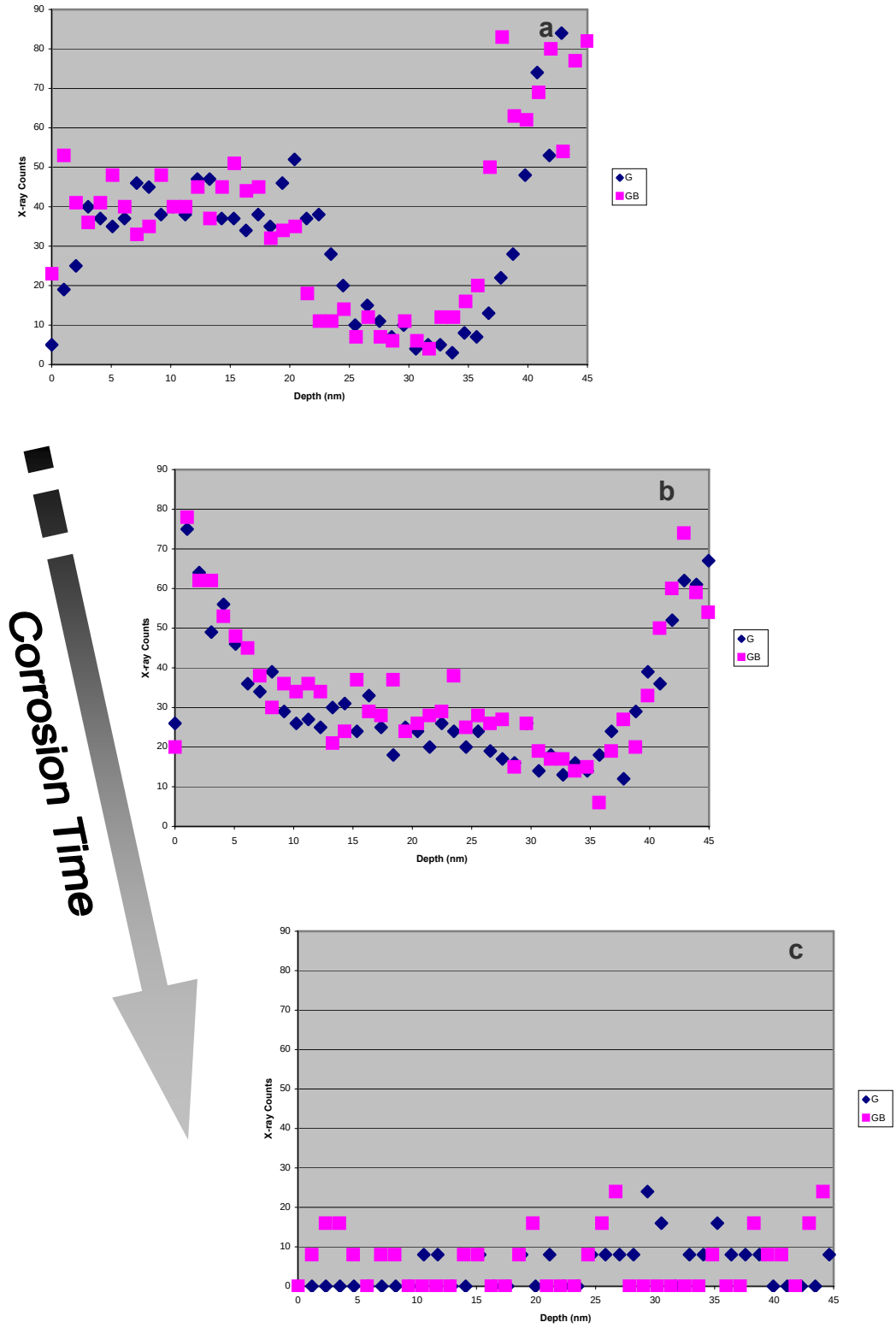

Figure 6.15(g). Comparison of X-ray emission profiles of P along a grain and a grain boundary for regions a, b, and c in the electrolyte shown in Figure 6.14

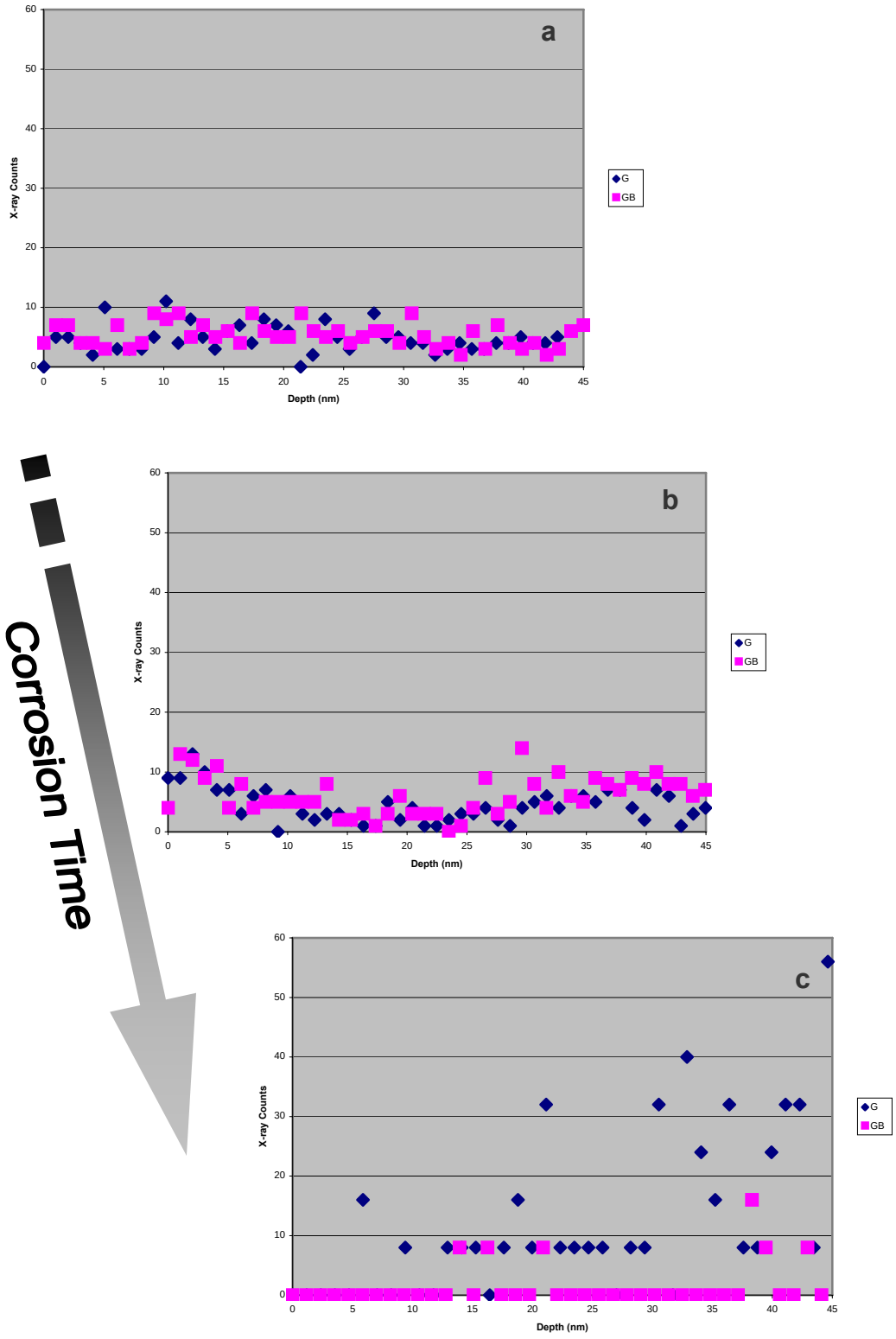

Figure 6.15(h). Comparison of X-ray emission profiles of N along a grain and a grain boundary for regions a, b, and c in the electrolyte shown in Figure 6.14

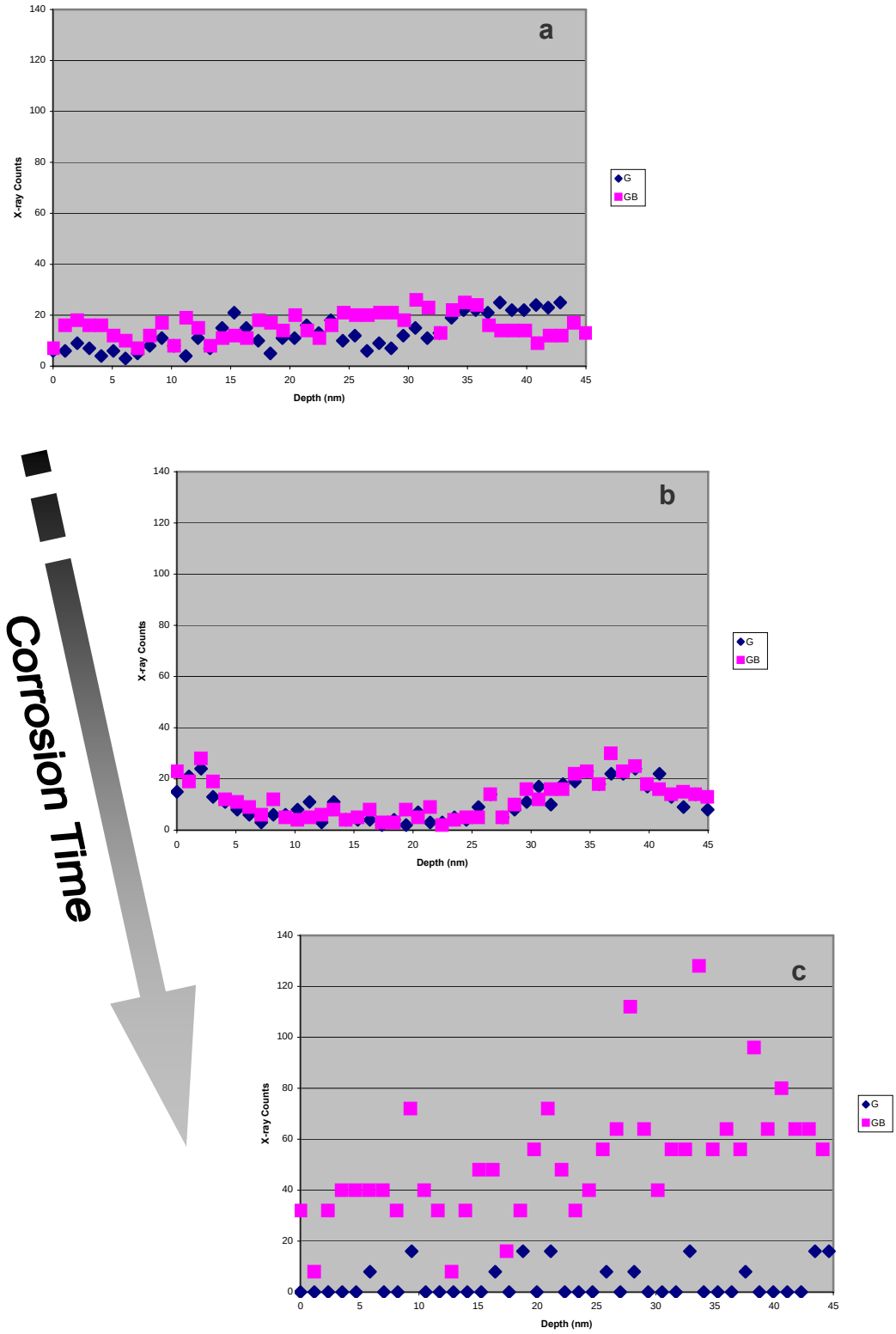

Figure 6.15(i). Comparison of X-ray emission profiles of O along a grain and a grain boundary for regions a, b, and c in the electrolyte shown in Figure 6.14

Commonly, X-ray emission intensity was dependent on sample thickness and structural orientation. In this experiment, since all TEM samples were prepared under the same conditions and final thinning was achieved using FIB, the thickness and sample surface conditions were fairly comparable. The quantitative X-ray counts recorded in the STEM mode could then be used for comparison studies.

Using CoCrPtB thin film about 30 nm in thickness, Co distribution in the samples with a short corrosion reaction time had no significant variation with regard to concentration profile, shown in Figure 6.15(a). As corrosion progresses, Co was depleted at and near grain boundaries. The lower concentration of Co at grain boundaries provided evidence that depletion of Co in the early stage of corrosion begins at and near grain boundaries, as shown in polarization experiments described in the previous chapter. The total Co content in the magnetic layer decreased as corrosion extends into the underlayer structures.

Cr is the element contained in all layers of the thin film structure but at varying concentrations, as shown in Figure 6.15(b). Initial loss of Cr could be identified from the magnetic thin film layer and then Cr gradually decreased with depth into underlayer. No significant changes could be measured between the grain center and grain boundary, which indicated that Cr loss due to corrosion from the thin film structure had no microstructural segregation. Therefore, Cr loss from the structure of the entire thin film stack was accounted for in corrosion electrolytes.

The loss of Pt from the thin film stack was primarily from the grain boundary, as indicated by the X-ray emission profile, shown in Figure 6.15(c). Since Pt was fairly immune to corrosion because of its high EMF potential, the depletion of Pt was presumed to be a consequence of structural degradation and degeneration as part of the depletion of Co from the microstructures. In comparison with what had been shown in ICP-MS quantification charts for Pt, the linearity of Pt electrochemical release behavior into electrolytes under most conditions was attributed to the constant migration of Pt from the decomposition of CoCrPtB structure in grain boundaries.

In different types of electrolytes, boron behaved differently depending upon the concentration of corrosion solutions and potential bias applied because of its electro-negativity variations. In these samples, the X-ray emission profile showed that B

segregates at and near grain boundaries and at the film surface. Aggregations of B atoms at grain boundaries seemed to constantly have higher concentrations than those within grains.

As part of the constituents in an underlayer, Mo, similar to Cr, maintained high structural integrity during the early stages of corrosion, as seen in Figure 6.15(e). However, unlike Cr behavior during later stages, drastic decreases in Mo concentration from the structure suggested high mobility and electro-affinity of Mo toward anodic reactions. The fact that Mo disappeared from the underlayer structure mirrors the experimental results from ICP-MS measurements in which Mo was completely depleted by anodic reactions in the electrolytes.

High concentrations of Ni were detected by the X-ray emission profile in large amounts, as shown in Figure 6.15(f), in the reservoir of the Ni/P substrate layer. The distribution of Ni along grains and grain boundaries was indistinguishable initially. However, a slight increase in Ni content at grain boundaries was observed when a logarithmic scale was used. In the later phase of corrosion, not only was the quantity of Ni reduced at the interface of Ni/P with the underlayer, but also the relatively high concentration of Ni both in the grains and at the grain boundary regions increases, which indicated that migration of Ni toward the surface was perpetuated. The extremely high concentrations of Ni ions measured in EC-ICP-MS experiments provided evidence to support the idea of Ni penetration.

The X-ray emission measurements of P in this study might partially interfere with Pt, since the Kα line of P was partially overlaps with the Pt Mα line. But the general trend of loss of P loss was expected. Meanwhile, N was redistributed into the thin film structure mostly through the grain structure due to ionic size.

6.4. Summary

TEM microstructural analysis is a powerful tool used to reveal structural characteristics and properties. It is important that microanalysis of the structures on the atomic and nanometer scales, revealed by high-resolution imaging, is performed to determine elemental distribution and crystal structures. In this research, TEM has been utilized

mainly to do analysis on images of nano-scale structures and electron microanalysis on FIB-produced TEM cross-sections of the thin film stack. The TEM cross-sectional study of the microstructures is important because corrosion on an epitaxial thin film stack is not a two-dimensional, but rather a three-dimensional event.

From images of cross-sectional structures, the grain growth in the multilayer thin films was oriented epitaxially, and interfaces between layers were well defined. Surface conditions were mostly flat, but, as corrosion occurs, surface topographic changes, especially inward depressions at certain locations, were seen. These changes confirmed findings from AFM topographic profiles of some of the small corrosion pits, which were reported in section 3 of Chapter 4. Changes in grain sizes in both the magnetic layer and underlayer were correlated with elemental quantification variations.

Based upon high magnification TEM images, the deterioration of grain boundaries under the influence of corrosion provided the primary diffusion channels where oxidation and reduction reactions occurred, which degraded grains within layers and interfaces between thin film layers. The degradation of grain boundaries was responsible for most metallic ionic depletion during corrosion, which accelerates corrosion rate. By analyzing elemental concentrations using electron microanalysis profiles in both grains and grain boundaries, most constituents of thin film compounds migrated through the grain boundaries, but some of them prefer to interact within grain structures. These elemental nano-probe profiles correlated with the results from EC-ICP-MS measurements, which provided a better understanding of thin film corrosion mechanisms.

Meanwhile crystal structure changes in grains in both the magnetic Co layer and Cr underlayer were analyzed in this study with the assistance of FFT patterns. As grain boundaries were of main concern in the early corrosion stage, integrity of Co grains was highly preserved, while structural defects formed prematurely due to the high mobility of either Mo or Ni penetration from the base layer as well as interfacial segregation.

In associating corrosion events with microstructural deviations, a meaningful explanation could be given to the phenomenon that localized corrosion on thin film structures normally aligns with surface imperfections, such as texture or waviness. However, with the assistance of detailed AFM measurements, localized corrosion occurred not at the

bottom of trenches but at slopes, which was fundamentally governed by grain boundary characteristics between different lattice structures due to surface stress and thin film compression tension during epitaxial growth.

Reference:

6.1. Kakehi, A., "Head and Media Technology for 20.4 Gbit/in^2 Demonstration", Presentation at *International Disk Drive Equipment and Materials Association* (IDEMA) Conference September 1999

6.2. Chang, H. S., K. H. Shn, T. D. Lee, and J. K. Park, "The magnetic properties and morphology of CoCrPtTa/Cr/AlN thin films", *Journal of Magnetism and Magnetic Materials*, 177-181(1998) pp.913-914

6.3. Lin, T., "Magnetic recording and structural characteristics of sputtered Co-Cr-Pt films for longitudinal recording", *Journal of Magnetism and Magnetic Materials*, 86(1990) pp.159-168

6.4. Nolan, T. P., R. Sinclair, R. Ranjan, and T. Yamashita, "Effect of microstructural features on media noise in longitudinal recording media", *Journal of Applied Physics*, Vol.73, No.10 (1993) pp.5566-5568

6.5. Demczyk, B. G. and D. E. Laughlin, "Growth Characteristics of Co-Cr Thin Films for Magnetic Recording", *Materials Research Society Proceeding*, Vol. 119, (1998) pp.159-165

6.6. Thompson, C.V., "Structure Evolution During Processing of Polycrystalline Films", *Annual Review of Materials Science*, 30 (2000) pp.159-190

6.7. Petrov, I., P.B. Barna, L. Hultman, and J.E. Greene, "Microstructural evolution during film growth", *Journal of Vacuum Science and Technology: A* 21(5), (2003) pp.S117-S128

6.8. Ratsch, C. and J. A. Venables, "Nucleation theory and the early stages of thin film growth", *J. Vac. Sci. Technol*. A 21(5) (2003) pp.S96-S109

6.9. Futamoto, M., F. Kugiya, M. Suzuki, H. Takano, Y. Matsuda, N. Inaba, Y. Miyamura, K. Akagi, T. Nakao, H. Sawaguchi, H. Fukuoka, T. Munemoto, and T. Takagaki, "Investigation of 2 Gb/in^2 magnetic recording at a track density for 17 kTPI", *IEEE Transactions on Magnetics,* Vol.27, No.6 (1991) pp.5280-5285

6.10. Laughlin, D. E., B. Lu, Y. Hsu, J. Zou, and D. N. Lambeth, "Microstructural and Crystallographic Aspects of Thin Film Recording Media", *IEEE Transactions on Magnetics,* Vol.36, No.1 (2000) pp.48-53

6.11. Xu, Y., J. P. Wang, Z. S. Shan, H. Jiang, and C. T. Chong, "Mangetic and structural properties of hexagonal-close-packed CoCrPt-C granular media for high areal density recording", *Journal of Applied Physics,* Vol.88, No.12 (2000) pp.7234-7241

6.12. Valcu, B. and H. N. Bertram, "Effect of Cr concentration gradient on the intergranular exchange in CoCr(TaPt) thin films", *Journal of Applied Physics*, Vol.91, No.2 (2002) pp.764-771

6.13. Kim, M. R., S. Guruswamy, and K. E. Johnson, "Experimental Observation of Solute Segregation in Longitudinal CoPtCr/Cr Magnetic Thin Films", *IEEE Transactions on Magnetics,* Vol.29, No.6 (1993) pp.3673-3675

6.14. Doemer, M. F., T. Yogi, D. S. Parker, S. Lambert, B. Hermsmeier, O. C. Allegranza, and T. Nguyen, "Composition Effects in High Density CoPtCr Media", *IEEE Transactions on Magnetics,* Vol.29, No.6 (1993) pp.3667-3669

6.15. Toney, M. F., E. E. Marinero, M. F. Doerner, and P. M. Rice, "High Anisotropy CoPtCrB Magnetic Recording Media", *Journal of Applied Physics*, Vol.94, No.6 (2003) pp.4018-4023

6.16. Hellwig, O., D. T. Margulies, B. Lengsfield, E. E. Fullerton, and J. B. Kortright, "Role of boron on grain sizes and magnetic correlation lengths in recording media as determined by soft x-ray scattering", *Applied Physics Letters*, Vol.80, Issue 7 (2002) pp.1234-1236

6.17. Tang, L. and G. Thomas, "Microstructure and texture evolution of Cr thin films with thickness", *Journal of Applied Physics*, Vol.74, No.8 (1993) pp.5025-5032

6.18. Mikami, M., D. D. Djayaprawira,a) H. Domon, S. Yoshimura, and Migaku Takahashi and K. Komiyama, "Study on increasing the coercivity of CoCrPtB media with high Pt content", *Journal of Applied Physics*, Vol.91, No.10 (2002) pp.7074-7076

6.19. Shoda, K., T. Matsubara, and S. Takeda, "Analysis of grain boundaries in CoCrTa and CoPtCrB HDD media by analytical transmission electron microscopy", *Journal of Electron Microscopy*, Vol.54, No.1 (2005) pp.1-9

6.20. Paik, C. R., I. Suzuki, N. Tani, M. Ishikawa, Y. Ota, and K. Nakamura, "Magnetic properties and noise characteristics of high coercivity CoCrPtB/Cr media", *IEEE Transactions on Magnetics,* Vol.28, No.5(2) (1992) pp.3084-3086

6.21. Nakai, J., E. Kusumoto, M. Kuwabara, T. Miyamoto, M. R. Visokay, K. Yoshikawa, and K. Itayama, "Relationship between microstructure of grain boundary and the intergranular exchange in CoCrTa thin film for longitudinal recording media", *IEEE Transactions on Magnetics,* Vol.30, No.6 (1994) pp.3969-3971

6.22. Roger, D. J., Y. Maeda, and K. Takei, "The Dependence of Compositional Separation on Film Thickness for Co-Cr and Co-Cr-Ta Magnetic Recording Media", *IEEE Transactions on Magnetics,* Vol.30, No.6, (1994) pp.3972-3974

6.23. Inaba, N., T. Yamamoto, Y. Hosoe, and M. Futamoto, "Microstructural segregation in CoCrTa and CoCrPt longitudinal magnetic recording media", *Journal of Magnetism and Magnetic Materials*, 168(1997) pp.222-231

6.24. Wittig, J. E., T. P. Nolan, C. A. Ross, M. E. Schabes, K. Tang, R. Sinclair, and J. Bentley, "Chromium Segregation in CoCrTa/Cr and CoCrPt/Cr Thin Films for Longitudinal Recording Media", *IEEE Transactions on Magnetics,* Vol.34**,** No.4 (1998) pp.1564-1566

6.25. Grogger, W., K. M. Krishnan, R. A. Ristau, T. Thomson, S. D. Harkness, and R. Ranjan, "Quantitative measurement of Cr segregation in $Co_{0.8-x}Cr_xPt_{0.1}B_{0.1}$ recording media by scatter diagram analysis", *Applied Physics Letters*, Vol.80, No.7 (2002) pp.1165-1167

6.26. Kemner, K. M., V. G. Harris, W. T. Elam, Y. C. Feng, D. E. Laughlin, J. C. Woicik, and J. C. Lodder, "Preferential site distribution of dilute Pt and Ta in CoCr-based films: An extended x-ray absorption fine structure study", *Journal of Applied Physics*, Vol.82, No.6 (1997) pp.2912-2917

6.27. Inaba, N, and M. Futamoto, "Effects of Pt and Ta addition on compositional microstructure of CoCr-alloy thin film media", *Journal of Applied Physics*, Vol.87, No.9 (2000) pp.6863-6865

6.28. Glijer, P. A., "Optimization of Composition and Structure of Cobalt Chromium Platinum and Cobalt Chromium Platinum Boron Thin Films for Very High-Density Longitudinal Magnetic Recording Media", *Thesis (PH.D)-University of Minnesota*, Vol.5-04, Section B (1995)

6.29. Alexopoulos, P. S. and R. H. Geiss, "Micromagnetic and Structural Studies of Sputtered Thin-Film Recording Media", *IEEE Transactions on Magnetics,* Vol. MAG-22, No.5 (1986) pp.566-568

6.30. Pan, G. D. J. Mapps, M. A. Akhter, J. C. Lodder, P. Berge, H. Y. Wong, and J. N. Chapman, "Microstructure and magnetic properties of very thin CoCr films deposited on different underlayers by rf-sputtering", *Journal of Magnetism and Magnetic Materials*, 113 (1992) pp.21-28

6.31. Laughlin, D. E., B. Cheong, Y. C. Feng, D. E. Lambeth, L. Lee, and B. Wong, "The Control of Micrstrcutural Features of Thin Films for Magnetic Recording", *Scripta Metallurgica et Materialia*, Vol.33, No.10/11 (1995) pp.1525-1536

6.32. Lambeth, D. N., W. Yang, H. Gong, D. E. Laughlin, B. Lu, L. Lee, J. Zou, and P. Harllee, "Magnetic Media Performance: Control Methods for Crystalline Texture and Orientation", *Materials Research Society Proceeding*, Vol.517 (1998) pp.181-192

6.33. Zhu, J. "New Heights for Hard Drives", *Materials Today*, July/August 2003, pp.22-31

6.34. Ishikawa, A and R. Sinclair, "Effects of Pt addition on the magnetic and crystallographic properties of Co-Cr-Pt thin-film media", *Journal of Magnetism and Magnetic Materials*, 152 (1996) pp.256-273

6.35. Fischione, P. E., "Materials Specimen Preparation for Transmission Electron Microscopy", *Application Note from E. A. Fischione Instruments, Inc*. Export, PA, USA

6.36. Müller, E. and D. Abou-Ras, "Preparation of cross-section samples for transmission electron microscopy (TEM)", A Publication from *Elektronenmikroskopie-Zentrum der ETH Zürich* (EMEZ) c/o Institut für Angewandte Physik ETH-Hönggerberg, Zürich, 2004

6.37. Peng, Y., T. Ohkubo, and D. E. Laughlin, "The investigation of nanostructures of magnetic recording media by TEM", *Scripta Materialia* 48 (2003) pp.937-942

6.38. Ohkijima, S. M. Oka, and H. Murayama, "Effect of CoCr Interlayer on Longitudinal Recording", *IEEE Transactions on Magnetics,* Vol.33, No.5 (1997) pp.2944-2946

6.39. Fox, S. P., and P. J. Grundy, "Magnetic interactions and microstructure in CoCrPt discs", *Journal of Magnetism and Magnetic Materials*, 155(1996) pp.179-181

6.40. Masuda, T., W. J. M. A. Geerts, and J. C. Lodder, "Surface chemical state of sputtered Co-Cr films", *Journal of Magnetism and Magnetic Materials*, 95 (1991) pp.123-132

6.41. Xu, Z. P. and H. C. Zeng, "Thermal evolution of cobalt hydroxides: a comparatice study of their various structural phases", *Journal of Materials Chemistry*, Vol.8, No.11 (1998) pp.2499-2506

6.42. Johnson, K. E., C. M. Mate, J. A. Merz, R. L. White, and A. W. Wu, "Thin film media – Current and future technology", *IBM Journal of Research and Development*, Vol.40, No.5 (1996) pp.511-536

6.43. Demczyk, B. G., "Structure and morphology o magnetron sputtered CoCr thin films", *Journal of Magnetism and Magnetic Materials*, 102 (1991) pp.238-246

6.44. Kawamoto, A. and F. Hikami, "Magnetic anisotropy of sputtered media induced by texture substrate", *Journal of Applied Physics*, Vol.69, No.8 (1991) pp.5151-5153

6.45. Khanna, G. and B. M. Clemens, "Characterization of Crystallographic Texture and Strain in Co-alloy Longitudinal Recording Media", Experimental Progress Reports in *1997 SSRL Activity Report* at Stanford University, pp.7-383 – 7-386

6.46. Dova, P., H. Laidler, K. O'Grady, M. F. Toney, and M. F. Doerner, "Effects of stacking faults on magnetic viscosity in thin film magnetic recording media", *Journal of Applied Physics*, Vol.85, No.5 (1999) pp.2775-2781

CHAPTER SEVEN

MAGNTIC MEASUREMENTS

7.1. Introduction to Thin Film Magnetization

Ferromagnetism is a magnetic phenomenon resulting from the strong anisotropic alignment of magnetic domains in materials, which is essential to non-volatile data storage applications. Grains in thin film structures can be longitudinally magnetized to closely parallel each other within magnetic transition zones, as shown in Figure 7.1, along with a nanocrystalline grain structure constructed with hard ferromagnetic cores and polarized soft magnetic shells surrounded.[7.1][7.2]

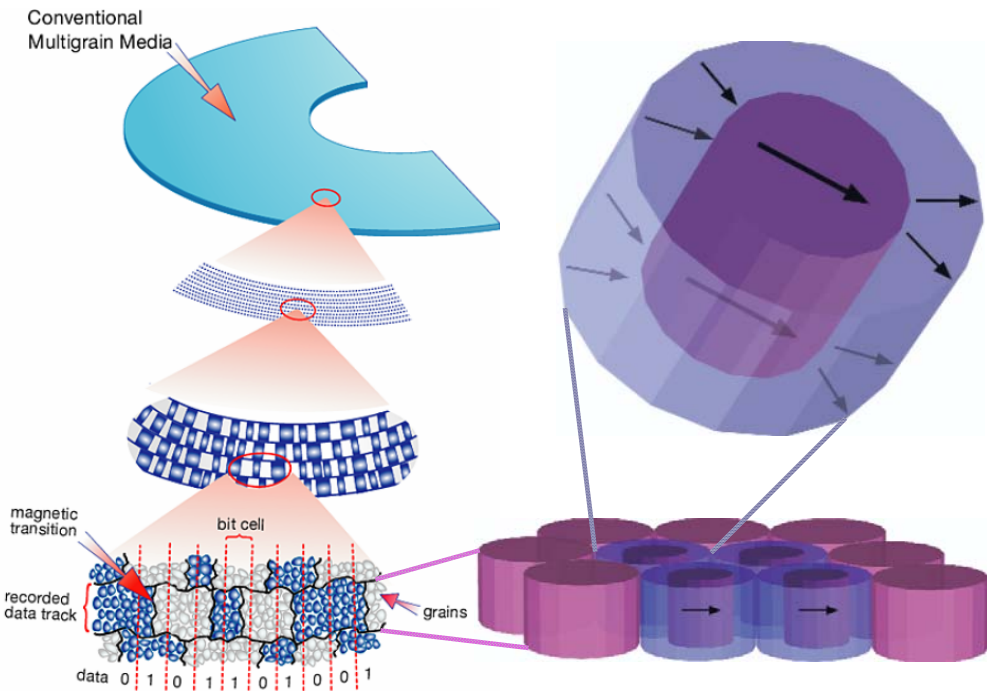

Figure 7.1. Magnetic domain orientations within grains in the form of magnetic transitions with nanocrystalline grain structures constructed by a ferromagnetic core and soft polarized magnetic shell surrounded (reproduced with permissions)

In magnetic thin film structures, grains with proximate domain orientations form transition boundaries in oppositely magnetized directions; for example, in this image, dark lines between “blue” grain clusters and “grey” ones. As a result, the magnetic field streaks within magnetized grain clusters exert same directions above the surface starting from one of these boundaries and ending to another side of boundary, which creates maximum field discretions at the boundaries. With such magnetic flux change at magnetic domain boundaries, changes in the electric resistance of a magnetic sensor can be induced to resemble a magnetic transition event. Commonly in CoCrPtB thin film alloys, each magnetic transition bit contains several structural grains.[7.3] The cores of the grains have been well known to exhibit strongly ferromagnetic properties due to *hcp* microstructure as mentioned in last chapter. However, magnetization at grain boundaries of the grains is mostly induced under the influence from core magnetism because of compositional segregations at grain boundaries. The details of magnetic recording principles and mechanisms are referenced in many general reviews and keynotes.[7.4]-[7.6]

When an anodic reaction occurs, microstructural degradation and compositional alteration in the magnetic thin films inevitably take place, which results in the deterioration of magnetic characteristics. Therefore, in addition to the results from electrochemical and structural analyses, studies of magnetization changes provide another invaluable opportunity to learn about the effects that corrosion causes. Since corrosion’s effect on the magnetic properties of magnetic thin films has never been reported, different approaches in this work were explored.

Many newly-developed magnetic measurement techniques have recently been reported in many published articles and summarized in Falicov’s paper.[7.7] In order to illustrate and measure magnetic field strength, an external magnetic force is applied along certain orientations, and magnetic responses from specimens are then measured using a Vibrating Sample Magnetometer (VSM), the principles of which are well-described in many publications including Niazi’s article.[7.8] VSM results normally represent the collective magnetism of a large area of thin film surface. On the other hand, magnetic imaging techniques developed in recent years are the most effective way to demonstrate the influence of domain variations on magnetism at the microscopic level.[7.9]

7.2. Magnetic Strength Measurements Using VSM

A series of VSM samples were made *ex-situ* from the same surface using concentric corrosion aperture under potentiometric conditions in 2% HNO_3 solutions. Each sample was then cut into a coupon 10 millimeters in diameter. The non-tested surface of the disk coupon was then sanded to eliminate background and interference. VSM measurements conducted in this research were facilitated by and conducted in the Magnetic Research and Application Laboratory of Fujitsu Magnetic Thin Film Group in Nagano, Japan. An alternative external magnetic field swept from zero to 5100 Os to saturate the magnetic domain orientations in the thin film structures and was then reversely executed. The magnetic responses to a complete full cycle were then recorded to construct a hysteresis loop, which is shown in Figure 7.2, for a fresh thin film sample. All detailed hysteresis loops of samples used in the VSM measurements can be found in Appendix V.

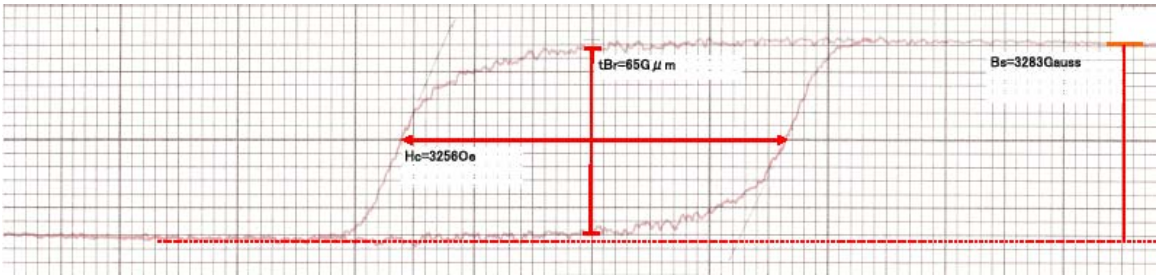

Figure 7.2. VSM measurement of the hysteresis loop of a fresh thin film surface

In these hysteresis plots, both saturated and remnant magnetization, marked as B_s and B_r, respectively, were the most important values, which represented the total internal magnetic domains that a thin film structure could hold when a maximum and zero external magnetic field was present. A decrease in total saturation magnetization as well as remnant magnetization was expected when a thin film structure underwent any transformation, such as electrochemical oxidation, *etc*. Coercivity (H_c value) represented a reverse external field applied to degauss the magnetic domain into complete randomness. A decrease in magnetic coercivity implied that the domain structure of a thin film had weak magnetic coupling capability. In order to better describe the influence of corrosion on magnetic properties, coercivity (H_c) and both saturation and remnant

magnetization (B_s and B_r) as a function of Co amount, quantified from EC-ICP-MS measurements, were charted in Figure 7.3(a) and in Figure 7.3(b), respectively.

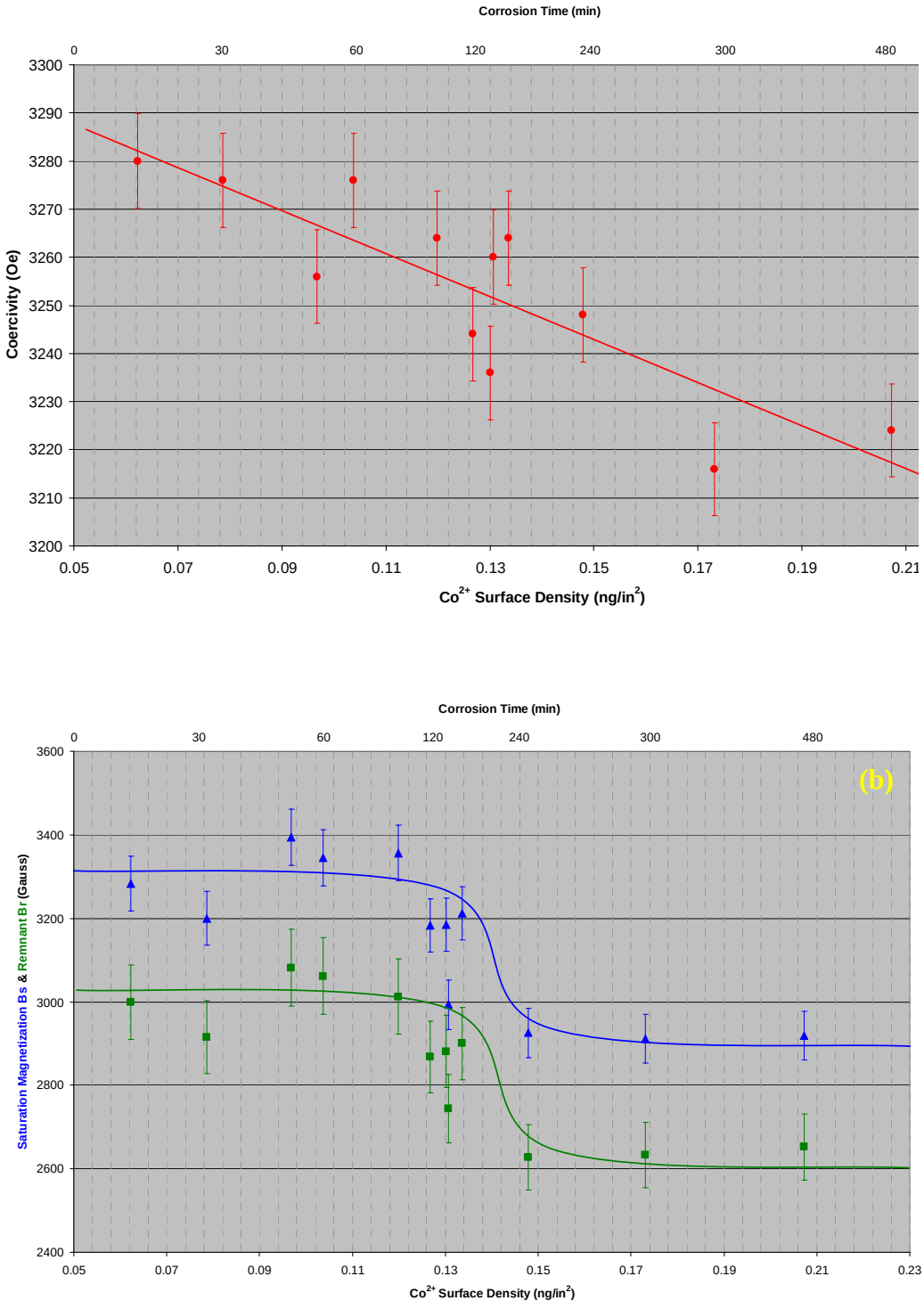

Figure 7.3. (a) Coercivity and (b) saturation and remnant magnetization as a function of Co amount dissolved in corrosion solutions and corrosion time

Since the samples were produced under voltammetric polarization, corresponding corrosion times were also labeled. In these measurements, although the same samples were not experimented with in both analyses, the correlation between magnetic performance and elemental quantity dissolved in electrolytes was still meaningful because the samples were made under identical experimental conditions.

Coercivity from VSM measurements, as shown in Figure 7.3(a), showed a linear decrease as the Co amount, detected in corrosion solutions of 2% HNO_3 using EC-ICP-MS potentiometric measurements, increased. However, the changes in the coercivity of these specimens were noticeably small, with a variation of 100 Oe, which was only a 3% decrease. Since coercivity value had a direct relationship with grain size distribution, grain composition, and thin film structure, such as underlayer thickness and texture, *etc*. in thin films,[7.10]-[7.12] the moderate changes in coercivity shown for these specimens suggested that the overall grain structural integrity of the magnetic thin film remained fairly strong under such potentiometric corrosion conditions, which matched the results from the microstructural analysis presented in Chapter 6. According to microstructural analysis, the impact of corrosion on grain structures of Co alloy thin film was not aggressive in the early stage of corrosion. Thus, the minor decrease in magnetic coercivity in this experiment could be explained by the fact that potentiometric corrosion was similar to the early stage of potentiodynamic corrosion, as shown by the EC-ICP-MS results in previous chapters. However, examining the plots of magnetization characteristics as a function of corrosion time and loss of Co, in Figure 7.3(b), revealed unexpected abrupt decreases in B_s and B_r.

Saturated and remnant magnetization, B_s and B_r respectively, are values of intrinsic magnetic indicators, which were governed mainly by magnetic domain structure. Domain structures in magnetic thin films have been found to be strongly influenced by many microstructural and compositional characteristics, such as grain boundaries, crystallographic orientations, and microstructural imperfections, *etc*.[7.13]-[7.17] Over the course of corrosion, the nonlinear decrease of B_s and B_r values that occurred in these samples was unexpected. Also, more than 15% decrease in magnetization values of both B_s and B_r was high in comparison to the value reduction of coercivity. Under the potentiometric conditions, most elements, except for Co, dissolved in solutions with

fairly linear rates of increases as corrosion time increased, as shown in Figure 4.2. By correlating Co content with the magnetization parameters in a corrosion experiment, the sharp decreases in magnetization corresponded well to the period of time when Co depletion rates changed from high dissolution rates into slow dissolution rates, as shown in Figure 4.2(a). Because sample sizes used in VSM measurements contained numerous corrosion nodules and pits, the causes of sharply decreasing magnetizations could not be specifically explained. However, based upon numerous references, magnetic active volumes [7.18] of Co alloys in magnetic thin film structures were very sensitive to characteristics of inter-granular magnetic coupling.[7.19][7.20] Incorporating non-ferromagnetic materials into grains, grain boundaries, surfaces, and interfaces, could alter and decouple magnetic interactions. In Co alloys, the oxidation of Co could transform the element's ferromagnetism into an anti-ferromagnetic property, while certain crystallographic structure would be formed. [7.21] The volume of magnetic material is reduced by the corrosion reactions.

Therefore, as localized events in thin film corrosion, magnetic disturbances due to the creation of corrosion nodules or pits must have much more significant consequences locally, which the limited applications of the VSM technique could be understood. However, VSM measurements provided valuable reference to and knowledge of collective trends of magnetization changes in large areas. In order to comprehend detailed magnetization behavior locally under the influence of corrosion, Magnetic Force Microscopy (MFM) technique was then applied.

7.3. Magnetic Force Microscopic Analysis

Since early 1990, MFM has become one of the most widespread tools for studying the magnetic structure of ferromagnetic samples.[7.22] Using the MFM technique to study Co alloy thin films was reported shortly after commercial instruments became available in mid-1990.[7.23] Because MFM is based upon the AFM technique, it has high sensitivity and superb resolution, which are important advantages in magnetic measurement applications. In this section, the MFM technique is briefly introduced, and important results from both images and calculations are presented.

7.3.1. Brief Introduction to the MFM Technique

The MFM technique is based on magnetic inductive forces between a very small ferromagnetic tip attached to a flexible cantilever and an inhomogeneous stray magnetic field immediately outside a specimen's surface. As the magnetic tip scans over a magnetic sample, the interaction forces between the magnetic tip and stray magnetic field on sample surfaces are sensed and used in the construction of maps, which are related to changes in the phase of the vibrational motion of a tip oscillating resonantly in the field above the sample.[7.24] The magnetic properties of magnetic thin films provide a unique opportunity to study corrosion and structure because MFM images offer excellent lateral resolution of specific characteristics. With proper interpretations of MFM imaging data, magnetic domain structures from the surfaces of samples can be visually presented via the magnetic stray field.[7.25] Therefore, among many other methods developed to evaluate magnetic properties, MFM is one of the most promising techniques in the quantification of magnetic structures and surface features based upon magnetization interactions.[7..26]

The principle of MFM is schematically illustrated in Figure 7.4 with a SEM image of a magnetized probe at tip of a cantilever. It consists of a cantilever, which is suspended on one side. On the free end, a small volume of magnetic material is mounted. When a magnetic surface is brought close to this tip, the tip will interact with the magnetic stray field.[7.27]

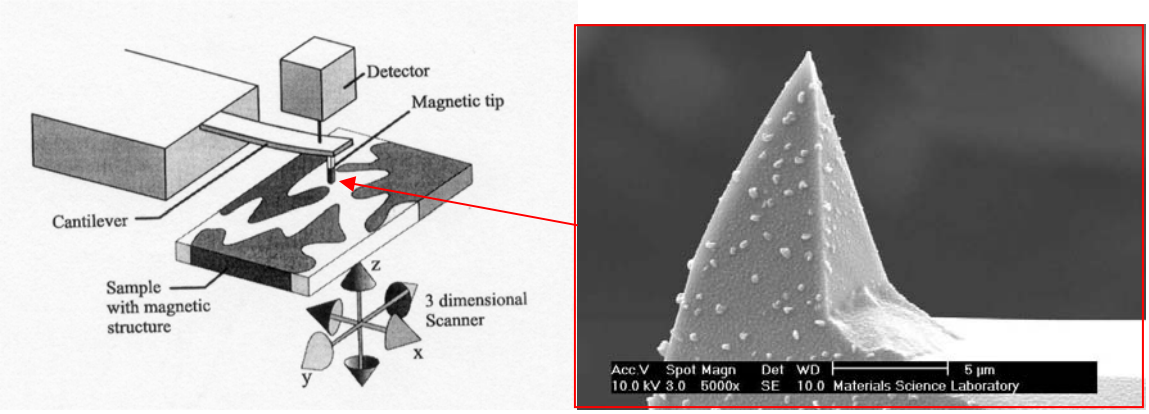

Figure 7.4. Illustration of the magnetic force microscopy technique (reproduced with permission) and a magnetized tip used in this research

The magnetic interaction between the MFM tip and magnetic thin film surface mimics the magnetic recording mechanism of a flying magnetic sensor. The MFM method has been demonstrated to correspond well to a magnetic recording signal.[7.28] Because of the high sensitivity of MFM, which is largely a function of tip properties, resolution of MFM measurements can reach as high as being able to differentiate the size of a single magnetic domain volume.[7.29]

7.3.2. Surface Magnetic Imaging

Surface magnetic profiling was achieved by scanning magnetic information on a thin film surface, which had been magnetized before corrosion tests. Surface scanning examples, which contained surface topographic images and corresponding magnetic patterns on corrosion spots like nodules and pits, are shown in Figure 7.5.

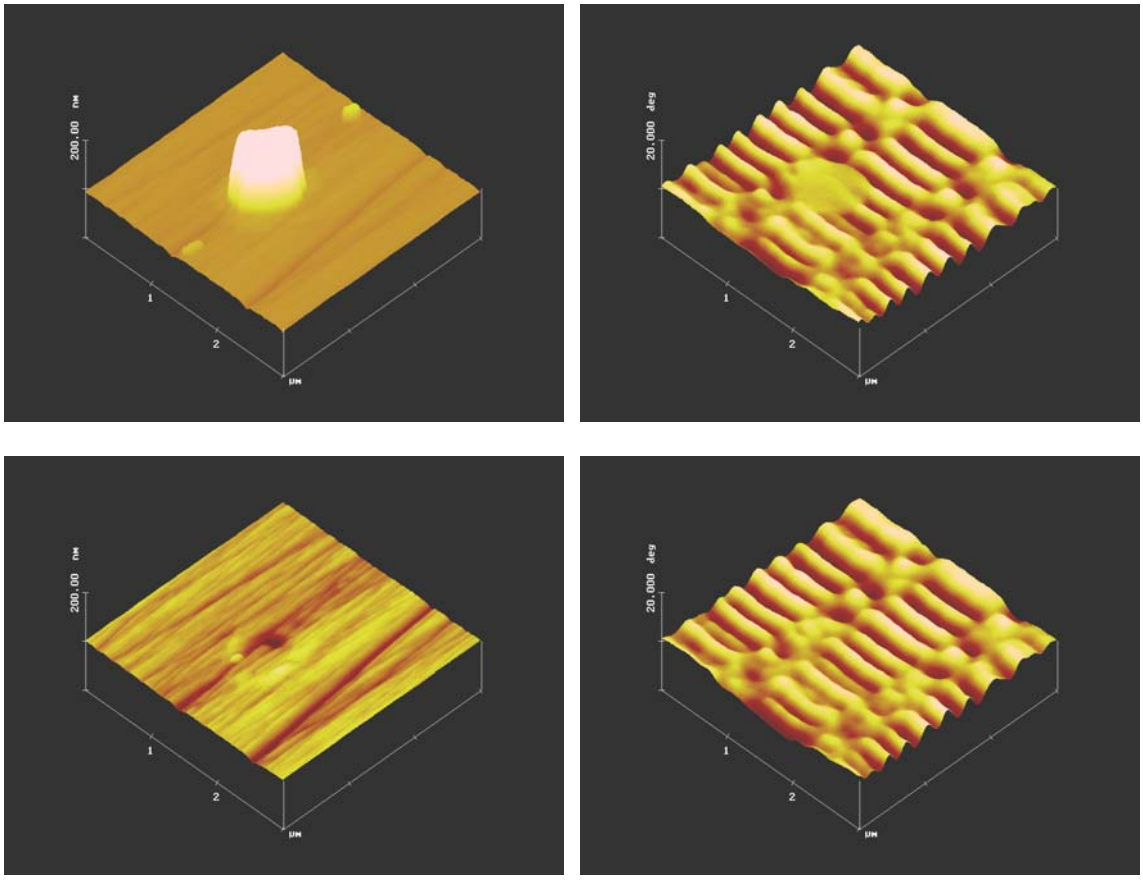

Figure 7.5. Surface topographic and magnetic images of a corrosion nodule (upper row) and corresponding pit (bottom row) after a surface cleaning was performed

This example was one of hundreds of corrosion nodules and pits measured using AFM and MFM. Besides the importance of observing geographic size changes during nodule to pit transformation, which was presented in Chapter 3, magnetic responses were also critical in practical applications. In this case, magnetic transitional information under a nodule was un-differentiable and was thus measured by phase changes, shown in Figure 7.6, and compared with what was measured when a pit was revealed.

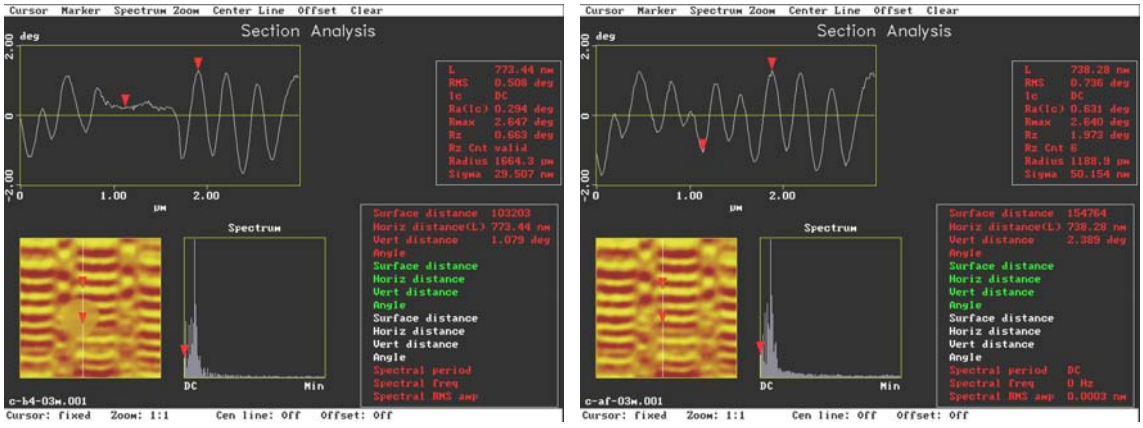

Figure 7.6. Quantitative measurement of the phase change of magnetic patterns on corrosion nodule and corresponding pit

Under the setup conditions, the normal magnetic phase transition grain was about 2.5 degrees from peak to peak. As a nodule was formed, this transition was largely reduced to about 1 degree, which was a 60% reduction in this case. When the nodule was cleaned and surface material was removed, the magnetic response could be recovered up to 90%; a 10% loss of original magnetic signal was mostly acceptable, while a 25% magnetic reduction was the cut-off specification.

Because magnetic transition strength suffered an insignificant amount even when corrosion pits could be measured, a statistic survey was then conducted to relate magnetism loss as a function of corrosion pit size. This comparison measurement with both AFM and MFM was repeatedly applied to about one hundred corrosion pits in order to obtain meaningful statistical comparisons. A survey of these hundred corrosion pits showed that corrosion pit size to result a 25% depreciation in magnetic strength after removing the corrosion nodule was about 5.0 m in diameters , as shown in Figure 7.7. In other words, corrosion pits sized less than 5 m in diameter and 200 nm in depth

suffered less than a quarter of their electric signal loss, which was acceptable in practical applications.

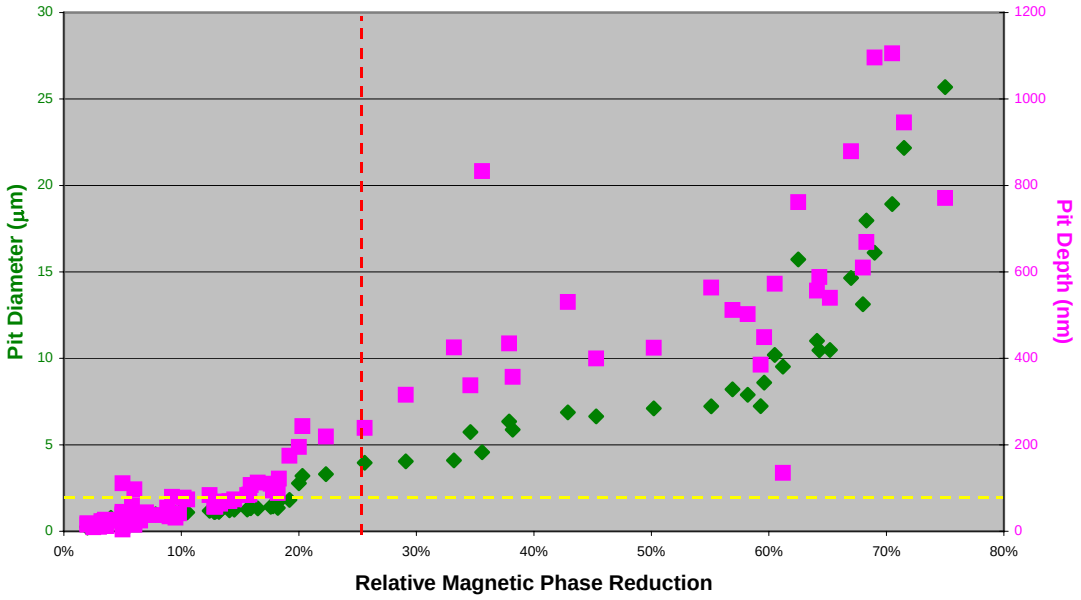

Figure 7.7. Relationship between relative magnetic phase reduction and corrosion pit size measured using AFM/MFM

The majority of corrosion pits with a relative magnetic strength reduction below 25% had a physical size of less than 2.0 μm, and depths of these pits were within the thin film thickness (yellow dotted line). This meant that when a corrosion pit was created within the magnetic thin film structure, the magnetization strength reduction was still tolerable. But when the corrosion pit grew large enough, to more than 5 μm in diameter, the reduction in magnetic field strength became unbearable to recovery. As expected, many large corrosion pits or nodules were completely destructive to the magnetic characteristics of thin film structures. However, Figure 7.8 shows an example of a deep corrosion pit that produces minor magnetic stray field diminishment.

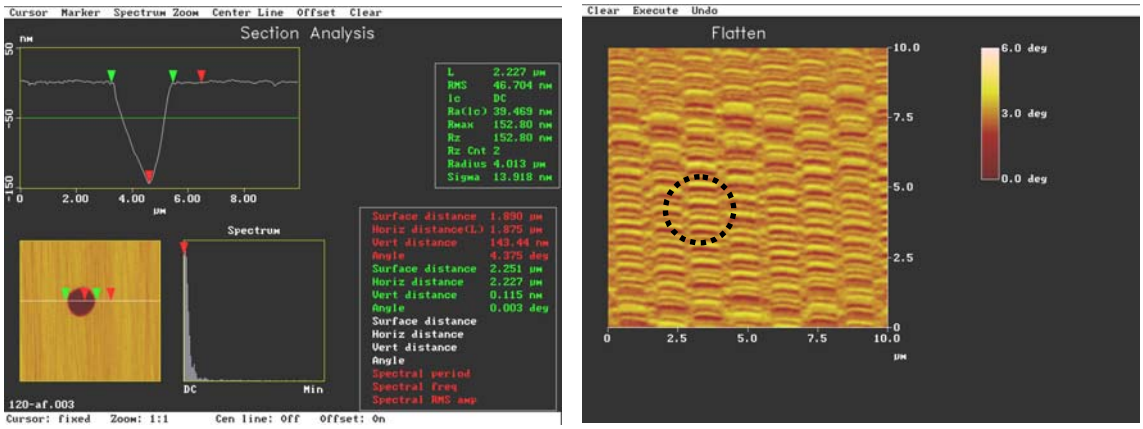

Figure 7.8. AFM profiling (left) a deep corrosion pit without magnetic stray field diminishment shown in the MFM image on the right

As seen in Figure 7.8, the depth of this corrosion pit was over 143 nm, which surpassed the thickness of magnetic thin film laid underneath the surface. The diameter of this pit was measured to be about 1.87 μm. This un-disturbed magnetic response suggested that the magnetic thin layer might be immune to a certain degree of corrosion attack, and the magnetic thin film might be still undetached from underlayer and substrate at the affected area. It also suggested that this thin layer of film could still reside at the bottom of the pit crater as the materials underneath diffuse out to the top surface.

7.3.3. Cross-sectional Magnetic Profile

To discover the reason for the insignificant amount of magnetic field loss in deep corrosion pits, the cross-sectional magnetic mapping technique was developed as an important part of magnetic study. Similar to cross-sectional analysis in microstructural studies, cross-sectional MFM measurements could also reveal how structures of a thin film stack were magnetically affected by corrosion. In this section, both MFM images and MFM phase measurements are summarized. Preparations of cross-sections from thin film disks included mechanical procedures and FIB, which are detailed in Appendix VI. FEI 610 FIB was used for final surface conditioning of these specimens.

A 45-degree angle view of an area of interest without corrosion defect, along with AFM and MFM images at selected locations in the middle of the section, is shown in Figure 7.9.

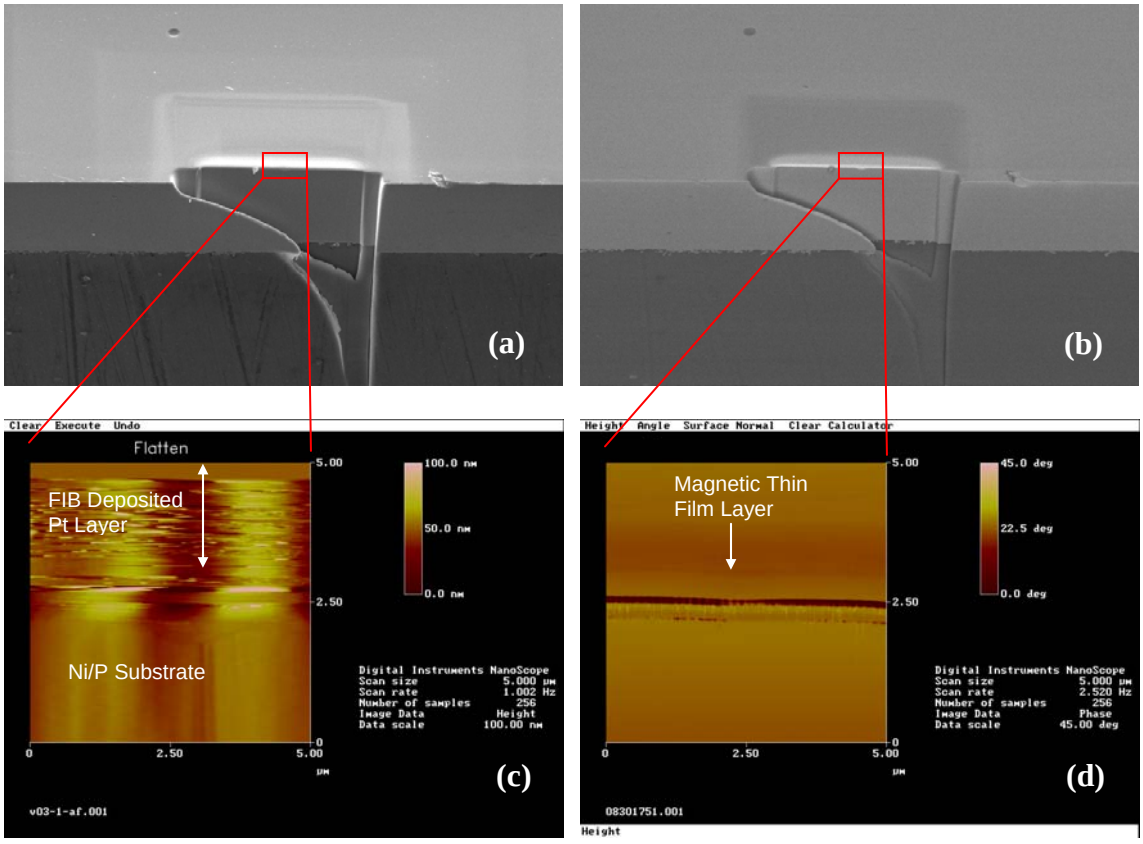

Figure 7.9. A normal cross-sectional surface image obtained using SEM with (a) secondary electron mode, (b) back scattering mode, and corresponding (c) AFM image and (d) MFM image

It was clearly seen that a Pt layer deposited above the thin film surface had no effect on the magnetic layer. The magnetic thin film appears in the MFM image as a dark line. These SEM, AFM and MFM images provided a background and a baseline for the comparison of corroded surfaces for further imaging analysis.

A cross-sectional image of a specimen shown in the SEM micrograph in Figure 7.10(a) contained the small formation of a corrosion pit without deep penetration. The surface pit was similar to the indentation found in the TEM cross-sectional image shown in Figure 7.10(b). The AFM and MFM images are shown in Figures 7.10 (c) and (d), respectively.

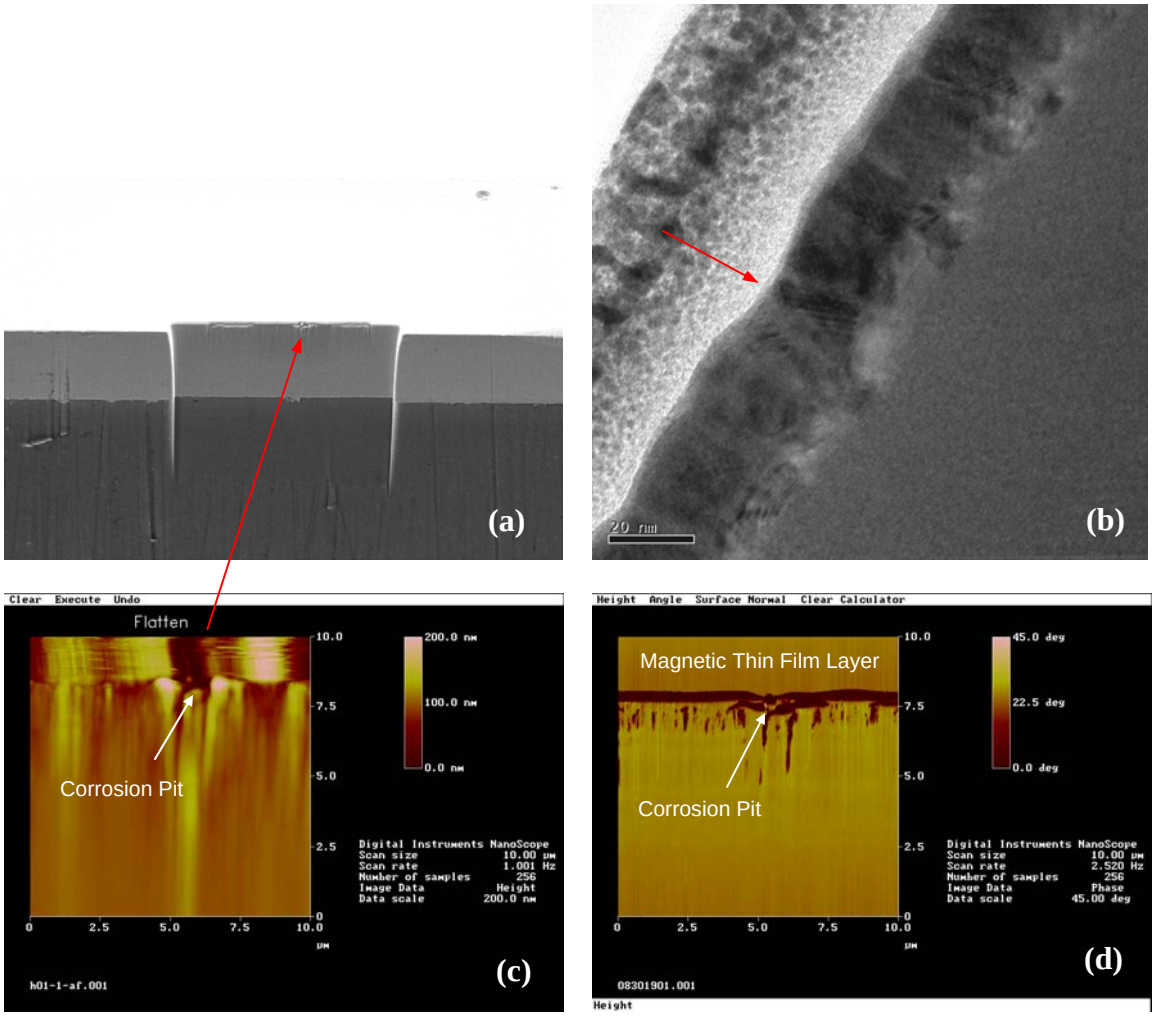

Figure 7.10. (a) A SEM cross-sectional image containing a small corrosion pit similar to pit formation shown in a (b) TEM cross-sectional image and an (c) AFM image and (d) MFM image of this pit

Barely detectable using scanning electron microscopy imaging, the corrosion pit was still magnetically integrated at the surface. At the bottom of the pitting area, aggregation of magnetic material was observed in a semi-spherical shape, which indicated that the electrochemical reaction during the early stage did not cause the magnetic thin film layer to erupt but rather to suppress the eruption by bending inward, probably due to residual stress and defects [7.30][7.31] inherited during the atomic growth history of the thin film.[7.32][7.33] Studies of some of the other corrosion nodules obtained similar results, which proved that the majority of the content in a corrosion nodule was non-magnetic and from the result of metal oxidation. As explained in previous chapters, nickel was not

only electrochemically active, but, importantly, its phase transformation created exceptional volume enlargement. The cross-sectional MFM images of such small corrosion pits also provided great insight into the reason early corrosion had less expected impact on magnetic responses. However, when a large corrosion pit was produced, a complete rupture of the magnetic thin film layer was inevitable, as shown in Figure 7.11.

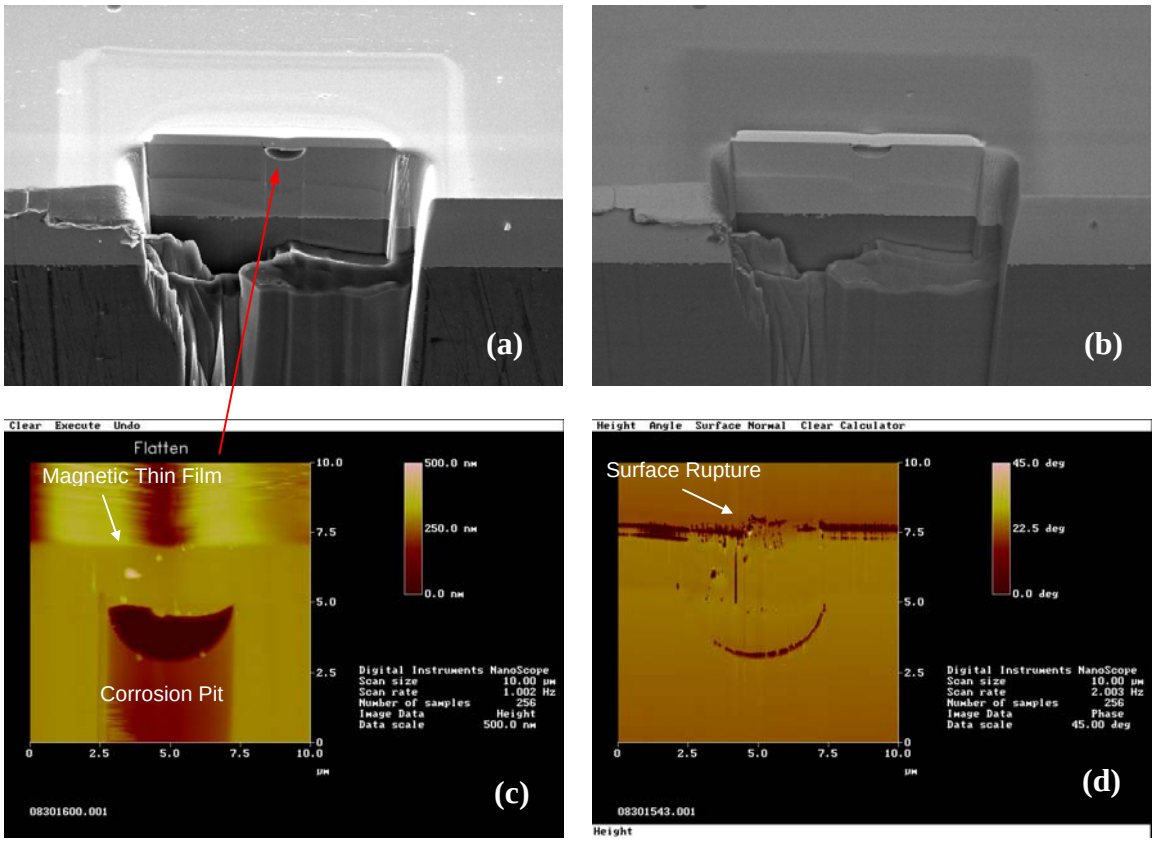

Figure 7.11. A cross-sectional SEM image of a surface containing a large corrosion pit with (a) secondary electron mode, (b) back scattering mode, and corresponding (c) AFM image and (d) MFM image

In such cases, although no visible surface rupture could be seen in both SEM and AFM images, the magnetic image of the surface clearly showed a corrosion event. Also, from both AFM and MFM images, corrosion pits were shaped like teardrops with large volumes under the surface but small openings on the surface. This characteristic, seen in the magnetic cross-sectional analysis, explained the findings from corrosion geometric studies, presented in Chapter 4, that the volume of the corrosion nodule was much bigger

than the leftover small pit. The material to form the corrosion nodule could come from underneath the surrounding area.

7.4. Magnetic Remnant Strength Determination

As discussed previously in section 7.2, demonstration of the effect of localized corrosion on the deterioration of magnetic strength from thin film surfaces was limited by the physical size of samples used in VSM measurements. To overcome the disadvantages of VSM, a different demagnetization method was developed and applied to small areas, which was suitable for MFM measurements. The random demagnetization method was reported for magnetic reversal switching in some studies.[7.34]-[7.36] The demagnetization in this study was accomplished using a series of small permanent magnets with different magnetic strength fields. The advantage of using small magnets is that they achieve random demagnetization on the magnetic structures, which resulted in the true values of magnetic strengths, and realize very localized magnetic responses due to localized corrosion events. Under an external magnetic field, magnetization strength due to partial re-arrangement of internal magnetic domains was evaluated based upon the degree of the phase shift of MFM patterns.

The permanent magnets were made of perm-alloy material in the shape of a cube 2.5 mm of each side. The magnetic field of original permanent magnets was measured to be 9800 Os on a specific surface using a DC Magnetometer supplied from AlphaLab Inc., Salt Lake City, UT. A series of magnets was made by placing them on a laboratory heating plate with different temperatures to reduce magnetic strength to desired values. Then, the magnets were marked and labeled with sign and field values from the DC magnetometer. To demagnetize the thin film in corroded samples, the magnets were placed sequentially, from a low magnetic field to a high one, each time at the same location for one minute, and images of the magnetic patterns on the surface were obtained using MFM with a scan range of 2 μm x 2 μm at three different locations. At each location, the mean of the magnetic strength, represented by the magnetic shift in degree, was statistically calculated for all magnetic transitions shown in the MFM image. In order to obtain meaningful comparisons of the magnetic phase changes based upon magnetic images,

important mathematic algorithms for image deconvolutions were needed; the detailed derivatives from interaction forces between the spatial distribution of the stray field and magnetized tip could be found in Egli's work.[7.37] The peak-to-peak magnetic phase changes in the MFM measurements were then calculated. The overall magnetic phase shifts indicated localized magnetic strength under demagnetized external field was then averaged for these three locations. Figure 7.12 shows the measurements for the samples with different polarization times in 2% HNO_3 solutions.

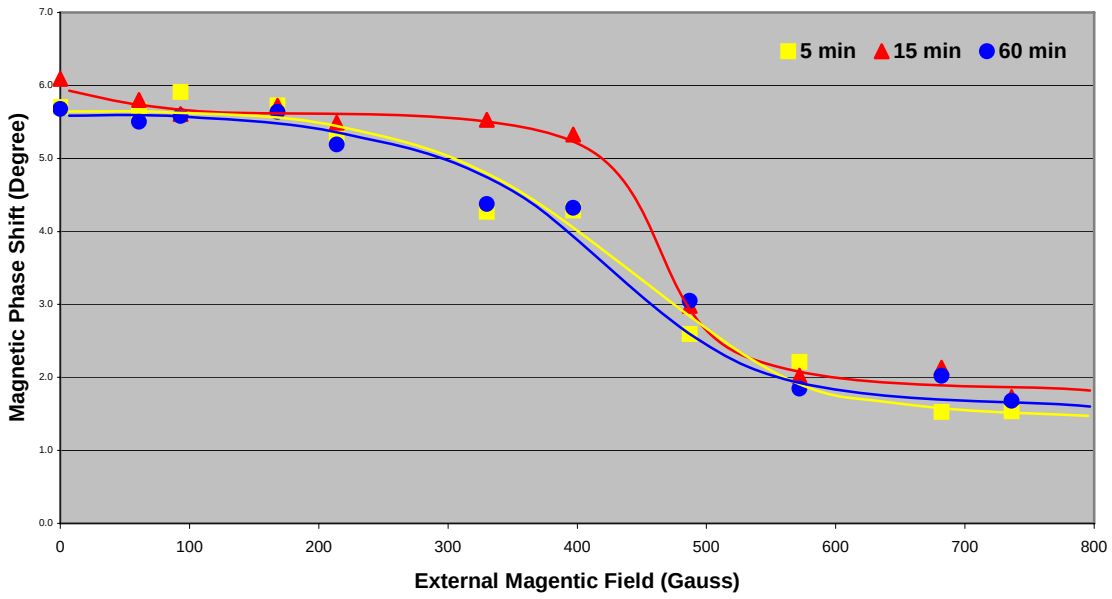

Figure 7.12. The averaged magnetic phase shift measurements of the magnetic thin films after using different electrochemical polarization tests under external magnetic fields

Importantly, from the series of measurements under the influences of external magnetic fields, the demagnetization behavior of thin film magnetization showed different resistances. Surprisingly, the sample polarized at 750 mV for 15 minutes exhibited the strongest demagnetization resistance. Again, from a magnetism perspective, this finding provided consistent supportive evidence of the discoveries made from both microstructural analysis and chemical quantifications in the *in-situ* EC-ICP-MS experiments. The explanations of the facts that increase magnetism of thin film structures were to logically relate microstructural changes to formation of oxides at localized areas within the grain structures. In this case, the magnetic Co alloy in thin film underwent

significant transformation due to dissolution during corrosion. Within 15 minutes of 750 mV polarizations, Co dissolution was most rapid compared to the other elements presented and this occurred at grain boundaries demonstrated in microstructural analysis. Strong magnetic decoupling of grains by loss of the magnetic Co portion of the thin film structures strengthened the polarization of magnetic dipoles within the grains, which in turn increased overall magnetic strength under these circumstances.[7.23] However, with the continuous corrosion process, of which oxidation was not only an effect for grain boundary structures but also grain and interface structures, serious deprivation of magnetism, as shown in Figure 7.12, was expected for the samples exposed to over 60 minutes of corrosion polarization.

Examples of a series of the magnetic patterns acquired for above the figure are referred in Appendix VII.

References:

7.1. "Conventional Multigrain Media", Image © 2008 Hitachi Global Storage and Technologies. www.hitachigst.com, Used by permission

7.2. Wismayer, M. P., S. Lister, S.L. Lee, T. Thomson, F.Y. Ogrin, C.D. Dewhurst, R. Cubitt, and C. Oates, "Mapping local flux density distribution in nanomagnetic recording media", ILL Annual Report, (2005) pp.30-31

7.3. Sato, K., Y. Yoshida, M. Yamagishi, H. Ueno, H. Akimoto, E. N. Abarra, H. Kanai, Y. Uehara, I. Okamoto, and Y. Uematsu, "Rigid Disk Medium for 20 Gb/in^2 Recording Demonstration", *IEEE Transactions on Magnetics*, Vol.35, No.5 (1999) pp.2655-2675

7.4. Chantrell, R. W. and K. O'Grady, "Magnetic characterization of recording media", *Journal of Physics D: Applied. Physics*, 25(1992) pp.1-23

7.5. White, R.L., "The physical boundaries to high-density magnetic recording", *Journal of Magnetism and Magnetic Materials*, 209 (2000) pp.1-5

7.6. Richter, H. J., "Recent advances in the recording physics of thin-film media", *Journal of Physics D: Applied Physics*, Vol.32 (1999) pp.R147-R168

7.7. Falicov, L. M., D. T. Pierce, S. D. Bader, R. Gronsky, K. B. Hathaway, H. J. Hopster, D. N. Lambeth, S. P. Parkin, G. Prinz, M. Slamon, I. K. Schuller, and R.H. Victora, "Surface, interface, and thin-film magnetism", *Journal of Materials Research*, Vol.5, No.6 (1990) pp.1299-1340

7.8. Niazi, A., P. Poddar, and A. K. Rastogi, "A precision, low-cost vibrating sample magnetometer", *CURRENT SCIENCE*, Vol.79, No.1 (2000) pp.99-109

7.9. Gormez, R. D., E. R. Rurke, and I. D. Mayergoyz, "Magnetic imaging in the presence of external fields: Technique and applications", *Journal of Applied Physics*, 79(8), (1996) pp.6441-6446

7.10. Zhou, H. anf H. N. Bertram, "Effect of Grain Size Distribution on Recording Performance in Longitudinal Thin Film Media", *IEEE Transactions On Magnetic*s, Vol.36, No.1, (2000) pp.61-66

7.11. Paik, C. R., I. Suzuki, N. Tani, M. Ishikawa, Y. Ota, and K. Nakamura, "Magnetic properties and noise characteristics of high coercivity CoCrPtB/Cr media"**,** *IEEE Transactions on Magnetics*, Vol. 28, Issue 5(2) (1992) pp.3084-3086

7.12. Inase, T., K. Ustumi, and A. Kondo, "Magnetic Properties and Recording Characteristics of Co-Cr-Ta-Pt Thin Film Media", *Japanese Journal of Applied Physics*, Vol.32(1), No.9A, (1993) pp.3823-3827

7.13. Song, L. W., R. A. Gardner, S. K. McLaurin, and M. Sedighi, "Magnetic Properties and Recording Performance of Multilayer Films of CoCrTa, CoCrPtTa, and CoCrPtTa with CoCrPtB", *IEEE Transactions on Magnetics*, Vol.30, No.6 (1994) pp.4011-4013

7.14. Snyder, J. E. and M. H. Kryder, "The magnetostatic contribution to perpendicular magnetic anisotropy in CoCr with grain boundary segregation", *Journal of Applied Physics*, 69(8) (1991) pp.5154-5156

7.15. Miles, J. J. and B.K. Middleton, "The Role of Microstructure in Micromagnetic Models of Longitudinal Thin Film Magnetic Media", *IEEE Transactions On Magnetic*s, Vol.26, No.6 (1990) pp.2137-2139

7.16. Mirzamaani, M., X. Bian, M. F. Doerner, J. Li, and M. Parker, "Recording Performance of Thin Film Media With Various Crystallographic Preferred Orientations on Glass Substrates", *IEEE Transactions On Magnetic*s, Vol. 4, No.4 (1998) pp.1588-1590

7.17. Ishikawa, A. and R. Sinclair, "Analyses of Stacking Fault Desnity in Co-Alloy Thin Films by High-Resolution Transmission Electron Microscopy", *IEEE Transactions On Magnetic*s, Vol.32, No.5 (1996) pp.3605-3607

7.18. Lauhoff, G., T. Suzuki, and R. Sbiaa, "Issues in Determining Activation Volume in Magnetic Recording Media", *Transactions of Magnetic Society of Japan*, Vol.2, No.2 (2002) pp.104 - 109

7.19. Muller, M. W. and R. S. Indeck, "Intergranular exchange coupling", *Journal of Applied Physics*, 75(4) (1994) pp.2289-2290

7.20. Kubota, Y., L. Folks and E. E. Marinero, "Intergrain magnetic coupling and microstructure in CoPtCr, CoPtCrTa, and CoPtCrB alloys", *Journal of Applied Physics*, Vol.84, (1998) pp.6202-6207

7.21. Getzlaff, M. J. Bansmann, and G. Schonhense, "A study of the oxidation states of Co(0001)", *Journal of Magnetism and Magnetic Materials*, 140-144 (1995) pp.729-730

7.22. Freeman, M. R. and B. C. Choi, "Advances in Magnetic Microscopy", *Science*, Vol.294 (2001) pp.1484-1488

7.23. Glijer, P. A., J. M. Sivertsen and J. H. Judy, "Magnetic Force Microscopy (MFM) Studies of Micromagnetic Structures of High Coercivity CoCrPtCr and CoCrPtBCr Thin Films", *IEEE Transactions On Magnetic*s, Vol. 31, No.6 (1995) pp.2842-2844

7.24. Rugar, D., H. J. Manin, P. Guethner, S. E. Lambert, J. E. Stern, I. McFadyen, and T. Yoji, "Magnetic force microscopy: General principles and application to longitudinal recording media", *Journal of Applied Physics*, 68(3), (1990) pp.1169-1183

7.25. Bottomley, L. A., "Scanning Probe Microscopy", *Analytical Chemistry*, 70, (1998) pp.425R-475R

7.26. Celotta, R. J., J. Unguris, M. H. Kelley, and D. T. Pierce, "Techniques to Measure Magnetic Domain Structures", in *Methods in Materials Research: A Current Protocols Publication*, Edited by E. N. Kaufman, John Wiley & Sons, 2000

7.27. Porthun, S. L. Abelmann, and C. Lodder, "Magnetic force microscopy of thin film media for high density magnetic recording", *Journal of Magnetism and Magnetic Materials,* 182(1998) pp.238-237

7.28. Babcock, K., V. Elings, M. Dugas, and S. Loper, "Optimization of Thin-Film Tips for Magnetic Force Microscopy", *IEEE Transactions on Magnetic*s, Vol.30, No.6 (1994) pp.4503-4505

7.29. Rice, P. and J. Hoinville, "Correlating MFM images and recording head output", *Data Storage*, Issue 1 (1997) pp.35-40

7.30. Fang, W. and C. Lo, "On the thermal expansion coefficients of thin films", *Sensors and Actuators* 84 (2000) pp.310–314

7.31. Thompson, C. V., "Structure Evolution During Processing of Polycrystalline Films", *Annual Review of Materials Science*, 30 (2000) pp.159–90

7.32. Ratscha, C. and J. A. Venables, "Nucleation theory and the early stages of thin film growth", *Journal of Vacuum Science and Technology: A*, Vol.21, No.5 (2003) pp.S96-S109

7.33. Frost, H. J., "Simulation of Microstructural Evolution in Polycrystalline Films", *Evolution of Thin-Film and Surface Microstructure* in Materials Research Society Symposium Proceedings, Vol.202 (1991) pp.115-130

7.34. Kuo, H. V., E. D. Dahlberg, and C. A. Merton, "Magnetic force microscopy studies of bit erasure in particulate magnetic recording media", Contributed Poster, *International Conference on Magnetism 2000*, Recife, Brazil, August 2000

7.35. Jander, A. P. Dhagat, R.S. Indeck, and M. W. Muller, "MFM Observation of Localized Demagnetization in Magnetic Recordings", *IEEE Transactions on Magnetics*, Vol.34, No.4 (1998) pp.1657-1659

7.36. Abarra, E. N., and T. Suzuki, "Magnetic Force Microscopy Studies of DC Erasure in a 5 Gbit/in^2 Medium", *IEEE Transactions On Magnetic*s, Vol.34, No.2 (1998) pp.363-365

7.37. Egli, S., "Numerical Methods for Magnetic Force Microscopy calibration", *Thesis of University of Basel*, December 2000

CHAPTER EIGHT

CORROSION MODELING

8.1. Commonly Known Surface Pitting Corrosion Mechanisms

8.1.1. Corrosion Models for Passive Films

There have been several pitting growth mechanisms commonly proposed and widely accepted in the electrochemistry community when passive thin films are subjected to corrosion studies.[8.1] Theories about passive thin film breakdown and pit corrosion initiation have involved three main mechanisms, passive film penetration, film adsorption, and film breaking, which are illustrated in Figure 8.1.

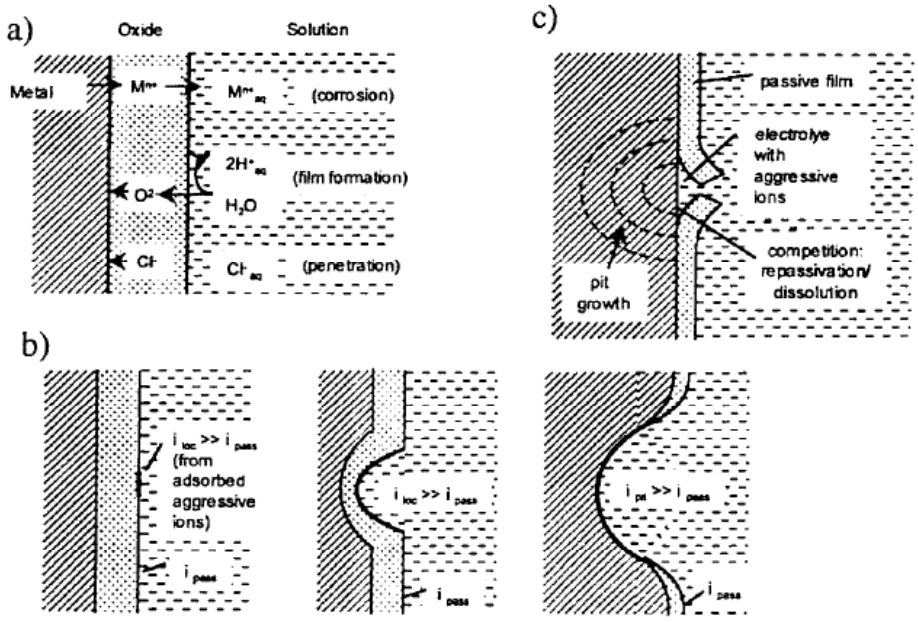

Figure 8.1. Schematic diagrams representing pit initiation by (a) penetration, (b) adsorption and thinning, and (c) film breaking (Graphs reproduced with permission)

The penetration mechanism for pit initiation involves the transport of aggressive anions through the passive film to the metal/oxide interface where accelerated dissolution is promoted. The adsorption theory of initiation is based upon the formation and reduction of passive film thickness due to the presence of oxygen in electrolytes. Pit initiation through the film breaking mechanism holds that the thin passive film undergoes a continual state of breakdown and repair. Surface defects at weak sites or flaws resulting from surface stress or electrostriction may cause these local breakdown events.

In addition, the point defect model (PDM) [8.2] was developed to explain the growth and breakdown of passive films and attributes passivity breakdown at a single site on a surface to the condensation of cation vacancies at the metal/film interface, as shown in Figure 8.2. This process is postulated to occur at structural inhomogeneities within the barrier layer of the passive film (e.g. at the edge of an inclusion), which is characterized by high cation vacancy diffusivity and/or by a high cation vacancy concentration.

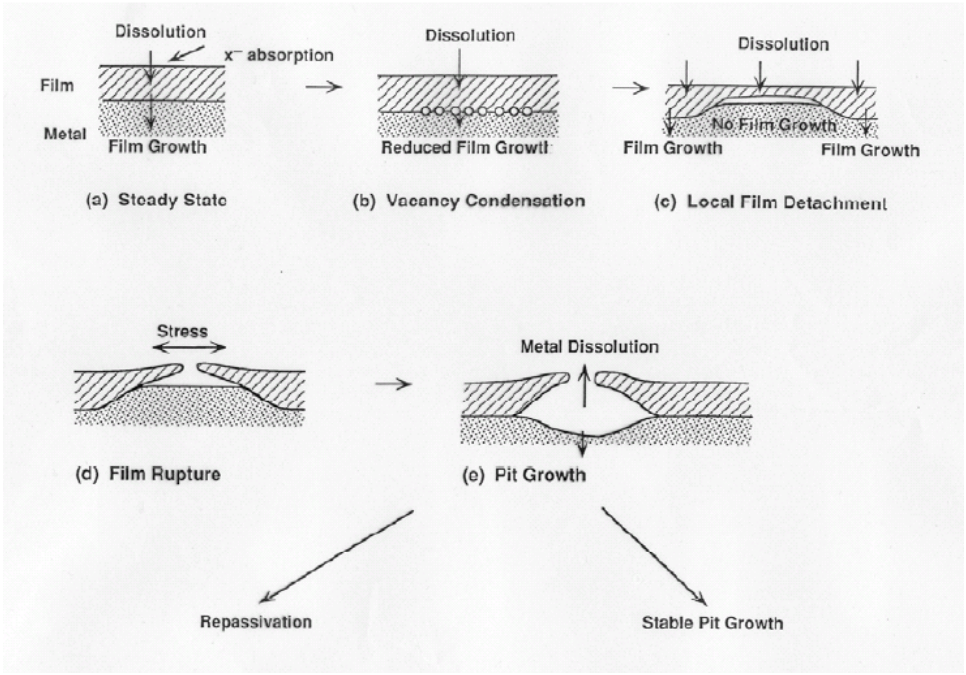

Figure 8.2. Cartoon of the passivity breakdown process as envisioned by the Point Defect Model (Graphs reproduced with permission)

A key condition in these corrosion models is that passive film exists before corrosion is introduced. The initiation of pitting corrosion in these models is due to the breakage of

the barrier layer, either chemically or physically. Continuation of the corrosion process comes from metal dissolution of the underlying metallic layer.

Godard developed a simple but effective equation based on the experimental data to estimate the rate at which pits grow.[8.3] In general, the rate of pit growth depends on several factors, such as temperature, pH, passive film properties, chloride ion concentration, presence of anions and cations in the solution, and orientation of the material.[8.4] Pit growth can be viewed as the direct interaction of the exposed metal with the environment.

8.1.2. Corrosion Models for Multilayer Magnetic Thin Films

One popular interpretation of the pitting corrosion mechanism is that it is the result of coverage imperfection. Due to surface roughness and defects, the thin overcoat is often unable to completely cover and seal the underlying magnetic thin film. Invasion of a corrosive species results in the formation of corrosion products at the surface and causes corrosion products to protrude through the service. A schematic view of this possible corrosion mechanism in a chloride-contaminated environment is shown in Figure 8.3.[8.5]

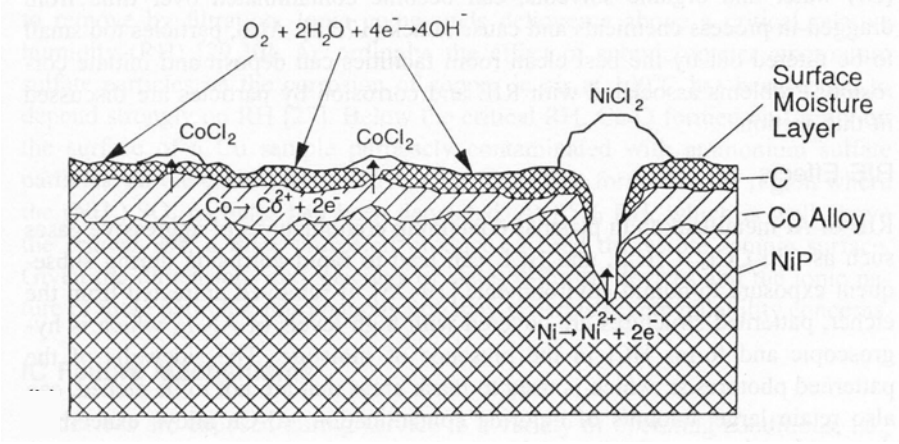

Figure 8.3. A schematic view of the corrosion of a rough disk structure in a Cl^- containing environment (Graph reproduced with permission)

From an electrochemical point of perspective, Novotny and Staud [8.6] proposed two different corrosion mechanisms depending mainly on the catalytic activity involved in

oxygen reduction and the electrical conductivity of a specific overcoat. These two models are illustrated in Figure 8.4.

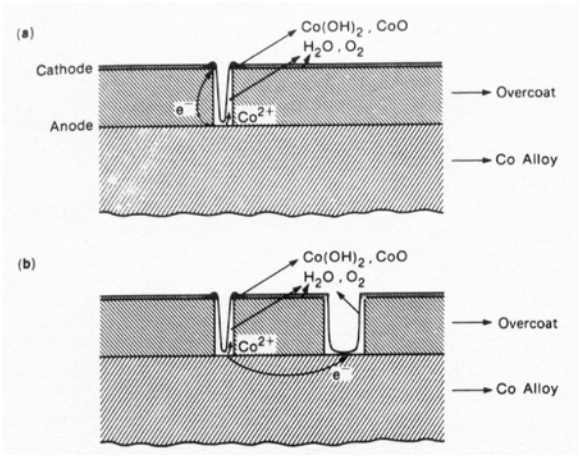

Figure 8.4. Schematic diagram of corrosion mechanisms for a porous overcoat with (a) high electrical conductivity and (b) very low electrical conductivity (Graphs reproduced with permission)

Figure 8.4(a) illustrates the model for a conductive overcoat, which acts as a large cathode surface area for oxygen reduction. Compared with chromium, cobalt and nickel are dissolved at the bottom of the pores. Dissolved ions are driven by diffusion and electromigration toward the top of the surface. With low surface conductivity, shown in Figure 8.4(b), differential aeration cells would mainly drive the corrosion process. Different pore size and pore structures lead to gradients in oxygen concentration at the cobalt alloy and water interfaces and therefore create different electrochemical potential in the pores. These electrochemical potential differences then form microscopic anodic and cathodic surface sites.

8.2. Micro-Corrosion Model for Magnetic Thin Film Structures

Modeling the micro-corrosion mechanism for magnetic thin film structures is the ultimate goal of this research. Unlike the two-dimensional corrosion models presented in much of the literature, construction of corrosion models for magnetic thin film structures takes 3-dimensional geographic consideration. Expansion of corrosion knowledge from a three-dimension model can potentially improve overviews of corrosion mechanisms and

provide opportunities to formulate better solutions to prevent occurrences of corrosion in future designs and applications. Both experimental results and comprehensive explanations in each part of the study contribute significantly to constructing the new 3-D micro-corrosion models.

8.2.1. Elemental Quantification Considerations

Traditional corrosion models are mostly based upon a single element and mono-structure with a focus on the characteristics of the surface protective layer. In the magnetic thin film stack, multiple elements, such as Co, Cr, Pt, B, Ta, Mo and Ni, are blended in the alloy matrix in different layers of thin films. Although Co is the predominant specie responsible for magnetic features of the thin film, other constituents are equally important in different aspects. As corrosion proceeds, breakage of bonds among the elements in the alloy thin film is unpredictable. In this research, owing to the development of the *in-situ* technique coupling electrochemical reactions with ICP-MS, each element depleted from the thin film structure has been quantified. Even though no oxidation state could be provided by ICP-MS measurements, the oxidation of metallic elements was generally presumed and understood, as described in many spectroscopic studies. Some of important facts and results obtained from the *in-situ* EC-ICP-MS experiments are reiterated here.

Different trends of corrosion dissolutions for every and each of alloy elements from magnetic thin film structures were well demonstrated quantitatively by the novel technique, which was to couple EC with ICP-MS. The corrosion response from each element depended on many corrosion factors, such as corrosive solutions, electric potentials, polarization rates, and corrosion time. Not only specific amounts determined in these experiments were important but also knowing the history of each corrosion process was valuable. Judged by quantity changes of elements in the course of corrosion, no sudden events of corrosion creation could be observed as a function of numerous parameters, which meant that thin film corrosion was indeed a constant process. However, the rates, to which corrosion products evolved from metallic state into ionic state, were a function of many factors.

Under spontaneous corrosion conditions, high concentration of Co in acidic solutions indicated that ionization of Co was initiated at the surface region but limited by the size of corrosion pores as anodic reactions were shut off when oxides or hydroxides were formed on the surface. The initial formation of Co derivative ions can be described with the following equation:

$$Co - 2e^- = Co^{2+} \quad (8.1)$$

Conventionally, Cr is added to improve the anti-corrosion capability of metallic alloys, since chromates are highly impermeable to further invasion of anions. This ability of Cr was supported by the fact that a constant Cr content in the film was promptly reached at the beginning of the corrosion process. Accordingly, chromates can be produced as:

$$Cr - 2e^- = Cr^{2+} \quad (8.2)$$

or

$$Cr - 3e^- = Cr^{3+} \quad (8.3)$$

Slight increases of Pt in the same solution as immersion time increases revealed that the dissolution of Pt was not necessary to completely form oxides, especially in high concentrations of electrolytes. On the other hand, boron exhibited high dissolution rates under these unbiased environments because it existed as energized radicals in a mostly free state. As part of the underlayer, Mo was slightly higher in solutions, which implied the oxidation of Mo was either hindered by Cr in the matrix or by the interfacial diffusion process into different thin film layers. In contrast, a large amount of Ni from Ni/P amorphous in acidic solutions suggested that the crystallographic transformation of Ni had extraordinary free energy to penetrate the upper cover layers, which could dramatically alter electrochemical balances and topographic uniformity. The oxidation of nickel can be written as:

$$Ni - 2e^- = Ni^{2+} \quad (8.4)$$

When a negative electric potential was applied to the surface of a multiple metallic layer, the equilibrium of the dissolution of metallic elements from alloys changed dramatically, as revealed in ICP measurements. Using three different polarization approaches with electric-biased systems, Co released its ions at fast speeds during the initial stage

followed by slow Co run-off rates. This finding indicated that initiation of corrosion to the surface was generally due to the uniform penetration of anions from solutions through the grain boundary of the upper layer. Because Co resides in the top magnetic thin film layer, initial reactions of Co with anions in exchanging electrons made Co run-off fast and interfered less with other elements. As corrosion continues, released Co ions no longer predominated the process, competitive oxidation occurs, and the release of Co slows down. Meanwhile, interestingly, using a quick electric scanning rate or under high electric potential influence, two consecutive Co run-off processed with two distinguishable curves were evident in ICP-MS measurements, which meant that Co from the magnetic layer and seed layer was corroded at different times or potential ranges.

Under different corrosion conditions in potentiometric measurements, the immunity of Cr was presumably predominant characteristics because of low Cr release rates into the corrosion solutions. However, Cr corrosion resistance was unsustainable when electric bias was applied at extended time, which implied that corrosion inhibit of Cr under electric-imbalanced environments was reduced drastically beyond certain time or potential. Since Cr was present in all layers of the multiple layer structure, Cr content in a solution was contributed from all layers. However, when a slow scan rate was used, Cr counts showed a distinguished plateau at 700 – 850 mV, which presumed that Cr from the base layer joins the release mechanism thereafter. In general, two magic numbers could be determined from these ICP measurements on Cr: a potential of 600 mV and a time of 10 minutes under voltammetry conditions. Therefore, the ability of Cr to inhibit corrosion in the thin film stack structure could be determined in limited circumstances using electrochemical reactions.

Pt release could be only promoted in high concentrations of acidic solutions and with high electric potentials, which indicated that Pt was in substitutional solution at lattice sites of the magnetic thin film layer when other elements were migrated to this magnetic layer, the Pt concentration would remain high.

Quantitatively compared to what was measured under unbiased conditions, B released less than half of its amount when an electric field was applied to the magnetic thin film structure, which clearly indicated that the negativity of B impedes its run-off rate. The

quantity of B in acidic solutions was very sensitive to potentials and pH levels. More acidic solutions did not attract more B into the solutions.

From an elemental change perspective, the magnetic thin film layer initially suffers the loss of Co from the matrix, which left high concentrations of Cr and Pt when the anodic reaction commences. When corrosion attack was started to underlayer, no immediate stop of Co was noticed until Cr was produced during the reactions. The continual reduction of Co and Cr under anodic reactions in the magnetic layer increased the relative contents of Pt and B in this layer, which altered electrochemical balances at the interface with the underlayer. Maintaining a large quantity of B in the upper layer was crucial because B possessed a much lower electrochemical potential than most other metals, such as Mo, as shown as in Table of Appendix IV. The low output of Mo from the underlayer could relate to the relatively high concentration of B from the upper layer, and a galvanic micro-cell between B and those elements was built up in electrolyte solutions. In such micro-bridges, Mo could act as a cathode instead of an anode, and consequently dissolutions of Mo become less probable.

As indicated in elemental quantification measurements using ICP-MS, as well as compositional analysis shown in the EDS spectra, Ni contributed tremendously to corrosion nodules. The substrate Ni/P structure was known as the amorphous phase and contained about 80% Ni and 20% P. Certain information obtained from many other studies indicate that changes in Ni/P amorphous structures and electron states were major contributors to producing Ni in electrolyte solutions under corrosion environments. Ni in the amorphous structure acted as an electron-deficient center and was prone to electron negative affinity, which was one of the causes of its reactivity.[8.7]

As an extremely large amount of Ni was detected in ICP-MS measurements, although Ni had a much higher electrochemical potential than other elements, the critical characteristics of Ni from the Ni/P amorphous alloy were related to the low activation energy of Ni in the Ni/P alloy in comparison to pure Ni in crystalline form.[8.8] Because of the low activation energy of Ni/P, hydrogen and amorphous Ni/P absorption changed the electron structure of the Ni/P metal greatly, which was caused by the barrierless electron transfer reaction mechanism.[8.9]

8.2.2. Microscopic Corrosion Mechanisms

The nature of the corrosion mechanism at the micro-scale was revealed by the microstructural analyses conducted in this research. Instead of conventional surface profiling, cross-sectional analyses provide valuable information about corrosion progression in three dimensions.

The first important area of study was to observe changes in grain and grain boundary morphologies under corrosion influences. Over the course of corrosion, both hexagonal Co and cubical Cr lattice structures were found to well-maintain crystallographic size and orientation. Major crystallographic changes were observed at grain boundaries and interfaces. Grain boundaries in the Co layer became wider as a result of an increase in corrosion time or other external forces.

Physical enlargement of grain boundary channels seen in TEM micrographic images implies that the initial corrosion process occurred at the grain boundary; the release of a significant amount of Co, measured in EC-ICP-MS experiments, was proved this hypothesis. Loss of Co content along the grain boundary was also confirmed by nano-electron probe profiles at the grain boundaries. By comparison, Co content in grains did not significantly change, whereas Co content along grain boundaries did. This conclusion supported similar findings and presumptions stated in some previous reports.[8.10][8.11] Similar distribution variations were also found when Pt was profiled. However, in the *in-situ* EC-ICP-MS studies, unlike that of Co, run-off of Pt was mostly proportional to many variable parameters externally enforced, such as electric field and pH levels of solutions, which indicated that there was a different mechanism for Pt corrosion. Because of its small ionic diameter,[8.12] the mobility of Pt atom had much less influence on oxidation, and therefore mitigation rates of Pt from the grain into the grain boundary could be constant, as shown in EC-ICP-MS results. Grain boundaries were favorable paths for high mobility elements where high Ni concentrations were detected. The migration of Ni along grain boundaries was the reason for the overwhelming amount of Ni measured in EC-ICP-MS experiments, which predominantly controlled the corrosion course.

Although crystallographic alignments in both Co and Cr grains were seen through the corrosion course, grain degradations were clearly shown in FFT patterns. Surprisingly, Cr

grains in the underlayer encountered deterioration much earlier than Co grains did, which suggested that the immunity of Cr to possible localized passivity became unsustainable when grain boundaries and interfaces turned into corrosion passages for other elements, such as Mo. Under these circumstances, a sharp increase in the amount of Cr detected in EC-ICP-MS measurements corresponded to low counts in electron probe profiles of grains.

As for other non-metallic ions, such as B and P, from the thin film alloys, their movements depended on many corrosion conditions including potential applied, bias polarity, and concentration of corrosive solutions. Though they were mostly detected in media solutions in EC-ICP-MS tests and general reductions in microscopic analysis, no specific tendencies of preferences of elements for either grain or grain boundaries could be postulated. With the assistance of nano-electron probe EDS profile capability in microanalysis, the distribution of N from nitric acids, in this case, penetrated from the surface down to the underlayer through the grain structure.

In summary, the microscopic corrosion mechanism is demonstrated from a kinetic point of view of how each metallic element migrates related to thin film microstructure under the influence of corrosion. The evolution of corrosion in thin film in relation to microstructural characteristics is proposed and is shown graphically in the following figures.

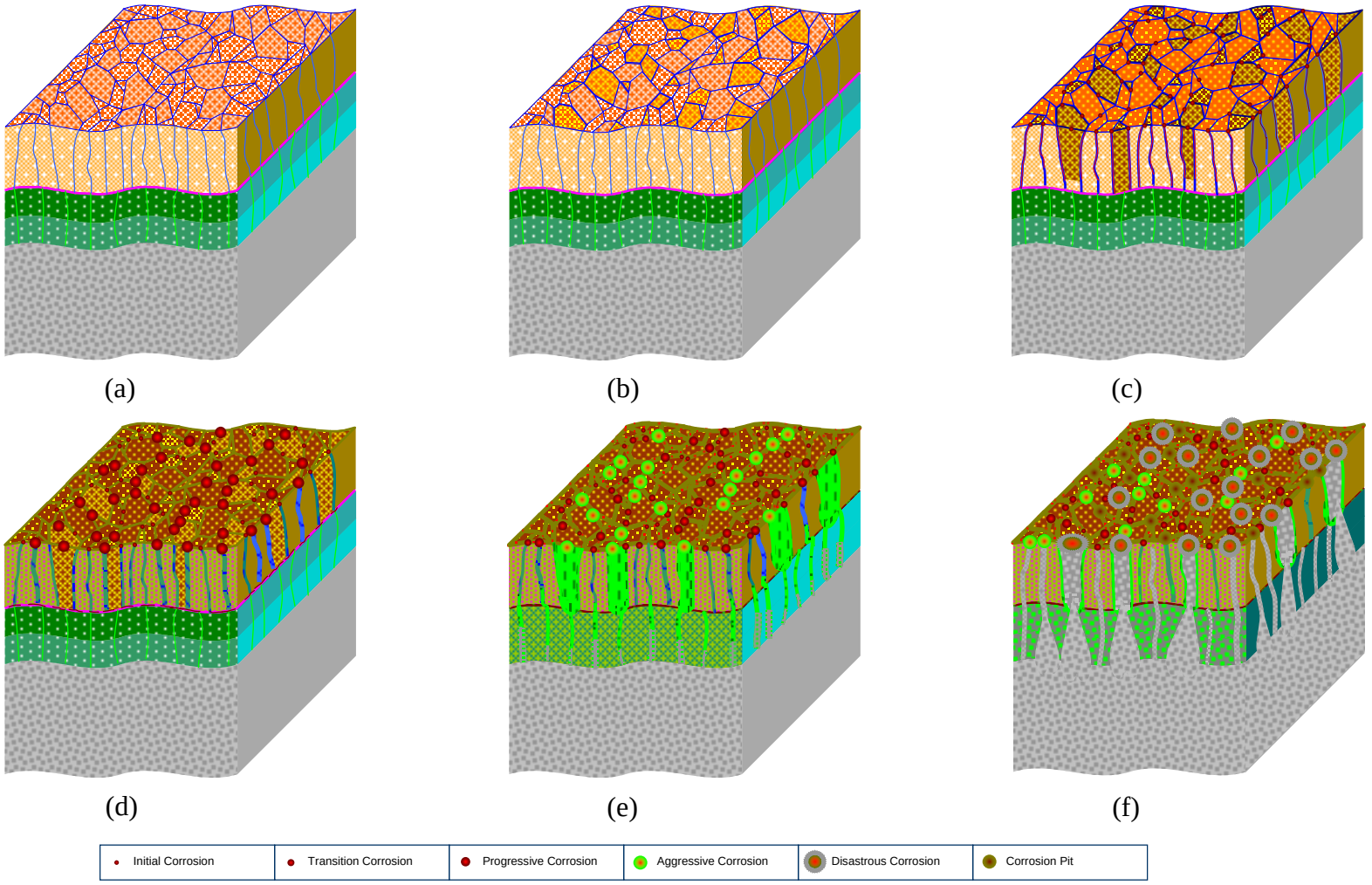

Figure 8.5. A 3D schematic sketch of elemental depletion mechanisms and steps of micro-corrosion formation for each layer of the multiplayer magnetic thin film structures

The above-proposed model briefly demonstrated the key steps in the micro-corrosion processes from a microscopic point of view. The major steps included dissolution and high run-off rates of Co from the grain boundary region along with consistent loss of Pt, shown in Figures 8.5(a) and (b). Consequently, general passages at grain boundaries were created, and oxidation reactions penetrated into deeper regions, as shown in Figure 8.5(c). Meanwhile, small accumulations of oxides at the top surface along the grain boundaries were shown in small red dots at the initial corrosion sites. On the other hand, anions, such as N, in this case, from nitric acid, started to penetrate through the grains, and the diffusion of Pt toward the grain boundaries continued. As grain boundaries progressively widen, much deterioration was seen even at the interfaces, shown in pink in Figure 8.5(d), which quickly interfered with the Cr underlayer. Importantly, deterioration at the interface with lateral movement of corrosion attack was expected, which increased the mobility of Mo from the underlayer. As a result of the depletion of Mo, grain structures of Cr in the underlayer became vulnerable, and degeneration of microstructures began. As external force increases, Cr migration, mainly through the grain boundaries, became inevitable, and chromate products were formed during the aggressive corrosion state, marked with green dots in Figure 8.5(e). The alignment of grain boundaries from the top thin film to the bottom layer eventually opened possible tunnels for the release of Ni from the Ni/P amorphous structure, by which Ni excited into an active state with certain crystalline structure in cooperation with hydrogen absorption processes. The oxide layer at the grain boundaries is not dense and contains low-density regions that are highly diffusive with large diffusion coefficients. Moreover, acceleration of Ni releasing to the surface sped up, which was defined as disastrous corrosion, shown in grey in Figure 8.5(f). Geographically, the crystallites grown from Ni nuclei from amorphous structures had tetrahedral or polyhedral shapes, depending on oxidation conditions, thus forming two different type of Ni crystals, Ni and Ni_3P.[8.13] Both of these contents could dramatically change the crystalline volumes of Ni/P. Creation of corrosion pits was obviously a consequence of pulling out oxide nodules from the surface with external forces, represented as green circles with red dots within. Pit formation actually might accelerate the corrosion process, and grain structural damage then results.

8.2.3. Macroscopic Corrosion Mechanism

The macroscopic corrosion mechanism explained geometrically large events as a consequence of extensive corrosion processes beyond microscopic activities. The descriptions of macroscopic corrosion model were based upon many optical microscopic observations, surface topographic analysis, microscopic elemental distribution profile, and magnetic measurements. In reality, no clear-cut transition between microscopic and macroscopic corrosion could be defined.

As illustrated in the last section, metallic ions inside the thin film matrix mobile eventually migrate to grain boundaries and surface region to produce oxides. The continuous evolution of corrosion depended on critical external conditions, namely electric potential bias. In natural spontaneous corrosion, no external influence from electric field was applied, while potential/galvanic corrosion was achieved with an external driving force under an electric field. In this research, these two circumstances showed different corrosion rates because of the macroscopic differences of corrosion mechanisms.

However, visual observations after occurrences of corrosion process under both situations showed similar surface geometric features with localized circular spots, as reported in many previous findings. The differences between the surface features with and without potential bias were that the density and size of corrosion spots appear relatively small under no bias corrosion environments. This was because when metallic ions travel to surface to form oxides or hydroxides to stay on the surface, which naturally created a passive layer to hinder further migration of ions from beneath. The corrosion rate then slowed down dramatically. However, as indicated in *in-situ* ICP-MS experiments without potential introduced, most metallic ions dissolved at a constant linearly rate, which suggested that the diffusion mechanism in macroscopic corrosion was not the primary cause but creation of new corrosion spot was more feasible way to this corrosion model. Therefore, small corrosion spots are normally seen under unbiased corrosion sample surfaces. The greatest impact of the application of an electric field to a thin film surface it that it accelerated metallic ion movement microscopically and provided opportunities to

dislocate and strip off passivasion from the localized oxides or hydroxides. The consequence at the macroscopic scale is to open and create voids or pits.

The following picture shows a model of the evolution processes of a typical corrosion spot under both unbiased and biased conditions.

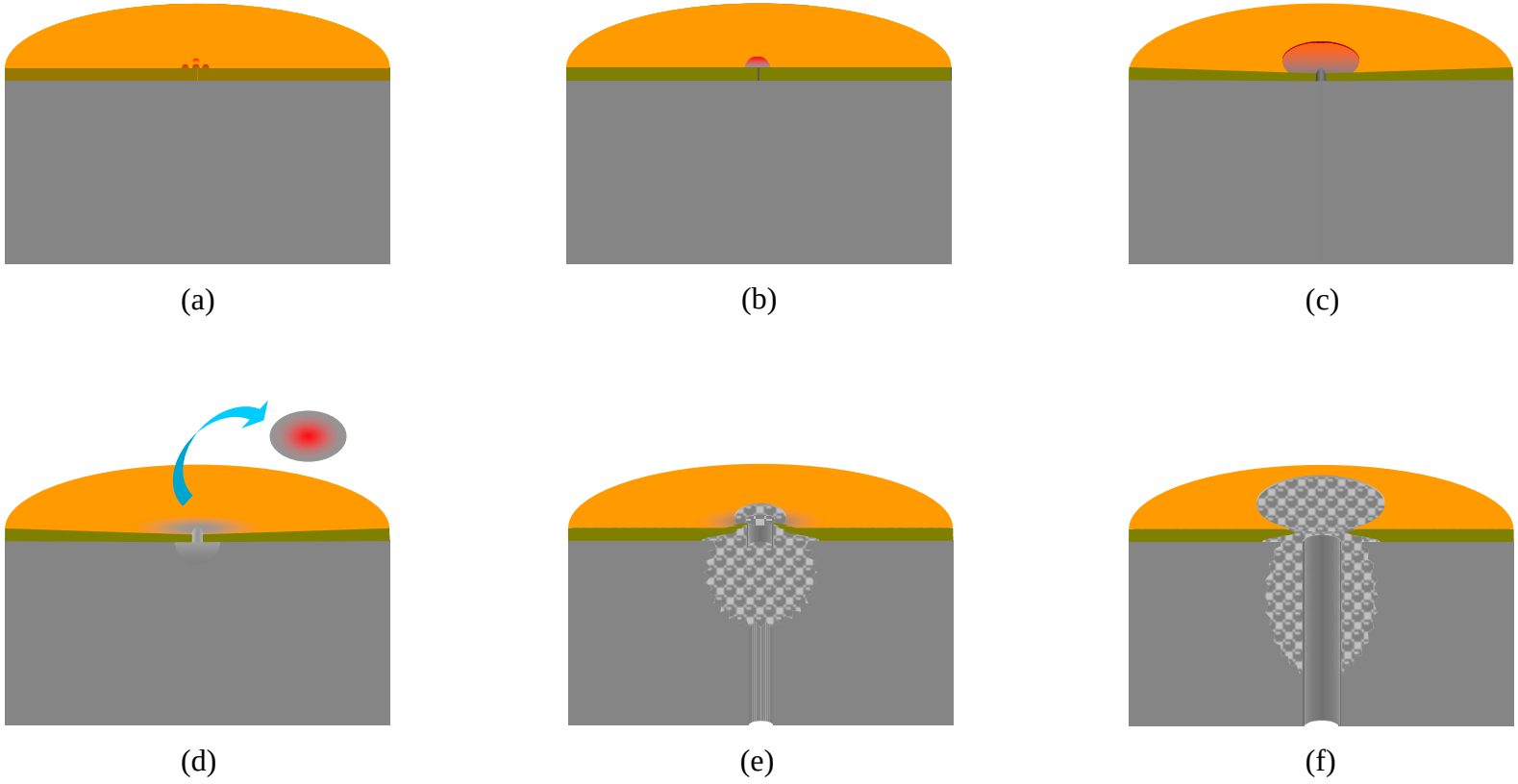

Figure 8.6. Macroscopic evolution processes of a corrosion spot

Macroscopically, small corrosion spots were formed based upon microscopic explanations described above, as shown in Figure 8.6(a). These small corrosion spots contain mostly elements from the magnetic layer and underlayer. As the progression of the corrosion process was prolonged, small corrosion spots grew to form large corrosion spots, as shown in Figure 8.6(b). At this point, the macroscopic structures of the magnetic layer remained largely unchanged. When the depletion of the Ni/P layer occurred, corrosion accelerated. However, nickel oxides or hydroxides formed on the surface created a possible passive layer that serves as a cap to prevent dissolution followed by more depletion, as shown in Figure 8.6(c). If no external disturbance is applied, as is seen in spontaneous corrosion processes, corrosion rate then decreases dramatically thereafter. As reported, the Ni/P alloy demonstrated the magnetic characteristic of super-paramagnetic properties in particulate formation, while paramagnetic behavior was in Ni/P clusters.[8.14] Therefore, a small amount of accumulation of Ni/P at the surface contributes slightly to magnetic disturbances was measured in many MFM studies.

When any external or internal mechanical force was applied, the adhesion of nickel oxides or hydroxides could be broken and a corrosion pit could be created. Meanwhile, due to thin film internal stress, upper layers then bent inward as Ni/P runs outward, as shown in Figure 8.6(d). The openness of the corrosion spot provided an opportunity for continuous reactions and to form a new hilltop. Instead of magnetic materials, excessive exposure of amorphous Ni/P to anodic corrosion then dominated the corrosion process.[8.15][8.16] Eventually, enlargement of Ni/P volume created a volcano shape and pushed the magnetic layer so that it bulges out, which dramatically increased the volume underneath, as illustrated in Figure 8.6(e). The cycling of the steps shown in Figures 8.6(d) and 8.6(e) promoted further catastrophic results, as demonstrated by elemental quantifications from EC-ICP-MS, elemental profiles in EDS analysis, and optical microscopic observations. The appearance of large open pores on corrosion spots on surfaces of those samples undergoing electric potential biased tests was a direct result.

With special privilege in this research, magnetization analysis and measurement was used to improve understanding of macroscopic corrosion with imaging of both surface and cross sections. Since only the magnetic thin film layer exerts a magnetic field, the study of magnetic images yielded valuable information for corrosion modeling at the

macroscopic level. When surface magnetic images showed no influence of magnetic patterns on small corrosion spot, cross sectional images of such multiple magnetic layers clearly demonstrated that the magnetic thin films were not completely bulged out but collapse inward, possibly due to thin film stress. TEM micrographic images of the inward bend direction aligned with a grain boundary supports this idea.

Because of the limited thickness of thin film layers, MFM images of several corrosion spots confirmed that the corrosion process began at the magnetic thin film layer, and then the flux of materials underneath penetrates through the top magnetic layer. The thickness of the magnetic layer became thinner and wedged at rim of corrosion volcanoes. No piling up of magnetic material was shown in those cross section micrographs, which proves that the pile up material indicated by surface topographic measurements using AFM were mainly non-magnetic compounds, such as oxides or hydroxides. When the macroscopic corrosion pit was formed, a certain amount of magnetic material was imaged at bottom of the corrosion cavity, which clearly indicated that the magnetic thin film could be imploded while substrate materials moved in the reverse direction.

The importance of understanding the surface topography of corrosion spots as they evolved from the disk surface was of great concern to the subject of head and media interface failure mechanisms.[8.17] As demonstrated in this research, the corrosion spots grew freely in controlled environments. However, in reality, when magnetic recording operations engaged a magnetic thin film disk and a magnetic sensor, which literally levitated several hundred nanometers above the disk surfaces. Such nanometer gaps in mechanical adjustments require very small tolerance to surface anomalies, including corrosion nodules, of any size.

References:

8.1. Frankel, G. S., "Localized Corrosion of Metals; A Review of the Rate-Controlling Factors in Initiation and Growth," in *Passivity of Metals and Semiconductors*, M. B. Ives, J. L. Luo, and J. R. Rodda, eds., The Electrochemical Society Proceedings Volume 99-42 (2001) pp.445-475

8.2. Macdonald, D. D., "The Point Defect Model for the Passive State", *Journal of Electrochemical Society*, 139(12) (1992) pp.3434-3449

8.3. Godard, H.P., W.B. Jepson, M.R. Bothwell, and R.L. Kane, "The Corrosion of Light Metals", John Wiley and Sons, N.Y., 1967, pp.732

8.4. Foley, R.T., "Localized Corrosion of Aluminum Alloys - A Review," *Corrosion*, Vol.42, No.5 (1986) pp.277-288.

8.5. Frankel, G. S., "Corrosion of microelectronic and magnetic storage devices", Chapter 15, *Corrosion Mechanisms in Theory and Practice*, edited by P. Marcus and J. Oudar, Marcel Dekker, Inc, 1995, pp.547-579

8.6. Novotny, V. and N. Staud, "Correlation between environmental and electrochemical corrosion of thin film magnetic recording media", *Journal of Electrochemical Societ: Electrochemical Science and Technology*, Vol.135, No.12 (1988) pp.2931-2938

8.7. Xia, W.S., Y. Fan, Y.S. Jiang, and Y. Chen, "Local surface state of amorphous NiP and NiB alloy catalyst", *Applied Surface Science*, 103(1996) pp.1-9

8.8. Li, H., H. Li, W. Dai, W. Wang, Z. Fang, and J. Deng, "XPS studies on surface electronic characteristics of Ni-B and Ni-P amorphous alloy and its correlation to their catalytic properties", *Applied Surface Science*, 152(1999) pp.25-34

8.9. Paseka, I, "Evolution of Hydrogen and Its Sorption on Remarkable Active Amorphous Smooth Ni-P(x) Electrode", *Electrochemica Acta*, Vol.40, No.11 (1995) pp.1633-1640

8.10. Yang, J., Q. Cai, S. Dong, H. Li, and J. Deng, "Morphology characteristic of surface crystallization on amorphous $Ni_{88}P_{12}$ film", *Applied Surface Science*, 147(1999) pp.33-38

8.11. Thompson, C.V., "Structure Evolution During Processing of Polycrystalline Films", *Annual Review of Materials Science*, 30 (2000) pp.159-190

8.12. Petrov, I., P.B. Barna, L. Hultman, and J.E. Greene, "Microstructural evolution during film growth", *Journal of Vacuum Science and Technology: A* 21(5), (2003) pp.S117-S128

8.13. "CRC Materials Science and Engineering Handbook", 3rd Edition, J. F. Shackeford and W. Alexander Editors, CRC Press LLC, 2001, pp.22-43

8.14. Burgstaller, A., W. Socher, and J. Voitländer, "Magnetic studies of amorphous Ni-P alloys", *Journal of Magnetism and Magnetic Materials*, 109(1992) pp.117-123

8.15. Li, H., H. Chen, S. Dong, J. Yang, and J. Deng, “Study on the crystallization process of Ni-P amorphous alloy”, *Applied Surface Science*, 125(1998) pp.115-119

8.16. Vlassak, J. J., "Channel cracking in thin films on substrates of finite thickness", *International Journal of Fracture*, 119 (4), (2003) pp.299-312

8.17. Uy, J. C., “Head/Disk Interface Failure Mechanism”, *IEEE Transactions on Magnetics*, Vol.26, No.5 (1990) pp.2697-2699

CHAPTER NINE

CONCLUSIONS AND PERSPECTIVES

9.1. General Conclusions

1. Traditionally, corrosion is considered to be an electrochemical phenomenon, and most studies are performed by electro-galvanic or electro-potential derivative methods. However, thin film materials have demonstrated different corrosion behaviors from bulky alloys due to their structural characteristics. This research proposed two different corrosion models corresponding to different corrosion stages in a single corrosion run.
2. In order to demonstrate corrosion mechanisms, extensive studies were conducted during which novel methodologies and techniques were used that systematically unveiled the effects of corrosion on microstructural characteristics, surface topography, magnetic performance, and electrochemical behavior. First of a kind thin film corrosion studies and strategies contributed significantly to the success of this research. Instead of phenomenological explanations of thin film corrosion mechanisms, this research provided quantitative characterization results on corrosion reactions at different points in time for a variety of corrosive conditions on the nano-scale.
3. Structurally, thin films used in many electronic devices are created by vacuum deposition techniques, which create unique epitaxial structural orientations. The columnar grain structures and perpendicularly oriented grain boundaries in thin films dominate the kinetics of corrosion. Grain boundaries and interfaces in the thin film stack provide the primary diffusion paths for reactants during oxidation process.

4. In magnetic thin films, microstructural changes taking place during corrosion start at grain boundaries where cobalt becomes vulnerable due to its unfavorable crystallographic structure resulting from chromium segregation. Reaction layers at grain boundaries expand into the interface between the magnetic layer and underlayer in a very short period under voltammetric conditions. High-resolution TEM images show a high penetration rate of nickel in the substrate, which results in the formation of crystals at the interface. However, grain structures maintain bulk volumes until excessive corrosion occurs. Degradations of grains and grain boundaries in both the magnetic layer and underlayer have been extensively studied with electron nano-probe EDS X-ray profiling and electron diffraction.

5. In addition, surface characteristics after corrosion occurs were also studied with a variety of techniques including optical microscopy, SEM, EDS, and AFM. Corrosion nodules are created initially regardless of corrosion conditions. However, a majority of the nodules remain in a slow growth phase under potentiometric conditions, while corrosion pits have been frequently identified on surfaces undergoing electro-galvanic or potential corrosion. The transformation of corrosion nodules into pits is explained as the result of the removal of oxides from the surface driven by an electric field. With the absence of surface nodules, the corrosion process is accelerated, and further corrosion is promoted. Consequently, extremely large amounts of nickel oxide can be detected in the form of needle-like nickel oxides. Surface textures were also profiled by AFM and MFM to explain the origin of surface corrosion at the slope of texture lines.

6. Due to the magnetism of Co alloy thin films, magnetic measurement and mapping techniques were implemented in this research project, and the magnetic characterization correlated with changes in microstructures during corrosion. Cross sectional MFM imaging and the random demagnetization method, for the first time demonstrated magnetic characterization at corrosion nodules. Magnetic measurements and calculations provide extensive three-dimensional views of the corrosion mechanism.

7. Conclusions about the microscopic and macroscopic corrosion mechanisms are not achievable without a confident demonstration of the individual corrosion behaviors of the metal constituents in thin film structures. Successful development of an on-line coupling EC-ICP-MS system made this task possible. The combination of electrochemical reactions and highly sensitive ICP-MS instrumentation to realize *in-situ* measurements for each metallic ion from the thin film stack. The dissection of collective corrosion reactions into single events provides unprecedented knowledge about the corrosion mechanism in thin film materials.

8. In the EC-ICP-MS experiments, cobalt is depleted from thin film structures into electrolyte solutions during two distinguishable stages with different dissolving rates. The initial high dissolution rate of Co is mainly associated with the corrosion event at the grain boundary region until a plateau is reached. The low dissolution rate thereafter is caused by structural degradations of the grains. The other elements in the structures, such as Cr, Pt and B, react to corrosive anodic attacks in different ways as was shown in many experiments involving *in-situ* quantifications, which clearly indicate that the overall corrosion process from thin film materials is the collective achievement of each individual reaction under certain conditions. Different responses to corrosion from different elements in thin films from different locations are due to their individual characteristics naturally inherited during thin film epitaxial growing history.

9. By revealing corrosion microstructure and electrical history, the “mystery” phenomena proclaimed in Chapter 1 were unveiled. The source of Co/Pt and Pt only detected on magnetic sensor surfaces could be practically from magnetic thin film structures resulting from corrosion processes under certain corrosive conditions. The precipitation of such “alloy”, from corrosion point of view, could occur during every early stage of corrosion. On the other hand, oxidation of nickel from substrate layer passing through grain boundaries could be linked to another mystic identification of nickel oxides on a sensor surface when the sensor sweeps a disk surface in proximate zero flying height. In addition, hypotheses of magnetic interferences in sensing magnetic streak from magnetic thin film structures

resulting “soft error” could be well explained by presence of magnetized particles, such as Co/Pt or crystallized NiO due to occurrences of localized corrosion. In ever-smaller sizes of magnetic transitional bits, small-magnetized objects produced from corrosion oxidation processes not only influence and distort localized magnetic field but also cause physical destruction when space between a magnetic sensor and a disk surface gets closer and closer to the nanometer range. The intolerance of small corrosion nodules from both physical and magnetic defects elevates the importance of more studies of corrosion in such advanced magnetic thin film structures.

9.2. Future Perspectives

1. As the magnetic recording industry continually races to achieve high recording density, the thin film structures and materials used in the alloys become much more complex. However, the fundamental characteristics of thin film structures remain the same because thin film deposition will continue to be used to produce such thin films. These research results can be implemented in many areas for quality verification and development improvements for realization of better corrosion resistance.
2. Even though, the method of quantification measurements with unconventional coupling technique between EC and ICP-MS has demonstrated to great benefit for thin film corrosion studies, the concept of combining new techniques with traditional approaches can be extended into many other types of corrosion studies, such as electrochemistry in coupling with ion chromatography (IC) or gas chromatography (GC), etc.
3. As was demonstrated in this research, nitric acid was used in all the corrosion experiments. Other corrosive solutions can be also applied in this coupled on-line technique with different calculations and setups, such as in alkaline solutions or biological aqueous.
4. Additionally, quantification of elemental changes using the coupling technique of EC-ICP-MS can shorten corrosion test time dramatically and give greater

accuracy in terms of/with regard to the empirical determination of the occurrence of corrosion.

5. Even though the results of this study are obtained based upon magnetic thin films, similar conclusions can be well applied to other non-magnetic thin film structures, such as medical components put into the human body during medical applications, in corrosive environments.

Appendix I:

The construction of the corrosion vessel for Electrochemical (EC) ICP-MS measurements

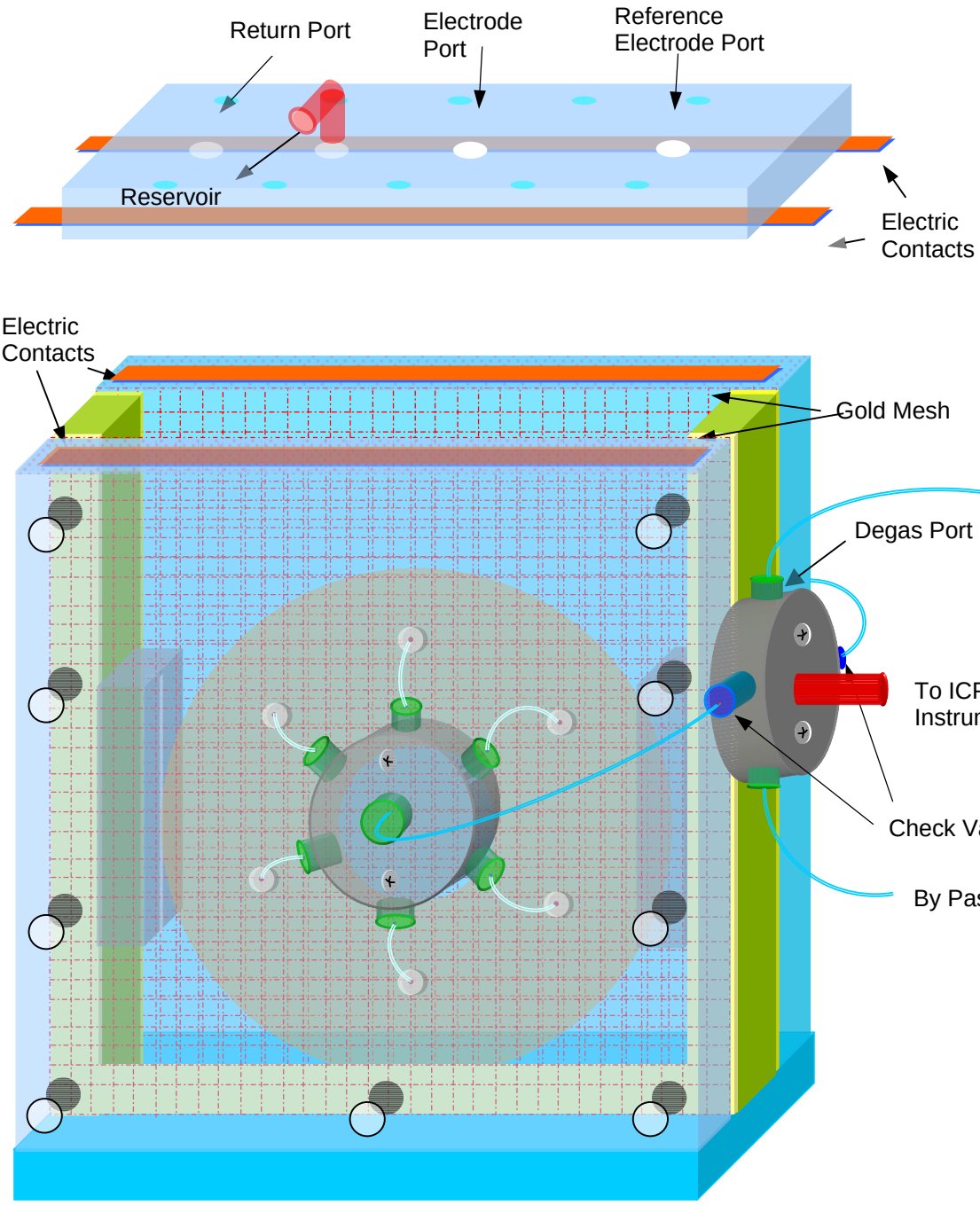

Appendix II:

Design and construction of an assembly of diametrical multiple cells for electrochemical reaction measurements

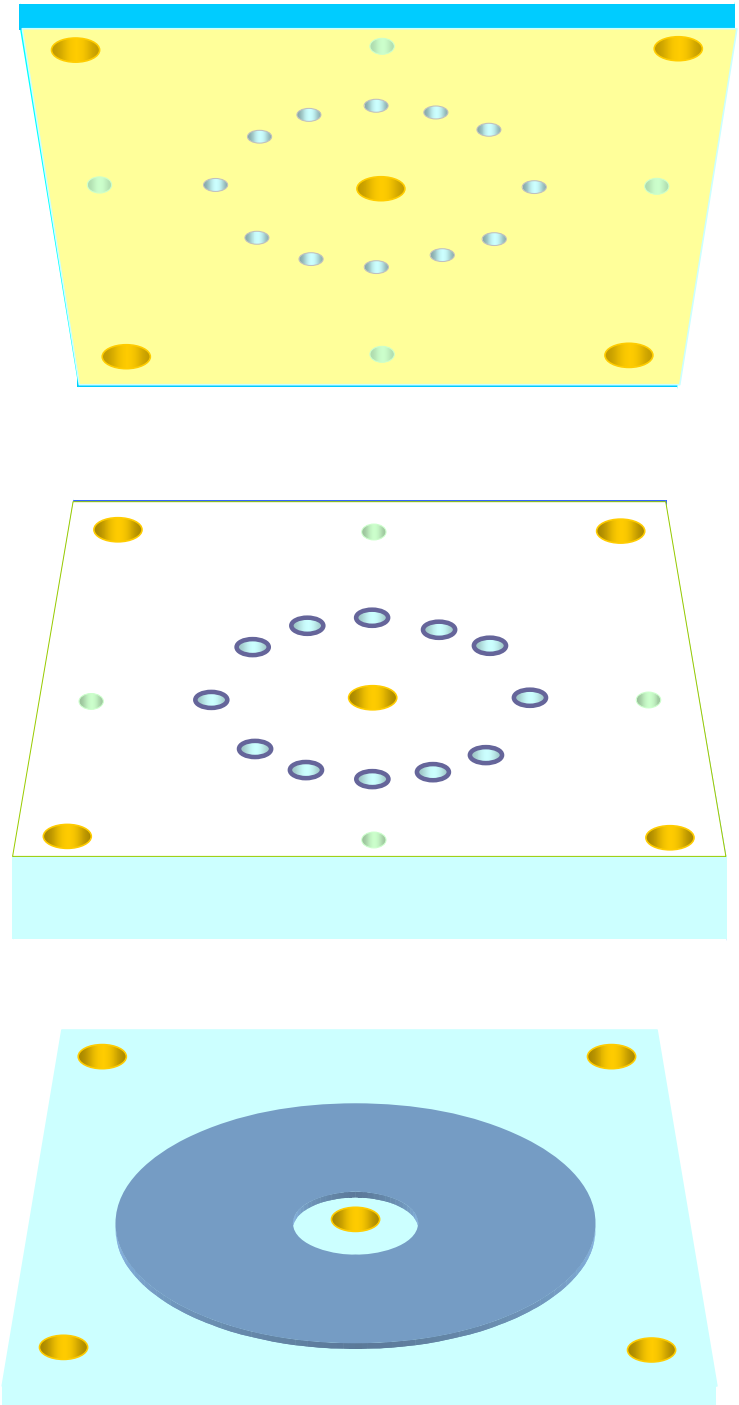

Appendix III: Digital Optical Micrographic Images at 200X Magnification

Following optical micrographic images are examples selected from a series of captured images, which were recorded a frame per minute in the experiments in nitric acid solutions with different concentrations.

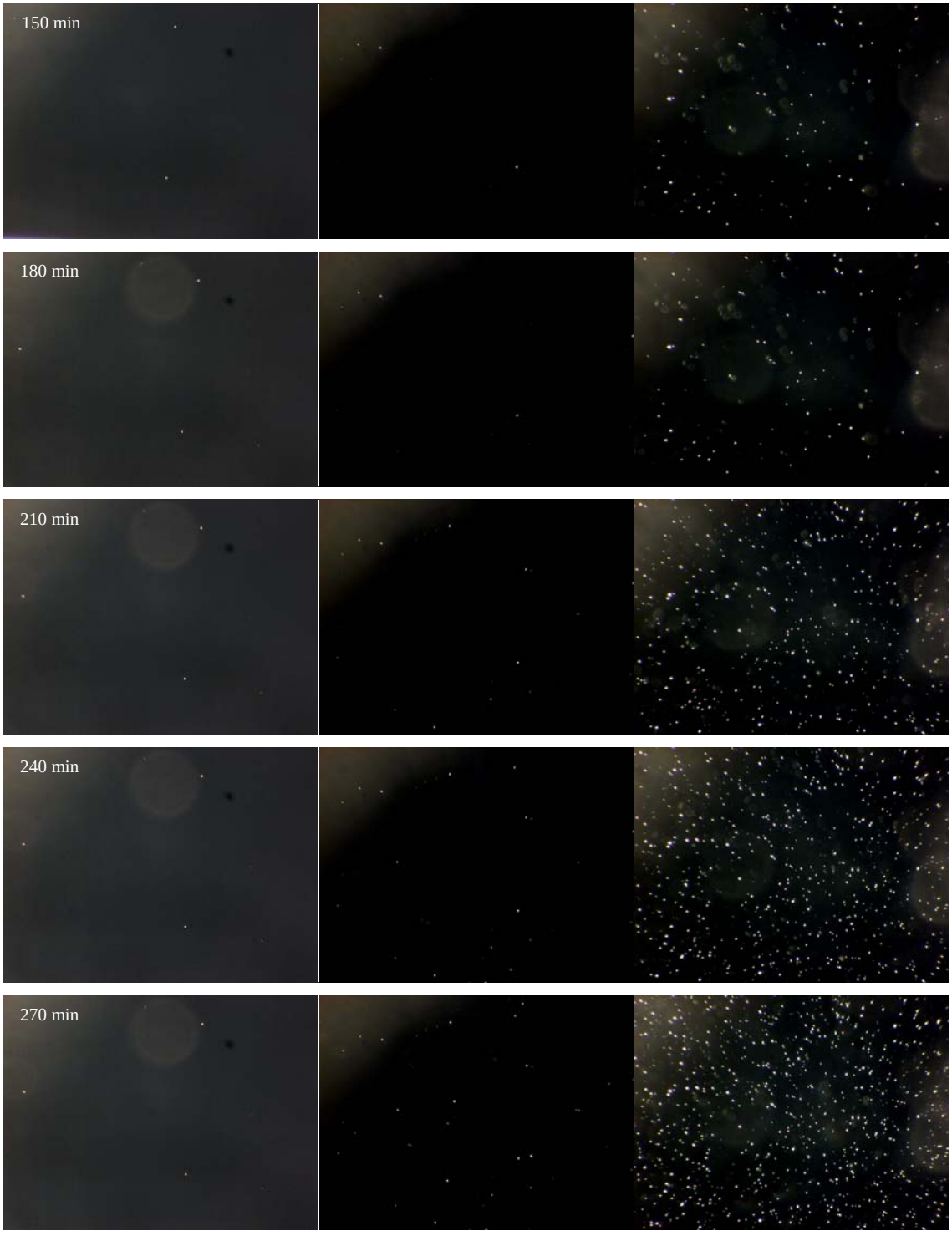
150 min
180 min
210 min
240 min
270 min

Appendix IV: Procedures of TEM Cross Section Samples

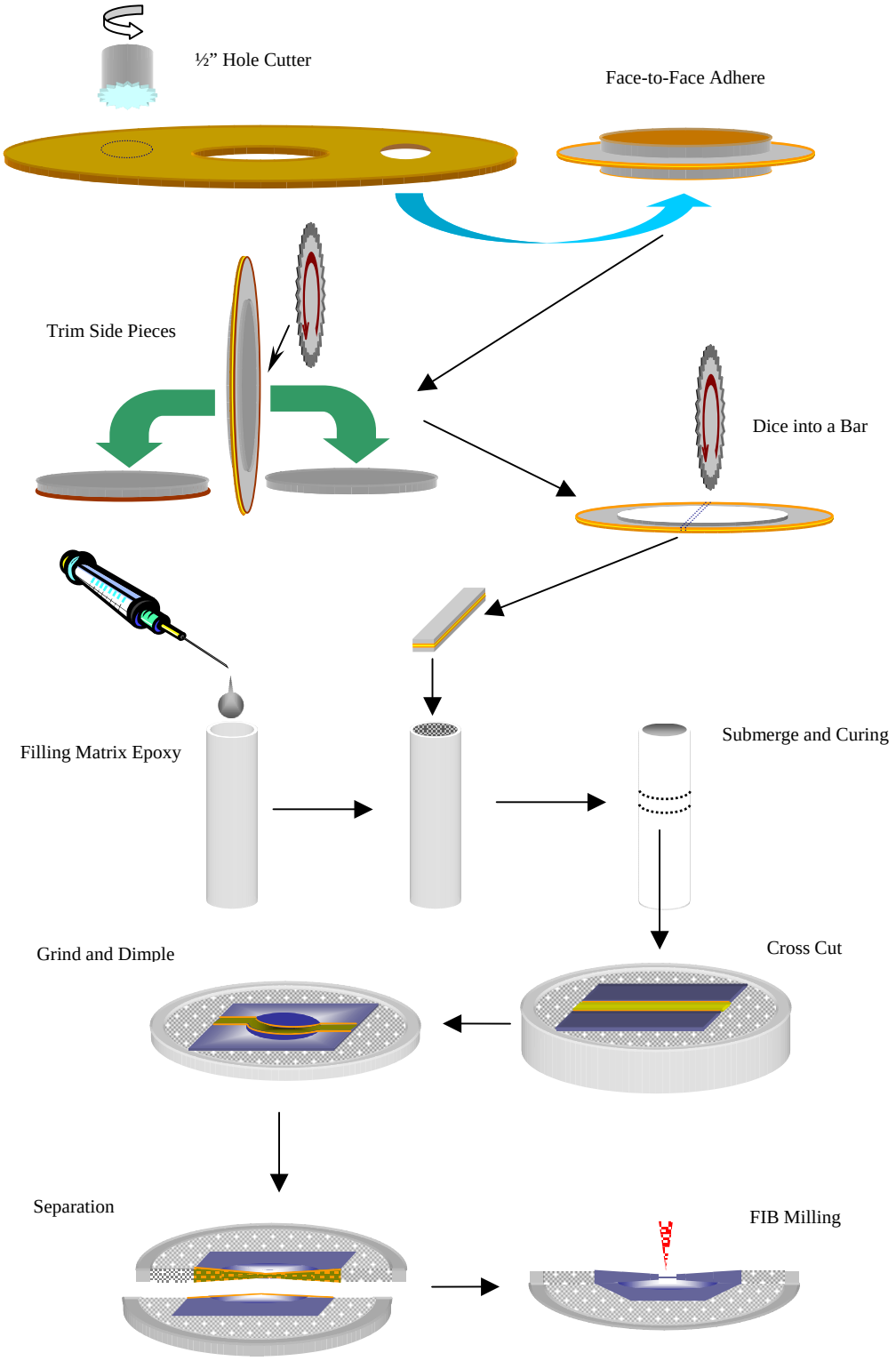

Appendix V:

Hysteresis loop measured by VSM for samples prepared in 2% HNO_3 at different time of potentiometric tests

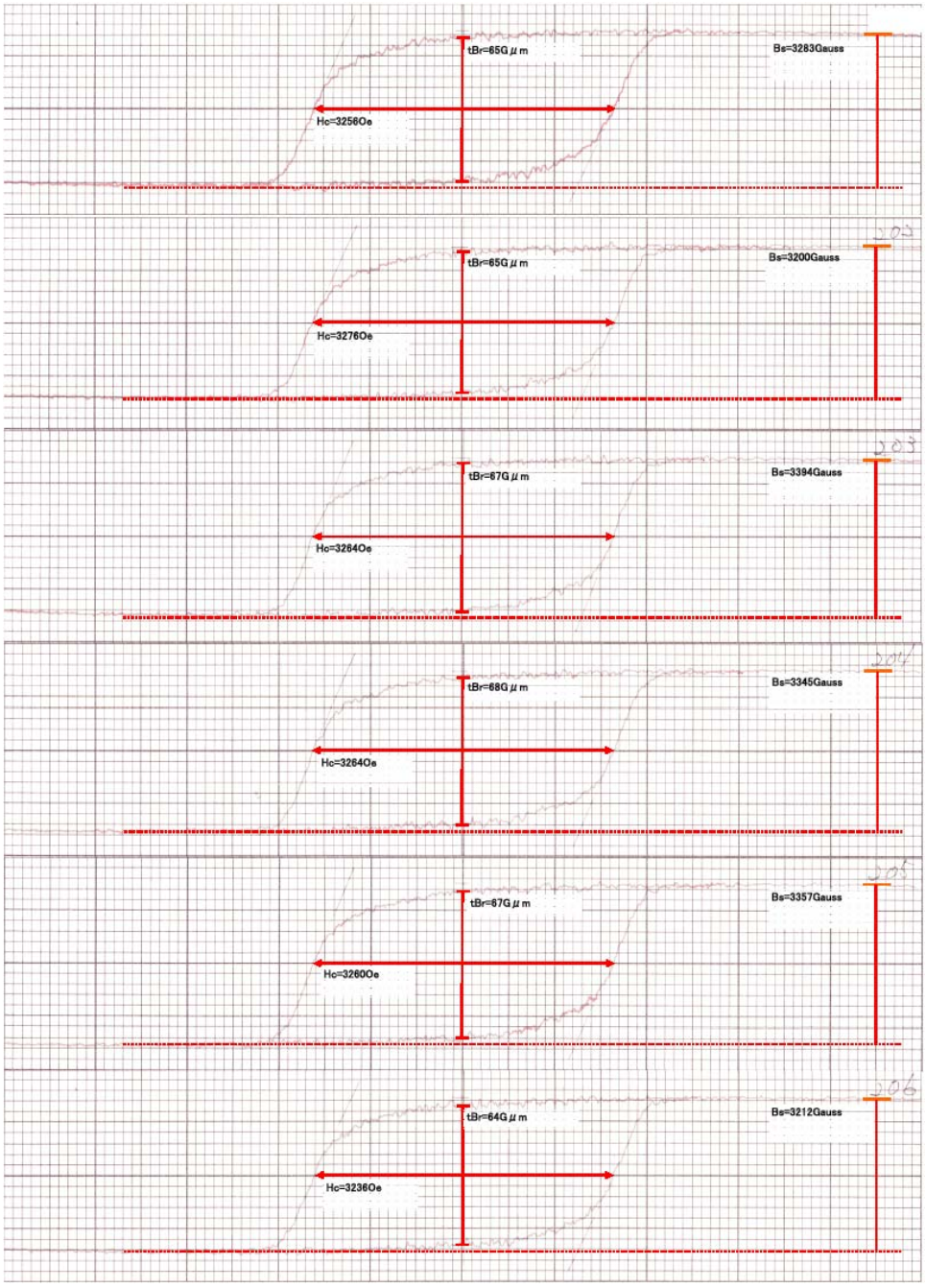

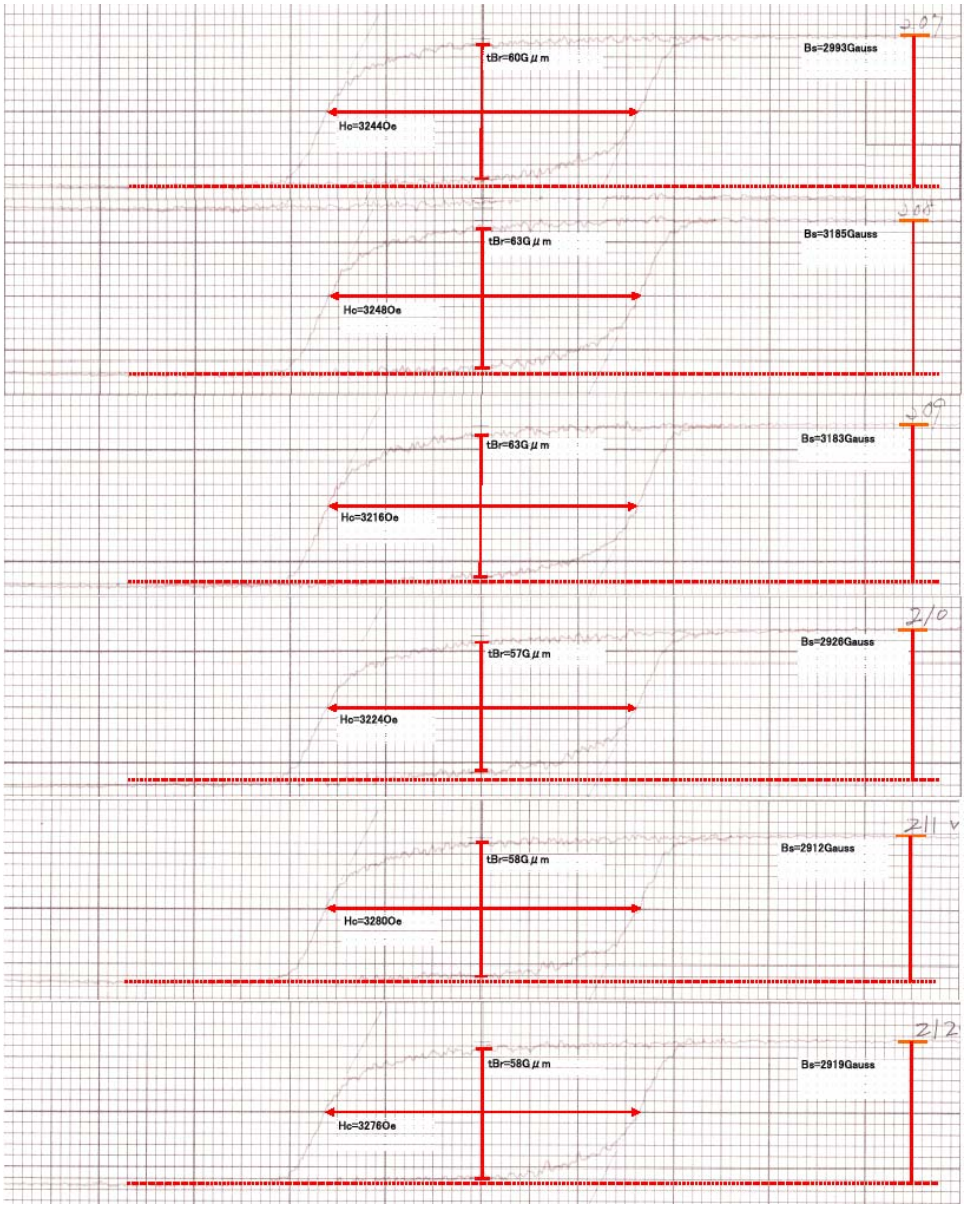
tBr=60G μ m
Hc=3244Oe
Bs=2993Gauss
tBr=63G μ m
Hc=3248Oe
Bs=3185Gauss
tBr=63G μ m
Hc=3216Oe
Bs=3183Gauss
tBr=57G μ m
Hc=3224Oe
Bs=2926Gauss
tBr=58G μ m
Hc=3280Oe
Bs=2912Gauss
tBr=58G μ m
Hc=3276Oe
Bs=2919Gauss

Appendix VI:

Cross-Section Preparation Procedures for AFM/MFM Analysis

Clamping two tested disks face-to-face with wax in between to protect interested area. Coupon disk with ¼" diameter with a hole-cutter is produced.

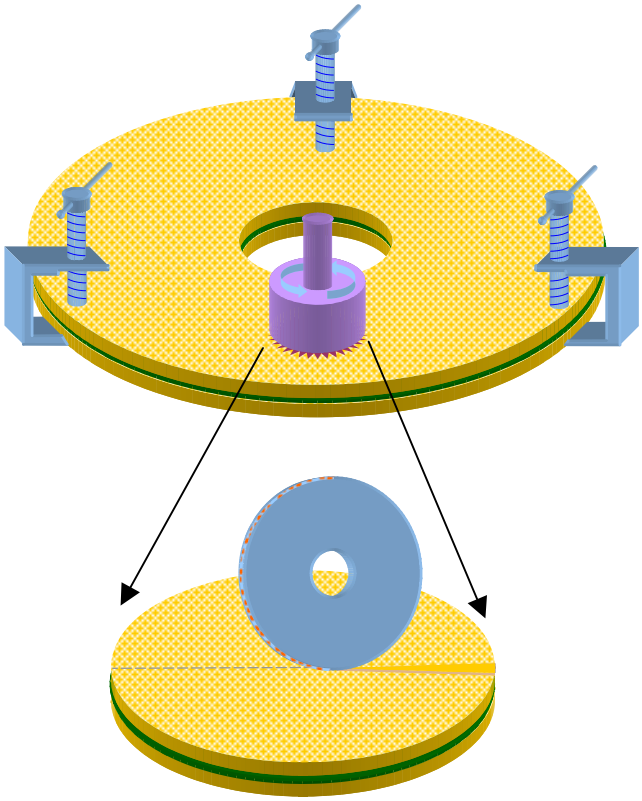

¼" coupon is then sliced into half along middle line by using a diamond saw.

The adhered cross-section surfaces are then polished on abrasive paper and separated and cleaned thereafter.

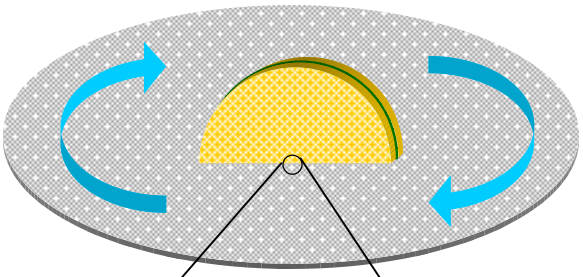

A Pt bar is deposited to protect defect and make space for tip scanning from AFM/MFM before ion milling in a FIB system with vertical trimming from the edge.

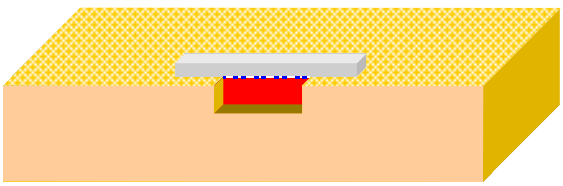

Appendix VII:

Examples of MFM images for a series demagnetized magnetic thin films prepared in 2% HNO_3 for 15 min after 750 mV polarization tests under external magnetic fields in range from 0 to 736 Oe.

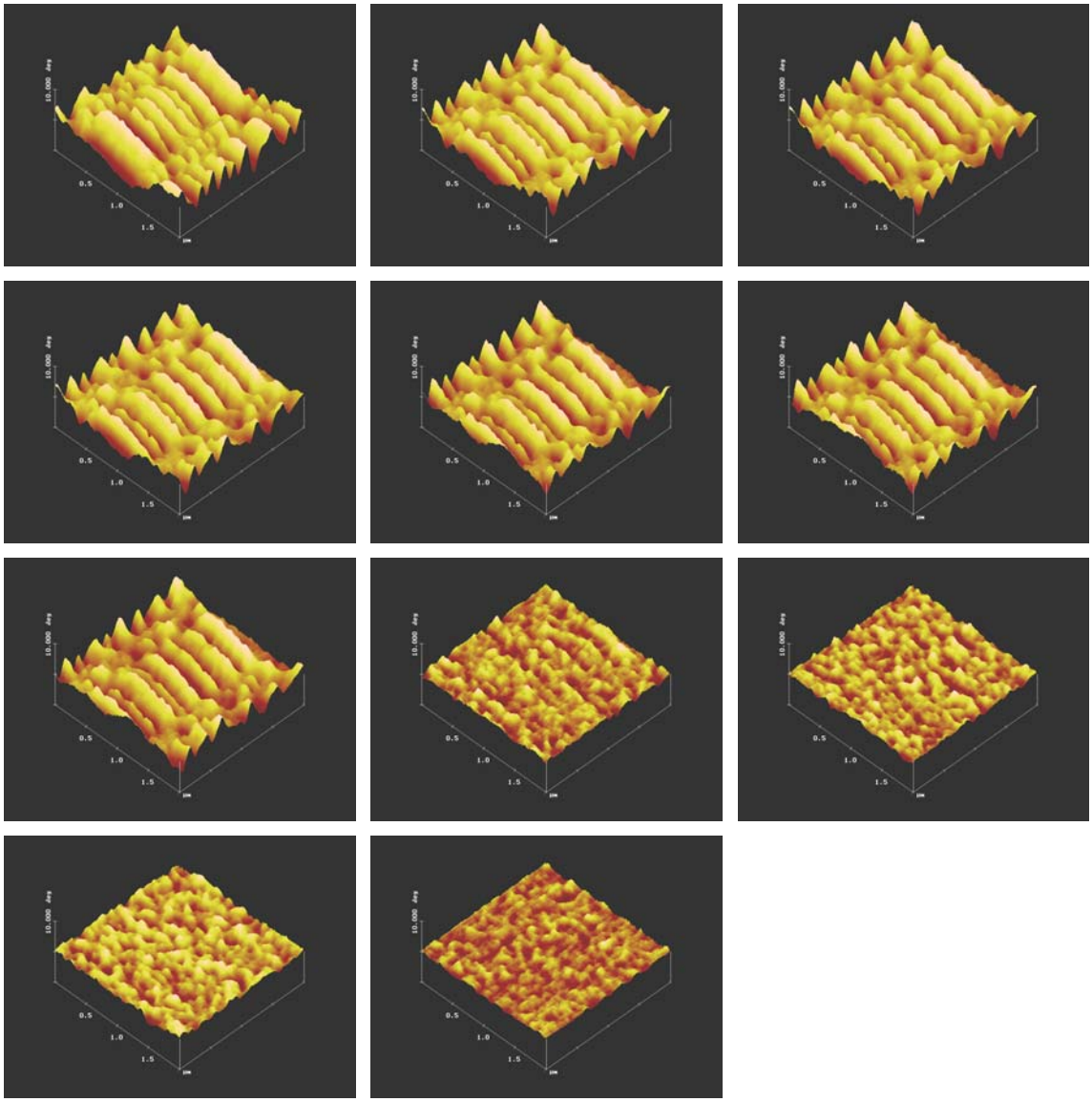

Appendix VIII:

List of Aquatic Electrochemical Reaction Potentials of Interested Elements

Electrochemical Reactions	Potential (V)
$Co^{3+} + e^- = Co^{2+}$	1.92
$Co(OH)_3 + e^- = Co(OH)_2 + OH^-$	0.17
$Co^{2+} + 2e^- = Co$	-0.28
$Co(OH)_2 + 2e^- = Co + 2OH^-$	-0.73
$CrO_2 + 4H^+ + e^- = Cr^{3+} + 2H_2O$	1.48
$HCrO_4^- + 7H^+ + 3e^- = Cr^{3+} + 4H_2O$	1.35
$Cr_2O_7^{2-} + 14H^+ + 6e^- = 2Cr^{3+} + 7H_2O$	1.232
$Cr_4^{2-} + 4H_2O + 3e^- = Cr(OH)_3 + 5OH^-$	-0.13
$Cr^{3+} + e^- = Cr^{2+}$	-0.407
$Cr^{3+} + 3e^- = Cr$	-0.744
$Cr^{2+} + 2e^- = Cr$	-0.913
$CrO_2^+ + 2H_2O + 3e^- = Cr + 4OH^-$	-1.2
$Cr(OH)_3 + 3e^- = Cr + 3OH^-$	-1.48
$PtO_3 + 2H^+ + 2e^- = PtO_2 + H_2O$	1.7
$PtO_3 + 4H^+ + 2e^- = Pt(OH)_2^{2+} + H_2O$	1.5
$Pt(OH)^+ + H^+ + 2e^- = Pt + H_2O$	1.2
$Pt^{2+} + 2e^- = Pt$	1.18
$PtO_2 + 4H^+ + 2e^- = PtO + 2H_2O$	1.01
$PtO_2 + 4H^+ + 4e^- = Pt + 2H_2O$	1.0
$Pt(OH)_2 + 2e^- = Pt + 2OH^-$	0.14
$Ta^{3+} + 3e^- = Ta$	-0.6
$Ta_2O_5 + 10H^+ + 10e^- = 2Ta + 5H_2O$	-0.75
$H_3Mo_7O_{24}^{3-} + 45H^+ + 42e^- = 7Mo + 24H_2O$	0.082
$MoO_3 + 6H^+ + 6e^- = Mo + 3H_2O$	0.075
$MoO_2 + 4H^+ + 4e^- = Mo + 4H_2O$	-0.152
$Mo^{3+} + 3e^- = Mo$	-0.20

$NiO_2 + 4H^+ + 2e^- = Ni^{2+} + 2H_2O$	1.678
$Ni^{2+} + 2e^- = Ni$	-0.257
$NiO_2 + 2H_2O + 2e^- = Ni(OH)_2 + 2OH^-$	-0.49
$Ni(OH)_2 + 2e^- = Ni + 2OH^-$	-0.72
$B(OH)_3 + 7H^+ + 8e^- = BH_4^- + 3H_2O$	-0.481
$H_3BO_3 + 3H^+ + 3e^- = B + 3H_2O$	-0.8698
$H_2BO_3^- + 5H_2O + 8e^- = BH_4^- + 8OH^-$	-1.24
$H_2BO_3^- + H_2O + 3e^- = B + 4OH^-$	-1.97
$P(white) + 3H^+ + 3e^- = PH_3(g)$	-0.063
$P(red) + 3H^+ + 3e^- = PH_3(g)$	-0.111
$H_3PO_4 + 2H^+ + 2e^- = H_3PO_3 + H_2O$	-0.276
$H_3PO_3 + 3H^+ + 3e^- = P + 3H_2O$	-0.454
$H_3PO_3 + 2H^+ + 2e^- = H_3PO_2 + H_2O$	-0.499
$H_3PO_2 + H^+ + 3e^- = P + 2H_2O$	-0.508
$P + 3H_2O + 3e^- = PH_3(g) + 3OH^-$	-0.87
$PO_4^{3-} + 2H_2O + 3e^- = HPO_3^{2-} + 3OH^-$	-1.05
$HPO_3^{2-} + 2H_2O + 2e^- = H_2PO_2^- + 3OH^-$	-1.65
$HPO_3^{2-} + 2H_2O + 3e^- = P + 5OH^-$	-1.71
$H_2P_2^- + e^- = P + 2OH^-$	-1.82
$2H^+ + 2e^- = H_2$	0.000
$O_2 + 2H_2O + 4e^- = 4OH^-$	0.401
$NO^{3-} + 4H^+ + 3e^- = NO + 2H_2O$	0.96
$O_2 + 4H^+ + 4e^- = 2H_2O$	1.229

Lide, D. R., "CRC Handbook of Chemistry and Physics", CRC Press, 81st Edition, 2000-2001, pp.8-21 – 8-31